Exploring the Influence of Non-Covalent Interactions on Electron Transfer Properties of Tyrosine and Tryptophan

by

Curtis A. Gibbs

B.Sc. (Chemistry), Mount Allison University, 2016

Thesis Submitted in Partial Fulfillment of the
Requirements for the Degree of
Doctor of Philosophy

in the
Department of Chemistry
Faculty of Science

SIMON FRASER UNIVERSITY
Spring 2023

Declaration of Committee

Name:	**Curtis A. Gibbs**
Degree:	**Doctor of Philosophy**
Title:	**Exploring the Influence of Non-Covalent Interactions on Electron Transfer Properties of Tyrosine and Tryptophan**
Committee:	**Chair:** **Paul Li** Professor, Chemistry
	Jeffrey Warren Supervisor Associate Professor, Chemistry
	Charles Walsby Committee Member Associate Professor, Chemistry
	Roger Linington Committee Member Professor, Chemistry
	Tim Storr Examiner Professor, Chemistry
	Cecilia Tommos External Examiner Professor, Biochemistry and Biophysics Texas A&M University

Abstract

Biological electron transfer (ET) is an intricate process, and in many cases, these ET events are coupled with proton transfer reactions, which can add complexity to reaction mechanisms. Importantly, there is a distance dependence at which these reactions can occur. Proton transfer must occur over short reaction distances. In contrast, the rate of ET decreases exponentially as the distance between the electron donor and acceptor increases. It is these long-range ET (or proton-coupled ET) reactions that require the use of reactive intermediates in functional biological systems, and in the context of this thesis, these reactive intermediates can be either tryptophan (Trp) or tyrosine (Tyr). Proton-coupled ET via Trp and Tyr residues in proteins has been deeply explored within the literature, however, much less is known about how nearby non-covalent interactions impact the properties of Trp and Tyr. Herein, an artificial protein model system was constructed using blue-copper azurin from *Pseudomonas aeruginosa*, such that we can study how substitution of the amino acids alanine, leucine, lysine, arginine, glutamine, and methionine can introduce or remove non-covalent interactions within the microenvironment surrounding a Trp or Tyr residue. Their effect on tuning the electronic properties of either of these aromatic residues is explored also using protein absorption and fluorescence, electron paramagnetic resonance, electrochemistry, and transient absorption spectroscopy.

Keywords: electron transfer; protein microenvironments; redox-active amino acid residues; non-covalent interactions; biophysical chemistry

Dedication

To my Nan, for her constant love, support, and curiosity.

Acknowledgements

When you actually come to the end of your PhD, you realize that there's a lot of people that have come and gone in your life over the course of the degree. From lab mates, to friends, to new family members, there's a whole slew of changes that happen in your life. It's nearly impossible to thank everyone and I barely even know where to start.

First, I need to thank my parents for supporting me, from pushing me to strive for the best all through my life. They might not understand much of what I'm doing, but they're always interested in hearing about what I'm working on and ensuring that I'm happy living on the other side of the country (no matter how much my mom wants me back in Nova Scotia). Second, I need to thank my nan and our (almost) weekly phone calls. No matter how many times she asked the same question over and over, just hearing her voice helped to get me through a tough day.

Third, I need to thank Jeff. With the chaos I brought along with me to every conversation, I can't imagine having worked with anyone else. From telling you to leave me alone to having some of the greatest conversations I've had (scientific or otherwise), you were there for me professionally and personally and I can't be more grateful. Somehow, every single time I came to you saying that I was ready to quit, you always talked me back down to reality (especially in the latter days when I was writing this thesis). I don't think I ever cried in front of you but I was definitely almost there a couple times. Thank you for keeping our fridge stocked with beer, some afternoons I just needed that beer to end the day (especially after spending hours and hours with that laser).

Now for all the friends I've had the chance to get to know since I've moved here. Jessica Miller was one of the first people who took me under her wing and showed me SFU. Not only did she introduce me to protein expression, characterization, and everything else that came with grad school, but our previous connection from MtA brought us that much closer. You showed me around the city, included me with your friends, and invited me to various events. Without you, my life in BC would've been drastically different and so many of my most memorable experiences would have never existed. I'm so proud of all your accomplishments and I can't wait to see you again. I'm going to lump Ryan in here too since I met him because of you. The two of you were two of my closest friends and I had so much fun spending time with you guys. The memories I have with you two (like

Ryan and I waking you up to ask permission to go to Church's Chicken at 4am) are some of my favourite moments still. Video games, board games, and more, you guys were there for the best times of my PhD and I can't be more grateful.

Next, Soumalya Sinha, aka Susu. I remember walking into that student office downstairs my first day and being so completely lost. Rhea was frantically clearing out the spot next to you so I had a spot to sit and that was when we first met. Since that day, I don't really know how we became so close, we just did. I was loud, obnoxious, and crazy, and I don't know how you dealt with me for such a long time. You always gave me your leftover food, you always made fun of me, and somehow we wrote a paper together in a week that ended in calamity with me submitting my NSERC application and the website failing. I made so many memories with you and you were one of my best friends. Seeing you walk into the office always made me excited, mainly because I had someone I could poke fun at. We always made fun of each other and lightened the mood when things were tough and I'm glad we've been able to stay in touch ever since you've left. I'm so excited to finally visit you and possibly taking a trip to India!

The entire Warren group over the years has been everchanging and every single person impacted my experience in grad school in some way or another. There are too many people to thank individually but it's important to mention all the personal and intellectual conversations I've had with each. Specifically, I wanted to thank all the students I've had the privilege of mentoring. You've taught me how to be a better teacher and these are skills I'll be able to apply in my everyday life moving forward. Next I have to thank a few specific Warren group members aside from Susu. Ana, Brooklyn, and William, the three of you have had your fair share of interactions with me. From arguing and fighting to long nights of destressing and getting to know each other, you were all so important in shaping the latter portions of my degree. William, you provided me so much insight into various biological techniques and always critiqued me when you saw me doing something dumb and wrong. As much I hated it in the moment, ultimately it was a huge help. Brooklyn, I'll never forget when I stormed into the office angry about someone breaking the P1000 and not realizing it was you. You've been sitting next to me for such a long time and I love how we began to have a non-verbal connection in every single situation and I'll never forget those late nights with you in the office. Ana, I don't even know where to start with you. I'll never forget my first impression of you, and I hope you don't either. Traveling to conferences with you was always a wild time, mainly IDW in Victoria when I yelled at

you for forcing me out of bed to only show up at the ferry 3 hours early. As much as we may have argued throughout our time together, I still consider you a really close friend that I could go to for anything if I needed. In all, the four of us together was always a chaotic mess, William screaming, Brooklyn having one beer and then talking a mile a minute, Ana “momaging” all of us, and then me just being overly dramatic with every situation. I also want to thank some more recent key people like Scheryn, Mike, Nick, Phil (who unofficially joined the Warren lab whether he wanted to or not) for somehow sharing an office with me and always being up to chat and have a good time. Nikta, you only just joined so I haven’t gotten to know you very well but you’ll be a great addition to the group!

I have to also thank Greg MacNeil. We met at MtA and didn’t really start talking to each other until our final year. Then you moved here and eventually we moved in together and you somehow stuck it out with me for 4+ years. We’ve been through a lot, from just getting to know each other, to seeing each other at emotional highs and lows. If you hadn’t been my roommate through the majority of this, I’m sure my PhD experience would’ve been completely different. I’ll never forget our late night chats (where copious amounts of alcohol may have been involved), our early morning ski trips, and all of the other wild experiences we’ve had together. Looking forward to many more to come, and especially the times to come once we both get our theses submitted.

In general, I have to thank all of the people I’ve become close with from volleyball. Without volleyball, I definitely wouldn’t have made it through this degree. It’s hard to go into personal experiences with everyone but I have a few that need to be mentioned. Daniel, one of my very first friends that I met in the VGVA. You introduced me to so many other people in the league and were the catalyst to me being where I am now in terms of friendships and on-court skills. I may have been absolutely terrified of you when I first met you but we’ve come so far from that. Jonathan and Alexis, we only recently became closer but some of my fondest memories are from dancing on the boat in False Creek during Pride and finally getting to play NAGVA with the two of you (until you rudely got uprated). Ren, Maz, and Peter, we also became a close group only recently but I am so grateful for the late night chats and wine we’ve had in each other’s company. The support system you guys provided was immaculate and I can’t ever give you enough thanks. Zach and Sam, you two were always so welcoming and would go above and beyond for me. More recently I’ve really enjoyed some of our more grown up chats that are very different from me just showing up and being another person at the party. Finally, I have to thank Maik. If you

hadn’t broken your ankle that one time in volleyball, we may have never have been as close as we are now. You’ve given me so much advice in life and are just such a joy to spend time with and destress. You’ve definitely gotten me through this tail end of my thesis from Mario Party to games of pool to bike rides.

The last person I have to thank is Aaryn, the gem from the east, my best friend. Writing this really had me thinking about the journey we’ve been through. From oddly meeting you when my sister taught you violin, fast forward 10 years and we are playing violin together, then we go to MtA together, then live together, and even after we had went our separate ways, we still made the time to call each other as much as possible (with it usually being at least 3 times per week). You were always there for me no matter what the situation was. Having you come visit me was always one of the things I looked forward to the most, and seeing you when I went home was the exact same. Once I’m done with this PhD, we have to go on a trip somewhere, even if we almost killed each other during that Europe adventure.

Table of Contents

Declaration of Committee ii
Abstract iii
Dedication iv
Acknowledgements v
Table of Contents ix
List of Tables xiii
List of Figures xiv
List of Acronyms xxi

Chapter 1. Introduction 1
1.1. Thesis Motivation 1
1.2. Semiclassical Electron Transfer Theory 2
1.2.1. Multi-Step versus Single-Step Electron Transfer 7
1.3. Biological Electron Transfer 11
1.3.1. Metalloproteins in Biological Redox Reactions 12
1.3.2. Type 1/Blue-Copper Proteins 13
1.3.3. Hopping Intermediates in Biological Electron Transfer 15
1.3.4. Aromatic Amino Acids: Tyrosine and Tryptophan 16
1.3.5. Proton-Coupled Electron Transfer 21
1.4. Intermolecular Forces Within Proteins 21
1.4.1. Methionine-Aromatic Motifs: Structures, Types, and Theory 21
1.4.2. The Two-Center, Three-Electron Bond 25
1.4.3. Cation-π Interactions 26
1.4.4. Other Non-Covalent Interactions Within Proteins 27
1.5. Microenvironment Effects on Tryptophan and Tyrosine in Metalloproteins 27
1.5.1. Microenvironment Effects on Protein Fluorescence 27
1.5.2. Microenvironment Effects on Reduction Potentials 28
1.5.3. Microenvironment Effects on Electron Paramagnetic Spectroscopy 29
1.6. Spectroscopic and Instrumental Methods 30
1.6.1. Protein Expression, Purification, and Modification 30
1.6.2. Time-Resolved Absorption and Luminescence Spectroscopies 31
1.6.3. Electron Paramagnetic Resonance 33
1.6.4. Biological Electrochemistry 33
1.7. Thesis Summary 35

Chapter 2. Electron Transfer Kinetics Involving Methionine-Aromatic Motifs in Proteins 36
2.1. Introduction 36
2.1.1. Biological Electron Transfer via Tryptophan 36
2.1.2. Methionine-Aromatic Interactions 38
2.2. Results and Discussion 40
2.2.1. Development of Protein Models 40

2.2.2. Absorption Properties of Trp109 Azurins 43
2.2.3. Tryptophan Fluorescence 44
2.2.4. Transient Absorption Spectroscopy 47
2.3. Summary and Future Directions 52
2.4. Experimental 53
2.4.1. Site-Directed Mutagenesis 53
2.4.2. Primer Design 54
2.4.3. Protein Expression and Purification 54
2.4.4. Tryptophan Fluorescence 55
2.4.5. Photosensitizer Labeling of Azurins 55
2.4.6. Transient Absorption Spectroscopy 56

Chapter 3. Methionine Effects on the Physical Properties of a Tryptophan Radical 57
3.1. Introduction 57
3.1.1. Tryptophan Radicals in Biology 57
3.1.2. Tryptophan Radical Characterization in Biological Systems 58
3.2. Results and Discussion 60
3.2.1. Development of Protein Models 60
3.2.2. Absorption Properties of Trp108 Azurins 61
3.2.3. Tryptophan Fluorescence 63
3.2.4. Steady-State UV-Visible Characterization of a Tryptophan Radical 64
3.2.5. EPR Spectroscopy 69
3.3. Summary and Future Directions 75
3.4. Experimental 76
3.4.1. Site-Directed Mutagenesis 77
3.4.2. Primer Design 77
3.4.3. Protein Expression and Purification 77
3.4.4. Tryptophan Fluorescence 78
3.4.5. Cu(II)/Zn(II) Substitution 78
3.4.6. Photosensitizer Labeling of Azurins 79
3.4.7. Steady-State UV-Visible Characterization 79
3.4.8. EPR Spectroscopy 80

Chapter 4. Protein Microenvironment Effects on the Physical Properties of Tyrosine in Azurin 81
4.1. Introduction 81
4.1.1. Overview of the Protein Microenvironment 82
4.1.2. Hydrogen Bonding and the Protein Microenvironment 83
4.1.3. Current State of Studying a Protein's Microenvironment 84
4.1.4. Tyrosine Fluorescence in Proteins 85
4.1.5. Fluorescence Quenching via the Backbone Carbonyl 87
4.1.6. Fluorescence Quenching via Amino Acid Sidechains 87
4.1.7. Microenvironment Influence on Tyrosine Reduction Potentials 88
4.1.8. Electron Transfer via Tyrosine 89

4.2. Results and Discussion 90
4.2.1. Development of Protein Models 90
4.2.2. Absorption Properties of Tyr109 Azurins 92
4.2.3. Emission Maxima Changes for Tyrosine 93
4.2.4. Hydrogen Bonding and Hydrophobicity Effects on Tyrosine Fluorescence 96
4.2.5. Quenching of Tyrosine Fluorescence 97
4.2.6. Possible pK_a Changes to Tyr109 101
4.2.7. Tyr109 Solvent Exposure 101
4.2.8. Reduction Potential Determination 102
4.2.9. Investigating Reduction Potentials with Cyclic Voltammetry 102
4.2.10. Investigating Reduction Potentials with Differential Pulse Voltammetry 103
4.2.11. Microenvironment Effects on Tyr109 Reduction Potentials 106
4.2.12. Transient Absorption Spectroscopy 106
4.2.13. Rate Constant Determination for Cu(I) Oxidation by Ru(III) 107
4.2.14. Rate Constant Determination for Ru(III) Reduction 109
4.2.15. (Met/Gln/Arg)122 Interactions with Tyr109 111
4.3. Summary and Future Directions 112
4.3.1. Tyr109 Fluorescence is Influenced by the Protein's Microenvironment 112
4.3.2. Tyr109 Reduction Potentials are Influenced by the Protein's Microenvironment 113
4.3.3. Rate Constants are Influenced by the Protein's Microenvironment 113
4.3.4. Future Work: Crystals, Absorption, pK_a Determination, and NMR 113
4.4. Experimental 114
4.4.1. Site-Directed Mutagenesis 114
4.4.2. Primer Design 115
4.4.3. Protein Expression and Purification 116
4.4.4. Tyr Fluorescence 116
4.4.5. Cyclic Voltammetry and Differential Pulse Voltammetry 117
4.4.6. Photosensitizer Labeling of Azurins 117
4.4.7. Transient Absorption Spectroscopy 118

Chapter 5. Clustering of Aromatic Amino Acid Residues Around Methionine in Proteins 119
5.1. Introduction 119
5.1.1. The 3-Bridge Cluster 119
5.2. Results 121
5.2.1. Frequency, Orientation, and Interactions of 3-Bridge Clusters 121
5.3. Discussion 127
5.4. Summary 133
5.5. Experimental 134
5.5.1. Identification of 3-Bridge Clusters in Protein Structures 134
5.5.2. Assessing the Position of Aromatic Residues Around Methionine 134
5.5.3. Density Functional Calculations 135

Chapter 6. Conclusions and Future Directions 137

6.1. Overall Conclusions 137
6.1.1. Conclusions from Chapter 2 137
6.1.2. Conclusions from Chapter 3 137
6.1.3. Conclusions from Chapter 4 138
6.1.4. Conclusions from Chapter 5 138
6.2. Structural Elucidations for Current Protein Models 139
6.2.1. Protein Crystallization Studies 139
6.2.2. Nuclear Magnetic Resonance Characterization 139
6.3. Development of New Protein Models 140

References 141

Appendix A Supplementary Information from Chapter 2 167

Appendix B Supplementary Information from Chapter 3 170

Appendix C Supplementary Information from Chapter 4 173

Appendix D Supplementary Information from Chapter 5 182

List of Tables

Table 1. Emission maxima of 60 µM His107Trp109(Ala/Met)56 in 1 M NH_4Cl, 20 mM NaP_i at pH 7.8. Error on all values is ± 1 nm. 45

Table 2. Emission maxima of 60 µM His107Trp108(Met/Leu)102 in 1 M NH_4Cl, 20 mM NaP_i at pH 7.8. Error on all values is ± 1 nm. 64

Table 3. Hyperfine- and g-values used for simulation of EPR data presented in Figure 39 and Figure 40. Values for other azurin Trp108 radicals are presented here for comparison. 72

Table 4. Emission maxima of 65 µM His107Tyr109(Met/Gln/Arg)122 across a pH range of 4-11 in 50 mM NaP_i. Error on all values is ± 1 nm. 96

Table 5. Experimentally determined E_p values for Tyr across a pH range of 5-9 for all three mutants (Met122, Gln122, and Arg122). 105

Table 6. Experimentally determined Cu(I) oxidation rate constants for three mutant azurins. Experiments were carried out with 35 µM protein in 100 mM NaCl, 250 mM imidazole, at respective pH values. $[Ru(NH_3)_6]^{3+}$ was added to a final concentration of 10 mM. A more detailed description of experimental setup and be found in section 4.4.7. 108

Table 7. Experimentally determined Ru(III) reduction rate constants for three mutant azurins. Experiments were carried out with 35 µM protein in 100 mM NaCl, 250 mM imidazole, at respective pH values. $[Ru(NH_3)_6]^{3+}$ was added to a final concentration of 10 mM. A more detailed description of experimental setup and be found in section 4.4.7. 110

Table 8. Calculated interaction energies in the 3-bridge cluster in cytochrome P450 from *T. bispora*.[a] 126

Table 9. Calculated interaction energies in the 3-bridge cluster in biphenyl dioxygenase from *C. testosterone*.[a] 126

List of Figures

Figure 1. Potential energy of reactants and products as a function of nuclear configuration for a general ET reaction. Q_R, Q*, and Q_P are the nuclear configurations of the e^- on the reactants, transition state, and products, respectively. Adapted with permission from Stubbe, J.; Nocera, D. G.; Yee, C. S.; Chang, M. C. Y. Radical Initiation in the Class I Ribonucleotide Reductase: Long-Range Proton-Coupled Electron Transfer? *Chem. Rev.* 2003, *103* (6), 2167–2202. https://doi.org/10.1021/cr020421u. Copyright 2003, American Chemical Society. 4

Figure 2. Complex between yeast cytochrome *c* peroxidase (cyan) and cytochrome *c* (green). The 19 Å distance between the heme aroamatic edges is shown with a black dashed line. PDB ID: 2BCN.[25] 6

Figure 3. Distance dependence of ET rates in ruthenium-labeled azurin (represented by the dashed line labeled "Ru-azurin") from *Pseudomonas aeruginosa*. The azurins are all His-mutated variants and can be seen in decreasing ET rates as His122, His83, His109, His124, His107, and His126. The solid line represents predicted ET rates for a β-strand in which $\beta = 1.0$ Å^{-1}. Adapted with permission from Gray, H. B.; Winkler, J. R. Electron Tunneling through Proteins. *Q. Rev. Biophys.* 2003, *36* (3), 341–372. https://doi.org/10.1017/S0033583503003913. Copyright 2003, Cambridge University Press. 8

Figure 4. General schematic of ET between a donor (D), intermediate (I), and acceptor (A). Forward and reverse rate constants are written as k_1, k_2, k_3, and k_4. 9

Figure 5. Example of a hypothetical hopping map generated using the code from reference 7.[7] The parameters used are for systems with a donor-acceptor distance of 20 Å, donor-intermediate distance of 5 Å, intermediate-acceptor distance of 15 Å, $\lambda = 0.8$ eV, and $\beta = 1.1$ Å^{-1}. 10

Figure 6. Hopping intermediate chain found in DNA photolyase from *Escherichia coli*. Chain from left to right is FADH$^{\bullet}$−W382−W359−W306. PDB ID: 1DNP.[61] 15

Figure 7. An example of an [FeFe] hydrogenase from *Desulfovibrio desulfuricans* in which one [2Fe] H-cluster and three [4Fe-4S] clusters are present. Orange spheres are Fe atoms and yellow spheres are S atoms. PDB ID: 1HFE.[63] 16

Figure 8. A schematic showing the ET chain of Tyr and Trp in Class Ia RNR proteins. The left and right panels show the radical initiation machinery of other classes of RNR that do not use Tyr/Trp chains. Reprinted with permission from Stubbe, J.; Nocera, D. G. Radicals in Biology: Your Life Is in Their Hands. *J. Am. Chem. Soc.* 2021, *143* (34), 13463–13472. https://doi.org/10.1021/jacs.1c05952. Copyright 2021, American Chemical Society. 18

Figure 9. Trp/Tyr chain found in cytochrome P450 CYP11A1 displaying both T-shape interactions (Tyr93/94, Tyr94/90, and Trp231/87) and parallel-

displaced interactions (Tyr90/Trp231). A 10-fold increase in energy is observed between parallel-displaced residues. PDB ID: 3N9Y.[68] 19

Figure 10. PCET reaction scheme of Tyr conversion to tyrosyl (TyrO$^{\bullet}$) through a tyrosinate (TyrO^{-}) intermediate. 20

Figure 11. PCET reaction scheme for the formation of a neutral Trp radical (Trp$^{\bullet}$) through a Trp cation radical (Trp$^{\bullet+}$). 20

Figure 12. Electrostatic map of Met illustrating the weak partial negative charge on the sulfur atom and the weak partial positive charge on the thioether CH_2 and CH_3 groups. Red indicates an electrostatic potential of –0.025 and blue represents +0.025 (units are kcal mol^{-1} e^{-1}). The image was rendered using Chimera.[81] 22

Figure 13. The Met(S)-aro interactions in C*c*P involving the redox active Trp191. PDB ID: 2CYP.[95] 24

Figure 14. Geometry optimized examples of a σ-type interaction (top) and a π-type interaction (bottom) seen in 1-electron oxidized (radical cation) thioanisole dimers. Close contact distances are designated between each in Ångstroms. The images are original, but the coordinates used to render the image are obtained from reference [97]. 26

Figure 15. Schematic of the laser system used in this thesis. The dotted blue line represents the pump pulse generated by the ND:YAG and OPO. The solid orange line represent to probe pulse generated by the Xe arc lamp. 32

Figure 16. A standard three-electrode cell set-up used for cyclic voltammetry experiments. The experiments carried out in this thesis do not use a cap as the samples did not need to be air-free during electrochemical characterization. Adapted with permission from Elgrishi, N.; Rountree, K. J.; McCarthy, B. D.; Rountree, E. S.; Eisenhart, T. T.; Dempsey, J. L. A Practical Beginner's Guide to Cyclic Voltammetry. *J. Chem. Educ.* 2018, *95* (2), 197–206. https://doi.org/10.1021/acs.jchemed.7b00361. Copyright 2017, American Chemical Society and Division of Chemical Education, Inc. 34

Figure 17. General plot of how potential is applied during cyclic voltammetry (left) and differential pulse voltammetry (right). T_i and T_f are the start and end times during the experiment, respectively. E_1 and E_2 are the starting and final applied potentials, respectively. Asterisks in the right panel represent points at which current is measured. Current is measured at all times throughout cyclic voltammetry (left). 35

Figure 18. The two amino acid mutations used in this chapter, alanine (Ala, left) and methionine (Met, right). 36

Figure 19. Three different types of structural motifs containing Trp; a Met-Trp-Met bridge from yeast cytochrome *c* peroxidase (top left, PDB ID: 2CYP[95]), a Trp-Met-Trp bridge from cytochrome P450 (top right, PDB ID: 5VWS[157]), and a singular Met-Trp motif from lipoyxgenase (bottom, PDB ID: 1IK3[158]). 37

Figure 20. Structure of (2,2´-bipyridyl)$_2$Ru(imidazole)(His107)(Trp109) azurin showing the connectivity between the Ru label (Ru is in cyan) and the Cu (Cu is in orange) active site. The structure was generated using the

mutagenesis function in PyMOL starting from the coordinates in PDB ID: 4HHG.[31] 40

Figure 21. PyMOL generated structures for the two mutations used in this chapter, Met56 (left) and Ala56 (right). Residues from left to right in the left panel are Met56, Trp109, and His107. Residues from left to right in the right panel are Ala56, Trp109, and His107. The structure was generated using the mutagenesis function in PyMOL starting from the coordinates in PDB ID: 4HHG.[31] 42

Figure 22. UV-Vis spectra of His107Trp109Ala56 (blue) and His107Trp109Met56 (orange). Spectra were normalized to the 280 nm peak for clarity. 43

Figure 23. Emission maxima for 60 μM His107Trp109Ala56 (blue) and Met56 (orange) in 1 M NH_4Cl, 20 mM NaP_i at pH 7.8. Samples were excited at 280 nm. 45

Figure 24. Comparison of two sulfur-containing amino acids, methionine (Met, left) and cysteine (Cys, right).....46

Figure 25. Flash-quench scheme to monitor ET kinetics for Ru(III) to Ru(II) reduction and Cu(I) to Cu(II) oxidation. The wavelength of light used for Ru(II) excitation was 480 nm and is represented by hν in the mechanism. W109 in this figure represents the Trp109 mutation. 48

Figure 26. TA kinetic traces for the reduction of Ru(III) to Ru(II) in 35 μM His107Trp109Ala56 (left) and His107Trp109Met56 (right) azurin. Experiments were carried out in 50 mM NaP_i at pH 7.5. $[Ru(NH_3)_6]^{3+}$ was added to a final concentration of 10 mM. A more detailed description of experimental setup and be found in section 2.4.6.....48

Figure 27. Newly proposed flash-quench scheme to monitor ET kinetics for Ru(III) to Ru(II) reduction and Trp109 to $Trp109^{\bullet+}$ oxidation. The wavlength of light used for Ru(II) excitation was 480 nm and is represented by hν in the mechanism. W109 in this figure represents the Trp109 mutation. 50

Figure 28. Electron hopping map generated using the parameters pictured in the box on the right side of this figure. These values are taken from the PDB ID: 4HHG[31] and distances are the reported through-bond distances. A-I represents conditions for the ET between the acceptor and intermediate, I-B represents conditions for the ET between the intermediate and donor, and A-B represents conditions for the ET between acceptor and donor, where r is distance, β is the distance decay constant, and λ is the driving force. The black box shows a likely range of driving forces considering $E°(Ru(III/II))$ = 1.05 V and $E°(Trp^{\bullet+/0})$ = 1 to 1.2 V. 51

Figure 29. The two amino acid mutations used in this chapter, leucine (Leu, left) and methionine (Met, right). 57

Figure 30. Absorption spectrum of a Trp108 radical in azurin. The insert is a single-wavelength absorption spectrum taken at 500 nm. Adapted with permission from Miller, J. E.; Grădinaru, C.; Crane, B. R.; Di Bilio, A. J.; Wehbi, W. A.; Un, S.; Winkler, J. R.; Gray, H. B. Spectroscopy and Reactivity of a Photogenerated Tryptophan Radical in a Structurally Defined Protein Environment. *J. Am. Chem. Soc.* 2003, *125* (47), 14220–14221. https://doi.org/10.1021/ja037203i. Copyright 2003, American Chemical Society. 59

Figure 31. PyMOL generated structures for the two mutations used in this chapter, Leu102 (left) and Met102 (right). Residues from top to bottom in the left panel are Leu102, Trp108, and His107. Residues from top to bottom in the right panel are Met102, Trp108, and His107. The structure was generated using the mutagenesis function in PyMOL starting from the coordinates in PDB ID: 4HHG.[31] 61

Figure 32. UV-Vis spectra of His107Trp108Leu102 (blue) and His107Trp108Met102 (orange). Spectra were normalized to the 280 nm peak for clarity. 62

Figure 33. UV-Vis spectra for the confirmation of the removal of Cu(II) from His107Trp108Leu102 (left) and His107Trp108Met102 (right). In both panels, blue curves represent Zn(II)-azurins and orange curves represent Cu(II)-azurins. The small amount of noise in the 300-400 nm range is due to the source changeover by the instrument. Spectra were normalized to the 280 nm peak for clarity. 63

Figure 34. Emission maxima for 60 μM His107Trp108Met102 (blue) and Leu102 (orange) in 1 M NH_4Cl, 20 mM NaP_i at pH 7.8. Samples were excited at 280 nm. 64

Figure 35. Flash-quench scheme for the irreversible photogeneration of $Trp108^{\bullet+}$ ($W108^{\bullet+}$ in this pathway). The wavlength of light used for Re(I) excitation was 355 nm and is represented by hν in the mechanism. 65

Figure 36. Schematic of the laser system used in this chapter. The dotted blue line represents the pump pulse generated by the Nd:YAG and OPO. The solid black line from the Photon Control represents the closed probe system generated by the deuterium-halogen lamp source. 66

Figure 37. Steady-state UV-Vis spectra for 100 μM His107Trp108Leu102 (H = His, W = Trp, L = Leu) in 50 mM NaP_i at pH 7.5. Each spectra was manually collected at the timepoints show in the legend. The timepoint, t = 0 (blue), represents the sample prior to irradiation. $[Re(CO)_3(4,7\text{-}Me_2phen)]^+$ was used as the photosensitizer label. 67

Figure 38. Steady-state UV-Vis spectra for 57 μM His107Trp108Met102 (blue) and His107Trp108Leu102 (orange) in 50 mM NaP_i at pH 7.5. $[Re(CO)_3(4,7\text{-}Me_2phen)]^+$ was used as the photosensitizer label. M = Met and W = Trp in this figure. 68

Figure 39. X-band (9.4 GHz) EPR spectra for the Trp radical in His107Trp108Leu102 in 50 mM NaP_i at pH 7.5 taken at 100 K. The experimental data are shown in blue and the simulation is in orange. An overlay of the experimental and simulated data can be found in Appendix B. 71

Figure 40. X-band (9.4 GHz) EPR spectra for the Trp radical in His107Trp108Met102 in 50 mM NaP_i at pH 7.5 taken at 100 K. The experimental data are shown in blue and the simulation is in orange. An overlay of the experimental and simulated data can be found in Appendix B. 71

Figure 41. Orientation of $H\beta_1$ and $H\beta_2$ protons and the protein backbone, denoted R, with respect to the Trp indole plane, denoted $C_4{-}C_3{-}C_2$. The $\chi_{2,1}$ dihedral angle between the Trp indole plane and the protein backbone is denoted as R. 73

Figure 42. PyMOL model of hydrogen bonding between the Trp108 indole nitrogen and H_2O in His107Trp108Leu102. The red spheres represent oxygen atoms. The dashed yellow line represents the distance between the indole nitrogen and the oxygen from H_2O as protons cannot be shown in this model. The distance between nitrogen and oxygen in this model is 2.3 Å. PDB ID: 1R1C.[140] 74

Figure 43. Structure of a neutral Trp108 radical with associated spin densities. Values and numbering system are from the literature.[132] Similar spin densities have been reported elsewhere.[137–139] 75

Figure 44. The three amino acid mutations used in this chapter, methionine (Met, left), glutamine (Gln, center), and arginine (Arg, right). 81

Figure 45. The metal-containing active site of *C. trachomatis* RNR showing the metal ions (green), their primary ligand set (purple), and all the outer coordination sphere residues (orange). The outer-sphere residues were selected as those that show any interaction under 3.5 Å with the primary ligands. PDB ID: 1SYY.[188] 83

Figure 46. PCET reaction scheme of Tyr conversion to tyrosyl ($TyrO^{\bullet}$) through a tyrosinate ($TyrO^{-}$) intermediate. B represents the proton acceptor which could be another amino acid of buffer. $Ru^{3+/2+}$ represent the $[Ru(bpy)_2(im)]^{2+}$ photosensitizer that is labeled to His107 in the protein's structure. 87

Figure 47. Flash-quench scheme to monitor ET kinetics for Ru(III) to Ru(II) reduction and Cu(I) to Cu(II) oxidation. The wavlength of light used for Ru(II) excitation was 480 nm and is represented by hν in the mechanism. Y109 in this figure represents the Tyr109 mutation. 90

Figure 48. Ruthenium-labeled His107Tyr109Lys122 from *Pseudomonas aeruginosa* azurin. Lys122 is the residue that is mutated for each of the experiments in this chaapter. The brown sphere represents Cu^{2+} and the complex to the right is $[Ru(bpy)_2(im)]^{2+}$ (bpy = 2,2'-bipyridine, im = imidazole) .This figure was based on the PDB ID: 4HHG.[31] 91

Figure 49. The three different mutations used to carry out the experiments in this chapter. The residues shown are Tyr109Arg122 (panel A), Tyr109Gln122 (panel B), and Tyr109Met122 (panel C). This figure was based on the PDB ID: 4HHG.[31] 92

Figure 50. Tyr109 absorbance across the three different mutants, Met122 (blue), Gln122 (orange), and Arg122 (yellow). The data presented here is for unlabeled azurins and was normalized to the 280 nm peak for better visualization. 93

Figure 51. 65 μM His107Tyr109Met122 (Met = M) fluorescence at a pH range from 4-11 in 50 mM NaP_i. Values for the emission maxima can be found in Table 4. 94

Figure 52. 65 μM His107Tyr109Gln122 (Gln = Q) fluorescence at a pH range from 4-11 in 50 mM NaP_i. Values for the emission maxima can be found in Table 4. 95

Figure 53. 65 μM His107Tyr109Arg122 (Arg = R) fluorescence at a pH range from 4-11 in 50 mM NaP_i. Values for the emission maxima can be found in Table 4. 95

Figure 54. Raw experimental data of 65 μM His107Tyr109Met122 (His = H, Tyr = Y, Met = M) fluorescence at a pH range from 4-11 in 50 mM NaP_i. 98

Figure 55. Raw experimental data of 65 μM His107Tyr109Gln122 (His = H, Tyr = Y, Gln = Q) fluorescence at a pH range from 4-11 in 50 mM NaPi.....98

Figure 56. Raw experimental data of 65 μM His107Tyr109Arg122 (His = H, Tyr = Y, Arg = R) fluorescence at a pH range from 4-11 in 50 mM NaP_i. 99

Figure 57. Cyclic voltammograms of each of the three mutants (Met122, Gln122, and Arg122). Protein concentrations were 100 μM in 100 mM NaOAc at the respective pH. A more detailed description of experimental conditions can be found in section 4.4.5.....103

Figure 58. Full DPV of Met122 in 100 mM NaOAc at respective pH values (left). Zoom of Tyr redox peaks normalized to 1 for easier visualization of the decrease in E_p as pH increases (right). Protein concentrations were 100 μM for both plots. 104

Figure 59. Full DPV of Gln122 in 100 mM NaOAc at respective pH values (left). Zoom of Tyr redox peaks normalized to 1 for easier visualization of the decrease in E_p as pH increases (right). Protein concentrations were 100 μM for both plots. 104

Figure 60. Full DPV of Arg122 in 100 mM NaOAc at respective pH values (left). Zoom of Tyr redox peaks normalized to 1 for easier visualization of the decrease in E_p as pH increases (right). Protein concentrations were 100 μM for both plots. 105

Figure 61. Raw TA kinetic traces for the oxidation of Cu(I) to Cu(II) in 35 μM Met122 (blue), Gln122 (orange), and Arg122 (yellow) azurin. Experiments were carried out in 100 mM NaCl, 250 mM imidazole, at pH 5. $[Ru(NH_3)_6]^{3+}$ was added to a final concentration of 10 mM. A more detailed description of experimental setup and be found in section 4.4.7.....107

Figure 62. Experimentally determined rate constants from Table 6 for Cu(I) to Cu(II) oxidation of His107Tyr109Met122 (blue crosses), Gln122 (orange squares), Arg122 (yellow diamonds), and Lys122 (purple circles) at their respective pH values. Rate constants are reported as logk (s^{-1}). 109

Figure 63. Experimentally determined rate constants from Table 6 for Ru(III) to Ru(II) reduction of His107Tyr109Met122 (blue crosses), Gln122 (orange squares), and Arg122 (yellow diamonds), at their respective pH values. Rate constants are reported as logk (s^{-1}).....111

Figure 64. Examples of Met-aro interactions in yeast cytochrome *c* peroxidase. Dashed lines indicate points of close contact and distances are from 3.4 to 4.4 Å. Red = oxygen, blue = nitrogen, gray = carbon, yellow = sulfur. The backbone residues are omitted for clarity. PDB ID: 2CYP.[95].....120

Figure 65. Summary of the identities and incidences of 3-bridge clusters. 122

Figure 66. Plots of clustering Phe (top, red), Tyr (bottom left, green), and Trp (bottom right, blue) around Met. The x, y, and z axes are in Ångstroms. The black V-shape at the origin depicts the CH_3-S-CH_2 thioether of Met. The arm pointing away from the reader (along +y) is the CH_2 group. Each point corresponds to an aromatic centroid for each respective amino acid....123

Figure 67. Electron density plots for the 3-bridge cluster in cytochrome P450 from *T. bispora.* The left panel shows the complete bridge, the center shows the

aromatic groups only, and the right panel shows Met only. Red corresponds to a charge of –0.03, white is zero, and blue is +0.03. PDB ID: 5VWS.[157] 124

Figure 68. Natural bond orbitals from the 3-bridge cluster in cytochrome P450 from *T. bispora*. Interactions that involve a Met24 C-H* acceptor (A), Phe41 C-C π-donor (B), Trp20 C-C π* acceptor (C), and Met24 lone pair donor from S (D). PDB ID: 5VWS.[157] 125

Figure 69. Structure of yeast catalase. The 3-bridge clusters are highlighted in gray and lavender, and the heme and other tyrosine residues are in green. PDB ID: 1A4E.[256] 128

Figure 70. Structure of prostaglandin H2 synthase 1. The 3-bridge clusters are highlighted in orange, green, and lavender, and the heme is shown in gray. PDB ID: 1Q4G.[257] 129

Figure 71. Structure of *X. autotrophicus* haloalkane dehalogenase. The 3-bridge cluster is highlighted in orange and the catalytic aspartate (Asp) and halide-stabilizing Trp are in cyan. PDB ID: 1B6G.[261] 130

Figure 72. Flexibility colour spectrum for yeast C*c*P using residue B-factors from the PDB. The spectrum from dark purple through white to dark red represent lower to higher areas of flexibility, respectively. PDB ID: 2CYP.[95] 131

Figure 73. Flexibility colour spectrum for cytochrome P450 using residue B-factors from the PDB. The spectrum from dark purple through white to dark red represent lower to higher areas of flexibility, respectively. PDB ID: 5VWS.[157] 131

Figure 74. Flexibility colour spectrum for yeast catalase using residue B-factors from the PDB. The spectrum from dark purple through white to dark red represent lower to higher areas of flexibility, respectively. PDB ID: 1A4E.[256] 132

Figure 75. Flexibility colour spectrum for prostglandin H2 synthase 1 using residue B-factors from the PDB. The spectrum from dark purple through white to dark red represent lower to higher areas of flexibility, respectively. PDB ID: 1Q4G.[257] 132

Figure 76. Flexibility colour spectrum for haloalkane dehalogenase using residue B-factors from the PDB. The spectrum from dark purple through white to dark red represent lower to higher areas of flexibility, respectively. PDB ID: 1B6G.[261] 133

List of Acronyms

2c−3e$^-$	Two-center, three-electron
A	Acceptor
ADP	Adenosine Diphosphate
ATP	Adenosine Triphosphate
C*c*P	Cytochrome *c* Peroxidase
CCSD	Coupled-Cluster
CE	Counter Electrode
CV	Cyclic Voltammetry
D	Donor
DA	Donor-Acceptor
DFT	Density Functional Theory
DI	Donor-Intermediate
DNA	Deoxyribonucleic Acid
DPV	Differential Pulse Voltammetry
EC	Enzyme Classification
ENDOR	Electron Nuclear Double Resonance
EPR	Electron Paramagnetic Resonance
EPT	Concerted Electron-Proton Transfer
ET	Electron Transfer
ET-PT	Electron Transfer-Proton Transfer
FADH	Flavin Adenine Dinucleotide
FF	Fast-Flow
FPLC	Fast Protein Liquid Chromatography
GE	General Electric
H	Histidine
HFCC	Hyperfine Coupling Constant
I	Intermediate
IA	Intermediate-Acceptor
ID	Identification
IEM	Interaction Energy Matrix
IMAC	Immobilized Metal Affinity Column
L	Leucine

LB	Luria-Bertani
LMCT	Ligand-to-Metal Charge Transfer
M	Methionine
MALDI	Matrix-Assisted Laser Desorption/Ionization
MS-EPT	Multiple Site Electron-Proton Transfer
$NADP^+$	Nicotinamide Adenine Dinucleotide Phosphate
NBO	Natural Bond Order
Nd:YAG	Neodymium-Doped Yttrium Aluminum Garnet
NEB	New England BioLabs
NHE	Normal Hydrogen Electrode
NMR	Nuclear Magnetic Resonance
OPO	Optical Parametric Oscillator
PCET	Proton-Coupled Electron Transfer
PCR	Polymerase Chain Reaction
PDB	Protein Data Bank
PMT	Photomultiplier Tube
PSII	Photosystem II
PT	Proton Transfer
PT-ET	Proton Transfer-Electron Transfer
Q	Glutamine
R	Arginine
RE	Reference Electrode
RNA	Ribonucleic Acid
RNR	Ribonucleotide Reductase
ROS	Reactive Oxygen Species
SFU	Simon Fraser University
TA	Transient Absorption
TL	Transient Luminescence
W	Tryptophan
WE	Working Electrode
Y	Tyrosine

Chapter 1. Introduction‡

1.1. Thesis Motivation

The central motivation for this thesis is the development of a deeper understanding of how proteins and large biological systems transfer electrons. At this point, a great deal is known about overall function in crucial cellular systems. One important example is electron flow in the respiratory electron transport chain. At least 35 individual electron transfer (ET) steps are needed for overall function, and the individual steps involve inter- and intramolecular reactions. The distances of some of the reactions span membranes of ca. 140 Å in thickness; see, for example, structures of photosystem II[1] or mitochondrial enzymes.[2,3] Despite this complexity, respiration is arguably one of the best understood series of ET reactions; this area is returned to below. This being the case, one naturally wonders "what are the next challenges?"

In my view, two important challenges that are related to this work are (1) understanding ET pathways, and (2) understanding the microenvironments of redox cofactors and how those short-range interactions influence ET reactions. A full discussion of (1) is beyond the scope of this thesis. Briefly, however, ET pathways refer to the nature of the protein matrix that separates an electron donor and acceptor. Early models were static and considered the pathway as a "square barrier," but modern treatments consider protein dynamics and networks of different pathways.[4–6] As such, there is ongoing interest in the discrete networks that promote function in redox proteins and how the dynamics of those networks are related to ET in health and disease. With respect to this thesis, I am primarily concerned with developing a more detailed understanding of how the local environment of redox cofactors influences their physical properties, in particular those properties that affect ET.

---

‡ Portions of this chapter are adapted from Gibbs, C. A.; Fedoretz-Maxwell, B. P.; Warren, J. J. "On the Roles of Methionine and the Importance of Its Microenvironments in Redox Metalloproteins." *Dalton Trans.* **2022**, *51* (13), 4976–4985. https://doi.org/10.1039/D1DT04387K**.** J.J.W. conceived the topics and co-wrote the paper. C.A.G. wrote the paper except for topics involving iron, edited, designed figures, and formatted the entire paper. B.P.F-M. wrote and designed figures for the iron section in the paper.

1.2. Semiclassical Electron Transfer Theory

To rationalize ET reactions in proteins, I will first outline the key concepts and theoretical treatments that can be applied to such macromolecules. The typical starting point for understanding ET reactions is semiclassical theory.[7] This is sometimes referred to colloquially as "Marcus theory" in the ET literature. In the context of semiclassical theory, the transferring electron is treated quantum mechanically, while the heavy atoms in the system are treated classically. Biological ET reactions typically involve weak interactions between electronic orbitals of an electron donor and electron acceptor; this situation is defined as an outer-sphere ET.[§8] As in any chemical reaction, the reaction proceeds from reactants to products, however, in an ET case, the absence of bond making/breaking affords a charge transition instead of the structural changes associated with other types of chemical reactions.[8,9] An example of ET in its simplest form is the electron self-exchange reaction of a mixture of $(H_2O)_6Fe^{2+}$ and $(H_2O)_6Fe^{3+}$. An electron can transfer between the two ions with the ratio of ET rate constants ($k_{forward}/k_{reverse}$) equal to 1, but no bonds are made or broken in the process.[10,11]

In general, the rate constant for a chemical reaction (in this case, ET) is related to the Eyring activation energy ($\Delta G^{\ddagger}$) as shown in $\mathrm{Eq.\,1}$.[12] The key contribution from Rudolph A. Marcus was to show that $\Delta G^{\ddagger}$ can be related to two parameters: the driving force ($-\Delta G^{\circ}$) and reorganization energy (λ), resulting in $\mathrm{Eq.\,2}$.[8,9,13–16] The reorganization energy is the key parameter in relating the laws of thermodynamics (ΔG°) to the theory of chemical kinetics ($\Delta G^{\ddagger}$) for ET reactions. $\mathrm{Eq.\,2}$ describes this where A (the Eyring prefactor in $\mathrm{Eq.\,1}$), is replaced by the rate constant, $k_{ET}(0)$ (which is the special case where $\Delta G^{\circ} = -\lambda$, see below).[7,15]

$$k_{\mathrm{ET}} = \mathrm{A}\exp\frac{-\Delta \mathrm{G}^{\ddagger}}{\mathrm{RT}} \qquad (\mathrm{Eq.\,1})$$

$$k_{\mathrm{ET}} = k_{\mathrm{ET}}(0)\exp\frac{-\left(\lambda + \Delta \mathrm{G}^{\circ}\right)^{2}}{4\lambda \mathrm{RT}} \qquad (\mathrm{Eq.\,2})$$

§ The other type of ET reaction, inner-sphere ET, is not discussed here. Inner-sphere ET occurs in complexes that share a common, or bridging, ligand (see: *J. Am. Chem. Soc*. **1953**, *75*, 4118–4119. https://doi.org/10.1021/ja01112a546). Inner-sphere ET also is discussed in the context on intervalence charge transfer reactions (see: *Chem. Soc. Rev*. **2002**, *31*, 168–184. https://doi.org/10.1039/B008034I).

In the context of ET reactions, the Franck-Condon principle states that ET occurs readily once the heavy atoms reach their transition state geometry. In other words, ET between donor and acceptor occurs without a change in the nuclear configuration at the transition state. This concept is illustrated using potential energy wells in Figure 1. Specifically, Figure 1 shows two 2D potential energy surfaces. The first, R, represents the energy of all reactants as a function of their nuclear configuration during ET. Likewise, the second surface, P, represents the energy of the products. The nuclear configuration at Q* is the transition state and represents the point in which ET can occur between the donor and the acceptor.[9,15] The reorganization energy is important here and it is defined as the amount of energy required to change the nuclear configuration of reactants (depicted Q_R in Figure 1) to the nuclear configuration of Q^*. The overall reorganization energy has two contributions, inner-sphere (λ_i; changes in bond length) and outer-sphere (λ_o; changes to the surrounding medium).[15]

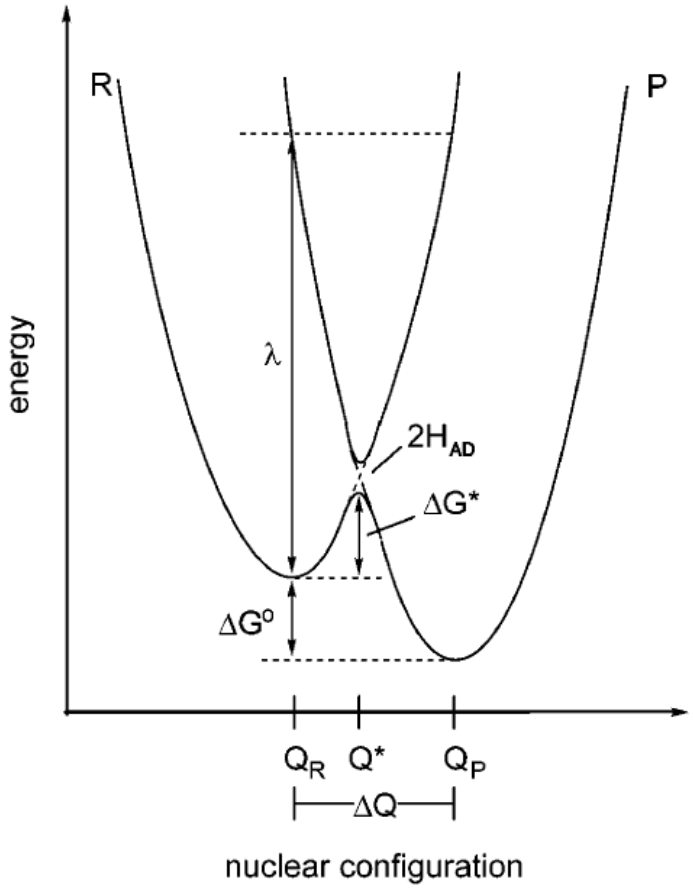

Figure 1. **Potential energy of reactants and products as a function of nuclear configuration for a general ET reaction. Q_R, Q*, and Q_P are the nuclear configurations of the e^- on the reactants, transition state, and products, respectively. Adapted with permission from Stubbe, J.; Nocera, D. G.; Yee, C. S.; Chang, M. C. Y. Radical Initiation in the Class I Ribonucleotide Reductase: Long-Range Proton-Coupled Electron Transfer? *Chem. Rev.* 2003, *103* (6), 2167–2202. https://doi.org/10.1021/cr020421u. Copyright 2003, American Chemical Society.**

The Marcus equation was originally given in terms of activation energy (Eq. 3), which allows one to visualize how changes to $-\Delta G°$ and/or to λ will affect the overall ET rate constant. When λ is held constant, a decrease in driving force will increase the activation energy and decrease the rate constant. Likewise, increasing λ at constant driving force will decrease the rate constant.[15] At the special condition where, the reaction is said to be driving force optimized and the maximum rate constant is achieved. At this point, increases to $-\Delta G°$ will decrease the rate constant.[17,18] When originally proposed in the 1950s, the idea that reactions with more favourable driving force could yield slower rates, was widely rejected. Soon after, the concept of these "inverted" ET rate-driving force

relationships was demonstrated experimentally in the late 1980s, with Marcus being awarded the Nobel Prize in Chemistry (1992). A detailed derivation of $\mathrm{Eq.}\,3$ can be found in reference 15.[15]

$$\Delta G^{\ddagger} = \frac{\left(\lambda + \Delta G^{\circ}\right)^2}{4\lambda} \qquad (\mathrm{Eq.}\,3)$$

ET reactions of small molecules share several important similarities with analogous reactions of much larger biomolecules, such as vibrational changes upon redox change, environmental changes (e.g., solvent reorganization), and the interrelated dependence of k_{ET} on λ and ΔG°. However, some notable differences also exist. The information on structural effects, such as a conformational change of a protein, is more limited for ET within biological systems. In metalloproteins, λ is difficult to measure directly. Typically, the temperature dependence of k_{ET} when the driving force is known allows for the determination of λ. Further, proteins naturally contain buried cofactors and the nature of the medium that surrounds those cofactors helps to minimize outer-sphere contributions to λ. Likewise, many proteins have geometrically fixed sites where ET occurs, which reduces the inner-sphere contributions to λ.[19] Perhaps the best biological example of this are blue-copper sites in cupredoxins. A network of interactions for the Cu ion in a geometry approximately halfway between tetrahedral (preferred for Cu(I)) and square planar (preferred for Cu(II)), dramatically reduces λ with respect to reactions of aquated Cu ions.[20,21]

Another important difference in biomolecular ET is the level of electronic coupling between reactants and products. In small molecule ET, the probability of an ET event occurring is heavily dependent on the contact of reactants, which typically occurs through a close-contact interaction brought about by the diffusion of a donor (D) and an acceptor (A). However, in a biological system, the reactants are often in a fixed position, embedded within the protein. Even interprotein ET involves well-defined interactions and fixed conformations. For example, Figure 2 shows the ~19 Å separation between heme cofactors in a crystallographically characterized complex between yeast cytochrome *c* peroxidase and cytochrome *c*. Consequently, donors and acceptors cannot achieve the close, or van der Waals, contact (about 3 Å) as is seen in small molecule diffusive ET systems. In both molecular and biomolecular cases, the rate of ET decreases exponentially as the distance between reactants, *r*, increases.[9,22,23] More specifically, the

rate of ET for separated redox sites is proportional to the square of the electronic coupling interaction energy for the D and A. The medium in which the electron must transfer also plays a critical role here.[24] Changes in distance between D and A was not a consideration when $\mathrm{Eq.}\,3$ was originally discussed.

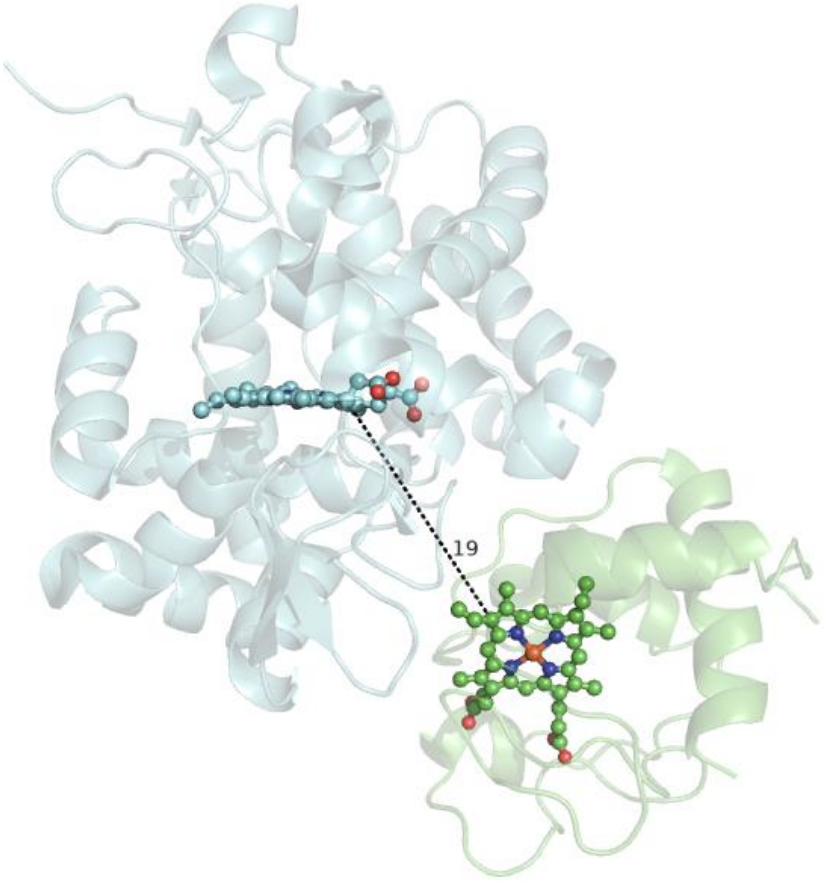

Figure 2. **Complex between yeast cytochrome *c* peroxidase (cyan) and cytochrome *c* (green). The 19 Å distance between the heme aroamatic edges is shown with a black dashed line. PDB ID: 2BCN.[25]**

To account for the distance dependence of long-range ET, a square barrier tunneling model has been employed. The probability for an electron to transfer, H_{AD}^2, which accounts for distance dependence, was then added and is shown in $(\mathrm{Eq.}\,4)$.

$$\mathrm{H_{AD}} = \mathrm{H_{AD}^0 exp}\,[-\beta(\mathrm{r_{DA}} - \mathrm{r_0})] \qquad (\mathrm{Eq.}\,4)$$

In this equation, r_0 represents the distance between the center points of both donor and acceptor at contact (taken as 3 Å), r_{DA} is the distance between wave functions for D and A, and β is the distance decay constant. The magnitude of β is dependent upon the

nature of the medium that separates the donors and acceptors. The empirical value of β in proteins is 1.1 ± 0.1 Å^{-1}. This is based on work completed by Harry Gray,[19,26] with similar conclusions made by P. Leslie Dutton.[27] By incorporating an exponential decay with increasing distance, the most commonly used functional form of the Marcus rate expression is shown in $\mathrm{Eq.}\,5$.[15,19,28]

$$k_{\mathrm{ET}} = \sqrt{\frac{4\pi^3}{h^2 \lambda k_{\mathrm{B}} T}} H_{\mathrm{AD}}^2 \exp\left[\frac{-(\lambda + \Delta G^0)^2}{4\lambda RT}\right] \qquad (\mathrm{Eq.}\,5)$$

1.2.1. Multi-Step versus Single-Step Electron Transfer

Biological ET in functional systems is thought to occur on timescales less than 10 ms, which is only possible to do in a single step when the distance between donor and acceptor is less than approximately 20 Å. An example of the distance dependence for ET in a ruthenium-labeled azurin from *Pseudomonas aeruginosa* is shown in Figure 3**.** However, some biological ET events must occur over distances greater than 20 Å, for example, in transmembrane redox systems.[22,29] In these cases single-step ET, even at high driving force, cannot support biological function.[29,30] Therefore, proteins use intermediates in a multi-step fashion for ET over greater distances.[15,26,29–32] Such multi-step ET reactions can also be called “hopping” and these terms become interchangeable in this thesis. In principle, the kinetics of each individual step in a hopping system can be described by $\mathrm{Eq.}\,5$. However, most hopping systems employ a series of low driving force ($\Delta G° \sim -50$ meV) hopping steps. This means that both forward and reverse ET reactions must be considered for each step in a hopping system. This situation compounds the derivation of an analytical rate expression for systems with more than one intermediate electron/hole carrier between the donor and acceptor.[7,33]

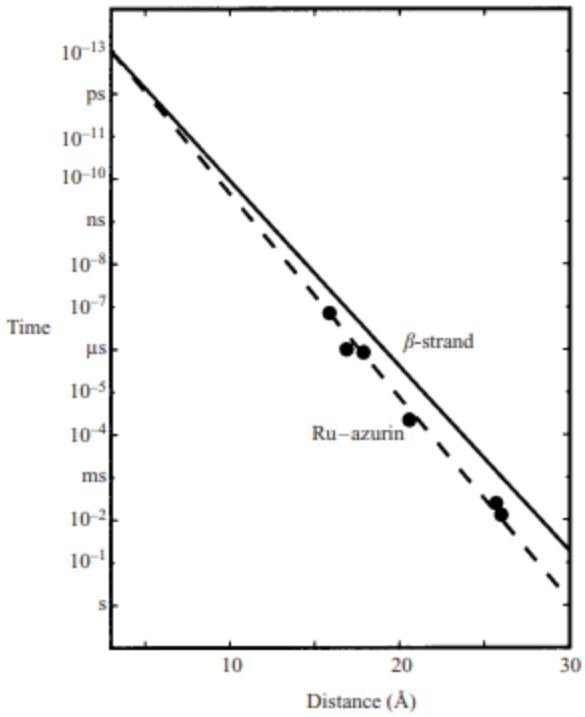

Figure 3. **Distance dependence of ET rates in ruthenium-labeled azurin (represented by the dashed line labeled "Ru-azurin") from *Pseudomonas aeruginosa*. The azurins are all His-mutated variants and can be seen in decreasing ET rates as His122, His83, His109, His124, His107, and His126. The solid line represents predicted ET rates for a β-strand in which β = 1.0 Å^{-1}. Adapted with permission from Gray, H. B.; Winkler, J. R. Electron Tunneling through Proteins. *Q. Rev. Biophys.* 2003, *36* (3), 341–372. https://doi.org/10.1017/S0033583503003913. Copyright 2003, Cambridge University Press.**

It is worth noting that some computational tools have recently become available to map multi-step ET pathways,[32,34] although many earlier modelling systems exist.[23,35] However, calculation of such ET rates relies on some assumptions, such as the reorganization energy which is assumed to be 0.8 in azurins, and a detailed computational analysis. In contrast, analyses based on Eq. 5 are more straightforward and use experimentally validated values as approximations. The newer computational tools provide straightforward access to modeling of the ET processes that are possible in complex biomolecules, but they are less suited to the development of the kinds of details that this thesis describes.

For cases where there is only one intermediate present between the D and A, an analytical rate equation (Eq. 6) was derived using Eq. 5.[7,31] Note that Eq. 6 shows the time

constant for ET, which is the inverse of the rate constant, k_{hop}, (net ET between D and A). This equation accounts for all variables within each of the individual ET steps. These derivations are outlined in detail elsewhere.[7]

$$\tau_{hop} = \frac{\left(\exp\left(\beta(r_2 - r_0) + \frac{(\Delta G^{\circ}_{IA} + \lambda)^2}{4\lambda RT}\right)\right)\left(1 + \exp\left(\frac{\Delta G^{\circ}_{DI}}{RT}\right)\right) + \left(\exp\left(\beta(r_1 - r_0) + \frac{(\Delta G^{\circ}_{DI} + \lambda)^2}{4\lambda RT}\right)\right)\left(1 + \exp\left(\frac{\Delta G^{\circ}_{IA}}{RT}\right)\right)}{(C_0)\left(1 + \exp\left(\frac{\Delta G^{\circ}_{IA}}{RT}\right) + \exp\left(\frac{\Delta G^{\circ}_{DA}}{RT}\right)\right)} \quad \text{(Eq. 6)}$$

In all cases, the values in Eq. 6 are analogous to those in Eq. 5 (where C_0 is a collection of constants that are described in reference 7). The values of ΔG° (with subscripts IA, DI, and DA) are defined as the driving force for ET occurring between D, intermediate (I), and A. The equilibrium constants corresponding to the ΔG° values account for the forward and reverse rate constants for each step. The distances are: r_1 (between D and I), r_2 (between I and A), and r_0 is defined as above. The reaction would proceed as seen below.[7]

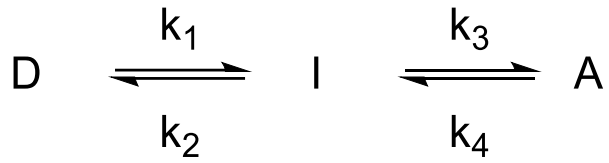

Figure 4. General schematic of ET between a donor (D), intermediate (I), and acceptor (A). Forward and reverse rate constants are written as k_1, k_2, k_3, and k_4.

It is important to compare single-step ET to multi-step ET. To do this Eq. 7 must be used.

$$\tau_{ss} = \frac{1}{(C_0)\left(\exp\left(-\beta(r_T - r_0)\right)\right)\left(\exp\left(\frac{-(\Delta G^{o}_{DA} + \lambda)^2}{4\lambda RT}\right) + \exp\left(\frac{-(\Delta G^{o}_{DA} - \lambda)^2}{4\lambda RT}\right)\right)} \quad \text{(Eq. 7)}$$

In this equation τ_{ss} is the average time for ET to occur and the inverse of this equation is equivalent to the single-step rate constant, k_{ss}. r_T is defined as the straight-line distance between D and A; this will not be the sum of r_1 and r_2 above. To derive Eq. 6 and Eq. 7, values for λ, β, and H_{AD}, are most commonly assumed to be equal across all ET reactions within the system.[7] These equations can only be used for prediction and cannot replace *in vitro* experimental designs. Thus, semiclassical ET theory plays a large role in

this thesis and predictions of ET rate constants are made using the equations outlined above.

The advantage of hopping over single step ET can be proposed through the construction and analysis of hopping maps, as shown in the example in Figure 5**.** A heat map is used to illustrate driving force regimes where hopping is favoured over single-step ET. The x-axis gives the overall driving force and the y-axis gives the driving force of the first step. As ΔG° (total and first step) becomes more negative, multi-step ET events become more favoured. The top white area represents driving forces where single step ET is predicted to be faster than hopping. Inspection of the relative driving force here reveals it as unfavourable and a prohibitor of hopping. The bottom white area shows driving forces where the electron (or hole) is "stuck" at the intermediate. The relative driving force here is very favourable for the first step, however, only a large total driving force (indicative of larger driving force in the second step) will allow for the hopping reaction to proceed.

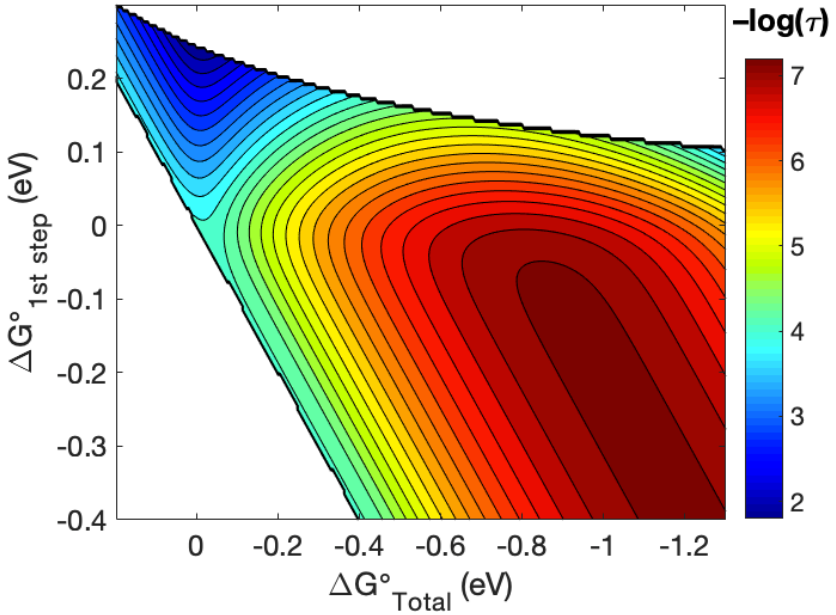

Figure 5. Example of a hypothetical hopping map generated using the code from reference 7.[7] The parameters used are for systems with a donor-acceptor distance of 20 Å, donor-intermediate distance of 5 Å, intermediate-acceptor distance of 15 Å, λ = 0.8 eV, and β = 1.1 Å^{-1}.

1.3. Biological Electron Transfer

As noted above, energy transduction in living organisms is intimately tied to robust and efficient ET within and between proteins. In many cases, ET reactions are associated with proton transfer (PT) reactions. Collectively, this class of reactions is called proton-coupled electron transfer (PCET). The family of PCET reactions are central to the viability of most organisms. The most common example is aerobic respiration, where organisms take in O_2 and produce water and oxidized products (ultimately CO_2). At a microscopic level, the O_2 that mammals breathe is converted to water as part of the mitochondrial respiratory chain. The processes associated with the reduction of O_2 involve many discrete ET steps across several proteins. Importantly, malfunction in any of those steps can result in free radical reactions that ultimately give rise to mitochondrial diseases.[36] Consequently, researchers have been interested in ET in proteins and organisms to better understand mitochondrial diseases.[37] Furthermore, there are many such examples of essential biological ET reactions in all kingdoms of life, not just within the mitochondria of a cell. For many examples, see reference 37.[38]

Another important example of biological ET is found in photosynthetic organisms. Here, where plants and cyanobacteria use light energy ($h\nu$) to convert CO_2 and H_2O to O_2 and carbohydrates (denoted $[CH_2O]_n$ in the equations below). In the first steps, light energy chemically splits H_2O to produce O_2, protons (H^+), and electrons (e^-) (light reaction, $\mathrm{Eq.}\,8$).[39,40] Those H^+ and e^- are then used to reduce atmospheric CO_2 to produce carbohydrates and H_2O (dark reaction, $\mathrm{Eq.}\,9$).[39]

$$2H_2O + h\nu \rightarrow O_2 + 4H^+ + 4e^- \qquad \text{(light reaction)} \qquad (\mathrm{Eq.}\,8)$$

$$CO_2 + 4H^+ + 4e^- \rightarrow [CH_2O]_n + H_2O \qquad \text{(dark reaction)} \qquad (\mathrm{Eq.}\,9)$$

$$H_2O + h\nu + CO_2 \rightarrow [CH_2O]_n + O_2 \qquad \text{(overall reaction)} \qquad (\mathrm{Eq.}\,10)$$

In the light reactions, a series of ET reactions move an electron from H_2O to nicotinamide adenine dinucleotide phosphate ($NADP^+$) to yield its reduced form, termed NADPH. PT across the thylakoid membrane generates a proton gradient that leads to the conversion of adenosine diphosphate (ADP) to adenosine triphosphate (ATP) that can then be used in the dark reactions, where ADP and $NADP^+$ are regenerated.[41] It is important to note that a series of ET reactions across several protein complexes are

required for both dark and light reactions to be carried out. These crucial redox-active biomolecules include photosystem II,[39,40] cytochrome b_6f, plastocyanin, photosystem I, and ferredoxin, to name a few. A more detailed description of the photosynthetic e^- and H^+ transfer chains can be found in the literature.[39]

In sum, biological ET is a foundational class of processes that governs life in plants and animals. The ongoing development of understanding surrounding the features that nature uses to move e^- through and between proteins is imperative. There is not one simple explanation to how these processes proceed because organisms have evolved conditions for their respective ET reactions. In this thesis, biological ET is studied using semiclassical ET theory with a specific focus on how a protein's microenvironment affects pathways that include the redox-active amino acids tyrosine (Tyr, Y) and tryptophan (Trp, W). The physical properties of both Tyr and Trp are also explored.

1.3.1. Metalloproteins in Biological Redox Reactions

Due to redox reactions playing such a major role in sustaining life, it is unsurprising that proteins employ redox-active metals to carry out these reactions.[42] Metal-containing proteins are termed metalloproteins and although many metals display redox properties, only a select few are found within biology. The three that encompass the majority of biological ET reactions are cupredoxins, iron-sulfur cluster-containing proteins, and cytochromes.[42] This thesis will focus primarily on the first of those classes, specifically *Pseudomonas aeruginosa* azurin, and how it can be used as a model for developing artificial ET pathways.

Copper and iron proteins have a range of functions such as substrate oxidation, electron transport, reactive oxygen species (ROS) scavenging, oxygen binding, and catalysis.[42–44] For copper proteins, the sizes of the proteins are diverse, ranging from small electron carriers to large multicopper enzymes. Copper proteins can be classified according to their spectroscopic properties, and are comprised of types 1, 2, or 3. As azurin is a type 1 copper protein (also called blue-copper proteins), these copper sites will be briefly mentioned below.

1.3.2. Type 1/Blue-Copper Proteins

Blue-copper proteins have unique properties that arise from the high degree of covalency between the copper ion and the ligating cysteine (Cys). In contrast, other copper sites lack Cys and have entirely different physical properties that can be attributed to differing primary and/or outer-sphere ligands. Thus, the major features of copper sites are largely determined by their primary ligands, but the outer-sphere also plays an important role.[45,46]

Blue-copper proteins have been characterized by their strong absorbance properties at ~600 nm, yielding an intense blue colour due to a sulfur → copper charge transfer. The distinct pseudo trigonal pyramidal geometry of the blue-copper site typically displays coordination by one Cys and two histidine (His) ligands with an axial methionine (Met) sometimes observed. A narrow four-line hyperfine splitting also is observed in electron paramagnetic resonance (EPR) spectra of blue-copper sites. Although many blue-copper proteins exist, azurin, a single-domain protein,[42] is the focal point in this thesis.

Interestingly, blue-copper proteins display a sequence identity of <20%, with the common cupredoxin fold being conserved. This fold is comprised of a β-barrel consisting of eight β-strands. The ligands for the type 1 copper center are housed in this key fold.[42] Met plays an important role in influencing the geometry and properties of this type 1 copper site. When the distance between the Met-sulfur (Met(S)) and copper decreases, several outcomes are possible. For example, replacement of the Met in azurin modifies the strength of the Cu−Cys bond, which can be quantified based on the metalloprotein's optical properties, X-ray spectroscopic features, and EPR properties.[47,48] Substitution with natural[46] and isostructural unnatural[47,48] groups at the native Met position can impact reduction potentials. While Met is an inner-sphere ligand, changes to the copper site often translate to outer-sphere motifs within the protein as well. This can be, at least in part, due to the movement of the copper ion and resultant changes in the geometry of other ligands and their outer-sphere interactions. One example of such behaviour is in "hard ligand" azurins, where constraints imposed by the outer-sphere ligands impact the electronic structure and reactivity of the copper ion, despite the lack of Met and Cys ligands.[49–51] In sum, outer-sphere bonding (often hydrogen bonds) can extend through large portions of

a protein and there is an interplay of these interactions responsible for geometry and physical properties of the copper site.[46]

The outer coordination sphere typically includes residues that affect the inner coordination sphere.[52] This is where the concept of the microenvironment plays a role. Hydrogen bonding and/or hydrophilic/hydrophobic effects are the two main effects that could affect the inner coordination sphere of the copper active site.[46] The hydrophilic effect has been demonstrated most clearly through the incorporation of phenylalanine (Phe) in the outer-sphere of azurin, where each Phe mutation adds about 30 mV to the azurin Cu(II/I) reduction potential.[53] However, the influence of the microenvironment on the properties of copper sites is often complex. In type 1 copper proteins, hydrophobicity and overall charge of nearby residues influences reduction potentials of copper sites. For example, His35 in azurin is an outer-sphere residue and His35Gln (Gln = glutamine) and His35Leu (Leu = leucine) point mutations influence Cu−S−Met121 bond distances.[54] The geometry of the copper site subtly changes and this finding suggests that different amino acids in the outer-sphere may introduce long-range structural changes that impact ET reactivity. A range of other outer-sphere mutations (with azurin Met121 intact) can shift the Cu(II/I) potential by over 300 mV, and a range of over 700 mV is possible if mutations are made to Met121.[55] Another great example of how changes to the outer coordination sphere affect the copper site is in Phe114Pro[56] (Pro = proline). This variant has a lower reduction potential, longer Cys−Cu bond (2.23 Å), and shorter Met−Cu bond (2.99 Å), while the higher potential Asn47Ser/Phe114Asn (Asn = asparagine, Ser = serine) mutant has shorter Cys−Cu (2.18 Å) and longer Met−Cu (3.23 Å) bonds. This is a consequence of the Cu ion moving “up” (away from Met) in the azurin active site. Interestingly, the position of Met is static in these two electronically very different proteins, and it is the structural features opposite Met that undergo changes.[55] Outer-sphere effects can all be considered as local, microenvironment effects with respect to certain motifs. These have been widely studied for their impact on biological metal centers, however, a lack of understanding on how the microenvironment affects other motifs still exists. This thesis aims to bridge that gap and focus specifically on how a protein’s microenvironment affects aromatic amino acids, Trp and Tyr.

1.3.3. Hopping Intermediates in Biological Electron Transfer

As stated in section 1.2.1, single-step ET over distances >20 Å is inefficient for biological systems.[22,30] Proteins use reactive intermediates to overcome this challenge. There are several reactive intermediates that are used for facilitating ET in biological systems. These range from inorganic iron-sulfur clusters[57] to organic amino acid residue side chains.[34,57] This thesis mainly focuses on amino acids, specifically the aromatic amino acids, Trp and Tyr. The participation of these amino acids in ET events has been extensively studied in the past,[29,33,58] however, my work aims to expand upon the already known redox activity of Trp and Tyr[59] and investigate how their interactions with other amino acids (i.e., the outer-sphere or microenvironment) affects their physical properties and reactivity.

Naturally occurring chains of aromatic amino acids exist and an example is set out in Figure 6. Here, deoxyribonucleic acid (DNA) photolyase utilizes a chain of three Trp residues for electron hopping. In this enzyme, these residues facilitate ET from the solvent exposed Trp306 to the flavin adenine dinucleotide radical ($FADH^{\bullet}$) active site.[60]

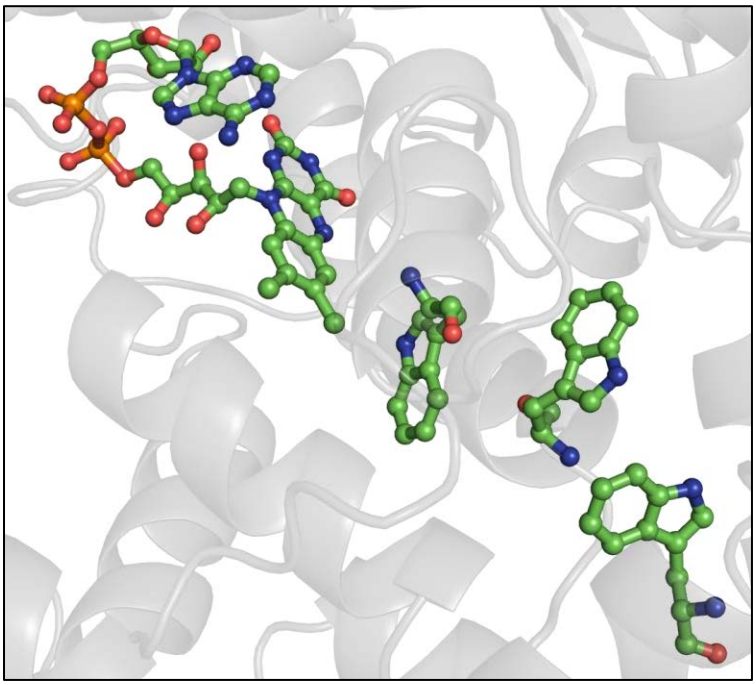

Figure 6. **Hopping intermediate chain found in DNA photolyase from *Escherichia coli*. Chain from left to right is $FADH^{\bullet}$−W382−W359−W306. PDB ID: 1DNP.[61]**

Hydrogenases are an example that use iron-sulfur clusters to facilitate ET. These enzymes catalyze hydrogen conversion in nature and their biological function relies on PCET reactions. In this example, an [FeFe] hydrogenase is comprised of a finely tuned tertiary structure that contains an embedded [2Fe] H-cluster and one (or more) [4Fe-4S] cluster(s) allow for efficient biological ET to occur.[62] Figure 7 provides an example of the structure of this enzyme. These remarkable enzymes cannot go unmentioned, but the majority of this thesis focuses on amino acids as hopping intermediates and not on such iron-sulfur clusters.

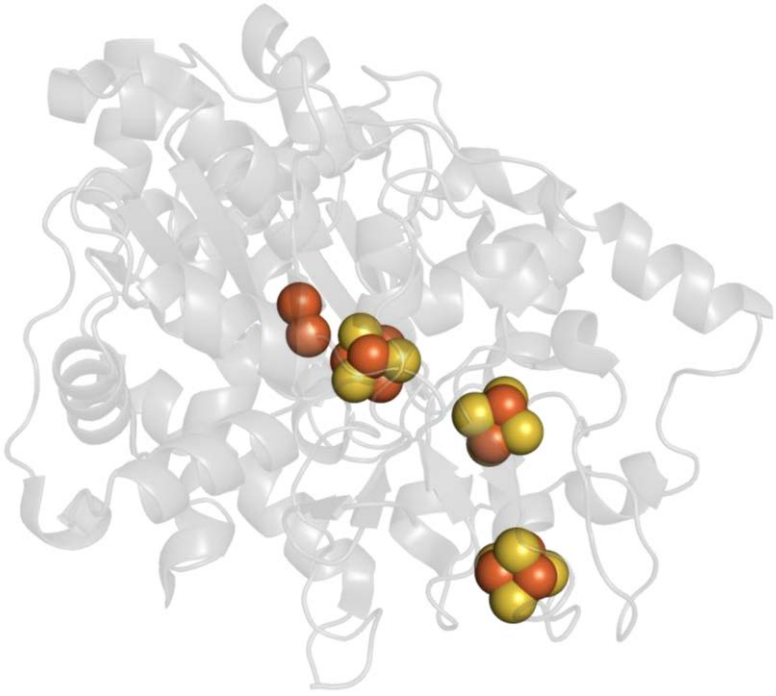

Figure 7. An example of an [FeFe] hydrogenase from *Desulfovibrio desulfuricans* in which one [2Fe] H-cluster and three [4Fe-4S] clusters are present. Orange spheres are Fe atoms and yellow spheres are S atoms. PDB ID: 1HFE.[63]

1.3.4. Aromatic Amino Acids: Tyrosine and Tryptophan

Closely spaced groups of Trp and Tyr have been attributed to stabilizing protein folding, however, it is now thought that such arrangements of residues could play other roles.[30,32,64] The most common redox reactions of amino acid residues involve Trp and Tyr, which participate in hole transfer reactions. A hole can be described as a site that can be occupied by an electron. Thus, hole transfer and ET are directly related wherein the hole

is the space that an electron transfers to and removal of an electron results in a hole. It is this idea that indicates that chains and clusters of these residues could facilitate long-range ET.[24,30]

The most well understood ET system involving a chain of Tyr residues is *Escherichia coli* (*E. coli*) ribonucleotide reductase (RNR). This protein is required for DNA biosynthesis, specifically in conversion of ribonucleotides to deoxyribonucleotides. The functional ET chain is shown schematically in Figure 8. The centre blue and red box show the most common class, Ia RNRs, which rely on thioredoxin (Trx) and thioredoxin reductase (TrxR) for turnover. The “P” indicates inorganic phosphate. Other classes of RNR’s are shown at the left and right of the figure. These also rely on amino acid radicals, but not on multi-step ET via Tyr/Trp.[65] The mechanism of ET in Class Ia RNR enzymes has been investigated in great detail,[66] including experimental studies of the energetic landscape of the ET chain.[67] RNR is an incredibly complex system and decades of effort have gone into elucidating its mechanism. Consequently, there remain open questions about how the protein, specifically the microenvironment around each redox active residue, affect their individual ET properties.

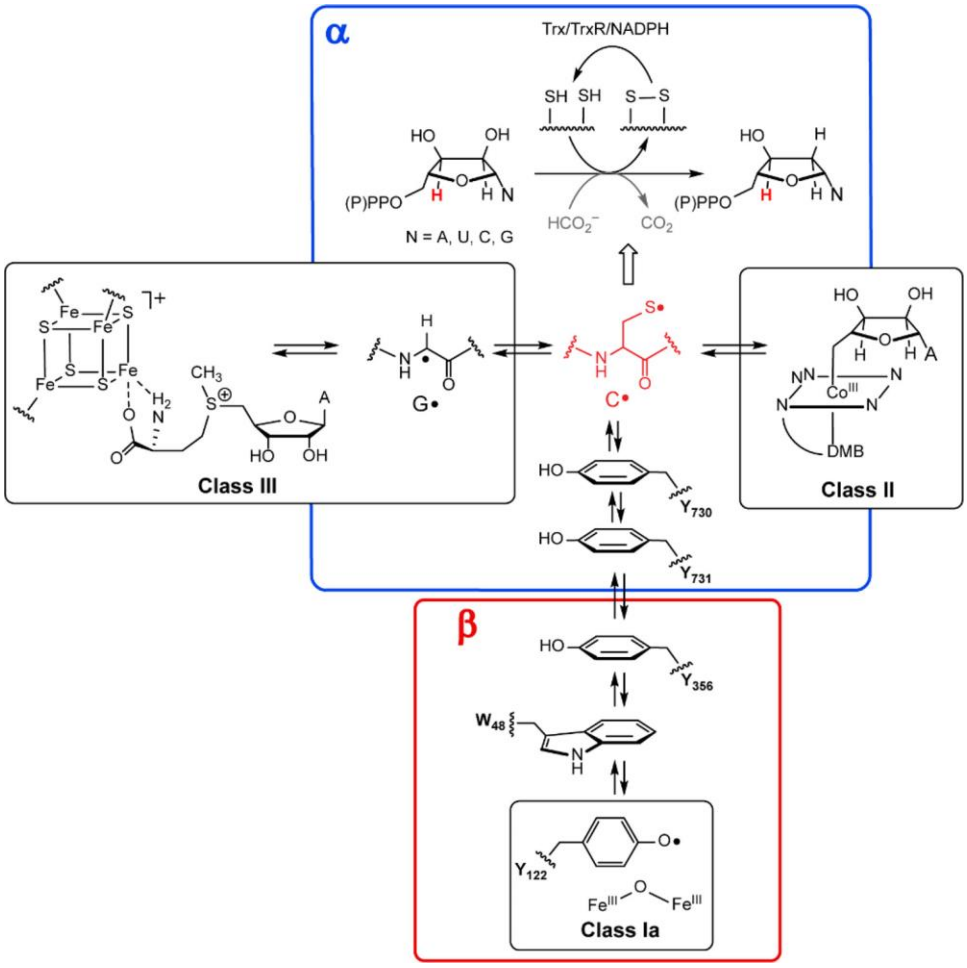

Figure 8. **A schematic showing the ET chain of Tyr and Trp in Class Ia RNR proteins. The left and right panels show the radical initiation machinery of other classes of RNR that do not use Tyr/Trp chains. Reprinted with permission from Stubbe, J.; Nocera, D. G. Radicals in Biology: Your Life Is in Their Hands. *J. Am. Chem. Soc.* 2021, *143* (34), 13463–13472. https://doi.org/10.1021/jacs.1c05952. Copyright 2021, American Chemical Society.**

ET also is crucial for combating irreversible oxidative damage *via* ROS. As such, it has been proposed that Trp and Tyr play a role in protection against oxidative stress.[24,29,30,32,52,64] For example, it has been suggested that strongly oxidizing electron holes may be shuttled away from protein-embedded sites by chains of Trp or Tyr (as well as other redox-active amino acids, Cys and Met). This has been proposed for monooxygenases, dioxygenases, and peroxidases.[32] Furthermore, a bioinformatic survey of the Protein Data Bank (PDB) revealed that 33% of proteins surveyed contained chains of at least three Trp or Tyr residues.[30,32] Such a large proportion of proteins strongly suggests some functional significance, though this is still an open field of research.

There are some initial hints about how a protein's microenvironment can affect Tyr/Trp ET properties. For instance, the orientation of aromatic residues can influence ET rates. Two types of orientations can be observed, the parallel-displaced and the T-shape types. In a parallel-displaced geometry, aromatic stacking interactions predominate and give rise to higher electronic coupling interaction energies over their T-shape counterpart. It is suggested that proteins could utilize geometric effects to fine-tune ET kinetics. For example, a five-residue Trp/Tyr chain was identified in cytochrome P450 CYP11A1, shown in Figure 9. Here, Gray and Winkler calculated a 10-fold increase in energy between Tyr90 and Trp231 in which a parallel-displaced geometry is seen compared to the T-shape interactions between all other residues in the chain. It was proposed that this chain may play a role in hole transfer for the conversion of cholesterol to pregnenolone. During the natural catalytic cycle of P450 enzymes, a highly oxidizing intermediate (compound I) is produced. It is thought that this oxidant could damage the protein in cases where substrate is not present.[24] Also, Met has been considered to participate in the removal of highly oxidizing intermediates, but those reactions are less understood.[52]

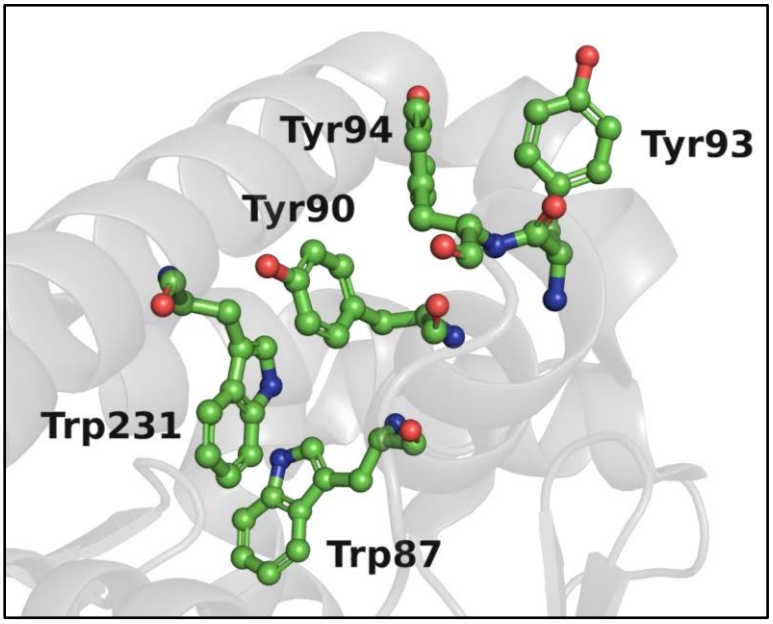

Figure 9. **Trp/Tyr chain found in cytochrome P450 CYP11A1 displaying both T-shape interactions (Tyr93/94, Tyr94/90, and Trp231/87) and parallel-displaced interactions (Tyr90/Trp231). A 10-fold increase in energy is observed between parallel-displaced residues. PDB ID: 3N9Y.[68]**

It is worth noting that, under most biological conditions, the redox behaviour of Tyr and Trp is actually PCET as opposed to pure ET. In water, this means that the formal reduction potentials of the Tyr and Trp are pH dependent. The formal reduction potentials

at pH 0 (i.e., $E°$) for Tyr and Trp are 1.4 and 1.15 V, respectively. The corresponding radicals, $Tyr^{\bullet+}$ and $Trp^{\bullet+}$, have pK_a values of –2 and 4.5, respectively. This means that Tyr always loses a proton upon oxidation, to yield the neutral Tyr• radical. In contrast, $Trp^{\bullet+}$ does not need to undergo a deprotonation upon oxidation and can participate in pure outer-sphere ET. This, of course, depends on the pH and other factors (e.g., the protein microenvironment). The PCET chemistry of Tyr and Trp are set out schematically in Figure 10 and Figure 11, respectively. For the free amino acid residues, Pourbaix diagrams have been developed in the literature to map out the pH dependence of the potentials across all pH values.[69]

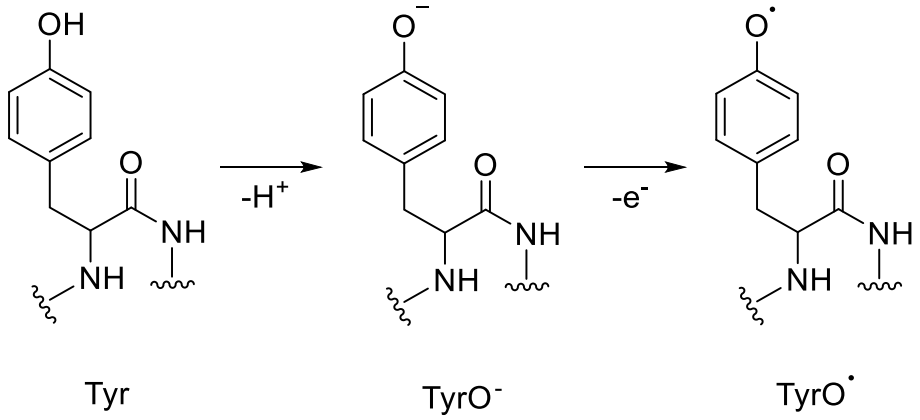

Figure 10. PCET reaction scheme of Tyr conversion to tyrosyl ($TyrO^{\bullet}$) through a tyrosinate ($TyrO^{-}$) intermediate.

In proteins, a neutral Trp radical ($Trp^{\bullet}$) can be formed through the reaction shown in Figure 11. Here, a cationic radical ($Trp^{\bullet+}$) can be formed without initial deprotonation; its pK_a is near 4.[69] Both Trp and Tyr radicals have been observed in proteins and both are the basis of the work in all chapters of this thesis except Chapter 5.

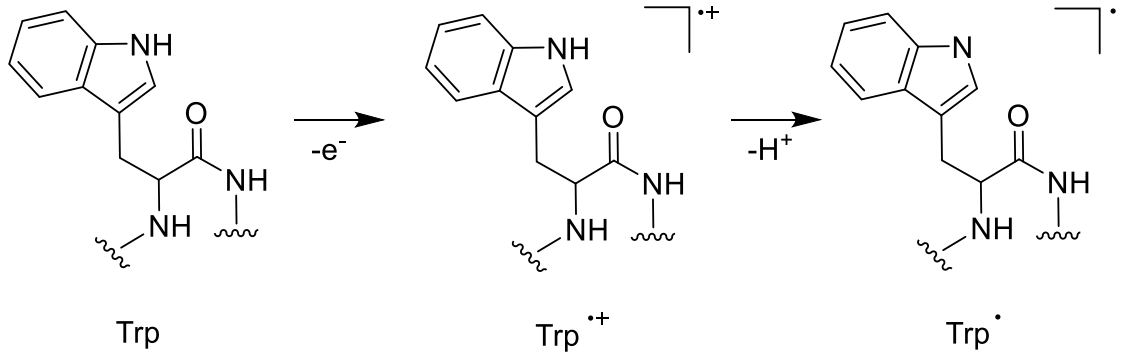

Figure 11. PCET reaction scheme for the formation of a neutral Trp radical ($Trp^{\bullet}$) through a Trp cation radical ($Trp^{\bullet+}$).

1.3.5. Proton-Coupled Electron Transfer

A brief overview of biological PCET reactions in the context of this thesis should be discussed at this stage. A more detailed review can be found elsewhere.[18] PCET combines PT with ET and describes a reaction in which electrons and protons transfer simultaneously. PCET reactions are central to many biological redox reactions. One such example is the coupled CO_2 reduction and H_2O oxidation that occurs during photosynthesis with an overall transfer of 24 e^- and H^+ during the entire course of photosynthesis.

PCET can occur through different elementary steps. These include ET, PT, and concerted electron-proton transfer (EPT). Typical PCET reactions occur by a combination of steps that are dictated by the reaction conditions such as temperature and/or pH. These can occur from a single donor to a single acceptor or across multiple sites (termed multiple site EPT, or MS-EPT).[18] For this thesis, the main focus will be on stepwise electron transfer-proton transfer (ET-PT; electron transfer followed by proton transfer) or the inverse, stepwise proton transfer-electron transfer (PT-ET; proton transfer followed by electron transfer). It should also be stated that for Chapter 2 and Chapter 3, an ET-PT dominates for Trp (as seen in Figure 11, above). For Chapter 4, a PT-ET dominates for Tyr (as seen in Figure 10, above).

1.4. Intermolecular Forces Within Proteins

1.4.1. Methionine-Aromatic Motifs: Structures, Types, and Theory

As noted above and in the context of ET, the most commonly discussed redox active amino acids are Tyr, Trp, and Cys. These amino acid residues are understood in terms of their single ET (or PCET) reactivity. On the other hand, the most common and established examples of Met redox reactions are interconversions of Met and its corresponding sulfoxide.[70,71] Thus, an ongoing question is if Met can participate directly in long-range ET reactions. The $Met^{\bullet+/0}$ potential has not been determined directly, but has been estimated to be in excess of 1.2 V.[72] One peptide-based model system suggests that, when situated halfway between two redox sites, Met can improve the efficiency of ET over a distance of about 20 Å.[73] However, oxidized Met intermediates were not detected in that study. The idea that Met can participate in long-range ET and that the side chain

microenvironment strongly influences such reactions is supported by calculations.[57,74] Other computational analyses have suggested that biomimetic sulfur-aromatic (S-π) models have lower reduction potentials than the individual components and may therefore influence biological ET.[75,76] It is of ongoing interest to identify potential redox active hole hopping pathways involving Met.[70,71]

Met is often classified in textbooks as a non-polar and/or hydrophobic amino acid residue,[77] but this can be an oversimplification. The sulfur atom has a different electronegativity value than the neighbouring carbons in the Met thioether, as well as two lone pairs of electrons. This means that Met is weakly polar. An example of an electrostatic map is shown in Figure 12 to illustrate this point. This feature of thioethers has been appreciated by physical organic chemists and there are models that show how thioethers can interact with aromatic systems in solution[78] through intermolecular interactions and weak dipolar interactions.[79,80]

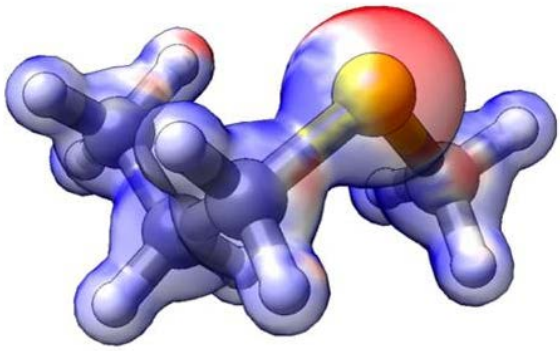

Figure 12. Electrostatic map of Met illustrating the weak partial negative charge on the sulfur atom and the weak partial positive charge on the thioether CH_2 and CH_3 groups. Red indicates an electrostatic potential of –0.025 and blue represents +0.025 (units are kcal mol^{-1} e^{-1}). The image was rendered using Chimera.[81]

The S-π interaction has been known in metalloproteins since the early days of the PDB.[82–84] As an example, in 1978, the first evidence of S-π interactions (sulfur-containing residues: Cys or Met) were found in eight globular proteins. This discovery consisted of chains of alternating sulfur-containing and aromatic (Trp, Tyr, or Phe) residues along ET pathways, suggesting that clusters of S-π interactions could have a strong impact on redox reactivity, not just protein structure.[82]

More recent bioinformatics investigations show how such interactions can stabilize proteins.[85] Experimental studies of artificial peptides suggest that interactions between Met(S) and Tyr, Phe, or Trp, stabilize structures by up to 0.5 kcal mol^{-1} for each instance.[86] Computational analyses of interactions between Met(S), Met−CH_2, or Met−CH_3 with benzene suggests that up to 3 kcal mol^{-1} per instance of stabilization is possible.[87] Interestingly, the interaction of the sulfur and the face of the aromatic is predicted to be the most favourable in two different computational investigations.[87,88] Similar results are indicated for calculations using other aromatics (indole and/or phenol) and show that the interaction lowers the potential at which the motif can be more easily oxidized.[75,76] The role(s) of methionine-aromatic (Met-aro) interactions in protein structures is important, but less is known about the specific roles of such motifs in metalloproteins or in redox reactions.

Chapter 5 focuses on a bioinformatic study on Met-aro interactions, more specifically, Met-sulfur-aromatic (Met(S)-aro) interactions occurring in a “three-bridge” fashion,[89] however, other recent computational works have been completed.[29,90] In the first, the locations of Met(S)-aro interactions were assessed in metalloproteins. That investigation revealed several noteworthy features. First, Met(S) can interact with any number of aromatic carbon atoms, but interactions with two carbons is the most common. Second, Met commonly interacts with one, two, or three aromatic groups, but interactions with one Met and one aromatic (Phe, Tyr, or Trp) are most common. Most structurally characterized proteins have at least one Met-aro interaction. Third, Met(S)-aromatic interactions are found throughout protein structures, from near metal sites to >20 Å away. The locations far from metal sites are consistent with structural roles in controlling a protein’s tertiary structure. Finally, in assessing the distribution of Met(S)-aro close contacts, it was noted that there is a range of distances in X-ray structures, between about 3.6 Å to over 4.6 Å. This suggests that the strength of the interaction is variable, consistent with a weak dipolar interaction that can be affected by its secondary interactions, revealing that it was possible for both lone pairs on Met(S) to interact with aromatic residues.[29] A follow-up systematic study of such interactions in known structures showed that an aromatic-Met(S)-aromatic (aro-Met(S)-aro) “bridging” interaction is widely distributed across many different protein structures. Bridges involving at least one Phe and one of either Phe, Tyr, or Trp accounted for almost 80% of the interactions identified. In most cases, bridges are isolated, but in about 10% of cases, the bridges were associated with

longer chains of aromatic groups or were located between active sites and protein surfaces.[90]

An example in which ET may be influenced by Met is in cytochrome *c* peroxidase (C*c*P). This enzyme has many oxidizable residues beyond the commonly studied Trp191 (Figure 13).[52,91,92] Analysis of the hole hopping routes within C*c*P found that the inclusion of these routes within the protein may prevent oxidative damage to the heme.[91,92] Met plays a role in at least one of the hopping chains in Figure 13 and it is noteworthy that formation of a sulfoxide at Met230 or Met231 prevents formation of the Trp191 radical.[93] In diheme MauG, another peroxidase, redox reactions of Met near one of the heme sites has been proposed as a regulator of the high valent compounds needed for enzyme function. The above findings suggest the possibility that Met-aro interactions could regulate hole hopping, and that Met itself may play a larger role in these interactions than has been previously appreciated.[94]

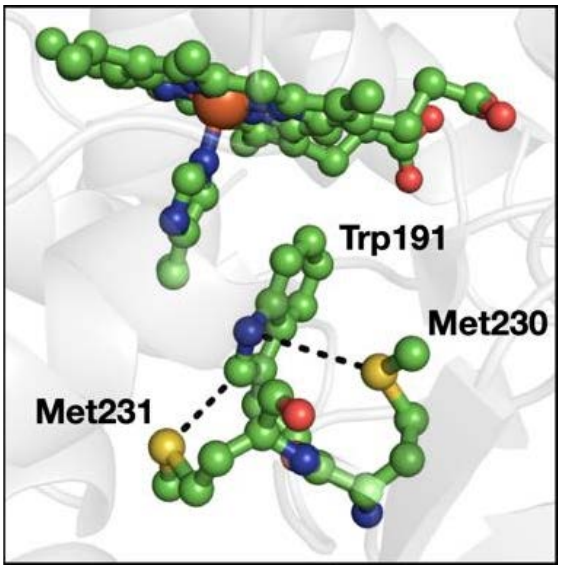

Figure 13. The Met(S)-aro interactions in C*c*P involving the redox active Trp191. PDB ID: 2CYP.[95]

Understanding of many of the physical properties of Met-aro interactions is incomplete and they have only been investigated experimentally using small molecule model systems.[78–80,96–98] While some such systems are pre-arranged to promote interactions between Met and another group,[79,80,98] they have led to suggestions about structures in proteins and have elucidated noteworthy spectroscopic properties, especially for the 1-electron oxidized compounds.[80] Chapter 2 and Chapter 3 in this thesis focus

primarily on the spectroscopic properties of Met-aro interactions. Although Chapter 4 features a Met-aro interaction, other mutations are also presented in that work.

1.4.2. The Two-Center, Three-Electron Bond

A thought-provoking idea supported by studies of radical-containing Met-aro species is the possibility of a two-center, three-electron ($2c-3e^-$) bond that involves Met and a second electronic system. A fundamental picture can be described as an orbital overlap between the unpaired electron in the radical cation and a lone pair of electrons from Met(S). This overlap leads to the formation of a new set of molecular orbitals that give rise to a bond with a bond order of ½.[99] To extend the concept of 2c−3e− bonds to biological models, some small molecule systems have been probed using a combination of experiment and theory.[97] Using a molecular model comprised of formally 1-electron oxidized pairs of benzenethiols, two types of bonding were described: σ-type and π-type (Figure 14). A σ-type interaction involves σ-type orbital overlap between the sulfur-based radical cation and a closed shell sulfur on an opposing molecule (Figure 14, top). A π-type interaction is one in which a radical cation is stabilized by overlap between the sulphur-based radical and a π-symmetry orbital on an opposing molecule (Figure 14, bottom).[97] Both arrangements are favourable and have similar energetics. The σ-type interaction is further supported by experimental and theoretical investigations of small thiols and their radicals in the gas phase.[99,100] It should be noted that the stabilization of thioether radicals could involve delocalization over many sites with energetically accessible orbitals.[101] While many of the models described above involve symmetric pairs of thiols, the S-π interaction resembles what has been described in proteins.

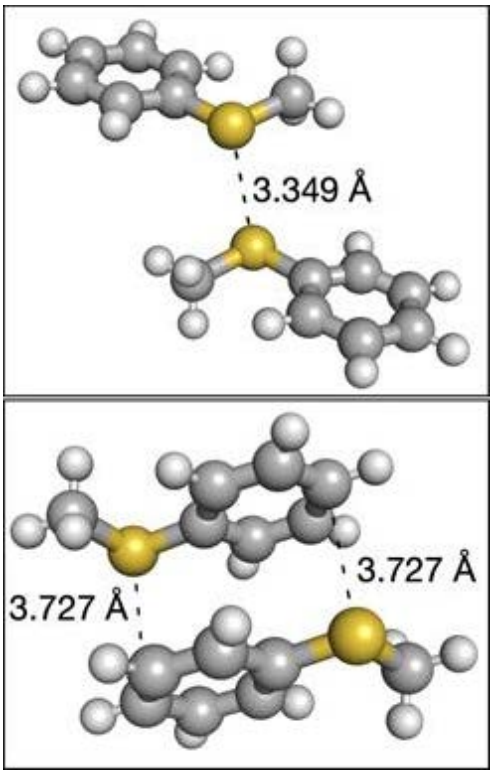

Figure 14. Geometry optimized examples of a σ-type interaction (top) and a π-type interaction (bottom) seen in 1-electron oxidized (radical cation) thioanisole dimers. Close contact distances are designated between each in Ångstroms. The images are original, but the coordinates used to render the image are obtained from reference [97].

1.4.3. Cation-π Interactions

Cation-π interactions are a relatively new interaction that has become accepted within proteins in the context of stabilizing structure and substrate binding.[102,103] Initial model systems provided a basis for the importance of these interactions, eventually extending to their applications within biological systems. In most cases, these interactions are found within substrate binding sites to increase the stability of the protein-binding complex. As the name suggests, the cation-π interaction is fundamentally described as an interaction between a cation and an aromatic π-system, although other intermolecular forces (i.e., the hydrophobic effect and hydrogen bonding, to name a few) should be considered that help to establish this motif in a protein.[104] In small molecule models, the binding energies for cation-π interactions have been reported from ~40-90 kJ mol^{-1} and could enhance protein-binding interactions by ~10-20 kJ mol^{-1}.[102] It is also important to note that cation-π interactions can be influenced by polarity and pH,[105] two factors which are a large consideration throughout the entirety of this thesis. Although not a main focus,

it is possible that positively charged amino acids could be considered similar to a cation-π interaction.

1.4.4. Other Non-Covalent Interactions Within Proteins

Met-aro interactions are part of a broad cross section of non-covalent forces that are at play in biochemical systems.[106] Other examples include anion-π interactions[107,108] and aliphatic CH-π interactions.[109,110] In particular, the interaction between the Met-thioether CH_2 and CH_3 groups with aromatics is related to CH-π interactions. Although the strength of any of these interactions, including Met-aro moieties, depends on the specific system under investigation, estimates of their energies are usually on the order of 0.5 to 1.5 kcal mol^{-1}.[106]

1.5. Microenvironment Effects on Tryptophan and Tyrosine in Metalloproteins

1.5.1. Microenvironment Effects on Protein Fluorescence

Three aromatic amino acids contribute to the overall fluorescence of a protein. These include (1) Phe, which absorbs 260 nm light and has an emission maximum at ~280 nm, (2) Trp, which has a broad absorption band from 260-290 nm and can display emission maxima on a broad range as well (305-350 nm), and (3) Tyr, which absorbs light on a similar range to Trp but emits light on the shorter end of the emission range (~305-315 nm).[111] Phe fluorescence will not be discussed further as it does not impact the work carried out in this thesis. Chapter 2 and Chapter 3 use Trp fluorescence for characterization and Chapter 4 investigates Tyr fluorescence.

In natural proteins, a combination of the amino acids mentioned above are typically present, and due to the anisotropic nature of Trp and Tyr, fluorescence of these amino acids can be used to study protein folding and associated local interactions. As stated, Trp emission occurs across a broad range of wavelengths, often due to solvent effects and local interactions with other amino acids (i.e., the microenvironment) through the indole sidechain. Understanding the emission spectrum of a Trp residue can be complex due to the overlapping π-π* transitions to the ^1L_a and ^1L_b excited states. Depending on the microenvironment around the Trp residue, either of these states could be lower in energy,

resulting in different emission patterns. In contrast, the emission of Tyr is attributed to solely from ^1L_b excited state.[111] Although beyond the scope of this thesis, full resolution of Trp emission can be achieved using a variety of techniques to probe the emitting state,[112] one such example is the study of excitation anisotropy spectra.[111]

For the context of this body of work, it must be understood how the indole sidechain is affected by the microenvironment. Solvent effects are commonly described with respect to polarity influencing hydrogen bonding. Excitation anisotropy spectra have been reported elsewhere for Trp[111] but are used to describe polarity effects here. In nonpolar solvents, the emission spectra mirrors that of absorption to the ^1L_b state, suggesting that emission in nonpolar solvents is from a lower energy ^1L_b state. As polarity increases, the emission spectra resembles the ^1L_a absorption pattern, suggesting that this excited state is more sensitive to changes in solvent and is at a lower energy in polar solvents than ^1L_b.[111] It should be noted that this result could differ when a residue is not solvent-exposed, however, the polarity of the microenvironment may play a similar role. Likewise, Tyr absorption exhibits two absorption bands due to π-π* transitions to ^1L_a and ^1L_b states. The near 280 nm absorption for Tyr is due to the ^1L_b transition and hydrogen bonding leads to a red-shift in its absorption as well as an increase to its extinction coefficient.[113]

As mentioned above, Tyr emission and absorption are less complex, however, the change in the hydroxyl pK_a between ground- and excited-states leads to its own complications. Ground-state Tyr has a pK_a of ~10 whereas excited-state Tyr has a pK_a of ~4, suggesting that ionization could occur at physiological pH. Furthermore, ground-state Tyr can experience ground-state complex formation. The experiments set forth in Chapter 4 aim to overcome these and are described in more detail there.

1.5.2. Microenvironment Effects on Reduction Potentials

The formal potentials of both Trp and Tyr are accessible to biological systems and allow holes to be transferred at potentials near 1 V at physiological pH[69] (note that all reduction potentials in this thesis are reported with respect to the normal hydrogen electron (NHE)). This is important for energetically demanding processes (e.g., water oxidation, C-H bond activation).[30] In general, simple redox reactions of these two residues is well-understood.[69,114–116] However, understanding how nature controls their reactivity is of ongoing interest. A few examples are highlighted here, but these are limited in scope and

a full review is beyond the scope of this thesis. For Trp, the lignin-oxidizing lignin peroxidases employ a surface exposed Trp radical as a redox mediator linking insoluble lignin substrate and the radical-generating heme.[117–119] This reaction is not possible without a high potential Trp (ca. 1.4 V) and it is thought that the microenvironment is crucial for maintaining that high potential.[118] For Tyr, the hydrogen bonding tyrosine$_z$-His191 in photosystem II (PSII) is a great example of how a protein microenvironment can maintain high driving forces. The function of PSII relies on ET via tyrosine$_Z$, which mediates electron flow between P680 (a strong oxidizer that acts as the primary donor in PSII) and the Mn_4CaCl oxygen evolving complex.[120–122] The importance of the Tyr-His hydrogen bond is supported by studies of model systems.[123–126]

Microenvironment effects also are important for embedded redox active metal ions. Briefly, direct axial ligand substitution of Cu in azurin has been extensively studied to determine changes to the formal potential of the Cu(II/I) redox couple.[42,127–129] It has been observed that by changing the axial ligand to certain residues can increase or decrease the formal potential, and in particular, hydrophobic residues have been shown to increase the formal potential of the Cu(II/I) redox couple in azurin. Likewise, microenvironments that display more hydrogen bonding have been shown to increase the formal potential of this redox couple as well.[42] Although in this work, the Cu(II/I) redox couple is not of concern as mutations in those systems are at a point in which no effect will be seen, the idea of hydrophobicity and changes to the hydrogen bonding network could be extended to that of Trp and Tyr.

1.5.3. Microenvironment Effects on Electron Paramagnetic Spectroscopy

Amino acid radicals are very often characterized using electron paramagnetic resonance (EPR); optical and vibrational spectroscopies also are used, but the measurements are typically done transiently using time-resolved spectroscopies. Steady state EPR provides vital information about the radical's spin density, geometry, and electronic structure. For azurin, EPR has been used to probe electronic changes to either Trp or Tyr radicals in the presence of different microenvironments. The work described in Chapter 3 utilizes this information to understand how the electronic structure of a Trp residue changes when a Met residue is added into the microenvironment. EPR of Tyr is not investigated in this work.

A common starting point for investigating protein radicals is to use small molecule models that mimic amino acid radicals (e.g., indoles for Trp and phenols for Tyr). The EPR hyperfine coupling and g-values are affected by the solvent that a given species is in, especially with respect to hydrogen bonding.[130] Herein, hydrogen bonding from the amino acid residue's protein microenvironment will be the main focus, but other non-covalent interactions are considered. For Trp, the presence or absence of hydrogen bonding with the indole nitrogen is a key factor and will be discussed further in Chapter 3. As stated above, solvent also plays a role here and exposed residues are, of course, more affected by solvation. The azurin Trp108 radical that is investigated in Chapter 3 is a partially solvent exposed residue, thus, microenvironment effects imparted by the aqueous environment may also play a role.

1.6. Spectroscopic and Instrumental Methods

The research described in this thesis employed different experimental methods and it is worth outlining their basic principles and their specific importance to this thesis. Many tools used in this thesis are commonly used in the literature[26,31,51,131–141] and, as such, are important for the reader to understand. Specifically, this section will focus on protein modification, flash-quench methodology, transient absorption (TA) spectroscopy, EPR, and protein electrochemistry in the context of the work conducted herein.

1.6.1. Protein Expression, Purification, and Modification

The ET reactions described here rely on protein-based model systems that are (1) straightforward to prepare and (2) provide a close relationship to the more complex functional biological ET systems. The *in vitro* studies in this thesis allow for manipulations so that specific ET reactions can be targeted (e.g., a single ET step between a donor and acceptor). To that end, recombinant protein expression and site-directed mutagenesis are powerful techniques for designing and producing biological systems. Here, site-directed mutagenesis was utilized to design plasmid DNA bearing a specific protein sequence derived from *Pseudomonas aeruginosa* azurin. This was used to obtain our model proteins. Site-directed mutagenesis involves controlled changes to nucleotides in a protein's genetic sequence that result in specific amino acid changes in the translated protein. All research chapters use site-directed mutagenesis, along with protein

expression, purification, and modification to develop artificial model systems. Individual mutations are set out in each chapter apart from Chapter 5 which only involved computational work.

The protein expression and protein purification experiments were carried out using standard techniques[142] using an *E. coli* expression system.[143,144] Such microbial systems are often used for small-scale research and design, but their industrial scale-up is possible. At present, about 30% of biopharmaceuticals are produced recombinantly from bacterial hosts. *E. coli* is a widely used laboratory organism due to its inexpensive growth conditions, ease of growth and DNA transformations, and high-density and high-yielding cell cultures.[144] Azurin, the protein used in this thesis, has well-developed protocols that use an *E. coli* expression system, specifically using the BL21(DE3) strain.[142,145,146]

1.6.2. Time-Resolved Absorption and Luminescence Spectroscopies

Biological ET often occurs on timescales less than 1 ms. To evaluate reactions on such timescales, we must use time-resolved TA and luminescence (TL) spectroscopies to probe reaction kinetics (Chapter 2 and Chapter 4), where TA is used to monitor the rate of ET through a given system and TL is used to measure the rate of Ru(II) excited-state quenching. In both cases, a laser pulse (pump-pulse) of a specific wavelength is used to promote photosensitizer molecules to an electronically excited state. For luminescence, samples emit light and the collected light is directed into the monochromator where the energy of the photons is converted into an electrical current using a photomultiplier tube (PMT). For TA spectroscopy, a time-delayed probe pulse (from a Xe lamp in many cases) follows the pump pulse. A difference spectrum is then generated by subtracting the absorption of the ground state system from the absorption of the excited state system, resulting in ΔA.[147,148] In the Warren lab, these experiments are carried out using a home-built spectrometer containing a Continuum Surelite SLI-10 neodymium-doped yttrium aluminum garnet (Nd:YAG) laser or a wavelength-tuneable (400-700 nm) Continuum Surelite optical parametric oscillator (OPO) pump sources, and a 75 W Xe arc lamp probe source. The system has a home-built detection system**.** A schematic of this system is shown in Figure 15**.** This laser system was also used in Chapter 3, however, the setup was different and the changes are described there.

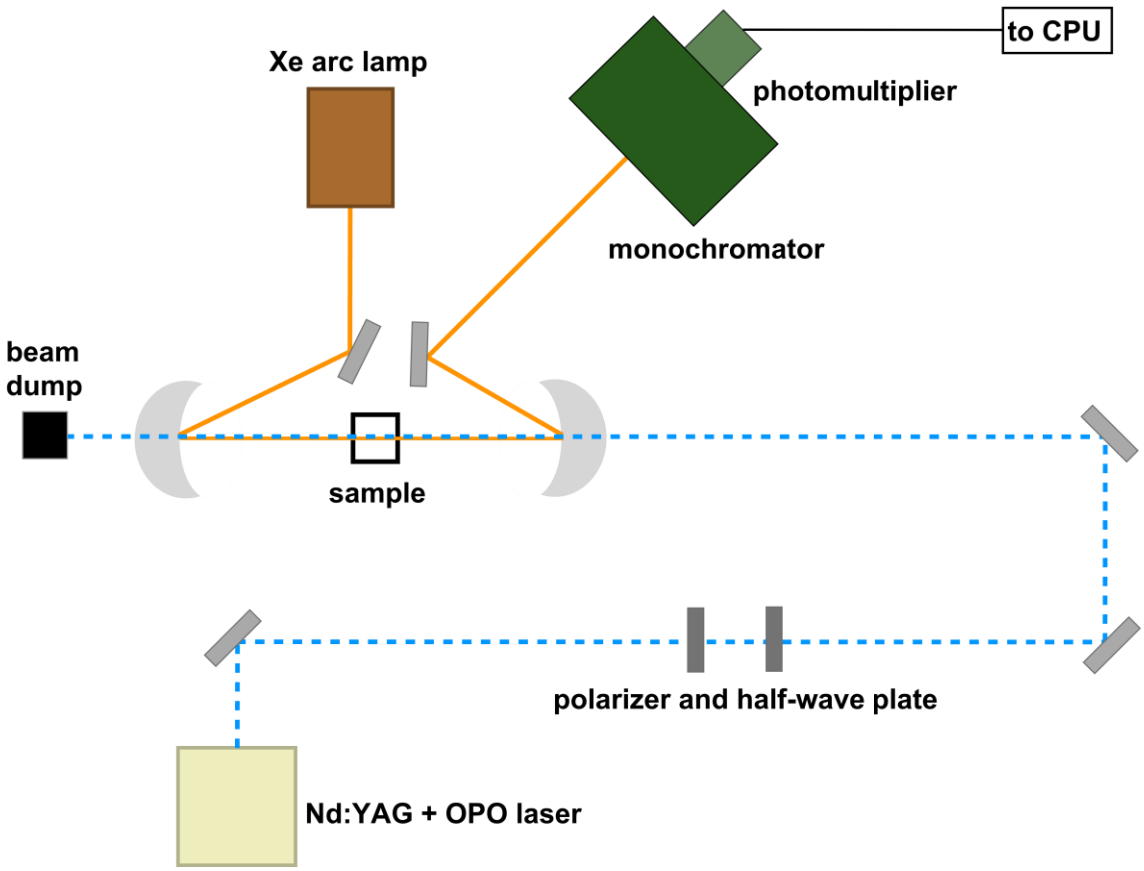

Figure 15. **Schematic of the laser system used in this thesis. The dotted blue line represents the pump pulse generated by the ND:YAG and OPO. The solid orange line represent to probe pulse generated by the Xe arc lamp.**

The flash-quench technique was used in all the time-resolved experiments described in this thesis. Detailed flash-quench schemes can be seen in each respective chapter in which it was used. To summarize this method, the "flash" is a laser pulse that excites the ground state of the system to an electronically excited state. Here, an exogenous quencher is added to the system. The quencher accepts an electron from the photosensitizer to give rise to a protein-tethered oxidant. Herein, $[Ru(NH_3)_6]^{3+}$ is used in any experiments in which ET kinetics are being monitored (Chapter 2 and Chapter 4). The irreversible quencher $[ClCo(NH_3)_5]^{2+}$ is used for experiments in which a product needs to be accumulated (Chapter 3). The use of reversible quenchers is desirable due to the ability to recover the protein used in each experiment, however, absorption intensities are sacrificed.

1.6.3. Electron Paramagnetic Resonance

The EPR technique is used to probe the physical properties of systems with unpaired electrons, i.e., organic radicals and paramagnetic transition metal ions.[149] In Chapter 3 of this thesis, EPR is used to study an organic Trp radical and how a nearby Met residue alters its electronic structure. This section briefly outlines some of the features of the EPR technique that are relevant to this thesis.

EPR experiments are performed by varying the magnetic field, *B*, at a constant frequency, ν. Experiments in this thesis were run with a frequency of ca. 9.3 GHz (X-band). The simplest possible EPR experiment measures the splitting of the two electron spin energy levels (m_s = +1/2 or -1/2). The energy of the transition is shown in $Eq.11$ where, *h* is Planck's constant, ν is the microwave frequency, *g* is the electron g-factor, *β* is the Bohr magneton, and *B* is the magnetic field.[149] Azurin has unique EPR properties associated with its Cu(II) metal center. A four-line hyperfine splitting can be observed due to the high covalency between Cu and sulfur.[42] EPR of the Cu metal center will not be discussed in this thesis as the main focus is on organic amino acid radicals. It is common for amino acid radicals to have simple observed EPR spectra, where only one transition is observed at g ~2. Tyr and Trp radicals have been observed, although less for Tyr, and they display some hyperfine coupling interactions that are sensitive to the environment surrounding the oxidized residue.[131–133,137,139,140] EPR spectroscopy is used in Chapter 3 and a discussion specific to that work can be found there.

$$h\nu = g\beta B \qquad (Eq.11)$$

1.6.4. Biological Electrochemistry

Electrochemistry is a powerful tool for probing ET events in small- and macro-molecules.[150] This allows for reduction potentials to be determined for various species present within a protein. Redox reactions are central throughout biological systems and are necessary for many biological functions to be carried out.[151] In this thesis, electrochemistry is used to determine peak potentials (E_p; all peak potentials are reported as V versus NHE). Both cyclic voltammetry (CV) and differential pulse voltammetry (DPV) are used in Chapter 4. These are complementary techniques that both determine formal reduction potentials (E°´), although the method for data collection differs slightly. In this

thesis, both experimental set-ups are similar and employ a common three-electrode cell containing a working electrode (WE), counter electrode (CE), and reference electrode (RE). A standard three-electrode cell is shown in Figure 16. The WE is where a potential is applied with respect to the RE and is where the electrochemical event of interest occurs. The CE is used so that a complete electrical circuit is achieved and allowing a current to be recorded as the potential is swept.

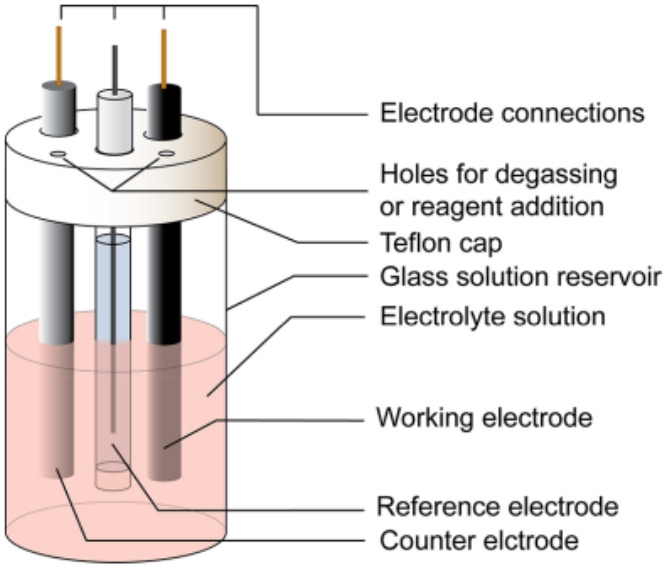

Figure 16. **A standard three-electrode cell set-up used for cyclic voltammetry experiments. The experiments carried out in this thesis do not use a cap as the samples did not need to be air-free during electrochemical characterization. Adapted with permission from Elgrishi, N.; Rountree, K. J.; McCarthy, B. D.; Rountree, E. S.; Eisenhart, T. T.; Dempsey, J. L. A Practical Beginner's Guide to Cyclic Voltammetry. *J. Chem. Educ.* 2018, *95* (2), 197–206. https://doi.org/10.1021/acs.jchemed.7b00361. Copyright 2017, American Chemical Society and Division of Chemical Education, Inc.**

For CV, potentials are swept in both the positive and negative directions between a pre-selected scan window. The current is measured as the potential is swept.[150,152] In DPV, a potential is applied in a pulse and the current is measured pre- and post-pulse with the difference in currents being reported.[153] An example of how the potential is applied for both of these methods is shown in Figure 17.

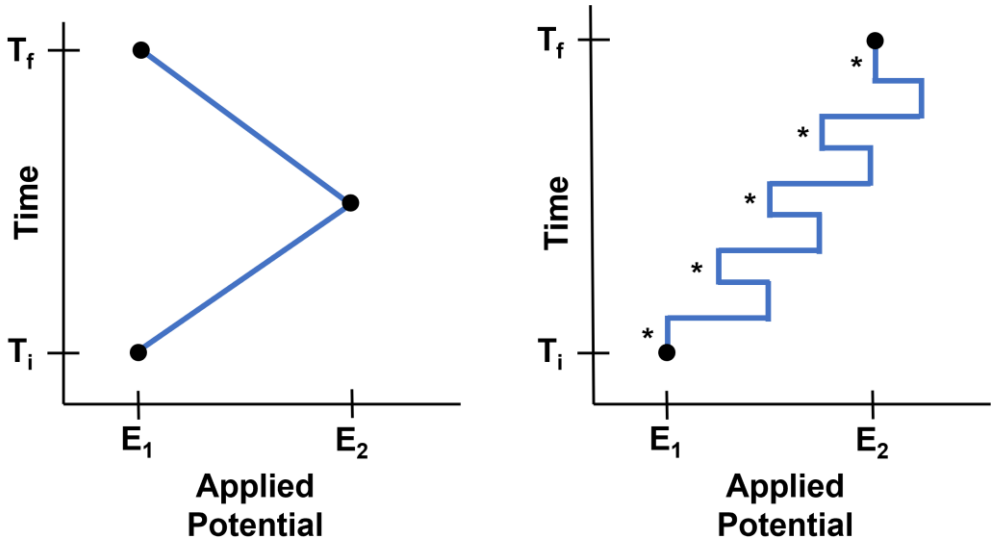

Figure 17. **General plot of how potential is applied during cyclic voltammetry (left) and differential pulse voltammetry (right). T_i and T_f are the start and end times during the experiment, respectively. E_1 and E_2 are the starting and final applied potentials, respectively. Asterisks in the right panel represent points at which current is measured. Current is measured at all times throughout cyclic voltammetry (left).**

1.7. Thesis Summary

The work described in this thesis aims to understand how non-covalent interactions within proteins can affect the properties of both Trp and Tyr residues using an artificial model protein derived from blue-copper azurin from *Pseudomonas aeruginosa*. Chapter 2 and Chapter 3 provide a study of Met-aro interactions with respect to a Trp residue, while Chapter 4 investigates non-covalent interactions in a broader context with respect to a Tyr residue. Chapter 5 is a computational study that evaluates the prevalence of Met-aro clusters across different enzyme classes in the PDB. In all, the work described herein proposes why certain residues may be found nearby to aromatic amino acids.

Chapter 2. Electron Transfer Kinetics Involving Methionine-Aromatic Motifs in Proteins

2.1. Introduction

Aromatic amino acid residues are central to facilitating long-range electron transfer (ET) in proteins. Tyrosine (Tyr) and tryptophan (Trp) are widely known for accomplishing this and much work has gone into understanding how these residues participate. This chapter uses artificial *in vitro* protein models that were developed using *Pseudomonas aeruginosa* azurin as a starting point to study an ET event through a Trp intermediate. Here, the effects of nearby amino acids and overall microenvironment (or local environment) effects imposed by methionine (Met) and alanine (Ala) are discussed with respect to polarity and the interaction with a thioether on the Met residue. These amino acids are pictured below in Figure 18.

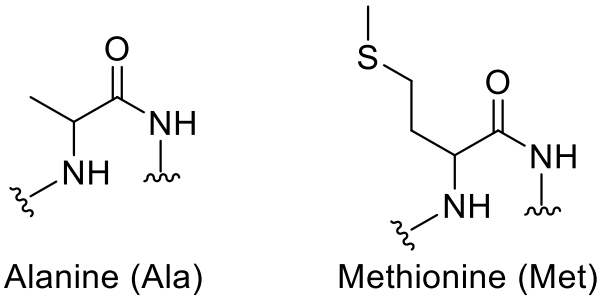

Figure 18. The two amino acid mutations used in this chapter, alanine (Ala, left) and methionine (Met, right).

2.1.1. Biological Electron Transfer via Tryptophan

Trp amino acid residues can act as reactive intermediates to facilitate long range ET in biological systems. Groups of Trp can form different types of structural motifs (examples seen in Figure 19) with respect to the orientations of their respective π systems, which has been proposed to play roles in protein structure and function.[154] Likewise, π-interactions with Trp can affect the binding of aromatic molecules (e.g., in drugs) in active sites[155] and cationic molecules.[156] With respect to the redox reactions of Trp, the subject of this chapter, some different reasons for this have been proposed for groups of Trp such as for protection against oxidative stress by shuttling radical species out of a protein[24,29,30] and for the control of biological redox reactions.[24,30] This study investigates how the

removal of a Met residue proximal to a Trp residue can affect ET kinetics in a long-range ET event through a protein.

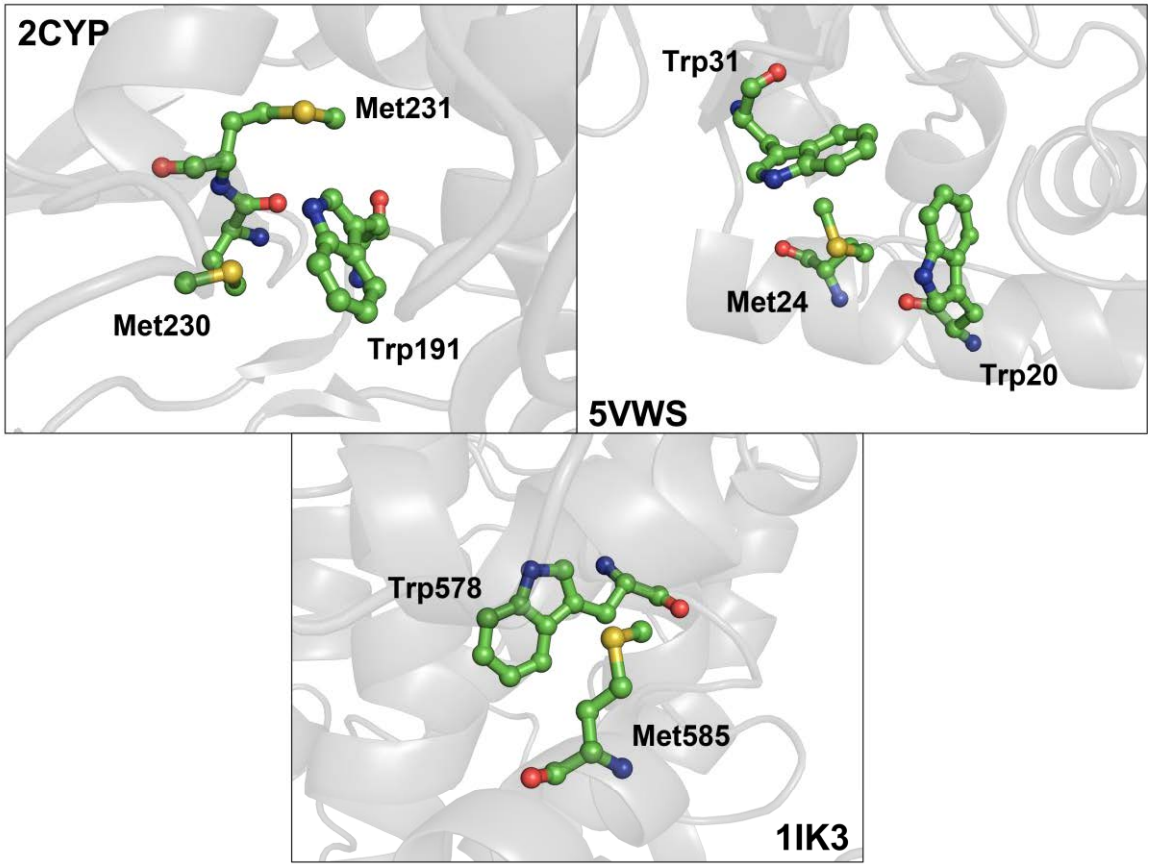

Figure 19. Three different types of structural motifs containing Trp; a Met-Trp-Met bridge from yeast cytochrome *c* peroxidase (top left, PDB ID: 2CYP[95]), a Trp-Met-Trp bridge from cytochrome P450 (top right, PDB ID: 5VWS[157]), and a singular Met-Trp motif from lipoyxgenase (bottom, PDB ID: 1IK3[158]).

An important aspect of biological ET via a Trp residue is the formation of a Trp radical[59,65] (this reaction sequence is set out in Figure 11, section 1.3.4) and characterization of these radicals have been a large topic of study in biology. Formally, a hole must be formed on Trp (i.e., oxidation) during an ET process; Trp anions are not known. As such, the formation of Trp cation radicals and the tuning of their functional properties in proteins are of great interest to the biological community. Although work has been ongoing for some time,[59] there is still much to learn about the factors that fine-tune Trp redox reactions. Trp residues exist in many different microenvironments within a protein and characterizing processes that they carry out is imperative to understanding

how the microenvironment impacts their physical properties and propensity to participate in redox reactions.

The microenvironments that house Trp amino acid residues are typically characterized by non-covalent interactions that include dipole-dipole interactions, van der Waals interactions, and electrostatic interactions.[159] In the work described in this chapter, the change to the microenvironment is influenced by the mutation of Met56 to Ala56 (the "56" is representative of the residue's position in the protein), resulting in the loss of a thioether sidechain. It is proposed that interactions with a thioether-sulfur atom can give rise to a 2-center, 3-electron ($2c{-}3e^{-}$) bond, which will be described in greater detail below. The work described herein will focus on how that bond may play an important role in ET through a Trp residue (Trp109 in this system) by either stabilizing or destabilizing the radical intermediate.

2.1.2. Methionine-Aromatic Interactions

Trp and Tyr residues are of great importance in electron hopping systems.[32,59,65] The ways in which nature controls diverse reactivity of these two amino acids is of ongoing interest. The work described in this chapter, and in this entire thesis, is motivated by the high incidence of closely placed Met residues near Tyr and Trp and the compelling computational results that are associated with this phenomenom.[29,83] This motif has been termed a methionine-aromatic interaction (Met-aro), and these motifs have been suggested to, at the minimum, play a structural role in proteins.[83] However, the ways in which Met affects ET in Tyr and Trp is not well understood.[85] The challenge with understanding this is in the development of biological *in vitro* systems that can probe ET kinetics that mimic a natural protein. Computational models exist that have probed the frequency of Met-aro motifs across different protein types[29,89,90] and have provided the basis for the work in this thesis. Small molecule models also have been studied showing evidence that these interactions may play a role outside of fundamental protein folding interactions and will be discussed below in more detail.[80,98]

First, it is important to note the frequency at which these Met-aro interactions appear in biology and their currently proposed roles. In the context of protein folding, intramolecular forces are vital and can also promote various binding interactions. Aromatic residues also are known to participate in π-stacking, cation-π, and anion-π interactions,

to name a few. These interactions are largely dependent on their spatial arrangement within the protein's structure.[29] With the large growth of the number and type of structures publicly available in the Protein Data Bank (PDB), a newly developed idea of a Met-aro interaction has become of interest. In a study by Weber and co-workers, the frequency of Met-aro interactions in oxidoreductases was evaluated. It was determined that 17% of the ~50,000 interactions studied contained a nearby sulfur lone pair to the aromatic ring of Trp. The frequency of the Met-Trp interaction is notably lower than that of phenylalanine (Phe) and Tyr but proportional to each overall frequency found in proteins.[29] It should also be noted that the high incidence of Met-Phe interactions that had been observed is likely attributed to protein folding, as Phe is not known to be redox active.

Small molecule model systems, and some biomimetic models, have been used to propose that redox activity is enhanced by the thioether-aromatic interaction. This may be due to the induction of a 2c−3e$^-$ bond between a thioether and an aromatic radical in small molecule studies by a nearby radical cation.[80] Historically, the first evidence of thioether-aromatic interactions in proteins was seen by Morgan and co-workers in 1978. This study revealed chains of alternating sulfur-containing and aromatic residues that were found between an electron donor and acceptor. This suggests that these motifs may participate in electron hopping pathways and interact in a way that enhances ET reactivity,[82] although no further characterization was completed at the time to support this theory. More recently, it has been proposed that the Met-aro interaction occurs primarily due to the sulfur atom (termed S-π), and similar interactions have been proposed for cysteine (Cys) proximal to an aromatic group.[82,84] These S-π interactions have been previously shown to stabilize protein structures,[85] although the understanding of these interactions is still meager beyond bioinformatic surveys.[29,89,90]

This chapter describes studies of an artificial electron hopping pathway in *Pseudomonas aeruginosa* blue-copper azurin. The pathway features a single Met-Trp motif placed between an electron donor (Cu(I)) and an electron acceptor (Ru(III)), as shown in Figure 20. This pathway has been described in more detail in section 2.2.1, where the protein model development is discussed. In this pathway, it is possible for a 2c−3e$^-$ bond to form between Trp and Met upon the oxidation of Trp to a Trp cation radical (Trp$^{\bullet+}$). This bonding can be described by the formation of molecular orbitals due to orbital overlap from the Trp$^{\bullet+}$ and a lone pair on the sulfur from Met (Met(S)), contributing to a formal ½ bond.[99]

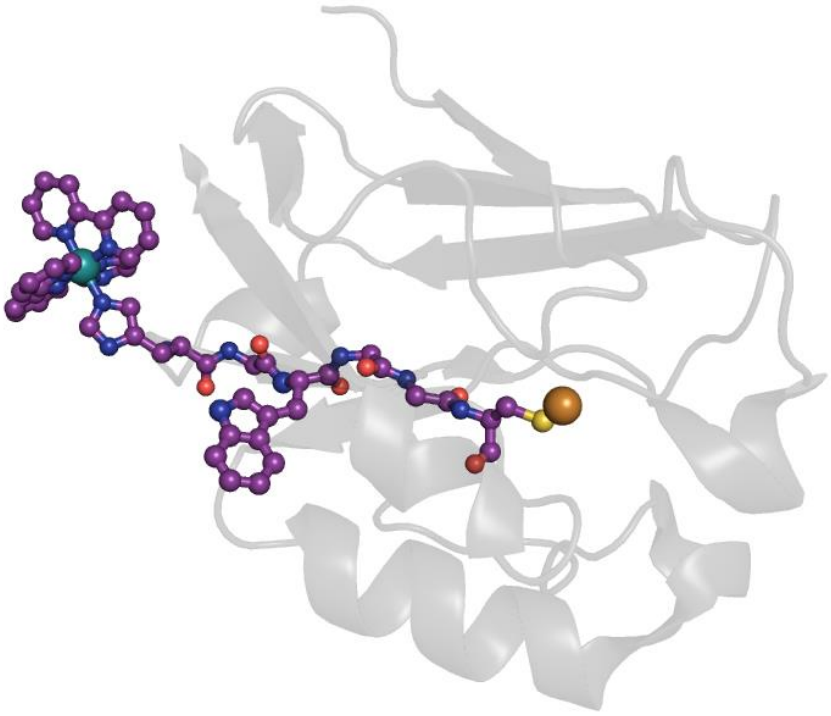

Figure 20. Structure of (2,2´-bipyridyl)$_2$Ru(imidazole)(His107)(Trp109) azurin showing the connectivity between the Ru label (Ru is in cyan) and the Cu (Cu is in orange) active site. The structure was generated using the mutagenesis function in PyMOL starting from the coordinates in PDB ID: 4HHG.[31]

2.2. Results and Discussion

2.2.1. Development of Protein Models

The work herein uses an “all-Phe” variant of azurin in which all native Trp and Tyr residues are mutated to redox-inactive Phe. This results in a stable, folded protein that allows for specific amino acid variations to be selected that can probe the physical properties and reactivity of a single Trp amino acid residue. Structures based on the all-Phe azurin variant have been structurally characterized in the literature.[31,140,160] The use of the all-Phe variant is necessary so that competing ET events cannot occur. To confirm the all-Phe mutation were correct, Sanger sequencing provided by Eurofins-Operon was used prior to further mutagenesis. Sequential point mutations were performed as follows: Met109Trp, Met56Ala, and Lys122Met (Lys = lysine) to produce distinct azurin mutants

(His107Trp109Ala56Met122 and His107Trp109Met56Met122, where His = histidine). The hypothesis was that the presence of two Met would allow for the systematic study of one and two Met-aro interactions. Unfortunately, these two model systems were not able to be expressed in adequate yields for characterization. It is possible that the presence of three hydrophobic groups on the protein surface prevented proper folding. For this reason, proteins with the Met122 variation were abandoned.

The two protein scaffolds designed for this work were His107Trp109Ala56 and His107Trp109Met56. While this limited the scope to only probing a single Met-aro interaction with our artificial proteins, the investigation of how Met-aro interactions play a role in ET could still be achieved. Crystal structures for both mutants were not determined and the precise orientation of the mutated amino acids is still unknown. However, PyMOL-generated models (Figure 21) can give some clues. These models are based off of a previously crystallized azurin (PDB ID: 4HHG),[31] which also contains the same Ru(II) label as used here. The built-in PyMOL mutagenesis tool was used to estimate the least sterically hindered orientation for each mutation, but I emphasize that the tool cannot be used to identify how the amino acid substitution affects the orientations of other amino acid residues in the model. Due to this, two possible orientations have been assumed, i.e., structures that are similar to the T-shaped and parallel-displaced orientations that are described in section 1.3.4. The same definitions are used here, however, Met and Ala are considered as the interacting residue. Briefly, T-shaped orientations are σ-like in terms bonding and parallel-displaced orientations are π-like.

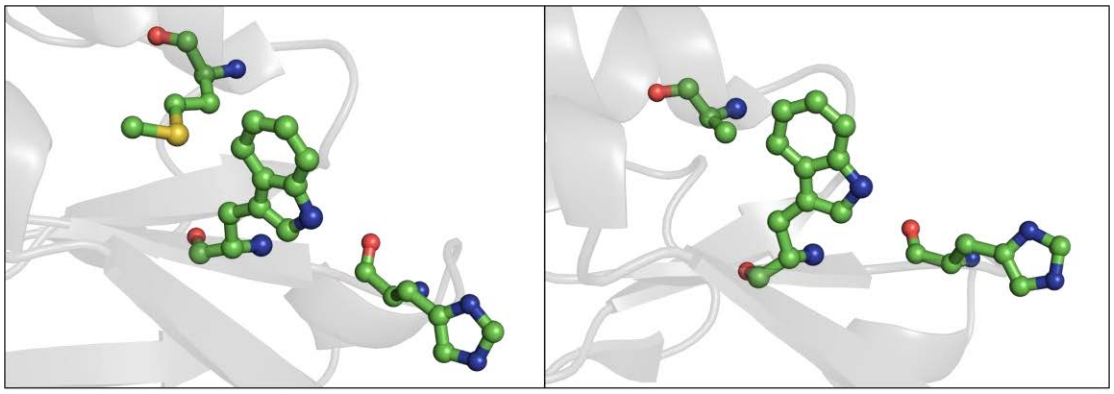

His107Trp109Met56 His107Trp109Ala56

Figure 21. PyMOL generated structures for the two mutations used in this chapter, Met56 (left) and Ala56 (right). Residues from left to right in the left panel are Met56, Trp109, and His107. Residues from left to right in the right panel are Ala56, Trp109, and His107. The structure was generated using the mutagenesis function in PyMOL starting from the coordinates in PDB ID: 4HHG.[31]

When Ala is substituted for Met within the core of a protein, the microenvironment loses the possibility to form a 2c−3e$^-$ bond by the loss of Met(S). There also is the obvious change in sterics. Furthermore, a small change in polarity should also be mentioned; both Met and Ala are considered as nonpolar amino acids, but the electronegativity difference between carbon and sulfur does afford Met with a slight increase in polarity over Ala. The lower polarity and the loss of the thioether sidechain are of interest in how these two properties may affect ET through a Trp residue. Likewise, the overall size of the two sidechains is very different, which may also be an important factor to consider.

Both His107Trp109Ala56 and His107Trp109Met56 were recombinantly expressed in *Escherichia coli* using standard techniques and the resultant proteins were characterized using UV-Visible (UV-Vis) spectrophotometry and mass spectrometry (MS) (Appendix A). The MS data confirmed that each the mutants were successfully prepared. The optical spectra of the proteins show the characteristic charge transfer transition of Cu(II) azurin at 628 nm (Appendix A). The band and intensity are as expected for azurin, indicating that the mutations introduced do not affect the Cu active site. This is a reassuring result given that the amino acid substitutions are far from the Cu ion and serves to support that the protein is intact.

2.2.2. Absorption Properties of Trp109 Azurins

In addition to the characteristic Cys-Cu charge transfer band, the UV-Vis spectra also show the π-π* transition for Trp109 (near 280 nm, Figure 22). Close inspection of this band, and comparing the two proteins studied here, show very small spectral shifts in the absorption bands. The bands positioned at 280 nm and at 290 nm are the major features arising from Trp. The multi-line features around 260 nm are from Phe. For Trp, the net absorption band is the sum of two excitations, denoted ^1L_a and ^1L_b. In general, the ^1L_a absorbance is broad and featureless, while the ^1L_b absorbance lies at slightly higher energy and has some fine structure, with maxima at about 282 and 291 nm in water.[161] The ^1L_a state has a large dipole moment and is sensitive to microenvironment changes, however, advanced spectroscopic analysis is needed to make firm conclusions about any changes to absorbance features.[162,163] The overall similarity of the band shapes and extinction coefficients suggests that there is no major change in the identity of the absorbing species whether in the presence or absence of Met. It also is possible that position 56 is at a distance too great for any major changes to be observed in the absorption pattern.

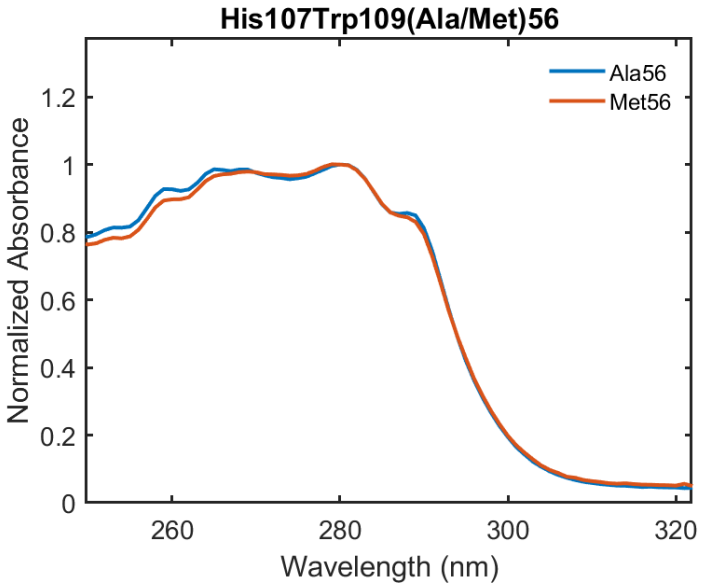

Figure 22. UV-Vis spectra of His107Trp109Ala56 (blue) and His107Trp109Met56 (orange). Spectra were normalized to the 280 nm peak for clarity.

2.2.3. Tryptophan Fluorescence

In contrast to Trp absorbance, its fluorescence properties are more sensitive to changes in the protein's microenvironment.[164,165] Protein fluorescence is most commonly attributable to the presence of Trp ($\lambda_{max,\ em,\ water}$ = 355 nm) and Tyr ($\lambda_{max,\ em,\ water}$ = 302 nm) residues in a protein's structure.[159] Phe also is fluorescent, but only weakly, and its emission is observed at a shorter wavelength ($\lambda_{em,\ water}$ = 278 nm).[111] In this study, the all-Phe derivative allows for the fluorescence of a single Trp residue to be studied that is not complicated by contributions from other Trp and Tyr in the structure. Phe fluorescence also does not play a role as it has negligible absorption at 280 nm.[111] Due to the anisotropic nature of Trp, changes to its emission spectra are indicative to a change in the microenvironment surrounding the residue. This is confirmed by the large range of Trp emission maxima that have been reported, from 305 nm to 360 nm.[111,166,167] Solvent polarity also plays a role,[111] as described above (section 1.5.1). In general, it is expected that a more polar microenvironment will have an emission that is lower in energy, thus, red-shifting the $\lambda_{max,\ em}$.

The emission spectra for the Ala56 and Met56 azurin mutants are shown in Figure 23 and the emission maxima are reported in Table 1. Here, a red-shift in Trp fluorescence is observed when Met is removed from the microenvironment surrounding Trp109. The microenvironment becomes slightly less polar in the absence of Met which should result in a blue-shifted emission. This is inconsistent with what is suggested such that more polar microenvironments result in a red-shifted emission. Due to both Met and Ala being considered nonpolar overall, it is unsurprising that such a small red-shift is observed and this suggests that more factors play a role here over a single amino acid change. Consequently, the microenvironment plays an intricate role in affecting the properties of Trp in proteins and more well-defined models are required to probe this. This also suggests that proteins may naturally select certain amino acids for fine-tuning a Trp residue's characteristics.

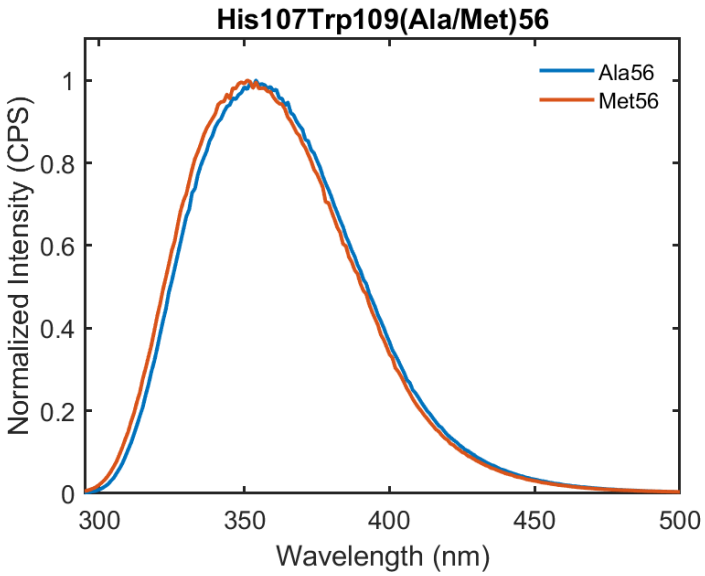

Figure 23. **Emission maxima for 60 μM His107Trp109Ala56 (blue) and Met56 (orange) in 1 M NH_4Cl, 20 mM NaP_i at pH 7.8. Samples were excited at 280 nm.**

Table 1. **Emission maxima of 60 μM His107Trp109(Ala/Met)56 in 1 M NH_4Cl, 20 mM NaP_i at pH 7.8. Error on all values is ± 1 nm.**

	His107Trp109Ala56	His107Trp109Met56
λ_{max} (nm)	354	351

As previously reported, Trp fluorescence can be quenched by a nearby Met residue.[168] The data presented here shows no quenching, which is not surprising since the π-π* transitions in the UV-Vis are also unperturbed, reinforcing the idea that the distance between residue 56 and Trp109 may be too great for a direct change in electronic structure to be seen. Determining the distance between these two residues would require more experimental data, such as a protein crystal structure. The raw data can be viewed in Appendix A in which the fluorescence intensity is higher for Met56 over the Ala56 mutation. Therefore, the main effect of Met56 in this system is the decrease in microenvironment polarity of the Ala56 variant. X-ay diffraction structures would aid in this analysis, but we have not yet been successful in obtained suitable crystals.

The polarity of the microenvironment can directly relate to the tendency for dipole-dipole interactions involving hydrogen to occur. Early descriptions of hydrogen bonding did not include sulfur[169] and the focus was mainly on the most electronegative atoms, oxygen, nitrogen, and fluorine.[164] Over time, hydrogen bonding via sulfur has become a

topic of interest due to its widespread involvement in proteins through amino acids Met and Cys.[170] Likewise, sulfur is biologically relevant in antioxidants, vitamins, and disulfide bonds which give rise to a protein's structure.[171] The differences between Met and Cys are in their sidechain structure, in which Met is a thioether and Cys is a thiol Figure 24. It has been reported that sulfur can participate as a hydrogen bond donor[171–175] or an acceptor.[164,171,176–178] Model compounds have been studied to mimic this interaction using indole and dimethyl sulfide (Me_2S). Interestingly, the results from an indole-Me_2S model compound show that the hydrogen bond strength for NH---S is larger than that of NH---O (in both cases, S and O are the hydrogen bond acceptors). The computations also showed a marginal increase in binding energy for the NH---S model.[164] This supports the idea that a favourable interaction between Trp(NH) and (S)Met is occurring. The analysis described herein focuses on the potential for a hydrogen bond involving the Met56 thioether and the Trp109 indole. Specifically, the indole NH proton from Trp109 could act as a hydrogen bond donor to the sulfur on Met56 via a Trp(NH)---(S)Met (where Trp(NH) represents the indole on Trp109 and (S)Met represents the sulfur on Met56).

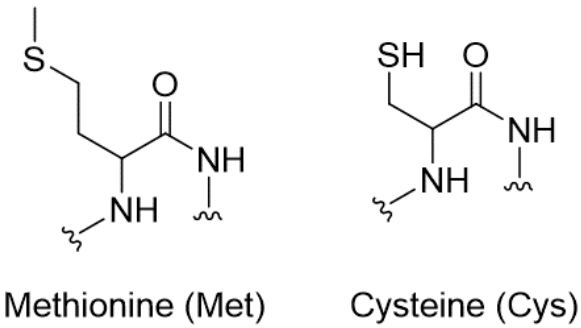

Figure 24. Comparison of two sulfur-containing amino acids, methionine (Met, left) and cysteine (Cys, right).

A Trp(NH)---(S)Met interaction may display π-type or σ-type hydrogen bonding interactions (analogous to interactions that were described in section 1.4.2). Using the indole-Me_2S model as described above, it has been revealed that the NH---S interaction can display both and may be limited by orientation.[164] In contrast to what is observed in the emission above, a hydrogen bond should red-shift the emission spectrum of Trp,[111] suggesting that the orientation of the (S)Met is important in the discussion of this experiment. If the Trp(NH) was rotated away from the sulfur atom, a hydrogen bonding interaction may not be present. This would help to describe why the red-shift is observed

when Met is removed instead of what is expected, although without a well-defined pocket, a more concise conclusion cannot be drawn.

2.2.4. Transient Absorption Spectroscopy

To better understand how Met may play a role in a protein's physical characteristics, ET kinetics also were explored. I note that changes in Trp fluorescence may help to describe the state of the Trp intermediate as it undergoes an ET event. ET kinetics between photogenerated Ru(III) and azurin-Cu(I) were assessed using time-resolved laser spectroscopy, also called transient absorption (TA) spectroscopy. The proteins were modified using Ru(2,2'-bipyridine)$_2$CO$_3$ ([Ru(bpy)$_2$CO$_3$]), and then imidazole to produce Ru(bpy)$_2$(imidazole)(His107)-modified proteins. Imidazole is important in the composition of this photosensitizer because it displaces a water molecule on Ru and increases the Ru(III/II) potential to above 1 V, which is a useful range for ET studies. In some cases, inactivation of the Ru-label can be seen if the imidazole is lost as a ligand. The UV-Vis spectra of pure Ru(II) labeled azurins are set out in Appendix A. It should be noted that small differences in the two absorption spectra of the Ru(II)-labeled proteins is likely due to incomplete imidazole ligation. As noted above, the ruthenium label allows for hole transfer between ruthenium and copper to be probed. The Ru-modified proteins were excited using 480 nm light from a neodymium-doped yttrium aluminum garnet- (Nd:YAG) pumped optical parametric oscillator (OPO) laser in the presence of 10 mM $[Ru(NH_3)_6]^{3+}$ as a reversible redox quencher. Further details about the flash-quench approach used here can be found in section 1.6.2 and a detailed sequence of reactions is shown in Figure 25. This approach to investigating ET allows for the reversible photogeneration of a cationic Trp radical ($Trp^{\bullet+}$), which reduces protein loss during the experiments. One important drawback is that direct characterization of the radical intermediate cannot be achieved. The reduction of Ru(III) and the oxidation of Cu(I) are used to infer the kinetics of ET through the Trp109 residue. Unfortunately, Cu(I) oxidation could not be observed and Ru(III) reduction was the sole measure of ET kinetics for this chapter. For reference, the attempted TA spectroscopy for Cu(I) oxidation can be found in Appendix A but will not be discussed in any more detail.

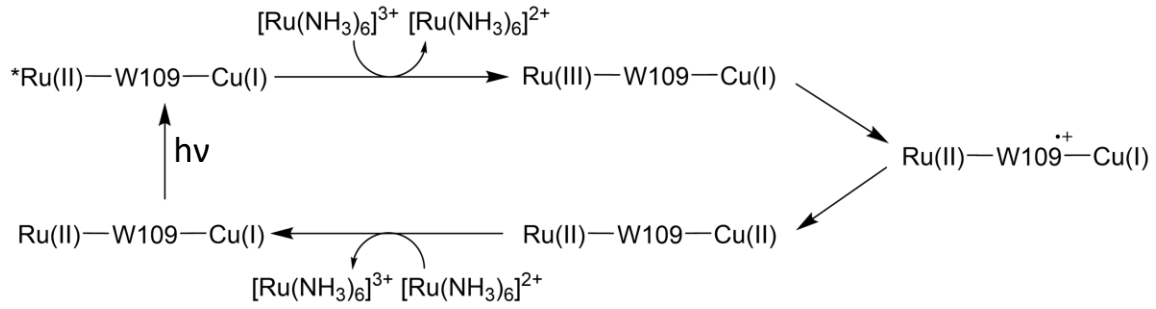

Figure 25. Flash-quench scheme to monitor ET kinetics for Ru(III) to Ru(II) reduction and Cu(I) to Cu(II) oxidation. The wavelength of light used for Ru(II) excitation was 480 nm and is represented by hν in the mechanism. W109 in this figure represents the Trp109 mutation.

The observed kinetics traces for the reduction of photogenerated Ru(III) to Ru(II) and their measured rate constants are set out in Figure 26. The removal of Met56 increases the observed ET rate constant only modestly (ca. 9%). As noted above, Cu(I) oxidation could not be achieved for this experiment, suggesting that the distance between Trp109 and the Cu metal center was too great for an ET reaction to occur. It is likely that the ET reaction observed in this experiment does not utilize Trp109 as a hopping intermediate and consequently is a single-step ET between Ru(III) and Trp109 (W109 in Figure 25).

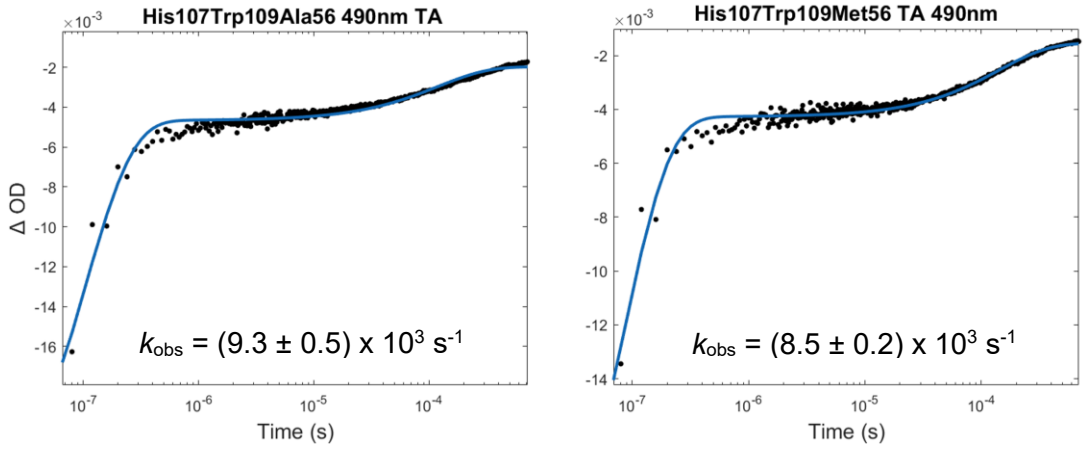

Figure 26. TA kinetic traces for the reduction of Ru(III) to Ru(II) in 35 µM His107Trp109Ala56 (left) and His107Trp109Met56 (right) azurin. Experiments were carried out in 50 mM NaP_i at pH 7.5. $[Ru(NH_3)_6]^{3+}$ was added to a final concentration of 10 mM. A more detailed description of experimental setup and be found in section 2.4.6.

Although the kinetics of an electron hopping event via Trp109 cannot be conclusively evaluated, the ET properties of this residue can still be rationalized. As seen

with the fluorescence data in Figure 23 and Table 1, a decrease in polarity of the microenvironment surrounding Trp109 red-shifts its emission. In the kinetics traces above, a less polar environment affords a larger rate constant. This is also be related to hydrogen bonding between the Trp(NH) and (S)Met. In the case that a hydrogen bond occurs between these two moieties, two factors may be affected that determine the rate with respect to the Marcus equation ($\mathrm{Eq.}\,5$). The Marcus equation was described in more detail in the introduction to this thesis, however, it is important to mention that three factors influence ET kinetics based on this equation: (1) the distance between the electron donor and acceptor, (2) the driving force of the reaction, and (3) the reorganization energy.[165]

Different non-covalent interactions between the indole on Trp109 and the amino acid residue at position 56 could impact the distance dependence for ET and the reorganization energy of the system. The original residue in this pocket is Met56, so substitution of this amino acid could play an unexpected role that was unaccounted for. In general, Ala is a much smaller residue than Met. The average C-C bond length when both carbons are sp^3 hybridized is 1.54 Å[179] and an average C-S bond is 1.82 Å. By comparing the structures of both Met and Ala, this yields a sidechain that is ~5.18 Å shorter for an Ala residue (not accounting for C-H bonds in the structure and only considering bond lengths). Thus, replacement of Met with Ala creates a pocket in which Trp109 may be flexible enough to distort in orientation and favour a decrease in distance between His107 (where the Ru-photosensitizer is positioned) and Trp109. Another option is a hydrogen bonding interaction between Trp109 and Met56. Such an interaction could constrain Trp109 in a position that is further away from the ruthenium photosensitizer than in the putatively more flexible Ala56 variant. Overall, both factors would increase the distance between the electron donor (Trp109) and electron acceptor (Ru(III)) when Met is present which would result in a decrease in the observed rate constant.

The above hypotheses can be further rationalized using Trp emission data. In comparison with the red-shifted emission seen for the Ala56 variant, I hypothesize that that hydrogen bonding between Met56 and Trp109 is not occurring. Thus, the increase in flexibility due to steric changes that would be imposed by the lack of Met is a more promising contributor. If Trp109 is found in a different orientation, the reorganization energy required for the ET event to occur would likely also change, which would impact the rate of ET. Finally, reduction potentials of the Trp109 residue in both mutations would be a factor that could affect the driving force for the reaction, however, reduction potentials

were not determined in this work and are something that should be considered in future experimental designs.

Since hopping via Trp109 was not likely occurring in this experiment, an alternative ET pathway can be proposed (Figure 27). In this pathway, a single-step ET event between Ru(III) and Trp109 is seen. This would explain the lack of Cu(I) oxidation. Trp oxidation by Ru(III) still occurs here to form a Trp radical, however, it is unknown the state that this radical is found in (either $Trp^{\bullet+}$ or a neutral radical ($Trp^{\bullet}$)). In either situation, the possibility for a 2c−3e⁻ bond to form is available when a sulfur lone pair is present from Met56. It was initially proposed that a 2c−3e⁻ bond would stabilize the Trp radical formed and it was thought that this would decrease the hopping reactivity. This would be due to the radical intermediate being more favoured over the Ala56 variant, which could not exhibit a 2c−3e⁻ bond formation. This argument is supported based on the smaller experimental rate constant observed for the Met56 azurin.

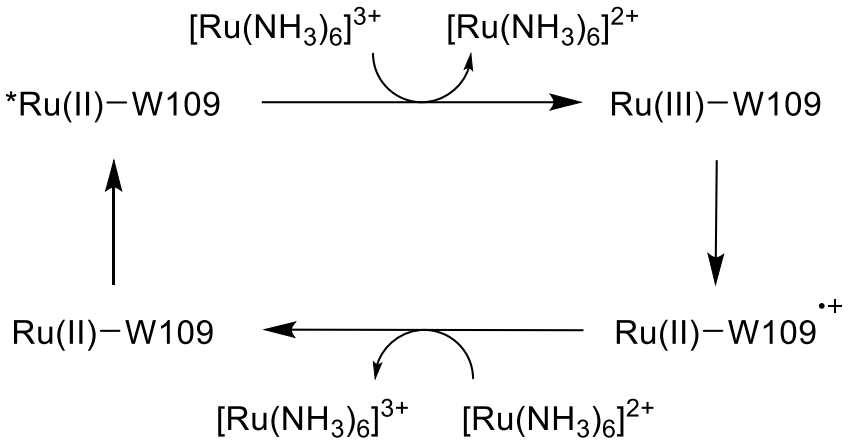

Figure 27. Newly proposed flash-quench scheme to monitor ET kinetics for Ru(III) to Ru(II) reduction and Trp109 to $Trp109^{\bullet+}$ oxidation. The wavlength of light used for Ru(II) excitation was 480 nm and is represented by h*ν* in the mechanism. W109 in this figure represents the Trp109 mutation.

Figure 28 is an example of an electron hopping map that was generated by values provided in the literature.[31] This hopping map describes a similar ET event that utilizes a Trp residue as a reactive intermediate between Cu(II) and Ru(III) in azurin. It was assumed that values for distance (r), the decay constant (β), and the reorganization energy (λ) would be similar to the values presented from that paper[31] because mutations are at the same residue positions. In this figure, the x- and y-axes show the driving force (ΔG°) required

for the entire hopping reaction, where the y-axis corresponds to the energy for Cu(I) oxidation by Ru(III) and the x-axis corresponds to the energy of the first step (i.e., Trp oxidation by Ru(III)). The black box found near the middle of this hopping map displays the values of ΔG° at which the ET event is most likely to occur. The colours in this figure represent the rate constant for this reaction with red being larger rate constants and blue being smaller, as show in the coloured heat bar at the right of the plot. Ultimately, the overall hopping reaction is predicted to have a smaller rate constant that what was observed (see above). This is further support that an ET mechanism distinct from pure hopping is at play in these systems.

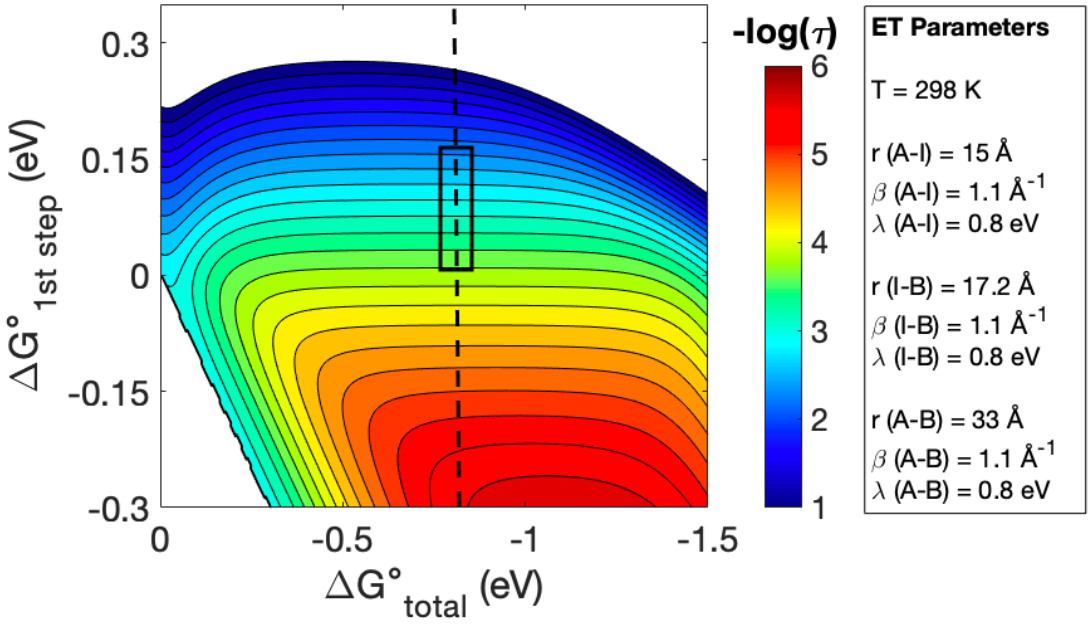

Figure 28. **Electron hopping map generated using the parameters pictured in the box on the right side of this figure. These values are taken from the PDB ID: 4HHG[31] and distances are the reported through-bond distances. A-I represents conditions for the ET between the acceptor and intermediate, I-B represents conditions for the ET between the intermediate and donor, and A-B represents conditions for the ET between acceptor and donor, where r is distance, β is the distance decay constant, and λ is the driving force. The black box shows a likely range of driving forces considering *E*°(Ru(III/II)) = 1.05 V and *E*°($Trp^{\bullet+/0}$) = 1 to 1.2 V.**

2.3. Summary and Future Directions

The results presented here suggest that the microenvironment affects the fluorescence properties and ET kinetics of a Trp amino acid residue. The small changes observed in Trp physical properties suggest that the protein's selection of specific amino acids very finely tune local interactions of redox active sites. There are a variety of reasons why this could occur, such as the widely accepted idea for stabilization of a protein's structure.[30] More importantly, the results presented in this chapter are not related to the overall stability of the protein but focus on electronic properties that would play a greater role in redox activity of a Trp residue.

Fluorescence properties are useful to describe how certain amino acids may influence the microenvironment around a Trp residue and complement any other experiments that probe the electronics. The sensitivity of the technique, and of Trp to its environment is a powerful tool. A shift in Trp fluorescence between the Met56 and Ala56 mutants suggests that polarity of the microenvironment and the lone pair on (S)Met influence the fluorescence properties of Trp109 in the models described above.

The observed change in ET rate constant suggests that less polar amino acids help to increase long-range ET rates when a Trp residue is used as the hopping intermediate. This is attributed to a potential hydrogen bonding interaction observed between the Trp(NH) and (S)Met residues. It would be interesting to compare and contrast the use of a Tyr at this position to determine whether the same microenvironment has the same effects. This would allow for results to be evaluated across all chapters of this thesis and would provide valuable insights into how microenvironments tune the properties of proteins.

It is important to note that the experiments described in this chapter probe only a relatively small change in the microenvironment surrounding Trp109. It has also been mentioned that some limitations were found while analyzing this work. First, a better understanding of the actual model proteins is necessary. PyMOL-generated figures of the pocket that contains Trp109 can only suggest a certain orientation and are not a detailed picture of the microenvironment and the possible interactions that could occur. Crystallization of these two protein scaffolds would benefit this study greatly by allowing the entire structure to be determined and would also note any other possible interactions

with other amino acid sidechains. Second, a nuclear magnetic resonance (NMR) study would help to investigate the structure as well. ^{1}H, ^{13}C, and ^{15}N NMR could aid in elucidating structural effects within these protein models. Furthermore, the incorporation of an unnatural, fluorinated Trp109 would allow for ^{19}F NMR to be carried out and any spectral changes in the absence or presence of Met to be easily observed. Furthermore, the design of a model system that incorporates two Met residues proximal to the Trp residue would be of great interest. Careful design of that system should be made to mitigate challenges in protein expression. Finally, cyclic voltammetry would describe the reduction potential of Trp109 in these two models and would provide context into the driving force required for the ET reaction to proceed although a distance dependence is likely more attributable to changes in the ET rate constant. The theoretical hopping proposed in this discussion can provide some estimation of the driving force, but without a crystal structure, these values cannot be considered as anything more than just an estimate.

2.4. Experimental

All reagents were obtained from Sigma-Aldrich and used without further purification unless otherwise noted. Luria-Bertani (LB) broth miller was purchased from BioShop Canada and prepared according to the manufacturer. Water used was from a Barnstead EASYpure system (18 MΩ cm^{-1}). UV-Vis spectrophotometry was carried out using a Cary 100-Bio spectrophotometer. MALDI mass spectrometry was carried out on a Bruker microflex LT MALDI Biotyper mass spectrometer. TA experiments were carried out using a home-built spectrometer containing an Continuum Surelite SLI-10 (Nd:YAG) laser, a Continuum Surelite OPO, a 75 W Xe arc lamp, and home-built detection system. Full details of the system are described elsewhere.[160]

2.4.1. Site-Directed Mutagenesis

A plasmid containing Phe mutations for all Trp and Tyr residues within azurin was a gift from Harry B. Gray and John H. Richards (California Institute of Technology). The Met109Trp mutation was added followed by Met56Ala so that two distinct protein scaffolds could be expressed (His107Trp109Ala56 and His107Trp109Met56). All mutations were introduced using site-directed mutagenic polymerase chain reaction (PCR) using standard

protocols.[180] DNA primers were purchased from Eurofins Genomics. Q5 DNA polymerase and DpnI enzyme were purchased from New England BioLabs (NEB). PCR products were transformed into competent DH5α *E. coli* competent cells obtained from NEB and selected using ampicillin-containing agar plates. Colonies were grown overnight at 37 °C and single colonies selected for liquid cultures in LB broth containing 100 μg/mL of ampicillin. Plasmid DNA was extracted and purified using a QIAprep Spin Miniprep Kit purchased from Qiagen and following the standard protocols provided. Purified plasmids were sequenced by Eurofins Genomics using their Sanger sequencing service. Plasmid purities and concentrations were obtained using a NanoDrop ND-1000 spectrophotometer.

2.4.2. Primer Design

Forward and reverse primers were designed to contain a single point mutation (Met109Trp and Met56Ala). Below, the bolded nucleotide bases represent where the mutation was added. Primers were designed as follows:

Met109Trp Forward: 5'-GAAGGTGAACACTTC**TGG**TTCTTCTGCACTTTCC-3'

Met109Trp Reverse: 5'-GGAAAGTGCAGAAGAA**CCA**GAAGTGTTCACCTTC-3'

Met56Ala Forward: 5'-CCACCGCGGCTGAC**GCG**CAAGGCGTTGTCACTG-3'

Met56Ala Reverse: 5'-CAGTGACAACGCCTTG**CGC**GTCAGCCGCGGTGG-3'

2.4.3. Protein Expression and Purification

Plasmids were transformed into competent BL21(DE3) *E. coli* cells obtained from NEB and selected using ampicillin-containing agar plates. Cells were grown overnight at 37 °C and single colonies selected for liquid starter cultures in LB broth containing 100 μg/mL of ampicillin. Starter cultures were grown at 37 °C with 180 rpm of shaking for 6 hours. Overnight expression cultures were prepared by adding a small portion of starter culture into LB broth containing 100 μg/mL of ampicillin and 0.4% glycerol. Overnight expression cultures were grown at 37 °C with 180 rpm of shaking. Cells were then pelleted by centrifugation at 4000 rpm for 20 minutes in a Beckman Avanti J-26XP centrifuge using a JSP F500 rotor. Cell pellets were resuspended in osmotic shock buffer (50 mM Tris, 1 mM EDTA, 20% sucrose, pH 8.1) and rest on ice for 20 minutes. Cell pellets were again

obtained by centrifugation at 4000 rpm for 20 minutes in a Beckman Avanti J-26XP centrifuge using a JSP F500 rotor. Pellets were resuspended in 500 μM $MgCl_2$ and rest on ice for 20 minutes. Proteins were isolated by centrifugation at 12000 rpm for 20 minutes in a Beckman Avanti J-26XP centrifuge using a JA 25-50 rotor. Supernatants were collected and 100 mM $CuSO_4$ and 500 mM NaOAc (pH 4.5) were added dropwise. These mixtures were incubated overnight at 37 °C to promote Cu(II) uptake by apo-azurin. Acid precipitated proteins were removed by centrifugation at 12000 rpm for 20 minutes in a Beckman Avanti J-26XP centrifuge using a JA 25-50 rotor. The resulting supernatants were collected and purified on a CM Sepharose column obtained from General Electric (GE) Healthcare using a NaOAc concentration gradient. Protein purities and concentrations were determined spectrophotometrically using reported extinction coefficients (ε_{628} = 5600 M^{-1} cm^{-1}).[42,160]

2.4.4. Tryptophan Fluorescence

Fluorescence experiments were carried out using a Horiba Jobin-Yvon Fluorolog-3 spectrofluorometer. Samples (60 μM protein) were prepared in 1 M NH_4Cl, 20 mM NaP_i at pH 7.8. Samples were placed into air-free cuvettes made by the Simon Fraser University (SFU) Glass Shop and deoxygenated with 15-20 pump-backfill cycles using N_2. Excitation was achieved using 280 nm light and spectra were recorded from 295 – 500 nm to monitor for Trp fluorescence. A total of 10 scans were performed per sample and emission maxima were determined by averaging each series.

2.4.5. Photosensitizer Labeling of Azurins

The protein-reactive label, $[Ru(bpy)_2CO_3]^{2+}$, was prepared by Jeff Warren according to the literature.[181] Labeled azurins were obtained by adding two equivalents of $[Ru(bpy)_2CO_3]^{2+}$ to a solution of azurin in 50 mM NaPi (pH 7.5). It is important that pH adjustments are not done with Cl^- containing solutions. These reaction mixtures were incubated overnight at 37 °C. Fast protein liquid chromatography (FPLC) was carried out using a HiTrap immobilized metal affinity column (IMAC) fast-flow (FF) obtained from GE Healthcare column metalated with Cu^{2+}. Reaction mixture was exchanged into binding buffer (1 M NaCl, 20 mM NaP_i, pH 7.8) and loaded to the previously equilibrated column under the same buffer system. Unmodified azurins bound to the column while ruthenium-modified azurins (Ru-His107Trp109Met56 and Ru-His107Trp109Ala56) elute with the

binding buffer wash. Unlabeled azurins were eluted using elution buffer (1 M NH_4Cl, 20 mM NaP_i, pH 7.8). Fractions were collected and monitored by UV-Vis spectrophotometry to pool correct fractions together. Concentrations of each Ru-modified azurin was calculated spectrophotometrically using reported extinction coefficients.[182] Both proteins were exchanged into storage buffer (500 mM imidazole, 1 mM $CuSO_4$, 100 mM NaCl, pH 7.5) and incubated for 2-3 days. Long term storage is carried out in this buffer at 4 °C.

2.4.6. Transient Absorption Spectroscopy

All laser experiments in Chapter 2 were carried out with a 480 nm excitation with 6 mJ/pulse energy. Samples were reduced using L-ascorbic acid and then desalted into 50 mM NaP_i at pH 7.5 for a final concentration of 35 μM. Sample volumes were 1.5 mL and special air-free cuvettes were custom made by the SFU Glass Shop to allow for deoxygenation. 15-20 pump-backfill cycles using N_2 were performed to remove O_2 from the sample and cuvette. Prior to TA experiments, time-dependent fluorescence scans were performed and spectra were collected at 670 nm on a 2 μs timescale where N = 100 and groups = 3. $[Ru(NH_3)_6]^{3+}$ dissolved in 50 mM NaP_i at pH 7.5 was added to a final concentration of 10 mM to each sample as an exogenous quencher. 15-20 pump-backfill cycles using N_2 were performed again to remove O_2 from the sample and cuvette. Fluorescence experiments were repeated to ensure fluorescence quenching. TA was then carried out on an 800 μs timescale where N = 100 and groups = 3. TA spectra were collected at 490 nm and 630 nm for Ru(II) reduction and Cu(I) oxidation, respectively. Data was plotted and analyzed using MATLAB and MATLAB's Curve Fitting Toolbox. Rate constants were determined using a two-exponential fit. The first exponential function describes signal from residual fluorescence due to excited state decay (and quenching) of the Ru photosensitizer and the second function describes the Cu(I) oxidation event. For the 490 nm (Ru traces), the first function is for excited state decay of *Ru(II) and the second function is for Ru(III) reduction.

Chapter 3. Methionine Effects on the Physical Properties of a Tryptophan Radical

3.1. Introduction

Biological electron transfer (ET) is dependent on an interplay of several factors. Such factors include solvent effects, temperature, and pH, all of which play a role in determining how and when an ET event proceeds within a protein. An aspect of long-range ET via a tryptophan (Trp) amino acid residue that is not well understood is how local structures affect formation and reactivity of the corresponding Trp radical, which is required for an ET event to occur. These radicals can exist in either a cationic or neutral form and both have been reported in the literature.[132] This chapter uses artificial *in vitro* protein models developed using *Pseudomonas aeruginosa* azurin to study a Trp intermediate as it undergoes an ET event by trapping the Trp in its radical form. Here, the effects of nearby amino acids, leucine (Leu) and methionine (Met), and the overall microenvironment surrounding Trp108 in the azurin model can then be studied. The amino acid residue side chains used in this chapter are shown in Figure 29.

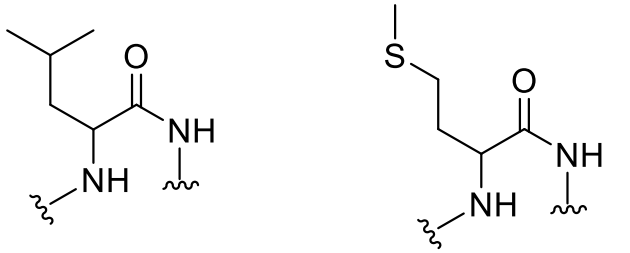

Leucine (Leu) Methionine (Met)

Figure 29. The two amino acid mutations used in this chapter, leucine (Leu, left) and methionine (Met, right).

3.1.1. Tryptophan Radicals in Biology

Redox-active aromatic amino acids play important roles in biology. As an example, aromatic amino acids act as intermediates to facilitate long-range ET.[132,136] One amino acid that accomplishes this is Trp. ET reactions of Trp can involve its radical cation and the neutral form (see section 1.3.4). Trp radicals are less understood with respect to tyrosine (Tyr) radicals. The crucial roles of Tyr ET sites in enzymes such as cytochrome *c* oxidase, photosystem II, and ribonucleotide reductase have made it a popular area of

research. However, Trp radicals possess similar redox properties and, depending on their microenvironment, can participate in single ET events without a change in protonation state, which is a contrasting feature with respect to Tyr. It has been noted that a challenge facing investigations of Trp ET in proteins is the lack of information on its spectroscopic properties and, more specifically, how different protein microenvironments affect Trp and Trp radical physical properties. In many cases, Trp oxidation is accompanied by a deprotonation, increasing the complexity of its radical form (i.e., either cationic or neutral).[132]

There are three processes in which Trp radicals can be generated within a protein. The first and simplest is outer-sphere ET to generate the cationic form ($Trp^{\bullet+}$) where the indole NH is intact. The second process is a stepwise proton-coupled electron transfer (PCET) reaction wherein the oxidation of Trp is followed by a deprotonation of the $Trp^{\bullet+}$ to give the neutral form ($Trp^{\bullet}$). The third is a concerted PCET (loss of H^+ and e^- in a single step) to generate the $Trp^{\bullet}$.[136] It is accepted that Trp radical formation follows a stepwise mechanism over the concerted pathway.[134]

As indicated above and in section 1.3.4, Trp can form $Trp^{\bullet+}$ and/or a neutral $Trp^{\bullet}$ species in proteins, and in model compounds, this is often dictated by pH.[132] Importantly, the reduction potential of Trp is ~1.0 V at neutral pH with an indole pK_a of 17. Following oxidation to generate $Trp^{\bullet+}$, the indole pK_a decreases to 4 which results in conversion to $Trp^{\bullet}$ in buffer systems with a pH >4. However, proteins can control this deprotonation through hydrogen bonding to the indole of the Trp sidechain. A key method to probe the hydrogen bonding environment surrounding a Trp residue is using EPR,[131] but the characterization of these radicals is challenging due to their instability.[134] Longer-lived Trp radicals can overcome this and have been reported in the literature.[132] To fully elucidate how Trp facilitates ET events within proteins, characterization of the Trp radical intermediate is crucial.

3.1.2. Tryptophan Radical Characterization in Biological Systems

In this chapter, two techniques were used to characterize biological Trp radicals, steady-state UV-Visible (UV-Vis) spectrophotometry and EPR. Trp radicals have a unique absorption pattern (Figure 30). The absorption maxima observed here are at 512 and 536 nm are for a neutral Trp108 radical species observed in azurin.[140] This experiment

provided the basis for the steady-state UV-Vis experiments carried out in this chapter as the system described herein uses Trp108. It was expected that similar absorption maxima would be observed. EPR has been used extensively for studying Trp radicals in the literature and is another tool that has been employed in this chapter.[131,132,134,140]

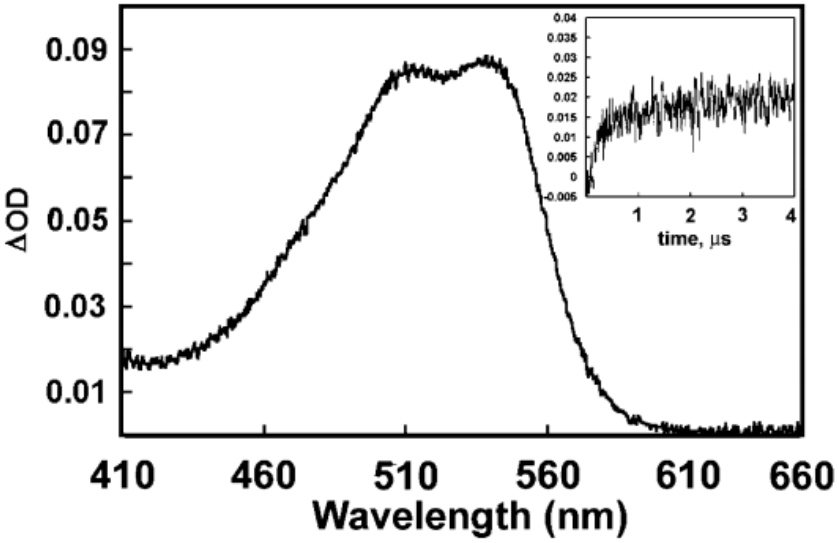

Figure 30. Absorption spectrum of a Trp108 radical in azurin. The insert is a single-wavelength absorption spectrum taken at 500 nm. Adapted with permission from Miller, J. E.; Grădinaru, C.; Crane, B. R.; Di Bilio, A. J.; Wehbi, W. A.; Un, S.; Winkler, J. R.; Gray, H. B. Spectroscopy and Reactivity of a Photogenerated Tryptophan Radical in a Structurally Defined Protein Environment. *J. Am. Chem. Soc.* 2003, *125* (47), 14220–14221. https://doi.org/10.1021/ja037203i. Copyright 2003, American Chemical Society.

The work described in this chapter focuses on the Trp amino acid radical. EPR is a powerful tool for studying radicals, like Trp, in proteins. EPR has been used previously to determine electron spin density, electronic structures, and the geometry of a Trp radical.[132] Although not used in this work, high-field EPR also has been reported.[132,133,137,139] Herein, EPR is used to determine the changes to a Trp residue's electronic structure in the presence of a proximal Met residue. A great amount of work has been completed in characterizing Trp radicals in model proteins and, in this context, azurin has been used as an excellent protein scaffold.[132–134,136]

In this chapter, *Pseudomonas aeruginosa* azurin was again used to generate an artificial protein that contains a single Trp residue that could be oxidized via an irreversible photogeneration. The Trp is at a site that has been widely studied for radical formation[131–

[133] and this allows for the characterization of this radical by EPR and steady-state UV-Vis spectroscopies. In particular, the work described herein is focused on generating a model system where a Met thioether is positioned proximal to the face of a Trp ring. By generating a controlled and well-defined pocket, the research in this chapter addresses some of the challenges associated with investigating Met-Trp interactions in proteins that were revealed in Chapter 2. Furthermore, this work complements the work in Chapter 2 by allowing for direct Trp radical characterization which was unattainable in the previously described system.

3.2. Results and Discussion

3.2.1. Development of Protein Models

The work herein uses a variant of azurin in which all Trp and Tyr residues are mutated to Phe (this will be termed the "all-Phe" variant). From this starting plasmid DNA, point mutations were added (Phe108Trp and Leu102Met) to produce two distinct azurin variants (His107Trp108Leu102 and His107Trp108Met102, both are shown in Figure 31). Each mutant contains only one Trp residue in which photochemical oxidation would be performed to irreversibly generate a $Trp^{\bullet+}$ in each**.** The presence of all mutations was confirmed using Sanger sequencing carried out by Eurofins-Operon. Proteins were expressed and purified using standard techniques, as described in section 3.4.3. Mutant azurins His107Trp108Leu102 and His107Trp108Met102 were successfully expressed and purified. Both proteins were confirmed by UV-Vis spectrophotometry (see Appendix B).

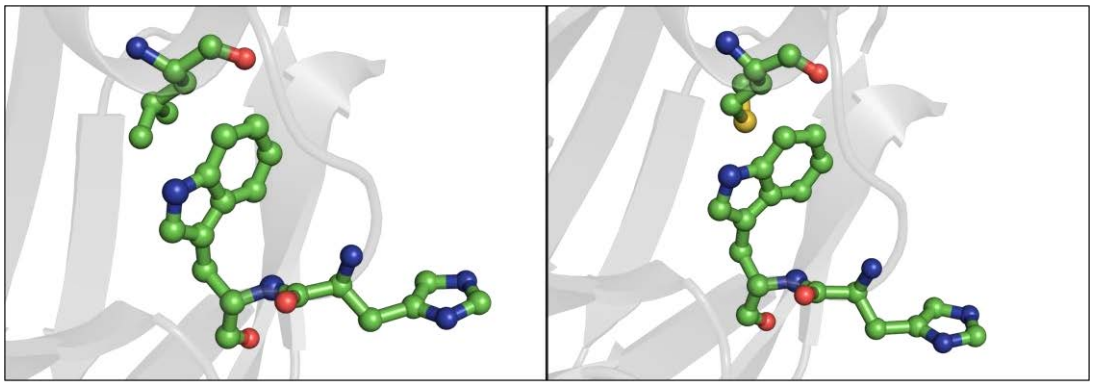

Figure 31. PyMOL generated structures for the two mutations used in this chapter, Leu102 (left) and Met102 (right). Residues from top to bottom in the left panel are Leu102, Trp108, and His107. Residues from top to bottom in the right panel are Met102, Trp108, and His107. The structure was generated using the mutagenesis function in PyMOL starting from the coordinates in PDB ID: 4HHG.[31]

3.2.2. Absorption Properties of Trp108 Azurins

The azurins described in this chapter all show a charge transfer band at 628 nm (Appendix B), just like the UV-Vis spectrophotometry characterization in Chapter 2. As will be described below, this is only found in Cu-containing azurins. The mutations made in this work are far from the Cu site and its properties are unperturbed. The work described here also employs Zn-containing azurins and the elimination of the 628 nm charge transfer band is important to note for the characterization of these variants. Also, as seen for azurins described previously, a π-π* transition band near 280 nm is observed for Trp108 (Figure 32). Close inspection of this π-π* transition band yields similar observations as before. No spectral shift is observed across the entire 240-300 nm range suggesting that the energies of overlapping transitions to the ^1L_a and ^1L_b states remains unchanged. A small difference in peak shape is noticed in 240-260 nm range, however, this is consistent with the π-π* transitions of Phe.

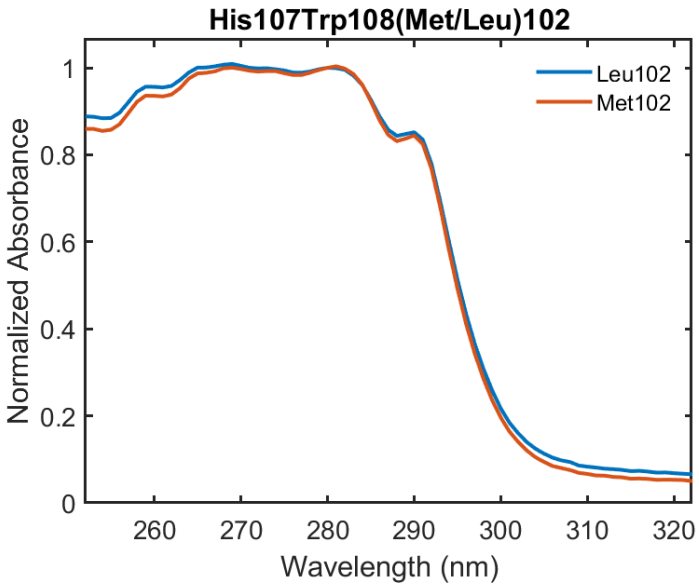

Figure 32. UV-Vis spectra of His107Trp108Leu102 (blue) and His107Trp108Met102 (orange). Spectra were normalized to the 280 nm peak for clarity.

Initial experiments involved Cu(II)-containing azurins because the intense blue colour of azurin facilitates purification. However, the Cu(II) site also is paramagnetic and therefore unsuitable for EPR investigation of Trp radicals. Consequently, the Cu(II) azurins were further modified to their Zn(II)-containing counterparts for EPR experiments. Although UV-Vis could only confirm the presence of protein by 280 nm absorbance, the loss of the charge transfer band at 628 nm confirms that Cu(II) is no longer present in the metalloprotein. The disappearance of the prominent Cu(II) EPR signature also was indicative of the removal of Cu(II). Further addition of a photosensitizer was required for ET experiments to be carried out as described above. Zn(II) replacement was confirmed by UV-Vis spectrophotometry and are shown in Figure 33.

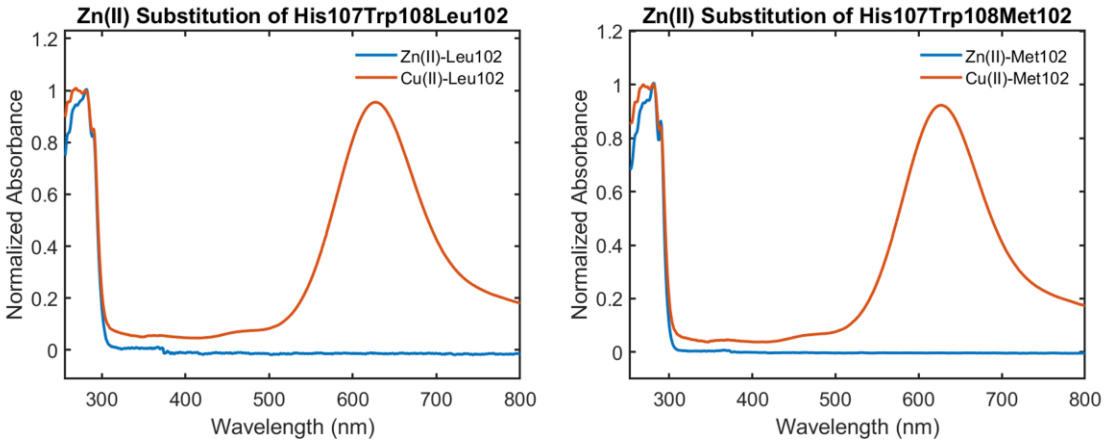

Figure 33. **UV-Vis spectra for the confirmation of the removal of Cu(II) from His107Trp108Leu102 (left) and His107Trp108Met102 (right). In both panels, blue curves represent Zn(II)-azurins and orange curves represent Cu(II)-azurins. The small amount of noise in the 300-400 nm range is due to the source changeover by the instrument. Spectra were normalized to the 280 nm peak for clarity.**

3.2.3. Tryptophan Fluorescence

As discussed in Chapter 2, Trp fluorescence is sensitive to changes in the Trp microenvironment.[164] The emission maxima for the Leu102 and Met102 mutants is shown in Figure 34. No major changes are observed when Met replaces Leu in the microenvironment surrounding Trp108, although it has been suggested that a more polar microenvironment is responsible for a shift in Trp emission to a longer wavelengths.[111] Trp108 is a partially solvent-exposed residue in azurin and in aqueous buffer, Trp108 is already surrounded by a polar microenvironment dictated by the solvent. Therefore, a change to the weakly polar Met102 is not likely to display any major changes in the emission maximum, resulting in the spectra found below. Also, no quenching of Trp fluorescence is observed in the presence of a Met residue (Appendix B), suggesting that Met may be too weakly interacting to play any major role in changing the Trp electronic structure. It should be noted that fluorescence experiments were carried out on the Cu(II)-azurins with no Re-label. It is important to note that an exact mechanism cannot be elucidated from fluorescence alone. Steady-state UV-Vis spectrophotometry and EPR can be used to complement these results and will be discussed below. Re(I)-labeled Zn(II)-substituted azurins were used for all further experiments.

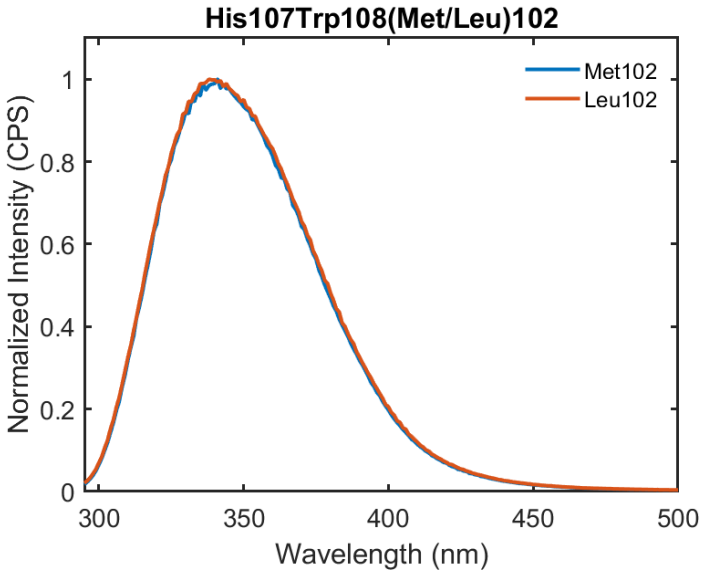

Figure 34. **Emission maxima for 60 μM His107Trp108Met102 (blue) and Leu102 (orange) in 1 M NH_4Cl, 20 mM NaP_i at pH 7.8. Samples were excited at 280 nm.**

Table 2. **Emission maxima of 60 μM His107Trp108(Met/Leu)102 in 1 M NH_4Cl, 20 mM NaP_i at pH 7.8. Error on all values is ± 1 nm.**

	His107Trp108Met102	His107Trp108Leu102
λ_{max} (nm)	341	338

3.2.4. Steady-State UV-Visible Characterization of a Tryptophan Radical

The S-π interaction was still the main focus of this chapter, as it was in Chapter 2. The major difference with these models was the distance between Trp108 and the Cu(II) (or Zn(II), as will be described below) that prevented hopping between the metal active site and the Trp108 radical. This prevented the study of an electron hopping reaction through Trp108 but allowed for the electronic environment of the Trp to be characterized instead.

A reversible pathway similar to that used in both Chapter 2 and Chapter 4 was considered initially using $[Ru(NH_3)_6]^{3+}$ as an exogenous quencher, however, after numerous inconclusive attempts, it was realized that the $Trp^{\bullet}$ was likely too short-lived to characterize as no EPR or UV-Vis spectra could be collected. This was also initially chosen such that ET kinetics could be simultaneously studied but was not the main goal of this work and will not be presented. The use of an irreversible quencher, $[Co(NH_3)_5Cl]^{2+}$, would allow for accumulation of the $Trp^{\bullet}$, thus increasing the concentration present in each

sample during EPR and UV-Vis experiments. This pathway is shown in Figure 35. It should also be noted that the photosensitizer used in this work differs from the previous chapter. Here, $[Re(CO)_3(4,7\text{-dimethylphenanthroline})Cl]^{2+}$ ($[Re(CO)_3(4,7\text{-dmp})Cl]^{2+}$) is used as $[Ru(bpy)_2CO_3]^{2+}$ absorption occurs near the same wavelength as Trp radicals. This presented a challenge as $[Re(CO)_3(4,7\text{-dmp})Cl]^{2+}$ is much less soluble in aqueous solutions leading to a near 50% loss in labeling efficiency of the protein. This also increases labeling reaction times to ~seven days. The UV-Vis for the Re-labelled proteins are shown in Appendix B.

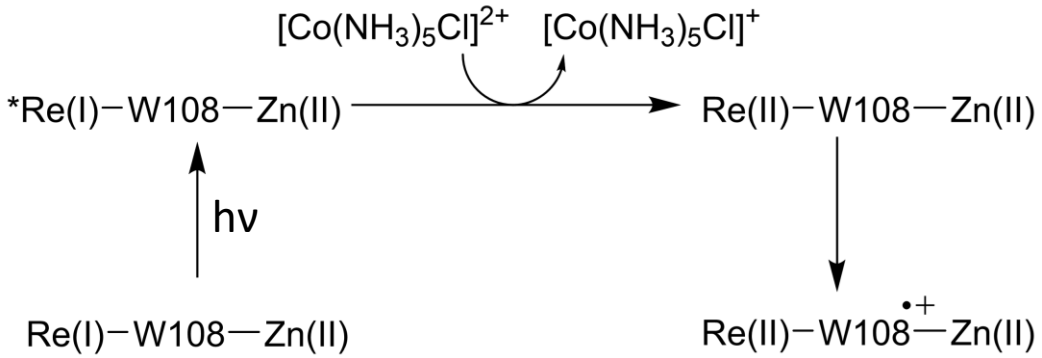

Figure 35. Flash-quench scheme for the irreversible photogeneration of Trp108$^{\bullet+}$ (W108$^{\bullet+}$ in this pathway). The wavlength of light used for Re(I) excitation was 355 nm and is represented by hν in the mechanism.

Steady-state UV-Vis was used to characterize the generation of the Trp108 radical and observe any changes to its absorption in the presence and absence of Met. The modified laser setup used for these experiments is shown in Figure 36. Here, the Xe arc lamp probe source is replaced with a deuterium-halogen lamp from a Photon Control UV-Vis spectrophotometer equipped with a sample holder that allows for a perpendicular probe in contrast to the parallel probe used for transient absorption (TA) experiments. The change in direction of probing results in a dramatic loss in signal intensity which increases the difficulty of observing Trp oxidation. This probe is in a closed loop that is connected to the Photon Control to allow for a full UV-Vis spectrum to be collected. The sample holder was outfitted with a cut off filter in the probing direction that prevented light <400 nm to be observed.

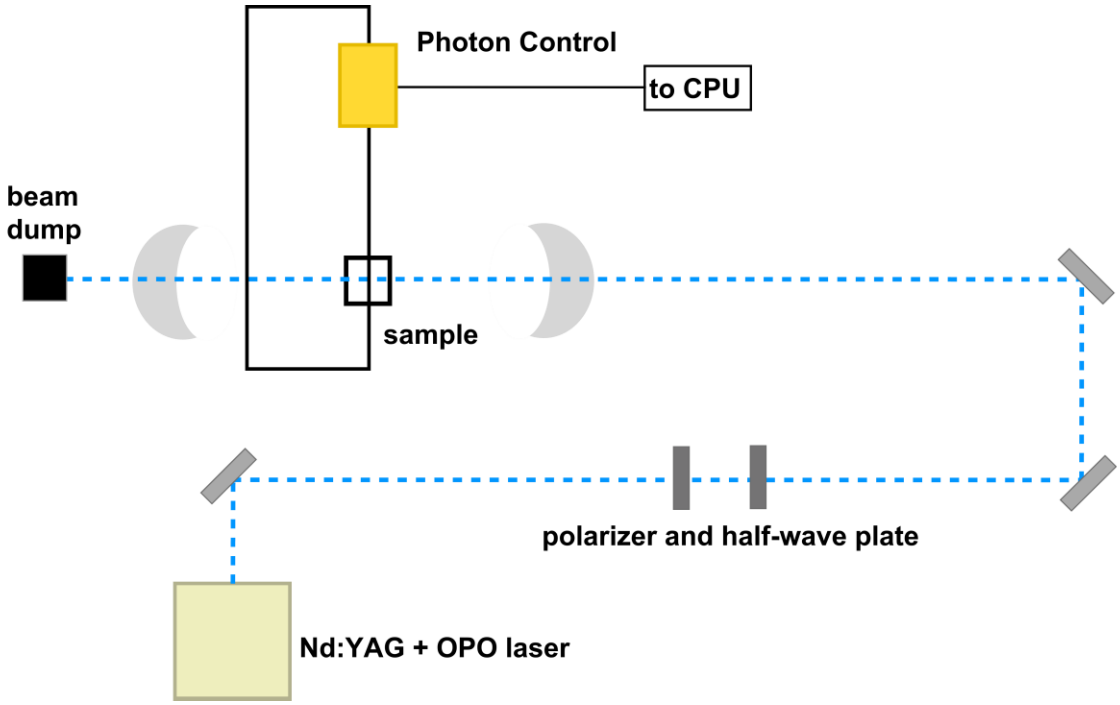

Figure 36. Schematic of the laser system used in this chapter. The dotted blue line represents the pump pulse generated by the Nd:YAG and OPO. The solid black line from the Photon Control represents the closed probe system generated by the deuterium-halogen lamp source.

Initial steady-state UV-Vis experiments were carried out to determine an optimal timepoint for laser irradiation. Zn(II)-substituted azurins were prepared to carry out this experiment due to possible interference with the Trp radical absorption as the Cu(II) ligand-to-metal charge transfer (LMCT) absorption band is a broad peak at 628 nm. Samples were prepared and degassed analogously to TA experiments carried out in the previous chapter, however, a different quencher was used, as mentioned in section 3.2.1. Spectra were manually collected at various timepoints to observe the formation of the Trp radical species and to determine a timepoint in which the Trp radical concentration maximizes. These data are presented in Figure 37 for the His107Trp108Leu102 variant. The Met102 variant presented many challenges in optimal yields for expression, Zn(II)-remetalation, and Re-labeling, resulting in this timepoint determination not being carried out due to lack of sample.

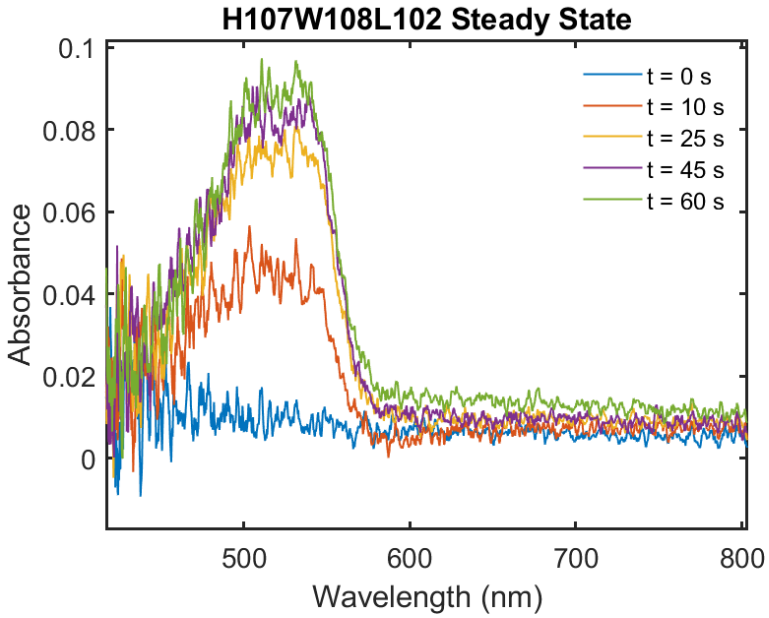

Figure 37. Steady-state UV-Vis spectra for 100 µM His107Trp108Leu102 (H = His, W = Trp, L = Leu) in 50 mM NaP_i at pH 7.5. Each spectra was manually collected at the timepoints show in the legend. The timepoint, t = 0 (blue), represents the sample prior to irradiation. $[Re(CO)_3(4,7\text{-}Me_2phen)]^+$ was used as the photosensitizer label.

Timepoint, t = 0 s, was collected prior to any irradiation of the sample to show that the ground-state Trp has no absorbance in the 400-600 nm range. This is also confirmed in any UV-Vis characterization of these mutants (Figure 33 and Figure B1 in Appendix B) where ground-state Trp absorption is found in the 240-300 nm range, as discussed previously. An increase in concentration of the Trp radical is observed in the first 25 s of 355 nm irradiation to a point at which the concentration negligibly increases. It should be noted that the Photon Control software only allows for the collection of 5 spectra at a time, so careful consideration had to be made when determining timepoints. This involved many iterations of troubleshooting to ensure an optimized time for irradiation was achieved. The timepoints determined here were then used to estimate the optimal irradiation required for EPR experiments to be carried out and was applied to Met102 samples as well.

Figure 38 shows a comparison between the Leu102 and Met102 variants at 57 µM protein concentration. Both spectra were collected at 60 s for consistency. Interestingly, a clear difference in absorption intensity is observed in the Met102 derivative. This was a surprising result because it was predicted that the introduction of Met would change the properties of the radical, but not the photochemical yield. This result might suggest that the introduction of a weakly polar Met residue at position 102 destabilizes the Trp108

radical. Along that line of reasoning, the introduction of Met102 could distort the protein pocket that otherwise would protect the Trp radical. The region surrounding Trp108 tends to be a more disordered region of azurin, as evinced by structural beta factors. Trp108 is also ~40% exposed to buffer, if a change to the pocket occurred, this could result in more or less exposure of Trp108 to the buffer. In addition, Trp108 is housed in a loop region of azurin. As such, mild structural changes would not be easily detected by techniques like circular dichroism and was not considered for carrying out this research. Finally, introduction of Met102 could alter the reduction potential of Trp108, lowering the efficiency for oxidation by Re(II).

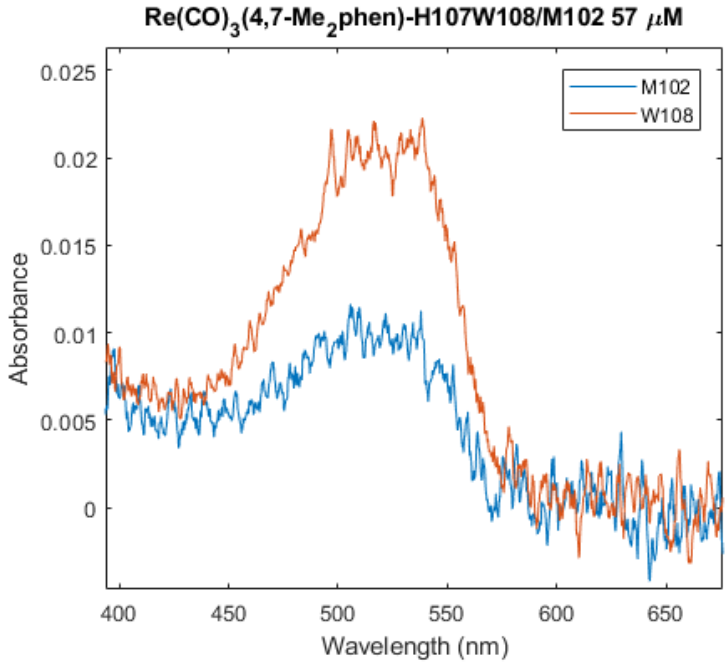

Figure 38. Steady-state UV-Vis spectra for 57 μM His107Trp108Met102 (blue) and His107Trp108Leu102 (orange) in 50 mM NaP_i at pH 7.5. $[Re(CO)_3(4,7\text{-}Me_2phen)]^+$ was used as the photosensitizer label. M = Met and W = Trp in this figure.

Steady-state UV-Vis supports the idea that that Trp radical formation is impacted by a nearby Met, specifically with respect to its photochemical yield of a Trp radical. Revisiting the idea of the formation of a 2-center, 3-electron ($2c{-}3e^-$) bond from the previous chapter, it was stated that a Met residue would stabilize a Trp radical and favour the radical formation. The results presented here suggest that a Met residue may have an opposite effect on Trp108 such that radical formation or stability is not favoured. This is corroborated by the photochemical yield of the radical being approximately half that of the Leu102 mutant based on the UV-Vis in Figure 38.

A lower photochemical yield of the Trp108 radical could be associated with two factors: (1) based on the proposed ET pathway, there may be less oxidation of Trp108 by Re(II), or (2) the driving force for Trp108 oxidation, or its protonation state, may change with Met102 present. Since Trp108 is partially solvent exposed, this suggests that contributions from the buffer could play a role. In a NaP_i buffer at pH 7.5, it is likely that deprotonation of the $Trp^{\bullet+}$ to $Trp^{\bullet}$ occurs quickly upon oxidation and due to solvent exposure, the indole proton would be lost to phosphate. The steady state UV-Vis in Figure 38 resembles that of what has been presented in the literature,[140] although the peaks at 512 and 536 nm (for a neutral Trp108 with Leu102 nearby) are not well resolved in the work seen here.

3.2.5. EPR Spectroscopy

To further complement the steady state UV-Vis experiments outlined above, EPR was used as another technique to probe the effects of the microenvironment surrounding the Trp108 residue. EPR is a powerful tool for studying radical species in biological systems but Trp radicals can be difficult to observe due to their limited stability. In azurin, two stable Trp radicals have been reported at positions 48[132,134] and 108,[131,132,140] and it is this that motivated this work to be carried out on Trp108 using azurin from *P. aeruginosa*.

The Trp108 radical in His107Trp108Leu102 azurin was previously characterized in the literature[131,132,140] and was used as a benchmark for the experiments carried out in this chapter. The experimental data acquired for the His107Trp108Leu102 protein prepared for this chapter was compared to that in the literature for reproducibility and to determine optimal experimental parameters for the Met102 variant. As stated previously, the Re-labeled-Zn(II)-His107Trp108Met102 mutant was more difficult to obtain, thus, using a higher yielding azurin mutant to develop EPR experimental parameters was a necessity. Due to the unknown lifetime of the Trp108 radical in the systems presented here, immediate freezing of the sample following photogeneration was desired. To accomplish this, samples were quickly moved to EPR tubes after being degassed and immediately irradiated with 355 nm pulses for before being frozen. Many iterations were completed at different concentrations (30, 60, and 100 μM) for optimal observation of a radical species in the EPR spectra. In all cases, spectra could not be achieved to the same resolution as previously published spectra.[131,132,140] This was likely due to an inadequate method of irradiation, which involved manually placing the sample in front of the excitation

pulses. A lack of fully air-free experiments may also play a role here as it has been shown that deoxygenation is necessary for Trp radical formation in another azurin mutation (Trp48).[132]

Comparisons between Trp108 radicals and other Trp radicals in azurin have been previously studied[132] and can be used to identify the spectral signatures that are affected by a protein's microenvironment. It is these signatures that have motivated the work described herein and previously described Trp radicals in azurin will be used here. The EPR spectra of Trp108 were collected for both mutations, His107Trp108Leu102 and His107Trp108Met102, using X-band EPR at 100 K (Figure 39 and Figure 40, respectively). The His107Trp108Leu102 radical is consistent with the spectra for the His107Trp108Leu102 radical reported in literature,[131,132,140] although not as well resolved. Importantly, the g-values for His107Trp108Leu102 reported here (Table 3) are consistent with organic π-radicals reported for Trp108 in azurin.[131,132,140] The g-values were originally constrained to literature values for reported Trp108 radicals obtained using high-field EPR (g_x = 2.00355, g_y = 2.00271, and g_z = 2.00221)[132,140] The simulations presented in this chapter fit better with the g-values set out in Table 3, but are very close to those reported in the literature. Closer inspection of the EPR spectrum for both mutations reveal a hyperfine structure and hyperfine coupling constants (HFCC) are set out in Table 3 as well. These values suggest that the spin density is primarily on nearby hydrogen atoms, although the specific atoms cannot be defined without further computations.

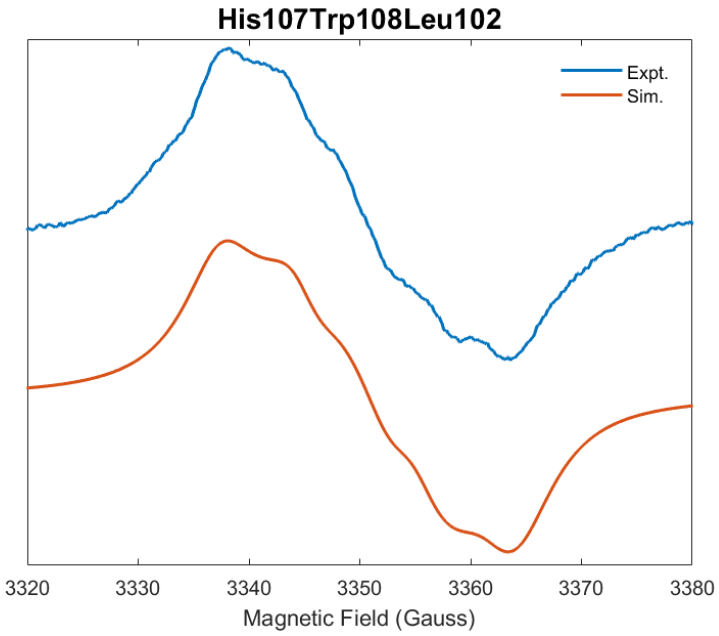

Figure 39. **X-band (9.4 GHz) EPR spectra for the Trp radical in His107Trp108Leu102 in 50 mM NaP_i at pH 7.5 taken at 100 K. The experimental data are shown in blue and the simulation is in orange. An overlay of the experimental and simulated data can be found in Appendix B.**

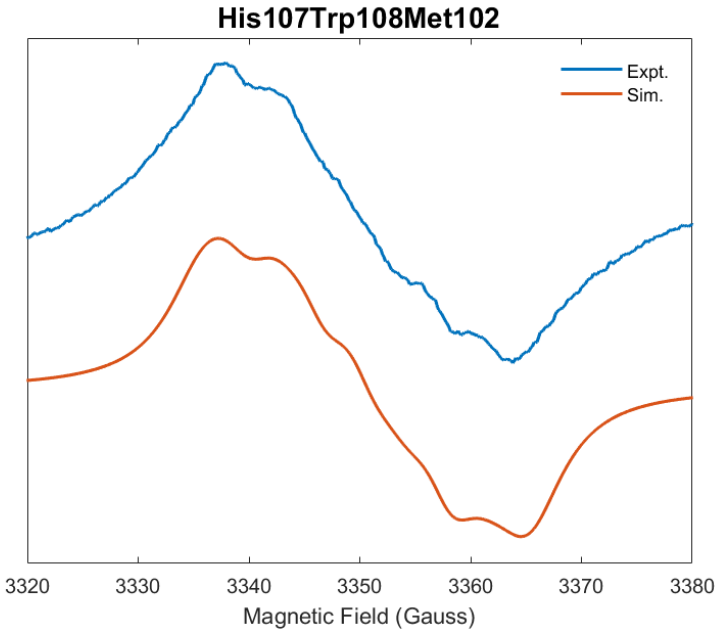

Figure 40. **X-band (9.4 GHz) EPR spectra for the Trp radical in His107Trp108Met102 in 50 mM NaP_i at pH 7.5 taken at 100 K. The experimental data are shown in blue and the simulation is in orange. An overlay of the experimental and simulated data can be found in Appendix B.**

Table 3. Hyperfine- and g-values used for simulation of EPR data presented in Figure 39 and Figure 40. Values for other azurin Trp108 radicals are presented here for comparison.

	g_x	g_y	g_z	$A_{iso, N}$ (Gauss)	$A_{iso, H}$ (Gauss)	$A_{iso, H}$ (Gauss)
His107Trp108Leu102	2.00336	2.00268	2.00121	3.09	10.62	6.54
His107Trp108Met102	2.00432	2.00240	2.00135	3.37	11.28	6.99
ReAzS-Trp108[a]	2.00346	2.00264	2.00216			
ReAz108W●[b]	2.00355	2.00271	2.00221	3.5-4.1	12.6	2.0

[a]Literature values for ReAzS-Trp108 were taken from the literature. A_{iso} values were not reported in this reference.[131]
[b]Literature values for ReAz108W● were taken from the literature.[132]

The g-values presented above are very close to what was reported in the literature.[132,140] The data in this chapter was collected using X-band EPR, however, literature g-values have been determined using high-field (i.e., values of g_x = 2.00355, g_y = 2.00271, and g_z = 2.00221)[132,140] and ultrahigh-field (i.e., values of g_x = 2.00346, g_y = 2.00264, and g_z = 2.00216)[131] EPR, which might attribute to differences in the simulated g-values. Other variabilities may include calibration or field effects between different instruments. Furthermore, differences in g-tensors for Trp radicals can be observed for two other reasons. The first is due to the dihedral angle, $\chi_{2,1}$, which is shown in Figure 41. Density functional theory (DFT) calculations suggest that $\chi_{2,1}$ can impact the spin density at the Trp indole nitrogen.[131] While this calculation was not carried out for the work shown here, a point mutation from Leu102 to Met102 may impart small changes in the protein's overall structure that could result in a change to the dihedral angle, $\chi_{2,1}$. Changes in this angle by even 10° have been shown to affect EPR spectra of similar neutral Trp radicals in azurin.

The second reason for small differences in the observed g-tensors is hydrogen bonding from the protein's microenvironment.[131] For Trp, hydrogen bonding to the indole nitrogen is the primary focus. It was previously noted that an azurin crystal structure (PDB: 1R1C,[140] Figure 42) displays an oxygen atom from H_2O nearby to the protonated indole nitrogen on Trp108 (2.3 Å). This suggests that a hydrogen bond to the aqueous solvent is present (NH--O).[131] It is unknown whether the deprotonated indole shows similar characteristics (N--HX) but resonance Raman data suggests that the hydrogen bond persists in this form.[131,132] Other experiments such as $^1H/^2H$ exchange with ^1H and ^2H electron nuclear double resonance (ENDOR) also suggest the presence of a hydrogen bond when Trp108 is oxidized. This N---HX bond (with H_2O) should be present in both the

oxidized Leu102 and Met102 species as the Trp108 would likely still be solvent exposed. However, it may be possible that the Met102 mutant induces a conformational change that decreases the solvent exposure of the Trp108 residue. This would prevent or reduce hydrogen bonding with H_2O and therefore shift the g-values observed. This is evident by an increase in the g_x value and has been observed in Trp radical EPR across various proteins that exhibit an absence of hydrogen bonding.[131] The more in-depth experiments mentioned above would help to elucidate whether this is occurring along with high-field EPR to provide more accurate g-values.

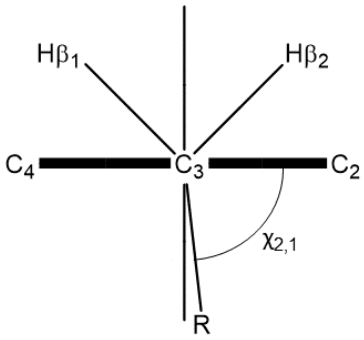

Figure 41. Orientation of $H\beta_1$ and $H\beta_2$ protons and the protein backbone, denoted R, with respect to the Trp indole plane, denoted $C_4{-}C_3{-}C_2$. The $\chi_{2,1}$ dihedral angle between the Trp indole plane and the protein backbone is denoted as R.

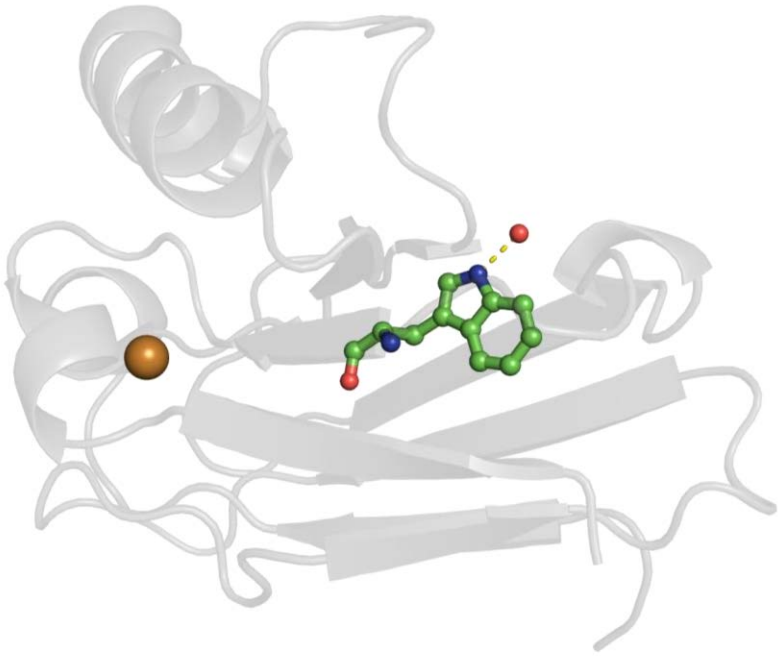

Figure 42. PyMOL model of hydrogen bonding between the Trp108 indole nitrogen and H_2O in His107Trp108Leu102. The red spheres represent oxygen atoms. The dashed yellow line represents the distance between the indole nitrogen and the oxygen from H_2O as protons cannot be shown in this model. The distance between nitrogen and oxygen in this model is 2.3 Å. PDB ID: 1R1C.[140]

The absence of hydrogen bonding to the indole nitrogen may also be explained by 2c−3e$^-$ bond formation between the Met102 thioether and the radical. Although the electron spin density is found mostly on the C_3 carbon, spin densities are still reported for the indole nitrogen, suggesting that the electron may be localized on this atom. In this case, a lone pair from the Met-thioether would interact with the radical on the nitrogen, preventing hydrogen bonding to that same nitrogen. This also would describe why an increase in the g_x is observed and as mentioned above, ENDOR measurements would be of great benefit to validating this hypothesis.

For both mutants, HFCC's reveal that the majority of coupling is occurring to the methylene protons from the protein backbone (labeled $H\beta_1$ and $H\beta_2$ in Figure 43). Some coupling can also be seen to the indole nitrogen. This is consistent with a literature report for a Trp108 radical in azurin.[132] The simulations shown in Table 3 do not account for all hyperfine that has been extracted in other reports for EPR spectra of similar Trp108 radicals in azurin, however, they better matched our experiments than those literature

values.[131,132,140] Small increases in the HFCC's can be seen in the Met102 derivative and although not large (ca. 0.2-0.7 Gauss), this suggests that the addition of Met102 imparts minor changes to the electronic structure of the Trp108 radical. Electron spin densities have been previously determined in the literature using DFT calculations. A more detailed description of these calculations can be found in the literature.[131,132,137–139] DFT calculations were not performed in this chapter, however, an example of these assignments can be found in Figure 43 (taken from the literature).[132] It has been noted that spin densities are primarily found on the indole nitrogen, C_3, C_5, and C_7 carbons on the neutral Trp108 radical. The results presented here for HFFC's are expected with the larger spin density being found on the C_3 carbon.

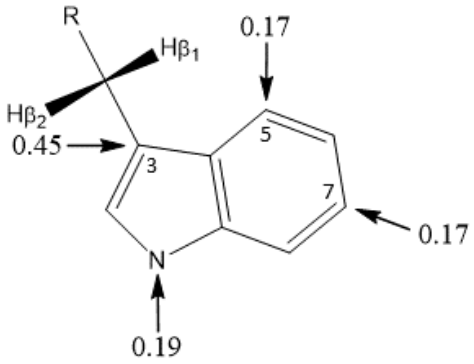

Figure 43. Structure of a neutral Trp108 radical with associated spin densities. Values and numbering system are from the literature.[132] Similar spin densities have been reported elsewhere.[137–139]

3.3. Summary and Future Directions

In this Chapter, it was determined that adding a Met residue in a proximal position to a Trp residue has a slight effect on the electronic properties of Trp108. No major changes to the Trp108 fluorescence spectra were observed for either mutant. This is likely because the polarity difference between Met102 and Leu102 is very small. Interestingly, the photochemical yield of the neutral Trp108 radical was reduced by almost half in the presence of Met102 which can be due to a variety of reasons that require further experimentation. The EPR spectra of both the Met102 and Leu102 mutants revealed changes to the g-values and hyperfine values. The increase in g_x suggests that the Met102 variant has access to less hydrogen bonding than when the Leu102 residue is present. This could be due to less exposure to the aqueous buffer by the Met102 changing the conformation of the pocket that contains Trp108 or the formation of a $2c-3e^-$ that prevents

the indole nitrogen from exhibiting any hydrogen bonding. In all cases, more experimental work could be done to complement these results.

As was stated for the work carried out in Chapter 2, crystal structures of these proteins would define the structural features in the Trp108 pocket above the assumptions made based on previous structures and PyMOL generated structures using the "mutagenesis tool." Many of the limitations noted in this chapter are related to unknowns in the protein's structure, distance and orientation of amino acids being the main two factors. We can conclude that changes to the electronic properties of Trp108 radicals in an azurin protein can be seen when there is an addition of a nearby Met residue. Along with this, more experimental techniques could be used to probe the microenvironment around Trp108. In particular, TA spectroscopy should be carried out to evaluate ET kinetics and electrochemical characterization to determine the reduction potentials of Trp108. In both cases, these would aim to compare and contrast the results presented in Chapter 2 with those presented here and may describe interactions with the microenvironment better. Furthermore, the EPR experiments could be paired with ^{1}H and ^{2}H ENDOR experiments to explore the presence of hydrogen bonding with the surrounding solvent. This would determine whether the Met102 mutant can still undergo hydrogen bonding *via* the indole nitrogen on Trp108

3.4. Experimental

All reagents were obtained from Sigma-Aldrich and used without further purification unless otherwise noted. Luria-Bertani (LB) broth miller was purchased from BioShop Canada and prepared according to the manufacturer. Water used was from a Barnstead EASYpure system (18 MΩ cm^{-1}). UV-Vis spectrophotometry was carried out using a Cary 100-Bio spectrophotometer. MALDI mass spectrometry was carried out on a Bruker microflex LT MALDI Biotyper mass spectrometer. TA experiments were carried out using a home-built spectrometer containing an Continuum Surelite SLI-10 (Nd:YAG) laser, a Continuum Surelite OPO, a 75 W Xe arc lamp, and home-built detection system. Full details of the system are described elsewhere.[160] Steady-state UV-Vis experiments were carried out using the same home-built laser system but with a Photon Control detector and deuterium-halogen light source.

3.4.1. Site-Directed Mutagenesis

A plasmid containing Phe mutations for all Trp and Tyr residues within azurin was a gift from Harry B. Gray and John H. Richards (California Institute of Technology). The Phe108Trp mutation was added followed by Leu102Met so that two distinct protein scaffolds could be expressed (His107Trp108Leu102 and His107Trp108Met102). All mutations were introduced using site-directed mutagenic polymerase chain reaction (PCR) using standard protocols.[180] DNA primers were purchased from Eurofins Genomics. Q5 DNA polymerase and DpnI enzyme were purchased from New England BioLabs (NEB). PCR products were transformed into competent DH5α *E. coli* competent cells obtained from NEB and selected using ampicillin-containing agar plates. Colonies were grown overnight at 37 °C and single colonies selected for liquid cultures in LB broth containing 100 μg/mL of ampicillin. Plasmid DNA was extracted and purified using a QIAprep Spin Miniprep Kit purchased from Qiagen and following the standard protocols provided. Purified plasmids were sequenced by Eurofins Genomics using their Sanger sequencing service. Plasmid purities and concentrations were obtained using a NanoDrop ND-1000 spectrophotometer.

3.4.2. Primer Design

Forward and reverse primers were designed to contain a single point mutation (Phe108Trp and Leu102Met). Bolded nucleotide bases represent where the mutation was added. Primers were designed as follows:

Phe108Trp Forward: 5'-GGTGAACAG**TGG**ATGTTCTTCTGC-3'

Phe108Trp Reverse: 5'-GTGCAGAAGAACAT**CCA**CTGTTCACC-3'

Leu102Met Forward: 5'-CCGTTACTTTCAAG**ATG**AAAGAAGGTGAACACTGG-3'

Leu102Met Reverse: 5'-CCTTCTTT**CAT**CTTGAAAGTAACGGAGTCTTTTTCACCGG-3'

3.4.3. Protein Expression and Purification

Plasmids were transformed into competent BL21(DE3) *E. coli* cells obtained from NEB and selected using ampicillin-containing agar plates. Colonies were grown overnight

at 37 °C and single colonies selected for liquid starter cultures in LB broth containing 100 µg/mL of ampicillin. Starter cultures were grown at 37 °C with 180 rpm of shaking for 6 hours. Overnight 1 L expression cultures were prepared by adding a small portion of starter culture (~ 3mL) into LB broth containing 100 µg/mL of ampicillin and 0.4% glycerol. Overnight expression cultures were grown at 37 °C with 180 rpm of shaking. Cells were then pelleted by centrifugation at 4000 rpm using a Beckman Avanti J-26XP centrifuge in a JSP F500 rotor for 20 minutes. Cell pellets were resuspended in osmotic shock buffer (50 mM Tris, 1 mM EDTA, 20% sucrose, pH 8.1) and rest on ice for 20 minutes. Cell pellets were then obtained by centrifugation at 7000 rpm using a Beckman Avanti J-26XP centrifuge in a JA 25.50 rotor for 20 minutes. Pellets were resuspended in 500 µM $MgCl_2$ and rest on ice for 20 minutes. Proteins were isolated by centrifugation at 12000 rpm using a Beckman Avanti J-26XP centrifuge in a JA 25.50 rotor for 20 minutes. Supernatants were collected and 100 mM $CuSO_4$ and 500 mM NaOAc (pH 4.5) were added dropwise. These mixtures were incubated overnight at 37 °C to promote Cu(II) uptake by apo-azurin. Acid precipitated proteins were removed by centrifugation at 12000 rpm using a Beckman Avanti J-26XP centrifuge in a JA 25.50 rotor for 20 minutes. The resulting supernatants were collected and purified on a CM Sepharose column obtained from GE Healthcare using a NaOAc concentration gradient. Protein purities and concentrations were determined spectrophotometrically using reported extinction coefficients (ε_{628} = 5600 M^{-1} cm^{-1}).[42,160]

3.4.4. Tryptophan Fluorescence

Fluorescence experiments were carried out using a Horiba Jobin-Yvon Fluorolog. 60 µM samples were prepared in 1 M NH_4Cl, 20 mM NaP_i at pH 7.8. Samples were placed into air-free cuvettes made by the Simon Fraser University (SFU) Glass Shop and deoxygenated with 15-20 pump-backfill cycles using N_2. Excitation was achieved using 280 nm light and spectra were recorded from 295 – 500 nm to monitor for Trp fluorescence. 10 scans were performed per sample and emission maxima were determined by averaging each series.

3.4.5. Cu(II)/Zn(II) Substitution

Protein samples were desalted into 10 mM NaOAc at pH 7.5 before the minimal addition of stripping solution (100 mM NaOAc, 1 mM EDTA, and 100 mM NaCN at pH 9)

dropwise with constant agitation. This is done until a colourless solution of azurin is observed. Proteins were exchanged into 10 mM NaOAc at pH 7.5 to remove cyanide before being exchanged into labeling solution (30 mM NaOAc at pH 4). 100 mM $Zn(OAc)_2$ (6 mL) was added to both protein samples and shaken at 180 rpm at 37 °C overnight. A white precipitate is formed overnight and spun down at 3000 rpm using an IEC Centra MP4R centrifuge in a Cat. 816 rotor. Samples were decanted and further concentrated before being stored at 4 °C. Samples were confirmed using UV-Vis spectrophotometry and observing a 280 nm absorbance peak consistent with Cu(II)-substituted azurin.

3.4.6. Photosensitizer Labeling of Azurins

Labeled azurins were obtained by adding two equivalents of $[Re(CO)_3(4,7\text{-dmp})OTf]^{2+}$ to a solution of azurin in 25 mM HEPES (pH 7.0). It is important that pH adjustments are not done with Cl^- containing solutions. These reaction mixtures were incubated for 5-7 days at 37 °C in the dark. FPLC was carried out using a HiTrap IMAC FF column (obtained from GE Healthcare) metalated with Cu^{2+}. The reaction vessel was spun down at 3000 rpm using an IEC Centra MP4R centrifuge in a Cat. 816 rotor to pellet any precipitated label or protein. Reaction mixture was then exchanged into binding buffer (1 M NaCl, 20 mM NaPi, pH 7.8) and loaded to the previously equilibrated column under the same buffer system. Unmodified azurins bound to the column while Re-modified azurins (Re-His107Trp108Leu102 and Re-His107Trp108Met102) elute with the binding buffer wash. Unlabeled azurins were collected and pooled for reuse. Re-modified fractions were collected and monitored by UV-Vis spectrophotometry to pool correct fractions together. Concentrations of each Re-modified azurin were calculated spectrophotometrically using reported extinction coefficients.[183]

3.4.7. Steady-State UV-Visible Characterization

Protein samples (57 μM concentration) were prepared in 50 mM NaP_i (pH 7.5) containing 5 mM $[Co(NH_3)Cl]Cl_2$ irreversible quencher. Samples were deoxygenated with 10-15 pump-backfill cycles prior to laser irradiation using air-free cuvettes made by the SFU Glass Shop. Irradiation was carried out with 355 nm pulses at 5 mJ/pulse and spectra were collected every 10 seconds from 350 – 700 nm using a Photon Control detector and deuterium-halogen light source.

3.4.8. EPR Spectroscopy

Protein samples (200 µL, 30-100 µM) were prepared in 50 mM NaP_i at pH 7.5 with 30% glycerol as a glassing agent and 5 mM $[Co(NH_3)Cl]Cl_2$ of irreversible quencher. Pump-backfill cycles (15-20 total) using N_2 were performed to remove O_2 from the sample and air-free cuvette (made by the SFU Glass Shop). Samples were quickly moved into EPR tubes and irradiated with 355 nm excitation pulses with a defocused beam at 8-10 mJ/pulse. Immediately following irradiation, samples were flash frozen and stored in liquid N_2 until same-day EPR was carried out. EPR was carried out using a Bruker EMXplus spectrometer using an X-band Premium X microwave bridge and HS resonator. Experiments were carried out at 100 K for two hours using a Bruker ER 4112HV temperature controller with a continuous flow cryostat using liquid N_2 to achieve a constant temperature of 100 K. Simulations for the His107Trp108Leu102 mutant were carried out by Greg MacNeil from Charles Walsby's lab at Simon Fraser University where noted. All simulations were generated using EasySpin software.[184] They were performed for S = ½ systems with anisotropic g-factors and HFCC's. Simulations were initially constrained to literature g-values for reported Trp108 radicals obtained using high-field EPR (g_x = 2.00355, g_y = 2.00271, and g_z = 2.00221).[132,140] Simulations were then performed by allowing g-values and HFCC's to vary within a range of 0.001 and 5 MHz, respectively.

Chapter 4. Protein Microenvironment Effects on the Physical Properties of Tyrosine in Azurin[**]

4.1. Introduction

There is a knowledge gap in understanding how a protein's microenvironment (the local environment in and around a protein) influences the properties of the aromatic amino acid, tyrosine (Tyr). It is known that Tyr is used as a hopping intermediate to facilitate long-range electron transfer (ET) within biology, but it is unknown how different nearby amino acids within the pocket surrounding the Tyr residue affect its reactivity and other physical properties. This chapter uses artificial *in vitro* protein models developed using *Pseudomonas aeruginosa* azurin to understand how three different amino acids affect the physical properties of a nearby Tyr. Here, methionine (Met), glutamine (Gln), and arginine (Arg) are discussed. These amino acids are pictured below in Figure 44**.**

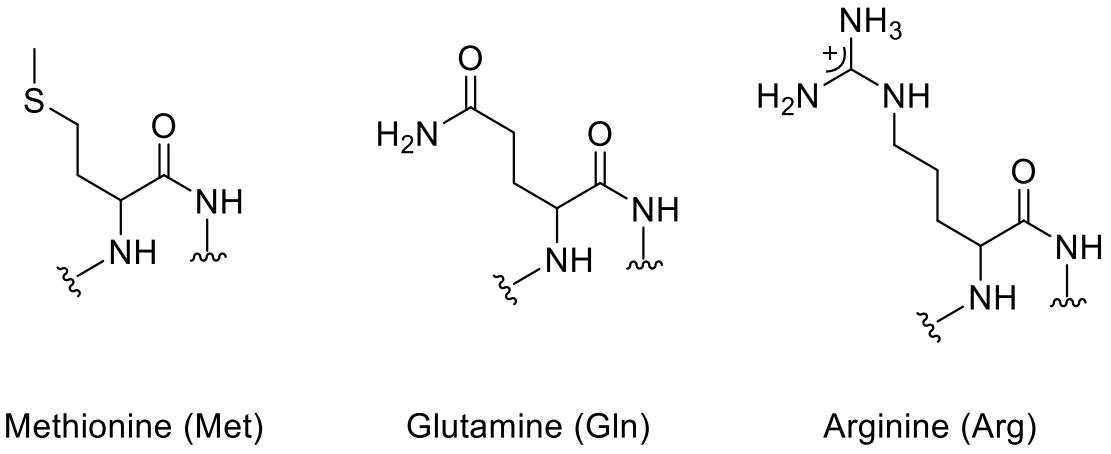

Figure 44. The three amino acid mutations used in this chapter, methionine (Met, left), glutamine (Gln, center), and arginine (Arg, right).

[**] Portions of this chapter are adapted from Gibbs, C. A.; Fedoretz-Maxwell, B. P.; Warren, J. J. "On the Roles of Methionine and the Importance of Its Microenvironments in Redox Metalloproteins." *Dalton Trans.* **2022**, *51* (13), 4976–4985. https://doi.org/10.1039/D1DT04387K**.** J.J.W. conceived the topics and co-wrote the paper. C.A.G. wrote the paper except for topics involving iron, edited, designed figured, and formatted the entire paper. B.P.F-M. wrote and designed figures for the iron section in the paper.

4.1.1. Overview of the Protein Microenvironment

The myriad factors that affect the physical properties of biological sites have been investigated for over 50 years.[42,185,186] The amazing growth of available protein structures in the PDB, as well as the advancement of new experimental technologies (synchrotron techniques, magnetic resonance methods, and electron microscopy), has enabled an even greater appreciation of local interactions in biological systems. For metal ions in a metalloprotein, the primary metal coordination is comprised of common ligands from a coordination chemist's view; examples include the carboxylates of aspartate (Asp) and glutamate (Glu), the imidazole of His, the thiol of Cys, the thioether of methionine (Met), and the phenol of Tyr.[185,186] In contrast, the residues that surround the inner sphere are much more diverse. Werner[187] defined the outer coordination sphere of a metal complex as "a group coordinated directly to a ligand in the first sphere", however, this is often too limited for metalloproteins. This definition has since been expanded to include any groups or interactions that affect the inner coordination sphere of protein-bound metal ions, highlighting the more wide-ranging concept of the microenvironment. More broadly, the collection of local interactions, such as hydrophobic effects and hydrogen bonding, that affect the physical properties of any molecular site can be termed the "microenvironment". It is now appreciated that microenvironment effects in proteins extend well beyond metals and can include any group, from organic cofactors to substrates to individual amino acid residues.

In an analogous manner to metal microenvironments, it is now recognized that local interactions affect the physical properties of individual amino acid residues, from acid/base chemistry to redox reactions. A common example is the hydrogen bonding interaction of tyrosine$_z$ in photosystem II.[120] For individual amino acid residues (i.e., no metal ion), the idea of "coordination" does not apply, but there are still many factors that the microenvironment contributes to influence the physical properties of embedded sites, from reorganization energy to hydrogen bonding to reduction potentials. In the context of individual residues, such local interactions are often described in the context of protein folding.[106] More specifically, the microenvironment surrounding amino acids is defined by the atom arrangement around said residue.

An illustration of the primary and secondary coordination sphere of metal ions is shown in Figure 45**,** where the structure of the R2 subunit of *C. trachomatis* ribonucleotide

reductase (RNR) as an example. The metal-ligating residues are shown in purple and the residues of the secondary coordination sphere (with any interactions < 3.5 Å) are in orange. The outer-sphere is a complex network of dipolar, hydrogen bonding, and hydrophobic interactions that involve amino acid side chains and the peptide backbone. It is this complex interplay of intramolecular forces that gives metal active sites privileged physical and electronic properties and illustrates the utility of the term microenvironment. While there are many second sphere amino acid residues show in Figure 45, many of their interactions occur via the peptide backbone.

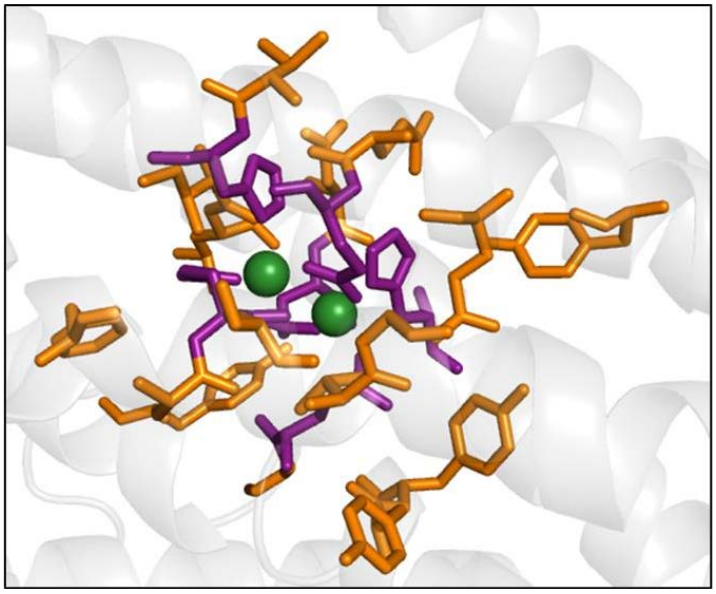

Figure 45. The metal-containing active site of *C. trachomatis* RNR showing the metal ions (green), their primary ligand set (purple), and all the outer coordination sphere residues (orange). The outer-sphere residues were selected as those that show any interaction under 3.5 Å with the primary ligands. PDB ID: 1SYY.[188]

A protein's structure is dictated by a plethora of interactions that are precisely tuned to result in a stable, tertiary structure. The most dominant of these interactions are hydrophobic interactions, electrostatic interactions, and hydrogen bonding, although other examples could be noted here as well.[189]

4.1.2. Hydrogen Bonding and the Protein Microenvironment

Hydrogen bonding plays a major role in the structural stability of a protein and is considered energetically comparable to the hydrophobic effect. Not only does hydrogen bonding impact stability, but it can also affect substrate binding in the context of

biocatalysis.[190] The sharing of a hydrogen atom between two other electronegative atoms, the donor and the acceptor, is what defines a hydrogen bond. The strength of this interaction is then dictated by the orientation of the hydrogen bond donor and acceptor and their respective electronegativities, however, this is typically 2-10 kcal mol^{-1}. In proteins, this can occur between amino acid side chains or through the protein's backbone carbonyls and amides.[189] An example of how hydrogen bonding interactions may change with respect to the microenvironment can be seen in cholesterol oxidase of *Streptomyces* sp., where at pH values > 7.5, the k_{cat} for substrate oxidation decreases 2000-fold while the K_m remains unaffected. Although not fully understood, the protonation state of the FADH may be responsible for this through a hydrogen bonding interaction. Furthermore, hydrogen bonding has been observed to be highly pH sensitive in biology, suggesting that a protein's microenvironment has a larger role in structural stability and catalysis.[190]

It is well known that hydrogen bonding plays a role in stabilizing protein structures, however, an interplay of many forces must be present. Due to hydrogen bonds being typically formed between backbone carbonyls and amides, it is suggested that if protein folding was dominated by hydrogen bonding alone, structures should be independent of their amino acid sequence.[189] This is not the case. As such, structural biologists have focused on understanding how amino acid side chains may impact sequence specificity. This chapter investigates how the physical properties of a Tyr residue changes when nearby residues are mutated and thus, aims to develop a new understanding of how the microenvironment could finely tune the properties of a Tyr residue.

4.1.3. Current State of Studying a Protein's Microenvironment

Protein structure and function are closely related.[191] From primary to tertiary structures, all aspects of a protein's structure can affect how it functions.[191,192] The fundamental interactions that determine this occur between amino acids, suggesting that the microenvironment plays a large role in determining a protein's overall structure and function.[191] A great amount of work has been done to study how changes to the macromolecular structure of a protein changes its structure-function relationship, from computational designs to site-directed mutants. Importantly, understanding these structure-function relationships can be applied to aid in improved pharmaceutical drug design or synthetic proteins.[193] There remains gaps in the knowledge of how the microenvironment around certain amino acid residues impacts a protein's local and/or

overall structure, and ultimately, that protein's function.[194] This chapter aims to elucidate a variety of factors that would affect the microenvironment within a protein.

Part of the reason that there are knowledge gaps in protein structure-function relationships is that experimental observations can be challenging to make without good model systems. The lack of appropriate models has made it difficult to determine the exact role that the microenvironment may have for specific sites. A few examples of techniques used for such studies are infrared spectroscopy,[195–197] quantum chemistry computations,[193,198,199] fluorescence sepectroscopy,[200–202] enzyme kinetics,[67,203,204] and electrochemistry.[141,205,206] These have all been used to investigate characteristics of protein microenvironments around different amino acids and some have been employed in this chapter, namely fluorescence, kinetics, and electrochemistry.

IR experiments utilize probes such as a cyano functional group, which can be tagged to amino acids to study changes in the proteins IR spectra. This method has its limitations in that the chromophore may bind to the metal center in a metalloprotein instead[195] (although this could be desirable also[196]), inhibiting the ability to observe changes directly at specific amino acid sites.[195] Computational work has expanded to predict how a protein's structure may impact its function by investigating predetermined microenvironments and matching them with known active sites that are associated with specific functions.[207] Computational work is imperative to the study of buried residues as they are exceptionally difficult to probe. Work that involves these amino acids requires naturally occurring fluorophores or only residues that can be fluorescently labeled, such as cysteine, to investigate changes to a buried residues microenvironment.[194,202,208] This chapter uses fluorescence spectroscopy, time-resolved transient absorption (TA) spectroscopy, and electrochemistry to probe the changes that a protein's microenvironment has on a Tyr residue within the blue-copper protein, azurin, as an artificial model system.

4.1.4. Tyrosine Fluorescence in Proteins

Tyr fluorescence is not as commonly used as tryptophan (Trp) fluorescence, but it is still a useful probe in cases where Trp is not present (as is the case here). Tyr fluorescence is often highly sensitive to local pH changes or other non-covalent interactions with its surrounding microenvironment.[209] One way to probe the

microenvironment of a Tyr amino acid residue is by investigating its fluorescence decay. This can sometimes be complicated by multiple-exponential decays due to nearby amino acids, which we have attempted to simplify in the models developed here. It is important to note that an excited-state Tyr also can undergo proton transfer (PT) and ET, resulting in multiple-exponential decays.[210] An added complication to studying Tyr fluorescence is the conversion of Tyr to tyrosinate ($TyrO^-$) (Figure 46). The ground-state pK_a of the hydroxyl group in Tyr is 10,[209] so it is expected that at pH values above ca. 10, $TyrO^-$ fluorescence should dominate a protein's emission spectrum at ~340 nm.[113,211] However, the pK_a of this hydroxyl group also dramatically decreases to 4 when Tyr is in its excited state, and in neutral solutions, can dissociate, resulting in Tyr fluorescence being quenched.[111] For the conversion of Tyr to $TyrO^-$ to occur, a PT is required from the aromatic hydroxyl to an external proton acceptor, commonly a nearby amino acid side chain.[211] This suggests that the microenvironment may play a key role in this reaction.

Many proteins contain both Tyr and Trp residues and in these cases, emission maxima are typically found at ~310 nm due to the intrinsic Trp fluorescence masking Tyr and $TyrO^-$. This problem has been mitigated in this chapter as a protein with no Trp residues was designed. In this chapter, the role(s) of specific amino acid residues in the Tyr microenvironment are probed. Three different amino acids (Met, Arg = arginine, and Gln) replaced the native azurin Lys122 (Lys = lysine) residue to evaluate how different amino acid types would impact the conversion to $TyrO^-$ at different pH values. It is thought that the conversion of Tyr to $TyrO^-$ is the rate-limiting step in this reaction and it is proposed that a change at this step would impact the electron hopping properties of this residue. The microenvironment also may play a role in quenching of Tyr emission through a variety of mechanisms via; (1) the backbone carbonyl, (2) a resonance energy transfer, (3) disulfide bridges, and (4) amino acid sidechains. For the context of this thesis, quenching via the backbone carbonyl and amino acid sidechains will be discussed.

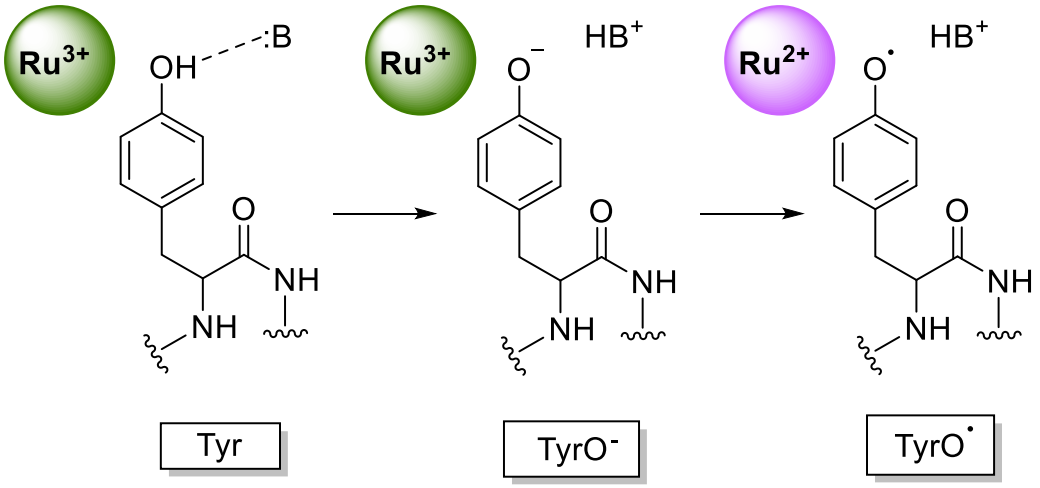

Figure 46. **PCET reaction scheme of Tyr conversion to tyrosyl (TyrO$^{\bullet}$) through a tyrosinate (TyrO^{-}) intermediate. B represents the proton acceptor which could be another amino acid of buffer. Ru$^{3+/2+}$ represent the [Ru(bpy)$_2$(im)]$^{2+}$ photosensitizer that is labeled to His107 in the protein's structure.**

4.1.5. Fluorescence Quenching via the Backbone Carbonyl

Fluorescence quenching of aromatic amino acids, in this case Tyr, is dependent on distance and orientation between the Tyr sidechain and the quenching group. Quenching groups can include the backbone carbonyl and amide groups or other amino acid sidechains. Quenching via the protein backbone has been shown to decrease fluorescence lifetimes of Tyr residues when the hydroxyl group is at an optimal distance from the quenching group. It should be briefly mentioned that this occurs through a charge transfer between the phenol ring and the carbonyl of the backbone[212] and was unknown as to whether this would play a role in the systems described herein. Another plausible method for the quenching of Tyr emission is via an excited-state PT or through a collisional interaction. This could occur with the amino acid sidechains of aspartate (Asp) or glutamate (Glu).[113]

4.1.6. Fluorescence Quenching via Amino Acid Sidechains

As mentioned above, Asp and Glu have been recognized to quench Tyr fluorescence due to their carboxylate sidechains. Effective quenching via these residues requires a small distance separation between Tyr and the quenching group. It has been suggested that fluorescence quenching by these two residues occurs by a collisional

interaction over an excited-state PT, although excited-state PT are likely to occur with other proton accepting sidechains.[113] Initially, the research in this chapter involved a Glu mutation in the series of mutations, however, it was unable to be expressed and will be discussed further in section 4.2.1.

The mechanism for collisional quenching and quenching by an excited-state PT are both considered dynamic and require an ionizable proton on the Tyr residue resulting in analogous pathways of quenching. Three different events can be considered. (1) Diffusion of the proton acceptor, allowing for a collisional interaction to occur between the excited-state Tyr and the accepting residue, (2) a constricted proton donor and acceptor in which the proton diffuses through-space, and (3) hydrogen bond formation between the Tyr hydroxyl and the accepting residue. It is important to recognize that all three of these mechanisms are possible within a protein and depend on factors from the microenvironment surrounding the residues undergoing the PT event.[113]

Other amino acid side chains have been observed to efficiently quench Tyr fluorescence. When uncharged, Arg, Lys, and His are able to accept a proton from the Tyr hydroxyl, which has been proposed to quench Tyr fluorescence. However, these residues have no effect when they are charged and protonated. This is due to a required PT from the Tyr hydroxyl to inactivate its emission.[113] Interestingly, although the pK_a values for Arg and Lys are ~13.8[213] and 10.5,[214] respectively, the microenvironment is able to perturb the residue's structure, resulting in pK_a values that are physiologically relevant. Amino acids such as Met and Gln cannot be protonated under normal biological conditions. As such, Met and Gln have not been observed to quench Tyr fluorescence,[113] although the sulfur-containing Met side chain has been identified as a somewhat efficient quencher of Trp fluorescence.[168]

4.1.7. Microenvironment Influence on Tyrosine Reduction Potentials

Protein reduction potentials can span large ranges and is attributed to the protein's microenvironment. The microenvironment is dictated by the protein's structure and the surrounding solvent leading to changes in noncovalent interactions that determine a protein's physical properties.[215] An example of the importance of the microenvironment's effect on reduction potentials is known for blue-copper proteins. Blue-copper proteins share nearly identical copper coordination spheres but have copper reduction potentials

that differ by ~150 mV. It has been suggested that differently charged amino acids such as Asp, Glu, Arg, Lys, and His could play a role in altering the reduction potential of a specific site within a protein,[216] two of which were initially considered for this work (Glu and Arg). Much research of protein reduction potentials utilizes the metal centers in metalloproteins,[160,215] however, some amino acids are redox active also. In this chapter, changes to the reduction potential of Tyr is investigated with respect to microenvironment changes. This will aid in determining how solvent pH and nearby amino acids fine-tune the redox properties of Tyr which would have an impact on how ET events throughout biological systems are facilitated by Tyr residues.

4.1.8. Electron Transfer via Tyrosine

ET in metalloproteins is a necessary process for living organisms. The study of these processes has been investigated for many years and although much is understood, there are still many knowledge gaps in how these ET events are controlled.[217] Many biological ET pathways require reactions to occur at distances > 20 Å, which consequently leads to ET rates occurring at timescales > 1 ms, or not happening entirely, due to the rate of ET decreasing exponentially as the distance between donor and acceptor increases. Proteins use aromatic amino acids such as Trp and Tyr (Tyr in this chapter) to facilitate these long-range ET reactions.[15,59,120] Computational analyses have been used to generate electron hopping advantage maps (an example is shown in Figure 5, section 1.2.1) that predict the point at which an ET pathway is optimized. These maps have suggested that the most efficient ET reactions occur when a variety of conditions are met; (1) when the electron donor, intermediate(s), and acceptor orient in a straight line, (2) when the intermediate-acceptor distance is shorter than the donor-intermediate distance, and (3) when the overall distance between donor and acceptor is shortest,[31] which is expected based on the Marcus equation ($\mathrm{Eq.}\,5$, section 1.2).

The flash-quench reaction pathway used in this chapter is shown in Figure 47**.** Two different wavelengths can be used to probe ET, 480 nm, which measures the recovery rate of Ru(II), and 628 nm, which measures the recovery rate of Cu(II). For the reaction to occur, an exogenous, reversible quencher must be used, otherwise, the excited state Ru(II) (Ru(II)*) will relax with no ET observed. This quencher can donate the electron back to the protein to allow the reaction mechanism to cycle.

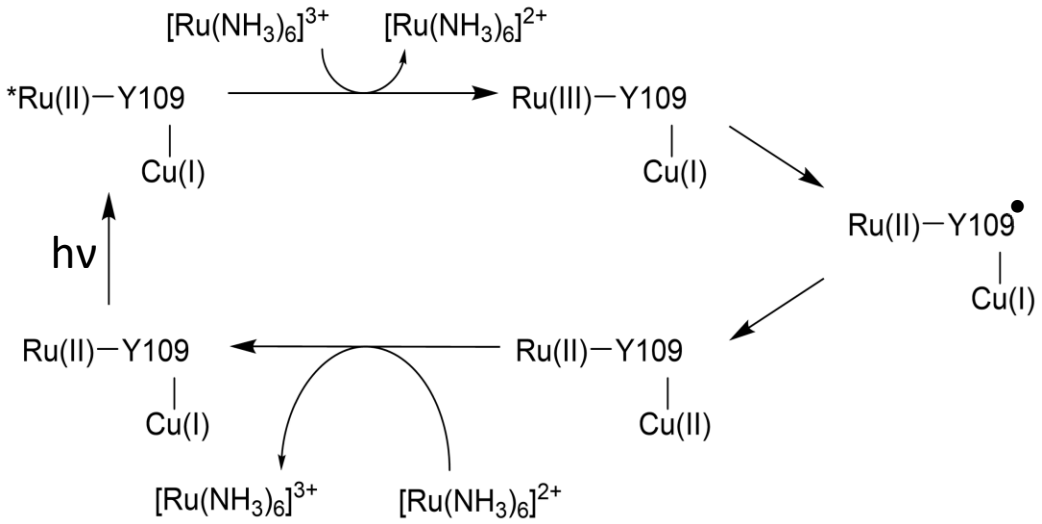

Figure 47. Flash-quench scheme to monitor ET kinetics for Ru(III) to Ru(II) reduction and Cu(I) to Cu(II) oxidation. The wavlength of light used for Ru(II) excitation was 480 nm and is represented by hν in the mechanism. Y109 in this figure represents the Tyr109 mutation.

4.2. Results and Discussion

4.2.1. Development of Protein Models

The work herein uses a variant of azurin in which all Trp and Tyr residues are mutated to Phe (termed “all-Phe”). This was confirmed by Sanger sequencing prior to further mutagenesis. Sequential point mutations were performed as follows: Phe109Tyr followed by either Lys122Met, Lys122Arg, Lys122Gln, or Lys122Glu to produce five distinct azurin mutants; His107Tyr109(Lys/Met/Arg/Gln/Glu)122. The added point mutations were again confirmed by Sanger sequencing before proceeding with protein expression. Unfortunately, the His107Tyr109Glu122 variant was unable to be obtained in the yields necessary for comprehensive study, even after multiple attempts. It is possible that the negatively charged Glu residue may destabilize this pocket, resulting in a microenvironment that prevents the protein from folding properly. Due to this, the use of this variant was abandoned and will not be discussed further. An example of the residues that participate in this electron hopping pathway are shown in Figure 48 (His107Tyr109Lys122). It should be noted here that ruthenium-labeled azurin was only used in TA experiments and was not required for electrochemistry or fluorescence studies.

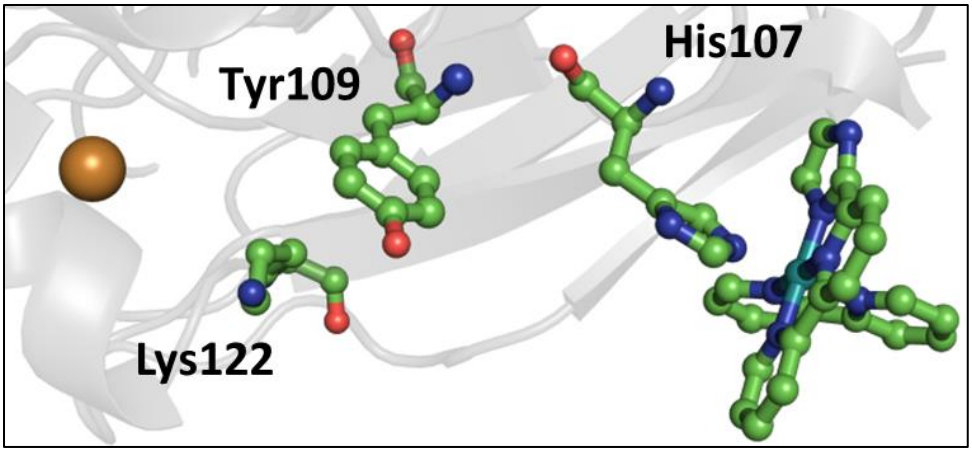

Figure 48. Ruthenium-labeled His107Tyr109Lys122 from *Pseudomonas aeruginosa* azurin. Lys122 is the residue that is mutated for each of the experiments in this chaapter. The brown sphere represents Cu^{2+} and the complex to the right is $[Ru(bpy)_2(im)]^{2+}$ (bpy = 2,2'-bipyridine, im = imidazole) .This figure was based on the PDB ID: 4HHG.[31]

The experiments carried out in this chapter utilized three different azurin variants, parts of which are shown in Figure 49. Each of the residue alterations were selected to probe a different type of microenvironment interaction with Tyr109. Specifically, Arg is a positively charged amino acid, Gln is neutral and polar, and Met is neutral but nonpolar (or slightly polar due to the electronegativity between sulfur and carbon, see above). The thioether group on Met may also play a role here in the formation of a 2-center, 3-electron ($2c\text{-}3e^{-}$) bond, similar to what was discussed in Chapter 2 and Chapter 3. It is important to mention that the orientation of these residues with respect to each other is unknown since crystal structures were not determined for any of the mutants discussed in this chapter. Figure 49 was generated using the mutagenesis tool in PyMOL and the least sterically and electronically hindered orientations were chosen.

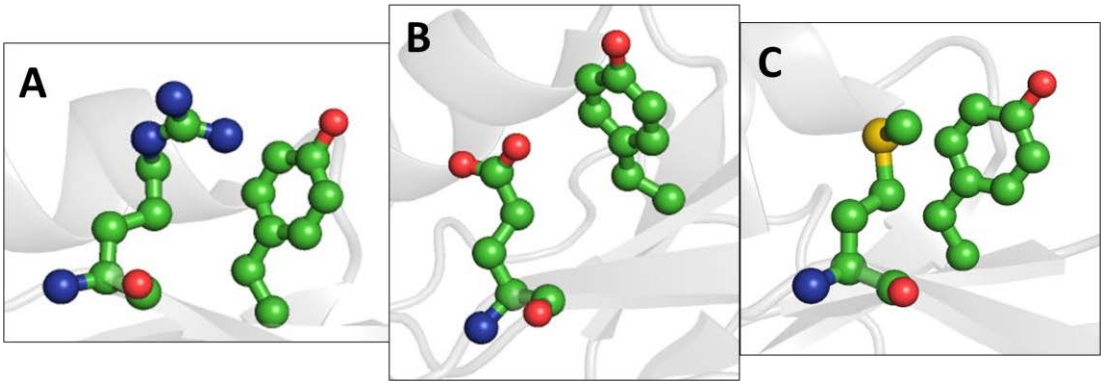

Figure 49. The three different mutations used to carry out the experiments in this chapter. The residues shown are Tyr109Arg122 (panel A), Tyr109Gln122 (panel B), and Tyr109Met122 (panel C). This figure was based on the PDB ID: 4HHG.[31]

Three azurin variants, His107Tyr109(Met/Arg/Gln)122, were successfully expressed and purified. His107Tyr109Lys122 was not expressed as some literature data was available for this protein.[135] All proteins were confirmed by UV-Visible spectrophotometry and mass spectrometry (Appendix D). All proteins used in Chapter 4 are Cu(II)-containing azurins and photosensitizer addition was only required for kinetic studies. Herein, $[Ru(bpy)_2(im)]^{2+}$ was used and production of the labeled azurins was confirmed using UV-vis spectrophotometry. Cu(II) azurin is deep blue in colour and a change to deep green is characteristic of successful modification with a $Ru(bpy)_2$-based label. The appearance of an absorbance band at 490 nm further confirms this labeling (Appendix D). Herein, the mutants will be described only by their mutation at position 122 (e.g., Met122).

4.2.2. Absorption Properties of Tyr109 Azurins

The absorbance spectrum of Tyr in water shows an absorbance maximum at 274 nm and a shoulder at about 280 nm.[218] Careful inspection of the UV-Vis absorption maxima for the azurin variants without ruthenium modification (Figure 50) shows a slight red-shift by 1 nm for Gln122 from 274 nm to 275 nm and suggests a slight perturbation to the pocket near Tyr109. As seen for the UV-Vis spectra of Trp variants in Chapter 2 and Chapter 3, the peak multi-line features around 260 nm are due to the Phe residues in the all-Phe azurin variant. It is also seen that effectively no changes to the extinction of Tyr109 occurs in these mutants.

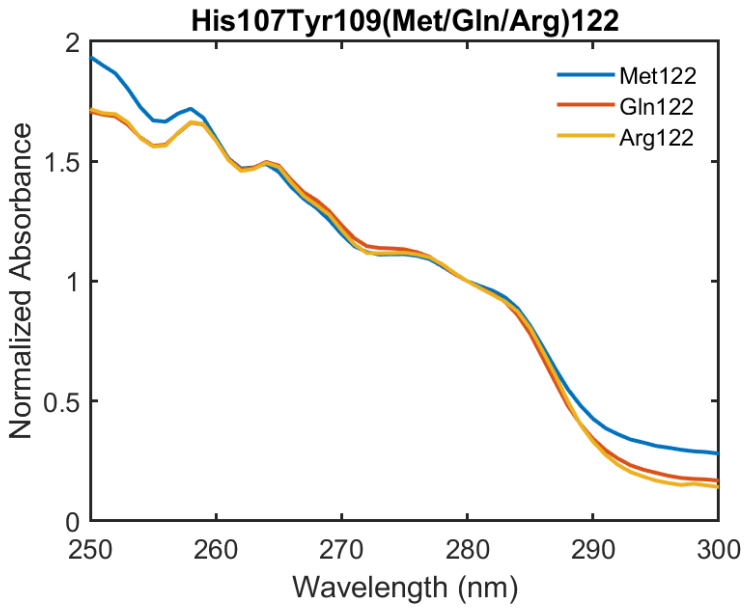

Figure 50. **Tyr109 absorbance across the three different mutants, Met122 (blue), Gln122 (orange), and Arg122 (yellow). The data presented here is for unlabeled azurins and was normalized to the 280 nm peak for better visualization.**

4.2.3. Emission Maxima Changes for Tyrosine

In proteins, the fluorescence contributors are Tyr, Trp, and Phe.[219] The mutations used in this chapter are all-Phe variants, meaning that all other Tyr and Trp residues were replaced with Phe residues. Phe fluorescence (280 nm) is very weak and is initiated by excitation at 260 nm,[220] so this feature does not impact the data presented below. The protein variants also contain no Trp residues. Consequently, it is straightforward to probe the fluorescence properties of Tyr alone. In neutral pH water, Tyr has an emission maximum of 303 nm,[218] however, proteins containing only Tyr can also exhibit emission maxima on the range of 315 to 350 nm. This can be due to $TyrO^-$ or hydrogen bonding of the phenolic hydroxyl group. In some cases, dimer formation of Tyr can also emit in this range. In the ground-state, the conversion of Tyr to $TyrO^-$ can occur at high pH or when a strong proton acceptor is present.[113] At higher pH values, the conjugate base of Tyr, $TyrO^-$, absorbs at 305 nm[221] and emits at around 350 nm.[222]

The fluorescence spectra of each of the (Met/Gln/Arg)122 azurins was investigated across a range of pH values, from 4-11, with spectra recorded at each pH value in increments of 1 pH unit. As seen in Figure 51**,** Figure 52**,** and Figure 53, a red-shift in the emission maxima occurs in the Gln122 and Arg122 variants, but not in Met122 variant.

However, in the Met122 protein, a red shifted shoulder does appear in the emission spectra as the pH increases, with a sharp increase in emission at pH 11. This is characteristic of $TyrO^-$ formation. All data in these figures were normalized to a fluorescence intensity of 1 for easier visualization of the red-shift. Raw data are presented further down in Figure 54, Figure 55, and Figure 56, where quenching of Tyr fluorescence is discussed.

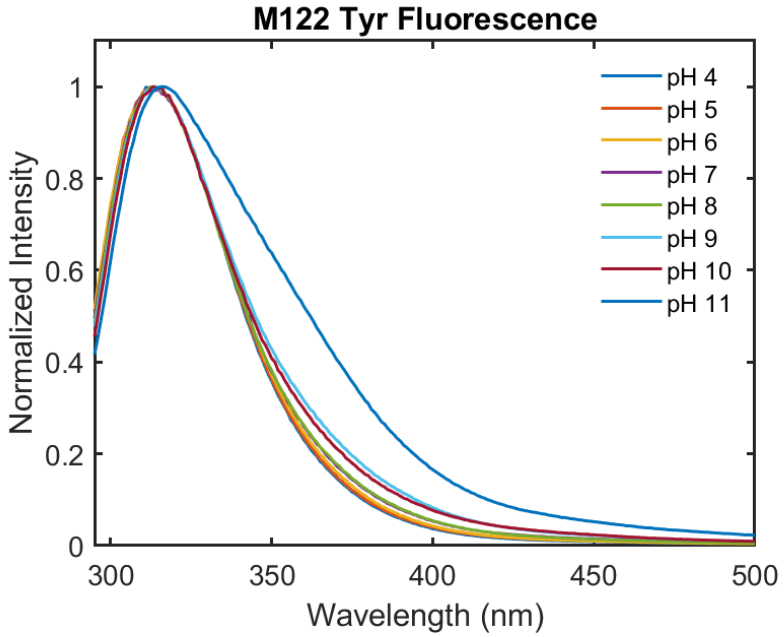

Figure 51. 65 µM His107Tyr109Met122 (Met = M) fluorescence at a pH range from 4-11 in 50 mM NaP_i. Values for the emission maxima can be found in Table 4.

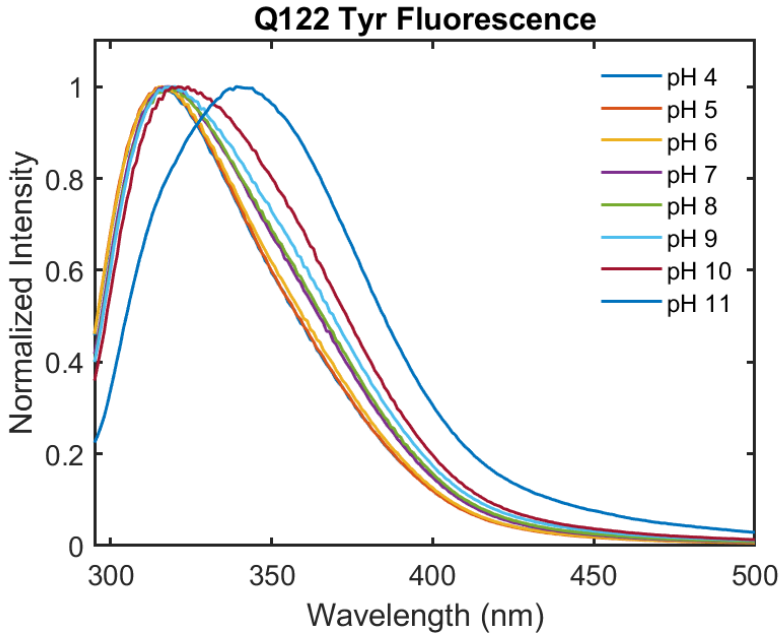

Figure 52. **65 µM His107Tyr109Gln122 (Gln = Q) fluorescence at a pH range from 4-11 in 50 mM NaP_i. Values for the emission maxima can be found in Table 4.**

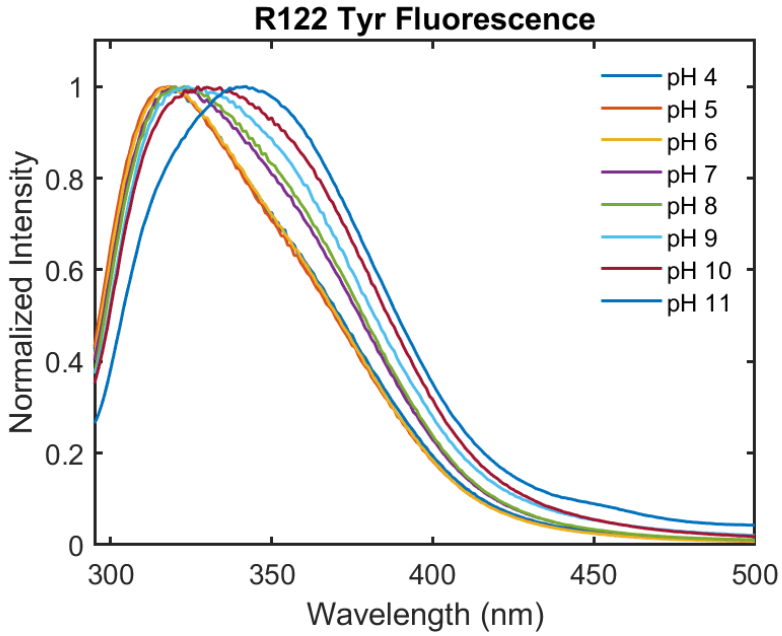

Figure 53. **65 µM His107Tyr109Arg122 (Arg = R) fluorescence at a pH range from 4-11 in 50 mM NaP_i. Values for the emission maxima can be found in Table 4.**

The ground-state pK_a of the phenolic protein in Tyr is 10. Thus, as pH values increase, $TyrO^-$ becomes the dominant species present. The observed red-shift is consistent with what is expected for Tyr to $TyrO^-$ conversion[111] and is seen for both the

Gln122 and Arg122 derivatives but not Met122. This suggests that either; (1) the Met122 mutation affects the pK_a of the Tyr hydroxyl group, inhibiting the formation of $TyrO^-$, (2) $TyrO^-$ fluorescence is being quenched by the sulfur-containing Met122, likely due to the thioether or the protein backbone, or (3) the orientation of this residue differs from the other mutations which could result in less solvent exposure. All of these points will be addressed below.

4.2.4. Hydrogen Bonding and Hydrophobicity Effects on Tyrosine Fluorescence

Table 4 shows all the recorded emission maxima for each of the three mutations. As mentioned above, at pH 11, it is evident that the spectra for Arg122 and Gln122 variants are dominated by $TyrO^-$ emission, indicated by the distinct red-shift in the emission maxima between pH 10 and 11 from 324 to 341 nm and from 319 to 340 nm, respectively. The lack of red-shift in the Met122 variant is also evident here and further supports the three hypotheses above. Another interesting observation is that the red-shift for the Arg122 mutant is observed to occur more readily, with a gradual shift in emission maxima across the entire pH range. This is clearly shown in Table 4 in which an overall change in emission maximum is seen from 317 to 324 nm for the Arg122 variant, while the maximum for the Gln122 variant shifts from 316 to 319 nm between pH values of 4-10. As mentioned in section 4.1.6, Arg residues can act as hydrogen bond acceptors and it is known that hydrogen bonding red-shifts Tyr emission.[113] This provides evidence that supports the increasing trend in emission maxima seen for the Arg122 variant over Met122 and Gln122. Furthermore, Met and Gln are not known to participate in hydrogen bonding interactions with the phenolic hydroxyl group on Tyr, emphasizing this result. The small increase for Gln122 could be due to the stronger dipole interactions over the Met122 variant, which is discussed more below.

Table 4. Emission maxima of 65 µM His107Tyr109(Met/Gln/Arg)122 across a pH range of 4-11 in 50 mM NaP_i. Error on all values is $\pm$ 1 nm.

	4	5	6	7	8	9	10	11
$\lambda_{max,\ em}$ His107Tyr109Met122 (nm)	313	313	314	313	314	314	314	315
$\lambda_{max,\ em}$ His107Tyr109Gln122 (nm)	316	316	316	317	317	318	319	340
$\lambda_{max,\ em}$ His107Tyr109Arg122 (nm)	317	317	318	319	321	321	324	341

The change in emission maxima ($\Delta\lambda_{max,\ em}$) can be compared across all three mutants to describe why Tyr109 is more pH sensitive depending on its microenvironment. Consistent with the description of hydrogen bonding, a less hydrophobic local environment leads to a larger red-shift in emission maxima. This can be seen in the $\lambda_{max,\ em}$ values reported in Table 4. Of the three mutations (and excluding pH 11 results) Met122 provides the most hydrophilic neighbouring group, which supports the negligible change in $\lambda_{max,\ em}$. Arg122 is the most hydrophobic, which supports the larger $\Delta\lambda_{max,\ em}$ over the Gln122 variant. Hydrophobicity also is used as a measure of polarity for amino acid residues. More hydrophobic residues contain oxygen and nitrogen in their side chains, making them more polar, thus, polarity of the microenvironment has an impact on a Tyr residue's fluorescence properties.

4.2.5. Quenching of Tyrosine Fluorescence

The raw data presented for the fluorescence studies is shown in Figure 54, Figure 55, and Figure 56, below. Inspection of these data indicate another key observation. For all variants, a decrease in Tyr fluorescence intensity is observed as pH increases. This suggests that less Tyr fluorescence is being affected and is likely due to the deprotonation of Tyr109 at more basic pH values. More specifically, a shoulder at ~340-345 nm increases in emission intensity for Arg122 and Gln122 at higher pH values. This is not seen in the Met122 variant until pH 11 is reached. The shoulder is indicative of $TyrO^-$ formation. Interestingly, the $TyrO^-$ fluorescence intensity is much lower for the Met122 mutant over the Arg122 and Gln122 variants at pH 11. Furthermore, ground-state Tyr fluorescence is the dominating species in the Met122 spectra, suggesting that deprotonation of Tyr109 is not occurring here. Note that the same concentration of protein was used for each experiment and the decrease in fluorescence intensity can be related to pH changes.

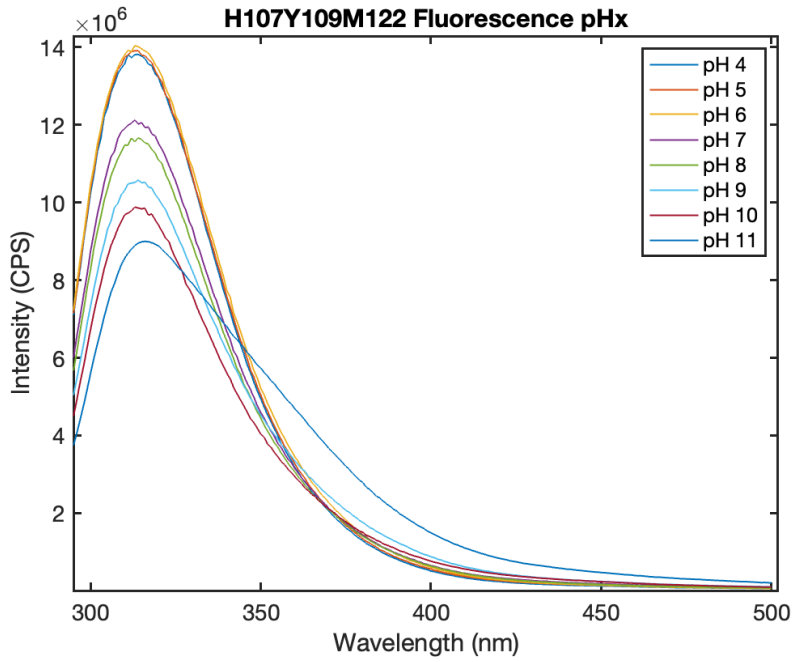

Figure 54. **Raw experimental data of 65 µM His107Tyr109Met122 (His = H, Tyr = Y, Met = M) fluorescence at a pH range from 4-11 in 50 mM NaP_i.**

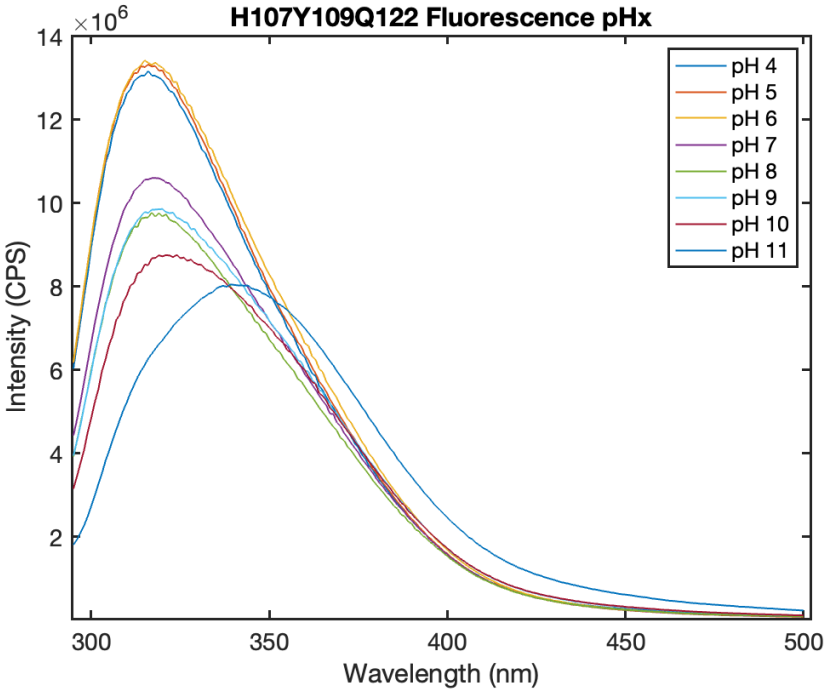

Figure 55. **Raw experimental data of 65 µM His107Tyr109Gln122 (His = H, Tyr = Y, Gln = Q) fluorescence at a pH range from 4-11 in 50 mM NaPi.**

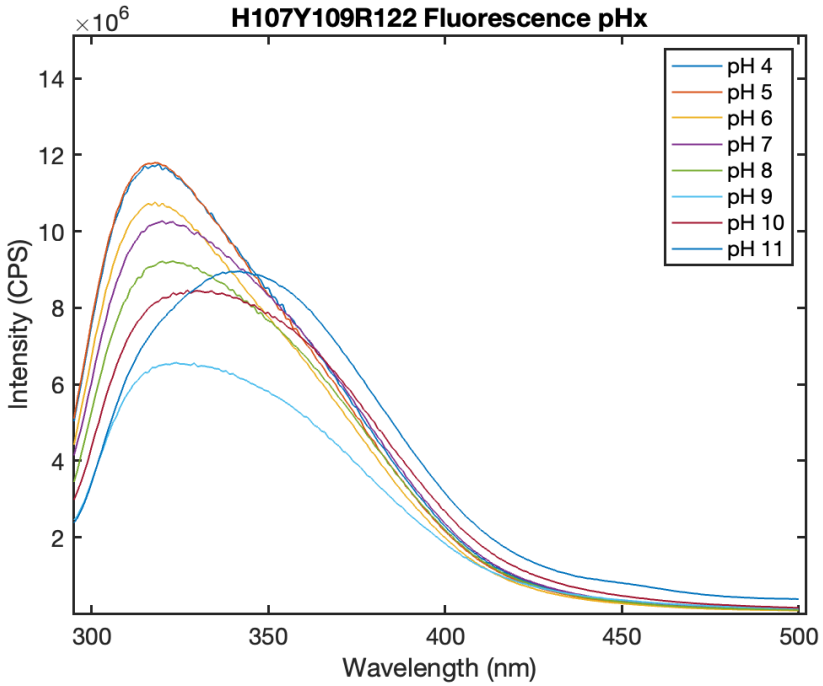

Figure 56. Raw experimental data of 65 µM His107Tyr109Arg122 (His = H, Tyr = Y, Arg = R) fluorescence at a pH range from 4-11 in 50 mM NaP_i.

It is expected that as the pH increases, a higher proportion of Tyr would be converted to $TyrO^-$ and this is seen in all three spectra, although less identifiable for the Met122 variant. Both the Arg122 and Gln122 variants display an increase in $TyrO^-$ fluorescence at more basic pH values, supporting the idea that less protonated Tyr is present at higher pH. Due to this idea, and the observation that Met122 also suffers a loss in fluorescence intensity at 313-315 nm at higher pH, $TyrO^-$ formation likely still occurs when the microenvironment contains a Met residue, but to a lesser extent, and the absence of $TyrO^-$ fluorescence may instead be quenched by the Met122 residue. $TyrO^-$ quenching is not widely discussed in the literature and mechanisms into possible quenching have not been defined. First, it is important to discuss quenching of ground-state Tyr.

Quenching of Tyr109 can occur by interactions with other amino acids (see above), although Met and Gln are not thought to accomplish this due to their inability to act as a hydrogen bond acceptor. In cases where hydrogen bonding is present, the $TyrO^-$ formation is favoured, as suggested by the data shown above with the Arg122 mutant. Other quenching mechanisms exist also such as via the protein backbone and could occur in this case if the phenolic hydroxyl from Tyr109 is oriented closely to the backbone

carbonyl or a nearby residue.[113] It's likely that hydrogen bonding is occurring to some extent as the red-shifted fluorescence maxima suggest. Conversely, quenching of $TyrO^-$ is much less understood, but likely occurs due to stabilization of the anionic species. The quenching residue for $TyrO^-$ may not be Met122, but the introduction of Met into this pocket could introduce structural constraints that change the position of Tyr109. A crystal structure of this protein would aid in defining the structure of the amino acids that participate in this microenvironment.

Ground-state complex formation with phosphate[111] is also a possible quenching mechanism as these experiments were performed in 50 mM phosphate buffer but is unlikely to have any major effect on the results presented here. In the case that complexation occurs, higher phosphate concentrations decrease Tyr emission and increases emission at ~345 nm, favouring the formation of either $TyrO^-$ or a new Tyr-phosphate species.[111] This is similar to the results seen above, although a constant phosphate concentration would overcome this effect. Monitoring the π-π* absorption band would determine whether this complexation is occurring as a distinct red-shift in the absorbance maximum has been reported previously.[111] It is possible that a Tyr-phosphate species is present in this set of experiments and, unfortunately, the absorbances were not collected across the same pH range but could be used to probe this potential effect, even against the same protein in a phosphate-deficient buffer. Furthermore, it is unlikely for any notable change in the absorbance spectrum across these experiments to occur as the phosphate concentration remains unchanged. Although a Tyr-phosphate species may be present, the same fluorescence would be seen across all pH spectra and would not explain the changes seen in these emission spectra.

At pH 11, the Tyr109 emission maximum for the Met122 variant is recorded at 315 nm, suggesting that ground-state Tyr is still the predominant species. This is unexpected as the pK_a for ground- and excited-state Tyr is below 11,[111,209] therefore, $TyrO^-$ should be the most prominent emitting species in the sample. This suggests that protonated Tyr is still present in this sample. This can be explained by either (1) an increase in the pK_a of the phenolic hydroxyl or (2) Met122 reducing exposure of Tyr109 to the solvent, thus, it would be less susceptible to pH effects. Other experiments are needed to fully elucidate this and will be discussed in the sections to follow.

4.2.6. Possible pK_a Changes to Tyr109

Perturbation of a species' pK_a can be due to factors such as changes to the electron density and/or hydrogen bonding microenvironment. Generally, the pK_a is affected if a neighbouring group can stabilize or destabilize another ionizable species.[223] In this work, it is proposed that the pK_a of the phenolic hydroxyl group on Tyr109 could be raised by the introduction of nearby Met122. For a pK_a to increase, Met122 must stabilize Tyr over $TyrO^-$ as the neutral species needs to be favoured over the deprotonated anion. This could occur through different methods, and it is unknown as to which is the most likely to occur in this system. Considering that the sulfur from Met122 has a slight negatively charged dipole, it could exhibit electron donating properties. This would cause an increase in electron density at the aromatic ring in Tyr and decrease the likelihood for deprotonation of the phenolic hydroxyl.[223] Hydrogen bonding may also play a role such that if the phenolic hydroxyl experiences a hydrogen bonding interaction, the pK_a may decrease.[224] This would help to explain why $TyrO^-$ fluorescence is most easily observed for the Arg122 mutant. However, an investigation of the other amino acids in this microenvironment is important, and hydrogen bonding does not provide an explanation for the potential increase in pK_a of Tyr109 in the Met122 variant although the presence of ground-state Tyr is evident.

4.2.7. Tyr109 Solvent Exposure

The pH dependency on $TyrO^-$ formation seen in the fluorescence spectra presented above could also be due to the influence of solvent on the protonation state of Tyr109. If Tyr109 in the Met122 is less solvent exposed due to structural changes imposed by the point mutation, the pH of the microenvironment may be different than the external environment surrounding the protein. This would explain why Tyr fluorescence is still the prominent emitting species in the Met122 variant. Although more cannot be said about this without structural studies being performed, it is interesting to note that a buried Tyr residue may not be affected by solvent changes and could explain how protein's fine-tune protonation and deprotonation of Tyr residues. However, other techniques were used to support the findings from these fluorescence results, and these include cyclic voltammetry (CV), differential pulse voltammetry (DPV), and time-resolved TA spectroscopy.

4.2.8. Reduction Potential Determination

Biological electrochemistry allows for the determination of formal reduction potentials (E_p) of a range of redox-active motifs within proteins. This can range from specific amino acids to metal centers within metalloproteins. In the mutations presented in this chapter, both the electrochemical potential for the Cu(II/I) redox couple and that for Tyr can be measured. In these experiments, the reduction potential of Cu(II/I) remains unchanged from all-Phe azurin (E_p = 0.3 V), where all other residues are wild type.[135] This is expected as residue 122 is not a coordinating residue. Likewise, position 122 does not affect secondary-sphere interactions involving the Cu ion, which is unlike other mutations that have been reported for blue-copper proteins.[160]

4.2.9. Investigating Reduction Potentials with Cyclic Voltammetry

Two forms of voltammetry were used to assess formal reduction potentials for Cu and Tyr in the azurins studied here: CV and DPV. A more detailed description of the basics of these techniques can be found in Chapter 1. All variants were studied across a pH range of 5-9 and these data are shown in Figure 57, Figure 58**,** Figure 59, Figure 60, and summarized in Table 5, below. The pH values of 4, 10, and 11 were omitted to match the pH range for the TA experiments outlined in section 4.2.12. In all cases, a reversible CV wave is observed in the CV for the Cu(II/I) couple at 0.3 V. This is consistent with reported Cu(II/I) redox couples for azurin. The cyclic voltammograms for Gln122 and Arg122 only show Tyr109 oxidation at potentials in the 0.8-1 V region with no wave observed in the reverse direction (i.e., reduction of the radical). Met122 displays similar behaviour such that there is no reversibility in the Tyr109 redox couple, however, pH 5 does show a small wave at about 0.9 V. Although not presented here, multiple scans of this sample revealed the loss of this peak suggesting that an irreversible chemical modification of Tyr109, or its radical, occurs. Irreversible reactions of tyrosine radicals are well known.[225,226]

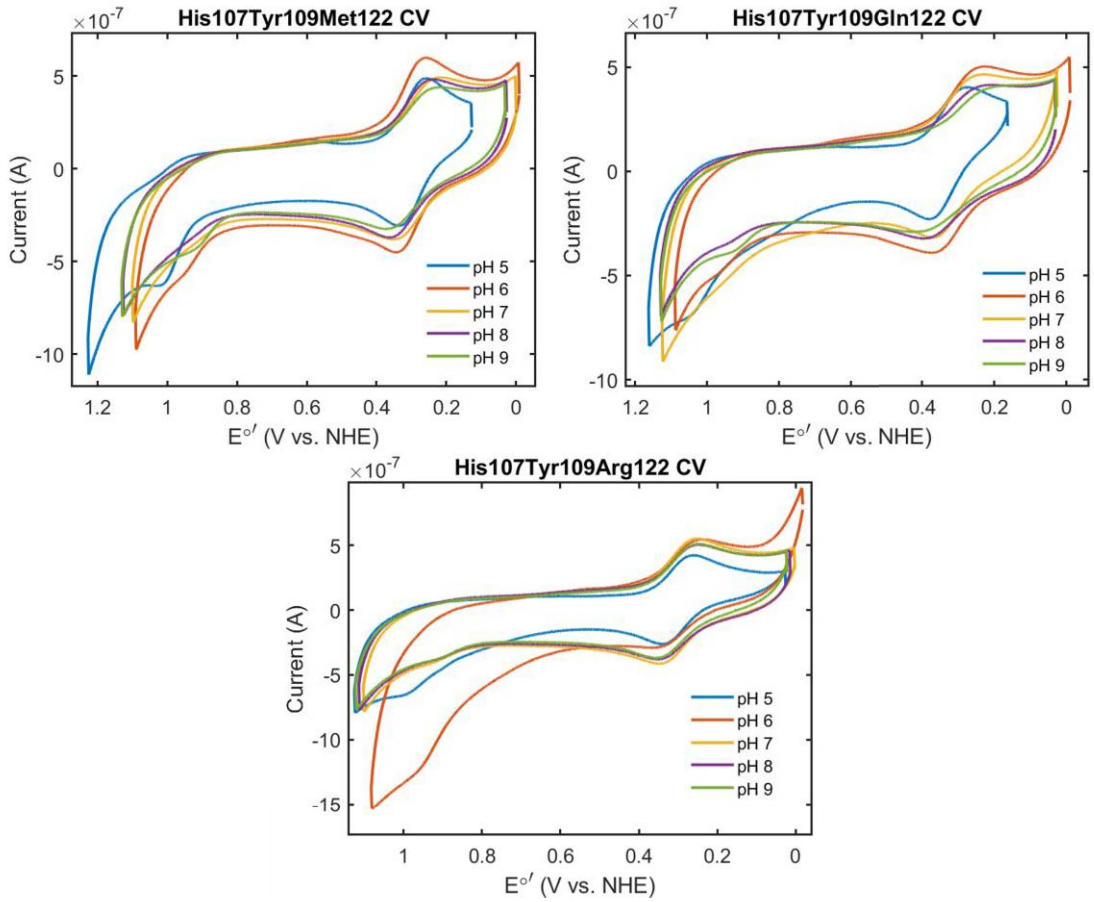

Figure 57. Cyclic voltammograms of each of the three mutants (Met122, Gln122, and Arg122). Protein concentrations were 100 µM in 100 mM NaOAc at the respective pH. A more detailed description of experimental conditions can be found in section 4.4.5.

4.2.10. Investigating Reduction Potentials with Differential Pulse Voltammetry

Although not easily observable in the cyclic voltammograms presented above, the Tyr109 reduction potential shifts to less positive potentials as pH increases. DPV allows this to be seen more clearly (Figure 58, Figure 59, and Figure 60), however, CV can be used to confirm a similar trend. The Tyr109 reduction potentials from the DPV scans are reported in Table 5. More specifically, the right panels that focus on the Tyr109 reduction potentials show a clear shift to less positive potentials as the pH increases from pH 5-9. A plateau is observed at pH 8 and 9, suggesting that at more basic pH values, Tyr109 is more easily oxidizable until it reaches a maximum. This is expected as Tyr oxidation requires an initial deprotonation from Tyr to $TyrO^-$, and at higher pH, we see that $TyrO^-$ formation is more favourable. Likewise, Tyr109 emission reinforces this result. More basic

pH values favour $TyrO^-$ formation as seen in the red-shifted emission spectra from the previous section.

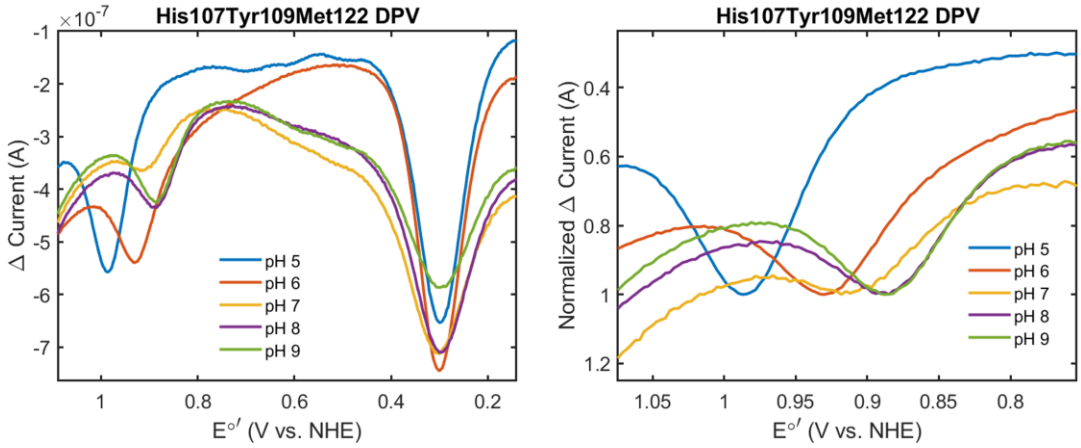

Figure 58. **Full DPV of Met122 in 100 mM NaOAc at respective pH values (left). Zoom of Tyr redox peaks normalized to 1 for easier visualization of the decrease in E_p as pH increases (right). Protein concentrations were 100 µM for both plots.**

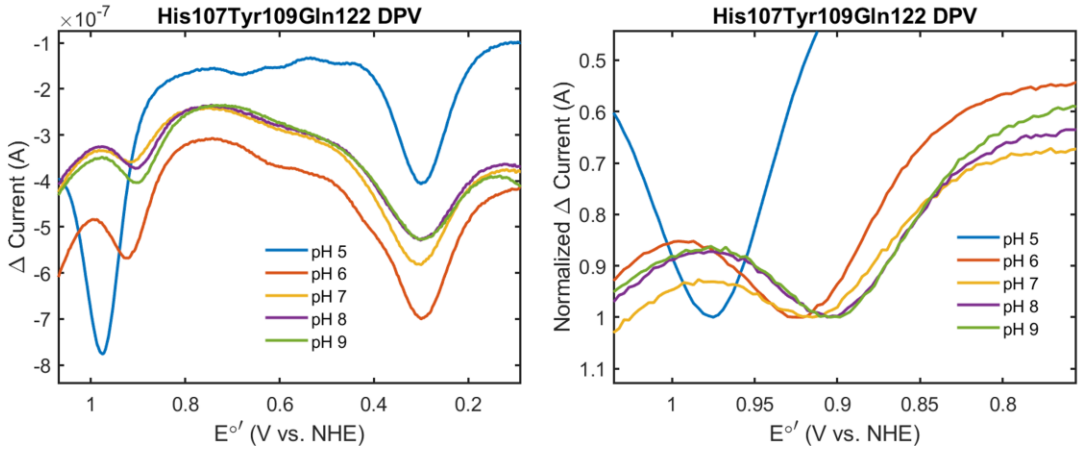

Figure 59. **Full DPV of Gln122 in 100 mM NaOAc at respective pH values (left). Zoom of Tyr redox peaks normalized to 1 for easier visualization of the decrease in E_p as pH increases (right). Protein concentrations were 100 µM for both plots.**

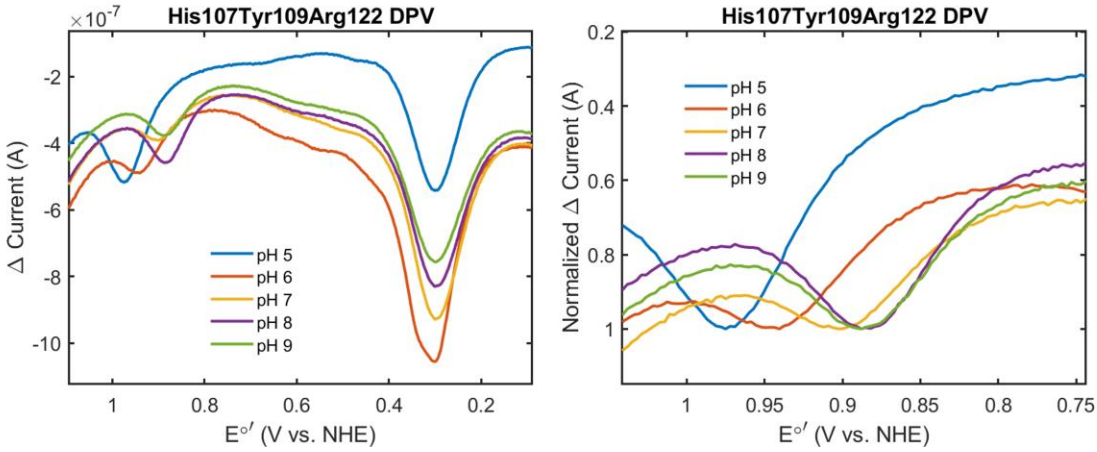

Figure 60. **Full DPV of Arg122 in 100 mM NaOAc at respective pH values (left). Zoom of Tyr redox peaks normalized to 1 for easier visualization of the decrease in E_p as pH increases (right). Protein concentrations were 100 µM for both plots.**

Table 5. **Experimentally determined E_p values for Tyr across a pH range of 5-9 for all three mutants (Met122, Gln122, and Arg122).**

pH	His107Tyr109Met122 E_p (V versus NHE)	His107Tyr109Gln122 E_p (V versus NHE)	His107Tyr109Arg122 E_p (V versus NHE)
5	0.987	0.975	0.975
6	0.936	0.923	0.941
7	0.918	0.915	0.900
8	0.885	0.906	0.888
9	0.888	0.905	0.888

Some deviations in trends exist when comparing the pH-dependent emission spectra and reduction potentials. However, only the pH range of 5-9 will be considered as the reduction potentials at other pH values were not determined. For the pH 5-9 reduction potentials, the largest change (to be discussed as ΔE_p below) is seen in the Met122 variant (ΔE_p = 0.099 V). This would suggest that the emission maxima should also have a greater red-shift, i.e., the highest concentration of $TyrO^-$. However, this is opposite to what is observed. Based on electrochemical data, $TyrO^-$ formation is occurring, but the stabilization of the anionic $TyrO^-$ affects the emission spectra. The ΔE_p for Gln122 and Arg122 are 0.070 and 0.087 V, respectively. These fit the observed trend for emission with respect to each other as the $\Delta\lambda_{max,\,em}$ is 2 versus 4 nm for Gln122 and Arg122, respectively.

4.2.11. Microenvironment Effects on Tyr109 Reduction Potentials

Comparing ΔE_p between Gln122 and Arg122 variants yields a trend with respect to the microenvironment surrounding Tyr109. A more positively charged microenvironment shows a greater ΔE_p, as does a more polar microenvironment. Arg is one of the most polar amino acids based on its hydrophilicity and positive charge over biological pH of its guanidino group. Gln is considered a polar amino acid, but it is less polar than Arg, due to its neutral (across all pH here) amide side chain. Thus, Gln can give rise to a comparatively less hydrophobic (than Arg) pocket which favours a greater ΔE_p. The magnitude of ΔE_p can also be an indicator of how sensitive Tyr109 is to pH changes, further suggesting that the microenvironment surrounding a Tyr residue, even in these weakly interacting cases, plays a larger role in the oxidation of Tyr redox than previously thought. In contrast, the Met122 variant would create the least polar microenvironment and the most hydrophobic microenvironment over Gln122 and Arg122, however, the ΔE_p is the largest measured of the three, again suggesting that another event is responsible for the lack of $TyrO^-$ emission.

Interestingly, at pH 5, the E_p for Tyr109 in the Met122 variant is greater and appears to be quasi-reversible (in CV scans) versus the Gln122 and Arg122 variants. The higher E_p could be indicative of a higher pK_a for the Tyr109 which would suggest that Tyr109 is harder to oxidize in the Met122 mutant. This would support the lack of $TyrO^-$ emission seen for this protein. Still, in the context of reduction potentials, the Met122 mutant remains an outlier, as it was in the fluorescence studies, and among the research carried out in Chapter 2 and Chapter 3. Further probing of the microenvironment was carried out to determine how ET kinetics would be affected by these changes in polarity, charge, and hydrophobicity. The role of sulfur also is of great interest as it is one of the greatest distinguishing factors between the proteins studied in this chapter.

4.2.12. Transient Absorption Spectroscopy

TA experiments were carried out for all three mutants across a pH range of 5-9. Rate constants (*k*) for oxidation of Cu(I) by Ru(III) were determined using a biexponential fit in MATLAB's curve fitting toolbox for both Ru(III) to Ru(II) (480 nm) reduction and Cu(I) to Cu(II) oxidation (628 nm). The equation used for fitting of the data is shown in $\mathrm{Eq.}\,12$ and experimentally determined rate constants for Ru(III) reduction and Cu(I) oxidation are

summarized in Table 6 and Table 7, respectively. A more detailed description of the fitting will be discussed in the sections to follow. Note that only a small amount of Cu(I) oxidation was observed at pH 5 (Figure 61), however, these data could not be fit to extrapolate a rate constant. This is consistent with what has been observed in a closely related literature report.[135] Raw data for all experiments and their respective fits can be found in Appendix C.

$$y = Aexp(-Bx) + Cexp(-Dx) + E \qquad (Eq.\ 12)$$

4.2.13. Rate Constant Determination for Cu(I) Oxidation by Ru(III)

For Cu(I) oxidation, the variables in Eq. 12 are represented as follows. A represents the preexponential factor for the residual fluorescence due to excited state decay (and quenching), B represents the rate constant for this same process, C represents the preexponential factor for the rate of Cu(I) oxidation, D represents the rate constant for Cu(I) oxidation, and E represents the ending Cu(II) absorbance.

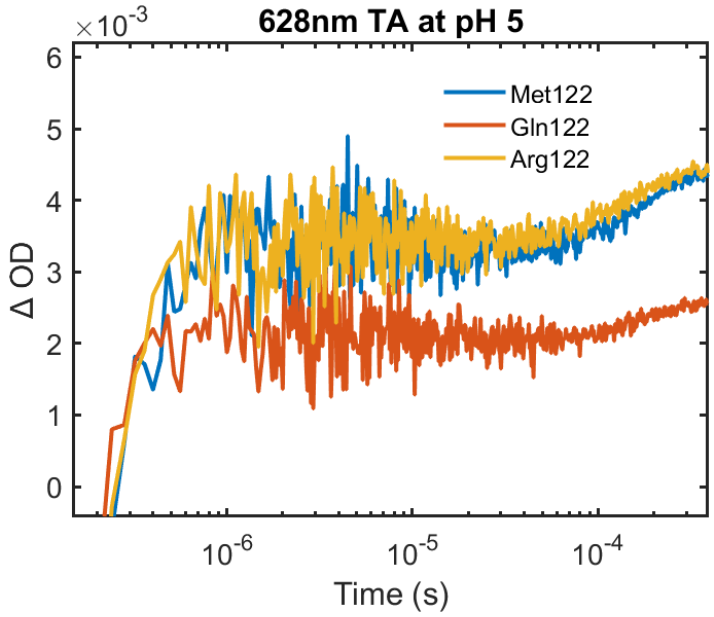

Figure 61. **Raw TA kinetic traces for the oxidation of Cu(I) to Cu(II) in 35 μM Met122 (blue), Gln122 (orange), and Arg122 (yellow) azurin. Experiments were carried out in 100 mM NaCl, 250 mM imidazole, at pH 5. $[Ru(NH_3)_6]^{3+}$ was added to a final concentration of 10 mM. A more detailed description of experimental setup and be found in section 4.4.7.**

In the data presented below for Cu(I) oxidation (Table 6), rate constants for the His107Tyr109Lys122 variant are also reported. These values are taken from the literature[135] and were not replicated in the research carried out in this chapter. Across all variants listed in Table 6, the one that includes Met122 has the fastest Cu(I) oxidation rate from pH 6-9. Gln122 and Arg122 share very similar rate constants across that same pH range, although there is a notable difference (ca. 15%) at pH 6. Furthermore, a clear trend is seen across all three mutants that can be related to each amino acid's properties. Figure 62 depicts the differences in the rate constants outlined below.

Table 6. Experimentally determined Cu(I) oxidation rate constants for three mutant azurins. Experiments were carried out with 35 μM protein in 100 mM NaCl, 250 mM imidazole, at respective pH values. $[Ru(NH_3)_6]^{3+}$ was added to a final concentration of 10 mM. A more detailed description of experimental setup and be found in section 4.4.7.

pH	His107Tyr109Met122 k_{obs} (s^{-1}) log$k$	His107Tyr109Gln122 k_{obs} (s^{-1}) log$k$	His107Tyr109Arg122 k_{obs} (s^{-1}) log$k$	His107Tyr109Lys122[a] k_{obs} (s^{-1}) log$k$[b]
6	$(6.8 \pm 0.53) \times 10^3$ 3.83	$(6.3 \pm 0.58) \times 10^3$ 3.80	$(5.4 \pm 1.09) \times 10^3$ 3.73	$(5.7 \pm 0.3) \times 10^3$ 3.76
7	$(1.23 \pm 0.06) \times 10^4$ 4.09	$(1.07 \pm 0.04) \times 10^4$ 4.03	$(1.12 \pm 0.06) \times 10^4$ 4.05	$(1.2 \pm 0.2) \times 10^4$ 4.08
8	$(1.84 \pm 0.05) \times 10^4$ 4.26	$(1.57 \pm 0.04) \times 10^4$ 4.19	$(1.56 \pm 0.05) \times 10^4$ 4.19	$(1.7 \pm 0.2) \times 10^4$ 4.23
9	$(2.55 \pm 0.06) \times 10^4$ 4.42	$(2.11 \pm 0.05) \times 10^4$ 4.33	$(2.15 \pm 0.06) \times 10^4$ 4.32	$(1.8 \pm 0.2) \times 10^4$ 4.26

[a]Literature values for His107Tyr109Lys122 were taken from reference [135]. [b]The log$k$ values in this column were calculated using the literature values for His107Tyr109Lys122.

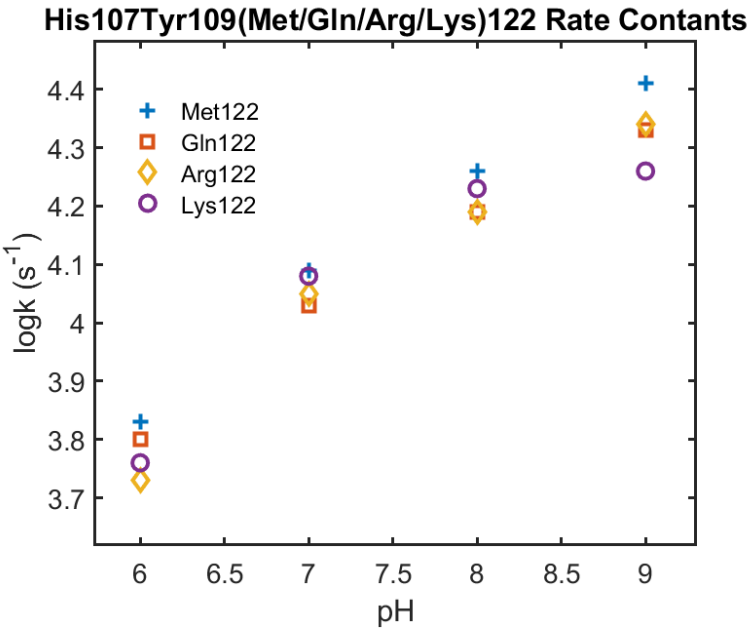

Figure 62. Experimentally determined rate constants from Table 6 for Cu(I) to Cu(II) oxidation of His107Tyr109Met122 (blue crosses), Gln122 (orange squares), Arg122 (yellow diamonds), and Lys122 (purple circles) at their respective pH values. Rate constants are reported as logk (s^{-1}).

Overall, as the pH of each buffer system increases, the rate constants increase as well. This was not a surprising result as this has been previously observed in the literature with the Lys122 mutant and is attributed to the PT of Tyr109 that is required for oxidation to occur.[135] In comparison to the three mutants used in this chapter, Lys and Arg have analogous properties. Both amino acids are polar, positively charged, and the sidechains are similar in size with both containing amine functional groups. Due to this, it was expected that the behaviours of both should be similar. Across the same pH range, rate constants for Arg122 are most closely related to Lys122, although Gln122 is comparable except at pH 6. Structurally, Gln122 contains an amine in its sidechain which likely attributes to more closely related values over Met122, although Gln122 is neutral overall.

4.2.14. Rate Constant Determination for Ru(III) Reduction

Experimentally determined rate constants for the reduction of Ru(III) to Ru(II) also were determined as described above. In general, the Cu(I) oxidation rate constants provide a better measure of net hopping kinetics since formation of Cu(II) relies on the formation of the Tyr109 radical. In contrast, reduction of Ru(III) can occur through several

processes, including intermolecular reactions between two proteins. As such, the Ru(III) decay rate constants are often faster than Cu(I) oxidation in these labeled azurin systems. The rate constants are set out in Table 7. Note that Lys122 is not listed here as those values were not explicitly reported in the literature, though the Try109Lys122 system is known.[135] As stated above, the known Lys122 variant was not used for the experiments carried out in this chapter, therefore, only Met122, Gln122, and Arg122 will be discussed in the context of Ru(III) reduction.

Table 7. **Experimentally determined Ru(III) reduction rate constants for three mutant azurins. Experiments were carried out with 35 µM protein in 100 mM NaCl, 250 mM imidazole, at respective pH values. $[Ru(NH_3)_6]^{3+}$ was added to a final concentration of 10 mM. A more detailed description of experimental setup and be found in section 4.4.7.**

pH	His107Tyr109Met122 k_{obs} (s^{-1}) log$k$	His107Tyr109Gln122 k_{obs} (s^{-1}) log$k$	His107Tyr109Arg122 k_{obs} (s^{-1}) log$k$
5	$(1.26 \pm 0.03) \times 10^4$ 4.10	$(1.23 \pm 0.02) \times 10^4$ 4.09	$(1.35 \pm 0.02) \times 10^4$ 4.13
6	$(1.75 \pm 0.02) \times 10^4$ 4.24	$(1.69 \pm 0.02) \times 10^4$ 4.23	$(1.45 \pm 0.02) \times 10^4$ 4.16
7	$(5.68 \pm 0.08) \times 10^4$ 4.76	$(2.91 \pm 0.07) \times 10^4$ 4.46	$(3.5 \pm 0.06) \times 10^4$ 4.54
8	$(5.44 \pm 0.08) \times 10^4$ 4.73	$(3.66 \pm 0.06) \times 10^4$ 4.56	$(4.71 \pm 0.08) \times 10^4$ 4.67
9	$(4.61 \pm 0.06) \times 10^4$ 4.66	$(4.85 \pm 0.06) \times 10^4$ 4.69	$(5.39 \pm 0.06) \times 10^4$ 4.73

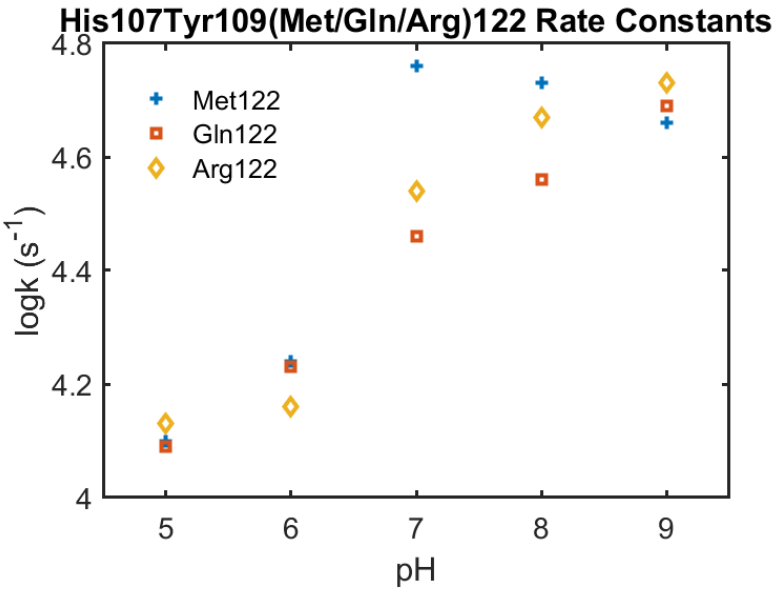

Figure 63. Experimentally determined rate constants from Table 6 for Ru(III) to Ru(II) reduction of His107Tyr109Met122 (blue crosses), Gln122 (orange squares), and Arg122 (yellow diamonds), at their respective pH values. Rate constants are reported as logk (s^{-1}).

4.2.15. (Met/Gln/Arg)122 Interactions with Tyr109

Previous work determined that Tyr-mediated ET likely proceeds via a stepwise proton transfer-electron transfer (PT-ET) reaction mechanism.[135,227,228] This means that in the proteins described here, deprotonation of Tyr109 must occur before an electron can be transferred. In these instances, the deprotonation step is rate limiting and the observed rate constants show a pH dependence that connects the tyrosine side chain pK_a and the solution pH. These reactions can be disrupted by several factors. First, strong hydrogen bonding can influence deprotonation kinetics, or even lead to concerted redox reactions where oxidation and deprotonation occur in a single kinetic step.[135,227,228] This is a comparatively rare case and is more common in embedded sites (e.g., photosystem II).[229] In the systems described here, other effects are more likely. Specifically, the positively charged sidechain of Arg122 should favour Tyr deprotonation to yield an arginine-guanidinium•tyrosine-phenolate ion pair. Such a case has been hinted at in a related azurin system when tyrosine is replaced with nitrotyrosine.[31] Similarly, the polar Gln also is likely to favour Tyr deprotonation, but to a lesser extent. Hydrophobic Met should disfavour Tyr deprotonation.

The mutants used in this chapter can be considered as inducing an increasingly more polar microenvironment around Tyr109. Based on their hydrophobicity, Met122 is considered the least polar of the three, followed by Gln122, and then Arg122. Consequently, rate constants fit this trend such that a decrease in rate constant is observed as the polarity of the microenvironment increases. In an increasingly polar microenvironment, the tendency for hydrogen bonding interactions to occur would also increase. The ET reaction studied in this chapter must proceed via the $TyrO^-$ form of Tyr109 and can be considered as rate-limited by the PT. This means that Cu(I) oxidation should be independent of the conversion of Tyr to $TyrO^-$, unless no formation of $TyrO^-$ occurs. For Arg122, the positively charged sidechain would likely display a strong hydrogen bonding effect due to the positively charged amine sidechain and the negatively charged oxygen on $TyrO^-$. Similarly, hydrogen bonding could also be observed between the Gln122 sidechain and $TyrO^-$, although Gln122 is neutral overall. There is likely a repulsive interaction that occurs between the sulfur-containing Met122 and $TyrO^-$, thus, explaining an increase in rate constant is observed over Gln122 and Arg122.

In comparison to the fluorescence data presented in section 4.2.5, the Met122 variant shows little evidence of $TyrO^-$ emission from pH 5-9 (referring only to the pH range used for TA kinetics). This suggests that there should be no Cu(I) oxidation as no reaction would occur without $TyrO^-$ formation. The TA data reported above contradicts this because clear evidence of Met122 increasing the rate constant for Cu(I) oxidation is observed. Likewise, the experimentally determined reduction potentials for Tyr109 in the Met122 derivative are indicative that Tyr109 is oxidized more easily as pH increases. In all, these observations suggest that deprotonation of Tyr is occurring across the pH range, but a different mechanism is preventing $TyrO^-$ emission. It could also be considered that the $TyrO^-$ intermediate may be too short-lived to observe any emission, and the nearby Met is participating in this phenomenon.

4.3. Summary and Future Directions

4.3.1. Tyr109 Fluorescence is Influenced by the Protein's Microenvironment

It is clear that the fluorescence properties of Tyr109 is not only influenced by the pH of the surrounding solution but also the nearby amino acids to the Tyr residue. In the

Arg122 mutant, Tyr109 fluorescence is the most red-shifted and the most sensitive to pH changes, displaying $TyrO^-$ emission at lower pH values than the reported pK_a for Tyr. The same can be seen for the Gln122 mutant, although the effects are less prominent and $TyrO^-$ emission is not observed until the surrounding solution pH is 9 or 10. The Met122 mutant shows no $TyrO^-$ emission until a pH of 11 is reached and even at this pH, little $TyrO^-$ emission is observed.

4.3.2. Tyr109 Reduction Potentials are Influenced by the Protein's Microenvironment

There is a clear pH dependency on Tyr109 reduction potentials in the protein's presented here. When the solution pH is more basic, reduction potentials decrease. In turn, this suggests that the phenolic hydroxyl is more easily oxidizable at more basic pH values. The ΔE_p across the pH series for Tyr109 in the Met122, Arg122, and Gln122 mutants are 0.099 V, 0.087 V, and 0.070 V, respectively. This was unexpected as the ΔE_p should be consistent with the $\Delta\lambda_{max,\,em}$, but it is seen that the Met122 $\Delta\lambda_{max,\,em}$, is negligible across the pH range of 5-9, suggesting that Tyr109 oxidation is still occurring in this sample.

4.3.3. Rate Constants are Influenced by the Protein's Microenvironment

As the solution pH increases, ET rate constants for Cu(I) oxidation and Ru(III) reduction increase. This is congruent with the decrease in E_p values, suggesting a more easily oxidizable phenolic hydroxyl on Tyr109, which is required for ET through these systems. Cu(I) oxidation is a more important metric for evaluating the ET properties of Tyr109 since Ru(III) reduction may occur through different reaction pathways (e.g., bimolecular reactions between proteins or charge recombination with the exogenous quencher). Rate constants for Cu(I) oxidation were determined and it was observed that the Met122 mutant displays the largest rate constant

4.3.4. Future Work: Crystals, Absorption, pK_a Determination, and NMR

An important aspect to the work presented in this chapter is solving the crystal structures for each protein. Solving the crystal structures for each system would determine

the residues that surround Tyr109. This would give an accurate representation of the microenvironment, overcoming the assumption that the orientation of all other residues remains unchanged.

An added experiment that would complement the fluorescence work in this chapter is investigating changes to the absorption pattern across the same pH range. If the phenolic hydroxyl group undergoes any hydrogen bonding in the ground-state, a red-shift to the Tyr absorption spectrum will be seen.[113]

Determining Tyr109 pK_a values is an experiment that should be carried out and should be carried out for all research that is concerned with microenvironment effects on Tyr residues. Methods for accomplishing this are straightforward and have been previously described.[135] Although it has already been proposed in the work described above, this would provide evidence for $TyrO^-$ formation in the Met122 mutant and would determine the pH at which it occurs. In the case that Tyr109 oxidation is evident at higher pH values, protein unfolding may limit the extent of this experiment.

4.4. Experimental

All reagents and materials were obtained from Sigma-Aldrich and not purified further unless noted. Luria-Bertani (LB) broth miller was purchased from BioShop Canada and prepared according to the manufacturer. Water used was from a Barnstead EASYpure system (18 MΩ cm^{-1}). UV-Visible spectrophotometry was carried out using a Cary 100-Bio spectrophotometer. MALDI mass spectrometry was carried out on a Bruker microflex LT MALDI Biotyper mass spectrometer. All laser irradiation was carried out using a home-built spectrometer containing a Continuum Surelite SLI-10 (Nd:YAG) laser, a Continuum Surelite OPO, a 75 W Xe arc lamp, and a home-built detection system.

4.4.1. Site-Directed Mutagenesis

A plasmid containing Phe mutations for all Trp and Tyr residues within azurin was a gift from Harry B. Gray and John H. Richards (California Institute of Technology). The Phe109Tyr mutation was added followed by Lys122Arg/Met/Glu/Gln so that four distinct protein scaffolds could be expressed (His107Tyr109Arg122, His107Tyr109Met122, His107Tyr109Glu122, and His107Tyr109Gln122). All mutations were introduced using

site-directed mutagenic PCR using standard protocols.[180] DNA primers were purchased from Eurofins Genomics. Q5 DNA polymerase and DpnI enzyme were purchased from NEB. PCR products were transformed into competent DH5α *E. coli* cells obtained from NEB and selected using ampicillin-containing agar plates. Colonies were grown overnight at 37 °C and single colonies selected for liquid cultures in LB broth containing 100 μg/mL of ampicillin. Plasmid DNA was extracted and purified using a QIAprep Spin Miniprep Kit purchased from Qiagen and following the standard protocols provided. Purified plasmids were sequenced by Eurofins Genomics using their sequencing service. Plasmid purities and concentrations were obtained using a NanoDrop ND-1000 spectrophotometer.

4.4.2. Primer Design

Forward and reverse primers were designed to contain a single point mutation (Phe109Tyr and Lys122Arg/Met/Glu/Gln). Bolded nucleotide bases represent where the mutation was added. Primers were designed as follows:

Phe109Tyr Forward: 5'-CACTTC**TAT**TTCTTCTGCACTTTCCCGGGTCAC-3'

Phe109Tyr Reverse: 5'-GCAGAAGAA**ATA**GAAGTGTTCACCTTCTTTAAGCTTGG-3'

Lys122Arg Forward: 5'-CACTGATG**CGT**GGTACCCTGACTCTGAAATAG-3'

Lys122Arg Reverse: 5'-GTACC**ACG**CATCAGTGCGGAGTGACC-3'

Lys122Met Forward: 5'-CACTGATG**ATG**GGTACCCTGACTCTGAAATAG-3'

Lys122Met Reverse: 5'-GTACC**CAT**CATCAGTGCGGAGTGACC-3'

Lys122Glu Forward: 5'-ACTGATG**GAA**GGTACCCTGACTCTGAAATAG-3'

Lys122Glu Reverse: 5'-GTACC**TTC**CATCAGTGCGGAGTGACC-3'

Lys122Gln Forward: 5'-CTGATG**CAA**GGTACCCTGACTCTGAAATAGAGATCC-3'

Lys122Gln Reverse: 5'-GTACC**TTG**CATCAGTGCGGAGTGACC-3'

4.4.3. Protein Expression and Purification

Plasmids were transformed into competent BL21(DE3) *E. coli* cells obtained from NEB and selected using ampicillin-containing agar plates. Colonies were grown overnight at 37 °C and single colonies selected for liquid starter cultures in LB broth containing 100 µg/mL of ampicillin. Starter cultures were grown at 37 °C with 180 rpm of shaking for 6 hours. Overnight 1 L expression cultures were prepared by adding a small portion of starter culture (~ 3mL) into LB broth containing 100 µg/mL of ampicillin and 0.4% glycerol. Overnight expression cultures were grown at 37 °C with 180 rpm of shaking. Cells were then pelleted by centrifugation at 4000 rpm using a Beckman Avanti J-26XP centrifuge in a JLA 10.5000 rotor for 20 minutes for 20 minutes. Cell pellets were resuspended in osmotic shock buffer (50 mM Tris, 1 mM EDTA, 20% sucrose, pH 8.1) and rest on ice for 20 minutes. Cell pellets were then obtained by centrifugation at 7000 rpm using a Beckman Avanti J-26XP centrifuge in a JA 25.50 rotor for 20 minutes. Pellets were resuspended in 500 µM $MgCl_2$ and rest on ice for 20 minutes. Proteins were isolated by centrifugation at 12000 rpm using a Beckman Avanti J-26XP centrifuge in a JA 25.50 rotor for 20 minutes. Supernatants were collected and 100 mM $CuSO_4$ and 500 mM NaOAc (pH 4.5) were added dropwise. These mixtures were incubated overnight at 37 °C to promote Cu(II) uptake by apo-azurin. Acid precipitated proteins were removed by centrifugation at 12000 rpm using a Beckman Avanti J-26XP centrifuge in a JA 25.50 rotor for 20 minutes. The resulting supernatants were collected and purified on a CM Sepharose column using a NaOAc concentration gradient. Protein purities and concentrations were determined spectrophotometrically using reported extinction coefficients (ε_{628} = 5600 M^{-1} cm^{-1}).[42,160]

4.4.4. Tyr Fluorescence

Fluorescence experiments were carried out using a Horiba Jobin-Yvon Fluorolog. 65 µM samples were prepared in 50 mM NaP_i at various pH values (4-11). Samples were placed into air-free cuvettes and deoxygenated with 15-20 pump-backfill cycles using N_2. Excitation was achieved using 280 nm light and spectra were recorded from 295 – 500 nm to monitor for Tyr and/or $TyrO^-$ fluorescence. 10 scans were performed per sample and emission maxima were determined by averaging each series.

4.4.5. Cyclic Voltammetry and Differential Pulse Voltammetry

Electrochemical experiments were carried out using a CH Instruments 6171B potentiostat. A standard three-electrode setup was used containing a basal-plane graphite (BPG) working electrode, and platinum wire counter electrode, and an AgCl/Ag reference electrode with all samples being reported versus NHE. Protein samples (100 μM) were prepared in 100 mM NaOAc at pH values ranging from 5 to 9. The BPG electrode surface were prepared by thoroughly washing with deionized H_2O, lightly coating with MicroPolish Powder (CH Instruments), and polishing using an microfibre polishing pad. CV spectra were collected using a 0.02, 0.04, and 0.1 V/s scan rate, however, the 0.02 V/s data are the only scans shown here unless otherwise noted. The scan window for DPV was -0.1 to 1 V at 0.003 V increments with a 0.05 V amplitude. The pulse and sample width were 0.1 and 0.02 s, respectively. The pulse period was 0.5 s.

4.4.6. Photosensitizer Labeling of Azurins

Labeled azurins were obtained by adding 1.1 equivalents of ($[Ru(bpy)_2CO_3]^{2+}$) to a solution of azurin in 300 mM $NaHCO_3$ (pH 7.5). It is important that pH adjustments are not done with Cl^- containing solutions. These reaction mixtures were incubated overnight in the dark at room temperature with gentle agitation. FPLC was carried out using a HiTrap IMAC FF column that was obtained from GE Healthcare (now called Cytiva Life Sciences) and manually metalated with Cu^{2+}. Reaction mixture was exchanged into binding buffer (1 M NaCl, 10 mM Tris, pH 8) and loaded to the previously equilibrated column under the same buffer system. Unmodified azurins bound to the column while ruthenium-modified azurins (Ru-His107Tyr109Arg122, Ru-His107Tyr109Met122, Ru-His107Tyr109Glu122, and Ru-His107Tyr109Gln122) elute with the binding buffer wash. Unlabeled azurins were eluted using elution buffer (1 M NH_4Cl, 20 mM NaP_i, pH 7.8). Fractions were collected and monitored by UV-visible spectrophotometry to pool correct fractions together. Concentrations of each Ru-modified azurin was calculated spectrophotometrically using reported extinction coefficients (ε_{628} = 5,600 M^{-1} cm^{-1} for Cu(II) and ε_{500} = 10,000 M^{-1} cm^{-1} for Ru(II)).[182] Both proteins were exchanged into storage buffer (500 mM imidazole, 1 mM $CuSO_4$, 100 mM NaCl, pH 7.5) and incubated over the weekend. Long term storage is carried out in this buffer.

4.4.7. Transient Absorption Spectroscopy

All laser experiments in Chapter 5 were carried out with a 480 nm excitation with 6 mJ/pulse energy. Samples were reduced using L-ascorbic acid and then desalted into 250 mM imidazole, 100 mM NaCl at various pH values (5-9) for a final concentration of 35 μM. Sample volumes were 1.5 mL and special air-free cuvettes were custom made by the SFU Glass Shop to allow for deoxygenation. 15-20 pump-backfill cycles using N_2 were performed to remove O_2 from the sample and cuvette. Prior to TA experiments, time-dependent fluorescence scans were performed and spectra were collected at 670 nm on a 2 μs timescale where N = 50 and groups = 5. The quencher $[Ru(NH_3)_6]^{3+}$, dissolved in 250 mM imidazole, 100 mM NaCl at the required pH, was added to a final concentration of 10 mM to each sample as an exogenous quencher. 15-20 pump-backfill cycles using N_2 were performed again to remove O_2 from the sample and cuvette. Fluorescence experiments were repeated to ensure fluorescence quenching. TA was then carried out on an 800 μs timescale where N = 100 and groups = 10. TA spectra were collected at 490 nm and 628 nm for Ru(II) reduction and Cu(I) oxidation, respectively. Data was plotted and analyzed using MATLAB and MATLAB's Curve Fitting Toolbox. Rate constants were determined using a two-exponential fit. The first exponential function describes signal from residual fluorescence due to excited state decay (and quenching) of the Ru photosensitizer and the second function describes the Cu(I) oxidation event. For the 490 nm (Ru traces), the first function is for excited state decay of *Ru(II) and the second function is for Ru(III).

Chapter 5. Clustering of Aromatic Amino Acid Residues Around Methionine in Proteins††

5.1. Introduction

Noncovalent interactions, such as hydrogen bonding, ionic interactions (i.e., salt bridges), and the hydrophobic effect play many roles in the three-dimensional structure of a protein,[230,231] interprotein interactions,[232] and protein-ligand binding.[233] The intramolecular forces at play in proteins are of great interest, and the increase in submissions to the PDB has allowed for the details of these interactions to be systematically surveyed in a wide variety of macromolecules. Furthermore, new ideas have emerged surrounding aromatic amino acid residues and how they might affect protein structure and function. These include interactions such as π-stacking,[234] cation-π,[231,235] anion-π,[236] and S-π interactions.[237] Understanding this array of interactions is of great importance for rationalizing protein structure and function.

5.1.1. The 3-Bridge Cluster

Previously, S-π interactions have been surveyed in metalloproteins[29] and S-π interactions that involve two aromatic groups interacting with both lone pairs of sulfur.[90] During the course of those studies we noticed a small but significant type of interaction where three aromatics clustered around the thioether of Met. At the time, we thought that these "3-bridge" clusters were outliers given the comparatively small size of sulfur (with respect to the aromatic groups), which we took as prohibitive in terms of interactions with three aromatic groups. However, ongoing work in our lab showed that such structures appeared in diverse proteins with different functions, and our focus solely on sulfur neglected other interactions of the Met-thioether. One such example is shown in Figure 64, where a bridging interaction exists between Trp191, Met230, and Tyr187 in yeast cytochrome *c* peroxidase (C*c*P).[95] In addition, Met231 forms a bridging interaction with Trp191 and Phe202. Close inspection of the structure shows an interaction between the

†† This chapter is modified from Gibbs, C. A.; Weber, D. S.; Warren, J. J. Clustering of Aromatic Amino Acid Residues around Methionine in Proteins. *Biomolecules* **2022**, *12* (1), 1–6. https://doi.org/10.3390/biom12010006. J.J.W. conceived the research, assisted in computations, and co-wrote the paper. D.S.W. wrote the bioinformatics code. C.A.G. wrote the paper, analyzed the data, and carried out calculations.

Met-CH_2 and Trp211. Oxidation of either Met in the apo-protein alters the ability of the protein to make Compound I (the oxidized C*c*P intermediate),[93] and mutations alter the properties and stability of the Trp191 radical cation.[238,239] This example using C*c*P demonstrates some potential roles of Met-aro clusters in protein structure and function. Here, we provide a detailed analysis of the incidence and composition of 3-bridge clusters in structurally characterized proteins.

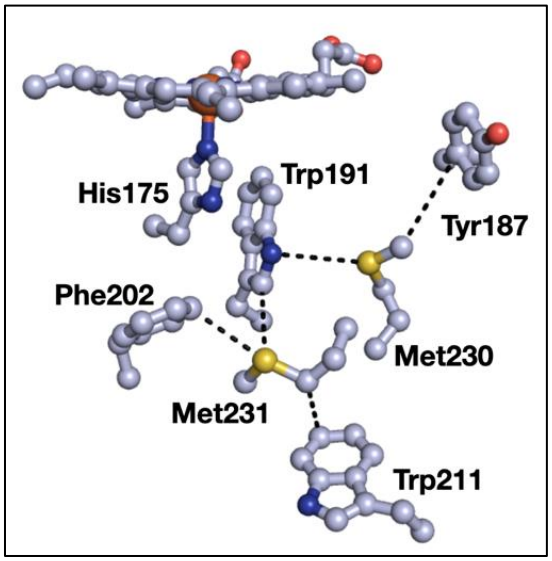

Figure 64. Examples of Met-aro interactions in yeast cytochrome *c* peroxidase. Dashed lines indicate points of close contact and distances are from 3.4 to 4.4 Å. Red = oxygen, blue = nitrogen, gray = carbon, yellow = sulfur. The backbone residues are omitted for clarity. PDB ID: 2CYP.[95]

In general, the sulfur-containing amino acid residues, Met and Cys, can stabilize protein microstructures through noncovalent interactions that involve a Met or Cys sulfur and an aromatic ring.[83] It is known that alternating chains of sulfur-containing amino acid residues with Trp, Tyr, or Phe impact the structural properties of proteins and it is suggested that the redox properties of proteins may also be affected.[82–84] Small peptide models show a net stabilizing effect (ca. 1 kcal mol^{-1}) of Met-aro interactions[86] and an extensive bioinformatics and computational analysis of membrane proteins show that several different Met-aro interactions are favourable.[87] In addition, bimolecular small molecule models of S-π interactions display advantageous enthalpies of formation of ~1 kcal mol^{-1} for the closed shell species.[78,82] S-π interactions also can confer unique redox and optical properties of small molecule models in their oxidized forms.[78–80] The distribution and properties of these interactions prompted us to investigate Met-aro clusters in greater detail, as described below.

5.2. Results

A total of 33,819 proteins were analyzed. The 3-bridge interaction was found 4,751 times in 4,093 unique structures (or 12% of the non-redundant dataset). A complete list of PDB codes and interacting amino acid residues are available online.‡‡ Most proteins showed one cluster, but there were examples of proteins with three or more 3-bridge clusters. About 48% of interactions were found in proteins without a stated Enzyme Classification (EC) number in their PDB entry; we note that 31% of PDB entries do not have an EC number attributed. The remaining 52% of hits are comprised of the following classifications, where the total percentage PDB-wide is given in parenthesis: 9.3% were EC 1 oxidoreductases (11% of PDB), 13% were EC 2 transferases (21% of PDB), 20.3% were EC 3 hydrolases (27% of PDB), 4.1% were EC 4 lyases (5% of PDB), 2.4% were EC 5 isomerases (2% of PDB), and 3.2% were EC 6 ligases (2% of PDB). No Met-aro clusters were observed for EC 7 translocases (1% of PDB). These data indicate that the Met-aro 3-bridge cluster is widely distributed in different classes of proteins and have about the same overall distribution as protein structures in the PDB.

5.2.1. Frequency, Orientation, and Interactions of 3-Bridge Clusters

The summary of the compositions of the three aromatic residues surrounding a given Met are shown in Figure 65. For reference, Phe has the highest occurrence in the UniProtKB/Swiss-Prot data bank of proteins[240] (3.9%), followed by Tyr (2.9%), and Trp (1.1%). In addition, Met occurs at a frequency of 2.4%. Given the relative incidences, the high occurrence of Phe as a member in 3-bridge clusters is not surprising. The higher counts for Trp in the 3-bridge clusters is interesting, given that Trp is found about one third as much as Phe and Tyr.[240] The overall larger degree of electron density on the face of the indole ring may promote stronger interactions with Met, providing a driving force for its relatively higher incidence.

‡‡ URL for the PDB code and interacting amino acids list is: https://www.mdpi.com/2218-273X/12/1/6.

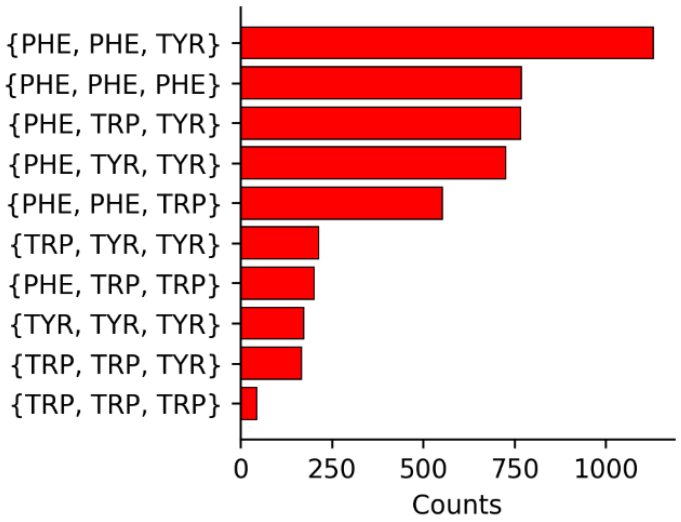

Figure 65. Summary of the identities and incidences of 3-bridge clusters.

Analysis of the spatial orientations of the aromatic groups around Met are set out in Figure 66. The black V-shape at the center of the images denotes the CH_3-S-CH_2 thioether of Met. Each dot corresponds to an aromatic centroid. Note that this figure shows the raw incidences of Phe, Tyr, and Trp, regardless of the composition of the cluster. Images for the locations of aromatics in the different bridge compositions (i.e., Figure 65) are set out in Appendix D. While the search algorithm used a cut-off distance of 6 Å, the vast majority of hits occur at distances between 2 and 4 Å from the Met-CH_3 or -CH_2 to the aromatic ring. Note that the sum of the van der Waals radii of C and H is 2.9 Å. In all cases, the aromatic groups can be found widely distributed around the thioether, but there is a noticeably higher incidence of aromatics near the -CH_3 and -CH_2 groups (i.e., an interaction between a CH and a π-system[241]). In some cases, this behaviour is more apparent in isolated bridge compositions, for example, Phe, Trp, and Tyr clusters in Figure D5. While this work focuses on the incidences, basic features, and distance metrics of 3-bridge clusters, there also are angular correlations (e.g., between Met and faces of aromatics) that can be considered. This is the subject of ongoing research.

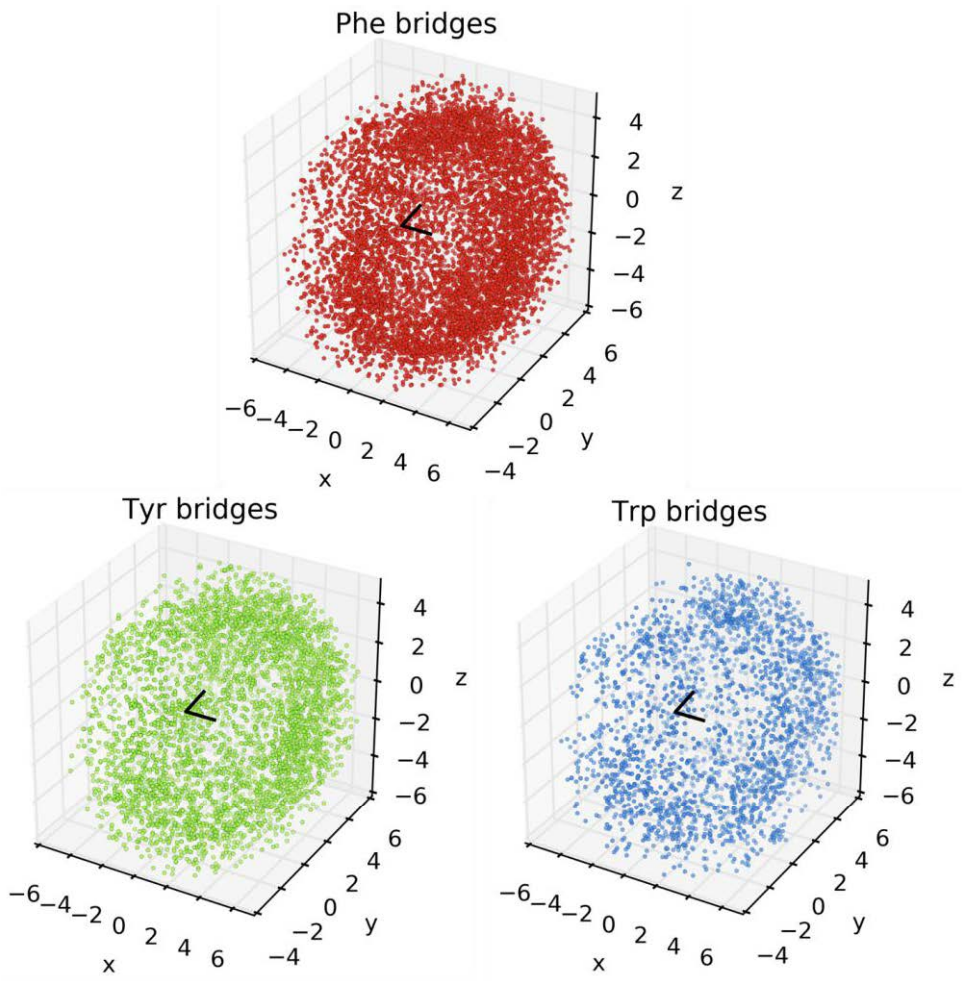

Figure 66. Plots of clustering Phe (top, red), Tyr (bottom left, green), and Trp (bottom right, blue) around Met. The x, y, and z axes are in Ångstroms. The black V-shape at the origin depicts the CH_3-S-CH_2 thioether of Met. The arm pointing away from the reader (along +y) is the CH_2 group. Each point corresponds to an aromatic centroid for each respective amino acid.

In order to better understand the inter-residue forces that are at play in 3-bridge clusters, quantum chemical calculations were carried out using an example of a 3-bridge cluster from a cytochrome P450 found in *Thermobispora bispora* (PDB ID: 5VWS).[157] Hydrogens were placed programmatically in PyMOL.[242] Hydrogen positions were optimized and electron density plots calculated using the ORCA *ab initio* quantum chemistry program.[243,244] Three versions of the bridge cluster were initially explored (Figure 67): the complete bridge, the aromatic groups only, and the Met only. As expected, the faces of the aromatic groups have partial negative charges and the edges have partial positive charges. Likewise, the sulfur in Met has a partial negative charge. However, the partial charges are more pronounced in the 3-bridge components (middle and right panel

of Figure 67) than in the whole cluster. While the effect is subtle, the decrease in the magnitude of the electron density is consistent with a weak dipole-dipole (van der Waals) interaction. The greatest change in electron density in the aromatics is observed in Trp20 and in Phe41, which is revisited below. Overall, this is an example of how the polarizability of the Met thioether and the delocalized aromatic systems may facilitate interactions in the 3-bridge clusters. Such dipole-dipole interactions have also been noted in detailed calculations of simple models of benzene and dimethyl sulfide.[87]

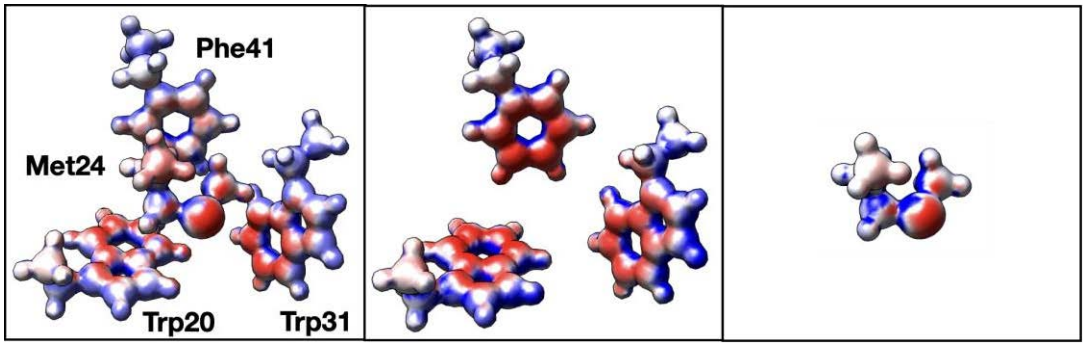

Figure 67. Electron density plots for the 3-bridge cluster in cytochrome P450 from *T. bispora.* The left panel shows the complete bridge, the center shows the aromatic groups only, and the right panel shows Met only. Red corresponds to a charge of –0.03, white is zero, and blue is +0.03. PDB ID: 5VWS.[157]

Additional insights can be gained through Natural Bond Orbital (NBO) analysis[245] and energy decomposition using coupled-cluster (CCSD) calculations.[246] Again, we use the 3-bridge cluster shown in Figure 67 as an example case. The calculated interaction energy from CCSD calculations is –7.49 kcal mol^{-1}, which is comprised of –7.73 kcal mol^{-1} of uncorrected interaction energy and 0.24 kcal mol^{-1} of geometric preparation energy.[246] The NBO calculation reveals that a complex network of orbital interactions are at play within the 3-bridge cluster. Two examples of contributing NBOs are shown in Figure 68. Interactions between all fragments can be observed, with the strongest interaction between Met24 and Phe41 and between Met24 and Trp20. The sum of all of the intermolecular interaction energies from the NBO second order perturbation theory analysis (E(2) values) is –6.4 kcal mol^{-1}, consistent with the interaction energy from the higher CCSD level of theory.

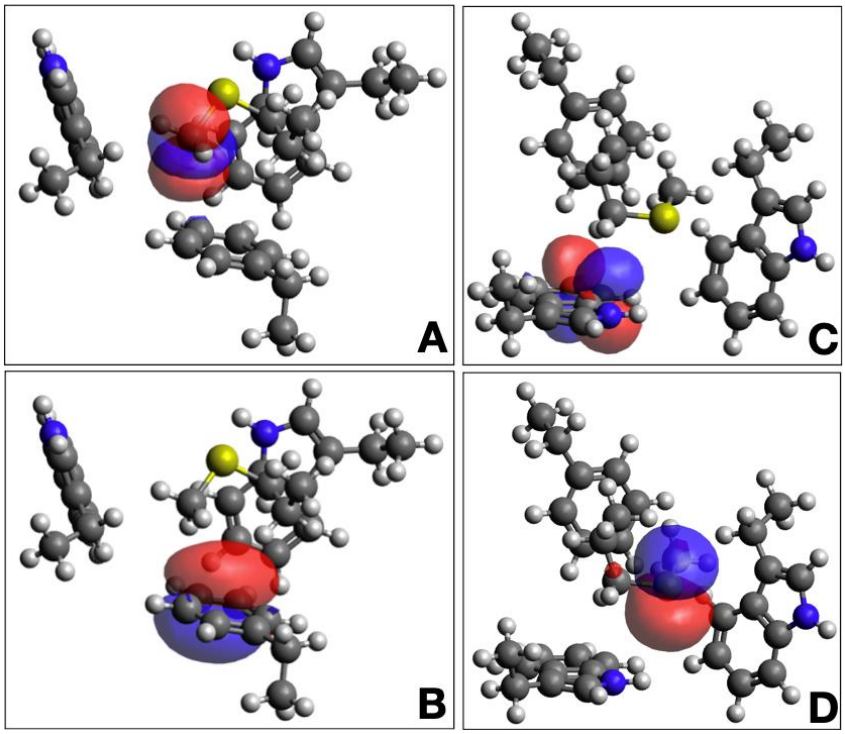

Figure 68. Natural bond orbitals from the 3-bridge cluster in cytochrome P450 from *T. bispora*. Interactions that involve a Met24 C-H* acceptor (A), Phe41 C-C π-donor (B), Trp20 C-C π* acceptor (C), and Met24 lone pair donor from S (D). PDB ID: 5VWS.[157]

In order to gain a more systematic view of how the interactions of aromatics affect the energetics of Met (and vice versa) in the context of the intact protein structure, the interaction energy matrix (IEM) web application[247] was used to evaluate interaction energies between Met and surrounding aromatic groups. Again, using the cytochrome P450 3-bridge cluster from Figure 67 as a model, a series of variants were programmatically produced where each member of the cluster amino acid residues were systematically replaced with alanine (Ala). Computations were carried out with the AMBER99 forcefield and using a water-like continuum, as set during submission in the IEM web application. Hydrogens were added programmatically by the web IEM application. The interaction energy values are set out in Table 8.

Table 8. Calculated interaction energies in the 3-bridge cluster in cytochrome P450 from *T. bispora*.[a]

	Met24b	Trp20[c]	Trp31[c]	Phe41[c]
Wild type	-10.9	-3.75	-2.02	-3.11
Trp20Ala	-7.44	-0.12	-2.01	-3.16
Trp31Ala	-9.12	-3.72	-0.31	-3.13
Phe41Ala	-7.54	-3.59	-1.87	-0.22
Trp20Ala/Trp31Ala	-4.21	-0.12	-1.86	-0.22
Trp20Ala/Phe41Ala	-5.68	-0.12	-0.31	-3.16
Trp31Ala/Phe41Ala	-5.98	-3.56	-0.37	-0.22
Trp20Ala/Trp31Ala/Phe41Ala	-2.68	-0.12	-0.37	-0.22
Met24Ala	-2.79	-0.65	-0.08	-1.23

[a]Energies in kcal mol^{-1}. [b]Net interaction energy (side chain versus side chain). [c]Pairwise side chain to side chain interaction energy with the residue at position 24.

The largest values for pairwise interaction energies in the wild-type protein are observed for Met24-Trp20 and Met24-Phe41 pairs. This interaction energy also is roughly consistent with that obtained from NBO analysis. Consequently, replacement of either of those residues with Ala results in large changes in the net interaction energy of Met24. Interestingly, removal of either Trp results in a modest increase of the Met24-Phe41 pairwise interaction energy. The same is not true for removal of Phe41, in which case the pairwise interactions of Met24 with both Trp residues decrease. Replacement of all the aromatics and Ala, or replacement of Met24 with Ala, results in a 75% decrease in the net energy of the residue at position 24. Analysis of a different bridge is shown in Table 9 and similar conclusions can be drawn. This analysis suggests that interactions in 3-bridge clusters are complex and depend on the nature of individual amino acid residues.

Table 9. Calculated interaction energies in the 3-bridge cluster in biphenyl dioxygenase from *C. testosterone*.[a]

	Met439[b]	Trp220[c]	Phe325[c]	Tyr440[c]
Wild type	-8.71	-0.60	-0.93	-2.29
Trp220Ala	-8.16	-0.01	-0.93	-2.28
Phe352Ala	-7.71	-0.58	-0.12	-2.28
Tyr440Ala	-6.55	-0.55	-0.92	-0.20
Trp220Ala/Phe352Ala	-7.18	-0.01	-0.12	-2.27
Trp220Ala/Tyr440Ala	-6.07	-0.01	-0.87	-0.20
Phe325Ala/Tyr440Ala	-5.58	-0.52	-0.12	-0.20
Trp220Ala/Phe325Ala/Tyr440Ala	-5.13	-0.01	-0.12	-0.20
Met439Ala	-1.52	-0.01	-0.20	-0.37

[a]Energies in kcal mol^{-1}. [b]Net interaction energy (side chain versus side chain). [c]Pairwise side chain to side chain interaction energy with the residue at position 439.

5.3. Discussion

In some ways, 3-bridge interactions have features that resemble cation-π interactions.[230,231] They also can include aspects of CH-π interactions.[241,248,249] Such non-covalent interactions are known to play roles in structural biology. In cation-π interactions, the aromatic faces of Trp, Tyr, or Phe provide a negative electrostatic potential to allow for an interaction with a cation.[248,249] In proteins, a 1-5 kcal mol^{-1} increase in binding energy has been observed for these types of interactions, suggesting that they play roles in interprotein stabilization[230,235] and protein-ligand binding.[248] However, binding energies of over 20 kcal mol^{-1} are possible when a cation (e.g., lysine-NH_3^+) is surrounded by aromatics. Such a physical arrangement is similar to the Met-aro clusters described here. The energies of single cation-π interactions are only slightly more favourable than for single Met-aro interactions (1-3 kcal mol^{-1}). The results presented here suggest that the 3-bridge clusters have interaction energies that are 5-10 kcal mol^{-1} indicating that the cluster is favourable, but not as favourable as the analogous cation-π interaction. Finally, we note that cation-π interactions occur preferentially when the amino group is between 3.4 and 6.0 Å of the aromatic-π system.[250] These distance metrics are similar to the Met-aro clusters described here.

Similar to cation-π interactions, the CH-π interaction occurs between polarized CH and aromatic rings resulting in an attractive interaction that is dependent on amino acid conformation.[251,252] Consequently, this type of interaction is likely part of the overall Met-aro interaction. Different sub-types of CH-π interactions have been observed within protein structures but Met most actively participates in the $C_{ali}H$-π interaction (aliphatic CH donor).[241] Overall, CH-π interactions could be part of the 3-bridge interactions, especially in those cases where favourable conformations between Met-CH and π-acceptors are possible. In addition, the proximity and orientation of the aromatic residues in each 3-bridge cluster could give rise to $C_{aro}H$-π interactions (aromatic CH donor). These interactions are thought to be stronger than their aliphatic counterparts.[253]

The complete dataset for Met-aro 3-bridge clusters shows several proteins of the same or similar types. For example, iron superoxide dismutases (17 entries), DNA and RNA polymerases (38 entries), cytochromes P450 (28 entries), and chitinase (17 entries) enzymes appear in the dataset. These are intensely studied enzyme classes, so perhaps their high degree of representation is unsurprising. However, in all cases, the individual

proteins show less than 90% sequence identity and can be found in different organisms. This suggests that the Met-aro clustering interaction is a general structural motif, rather than an isolated example in a single organism or class of proteins.

A redox role of closely placed Tyr and Trp that has been proposed is the protection of redox-active proteins from off-cycle production of strong oxidants.[24,30,32,64] In some cases, the chains of Tyr and Trp can be both functional and protective, as in C*c*P (Figure 64).[91,92] In our survey of 3-bridge clusters, we found examples of cases that could be part of protective Tyr/Trp pathways. For example, in yeast catalase (Figure 69), Tyr228, Met281, Trp300, and Phe305 form a cluster near the surface of the protein. A series of Tyr (shown in green in Figure 69) connect the catalytic heme to the protein surface, with one potential pathway involving the 3-bridge cluster. Using Beratan's pathway modeling tools,[32] we find that Tyr228 is the favoured hole acceptor (where the heme is the hole donor). The degree of electronic coupling between distant sites is an important determinant of electron/hole transfer rates, and such coupling is influenced by structural dynamics of electron/hole carriers.[254,255] In this context, the balance between stability and flexibility of Met-aro clusters may provide pathways for electron/hole flow in proteins.

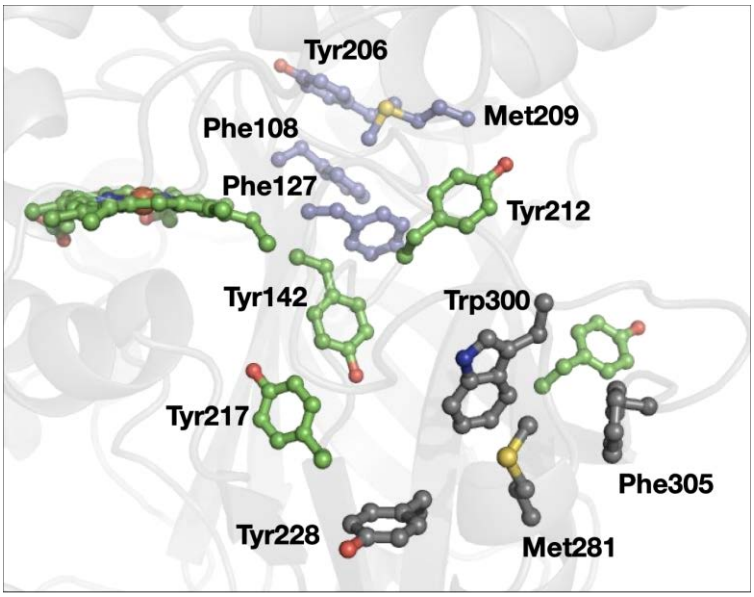

Figure 69. Structure of yeast catalase. The 3-bridge clusters are highlighted in gray and lavender, and the heme and other tyrosine residues are in green. PDB ID: 1A4E.[256]

Interestingly, yeast catalase has another 3-bridge cluster (Phe108, Phe127, Tyr206, and Met209, shown in lavender in Figure 69). This case provides an example of

another common feature in the dataset: 3-bridge clusters that connect different parts of the protein (as evidenced by large separations in the primary structure). Again, the weak polar interaction of the Met and aromatics support the balance of stability and flexibility required for functional protein structures that is beyond a simple hydrophobic interaction.

One example of a protein that contains multiple 3-bridge clusters is prostaglandin H2 synthase 1 (Figure 70). Three different 3-bridge clusters localize between the heme and the protein surface. This is a particularly unusual example because of the close spatial proximity of the bridges in a medium-sized protein. Two Tyr residues (Tyr402 and Tyr417) are localized at the protein surface, making them strong candidates for a protective role.[24,30,64] The Tyr involved in the catalytic cyclooxygenase reaction (Tyr385 in this protein, not shown in Figure 70) is located toward the protein interior. The third bridge, involving Met197, Tyr301, Phe426, Phe580, connects several different parts of the primary structure, which is consistent with a role in promoting tertiary structure and the enzyme active site via weak dipole-dipole interactions.

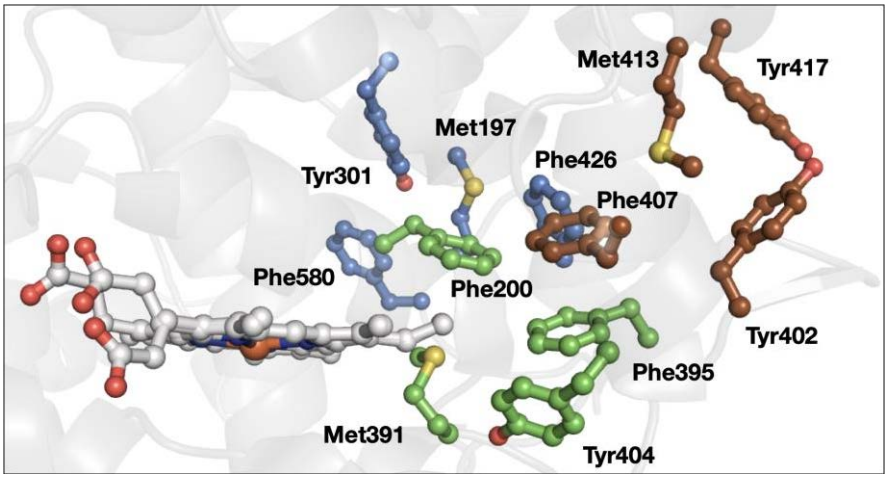

Figure 70. Structure of prostaglandin H2 synthase 1. The 3-bridge clusters are highlighted in orange, green, and lavender, and the heme is shown in gray. PDB ID: 1Q4G.[257]

As noted above, the 3-bridge clusters were found in all classes of enzymes, not just in oxidoreductases. *Xanthobacter autotrophicus* haloalkane dehalogenase catalyzes the dehalogenation of halogenated *n*-alkanes to generate the halide anions and corresponding alcohols. The chloride-bound X-ray structure of this protein (Figure 71) shows the leaving halide stabilized by the indole rings of two Trp residues (Trp125 and Trp175). Halide loss is rate limiting during catalysis.[258] Trp175 is supported by two Phe

residues (Phe190 and Phe290) that are part of a 3-bridge cluster. The motions of those Phe have been implicated in halide migration from the active site.[259,260] The dipole-dipole interactions that could be involved in the Met-aro 3-bridge cluster may have an impact on both maintaining local protein structure and enabling motions that promote loss of a charged halide product.

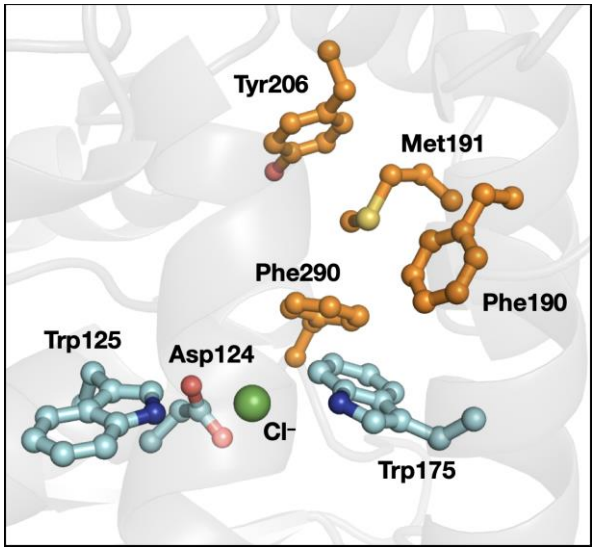

Figure 71. Structure of *X. autotrophicus* haloalkane dehalogenase. The 3-bridge cluster is highlighted in orange and the catalytic aspartate (Asp) and halide-stabilizing Trp are in cyan. PDB ID: 1B6G.[261]

The intermediate energy of interaction in 3-bridge clusters can provide proteins with a balance of stability and flexibility. In the examples discussed above, B-factors can be investigated to evaluate the level of flexibility around a 3-bridge interaction. B-factors are commonly used when measuring the flexibility of protein-protein or protein-ligand binding sites.[262,263] In the examples provided above, 3-bridge clusters are within an intermediate range of flexibility with respect to the entire protein structure. Inspection of the individual B-factors suggests that a level of stability is imposed upon protein structures around the 3-bridge clusters. A series of images that are coloured to represent B-factors around each of the 3-bridge interaction sites are set out in the figures below. Ultimately, the intermediate values of the B-factors suggest that a degree flexibility remains in those sites.

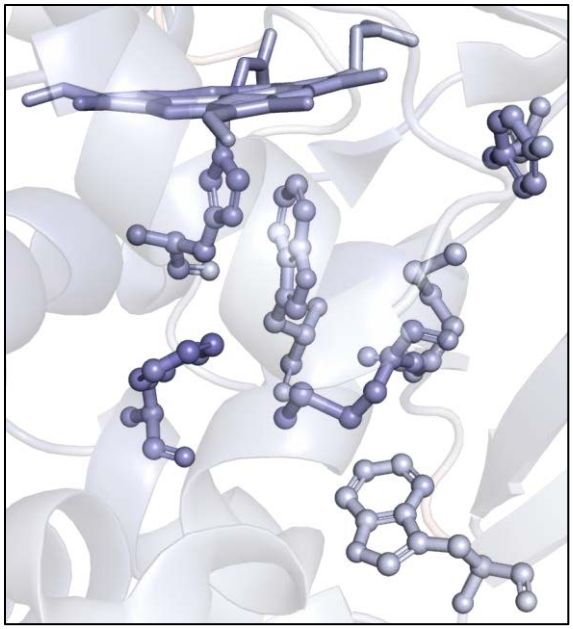

Figure 72. **Flexibility colour spectrum for yeast C*c*P using residue B-factors from the PDB. The spectrum from dark purple through white to dark red represent lower to higher areas of flexibility, respectively. PDB ID: 2CYP.[95]**

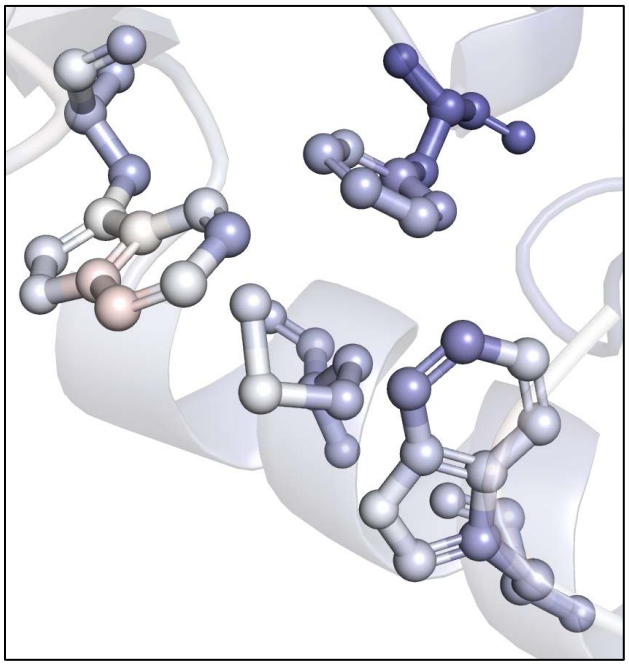

Figure 73. **Flexibility colour spectrum for cytochrome P450 using residue B-factors from the PDB. The spectrum from dark purple through white to dark red represent lower to higher areas of flexibility, respectively. PDB ID: 5VWS.[157]**

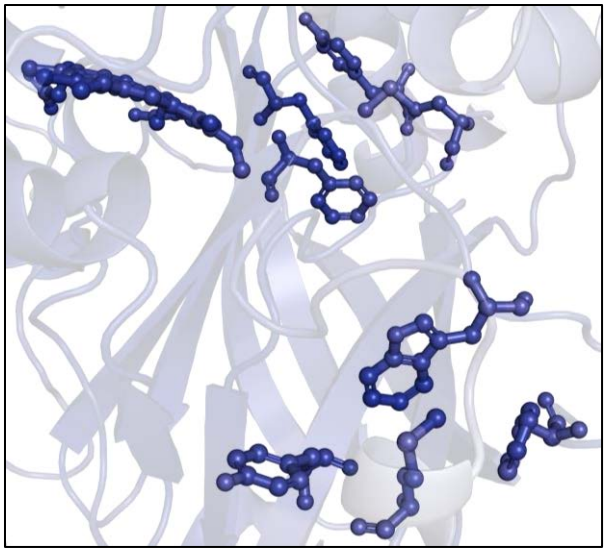

Figure 74. **Flexibility colour spectrum for yeast catalase using residue B-factors from the PDB. The spectrum from dark purple through white to dark red represent lower to higher areas of flexibility, respectively. PDB ID: 1A4E.[256]**

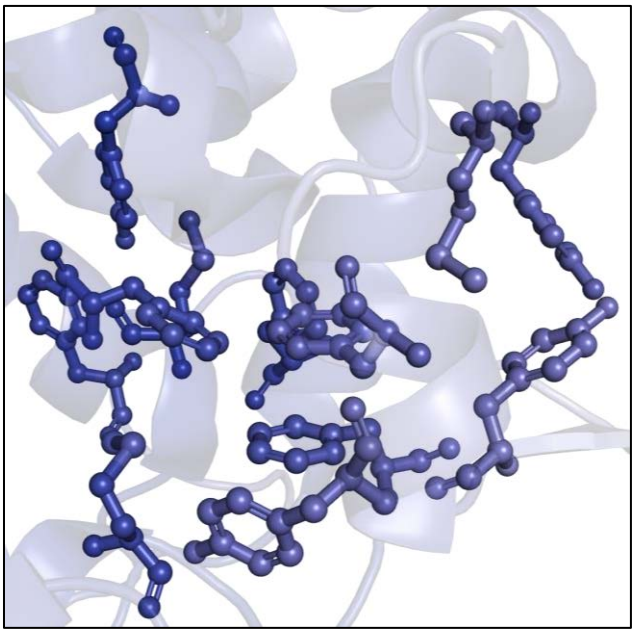

Figure 75. **Flexibility colour spectrum for prostglandin H2 synthase 1 using residue B-factors from the PDB. The spectrum from dark purple through white to dark red represent lower to higher areas of flexibility, respectively. PDB ID: 1Q4G.[257]**

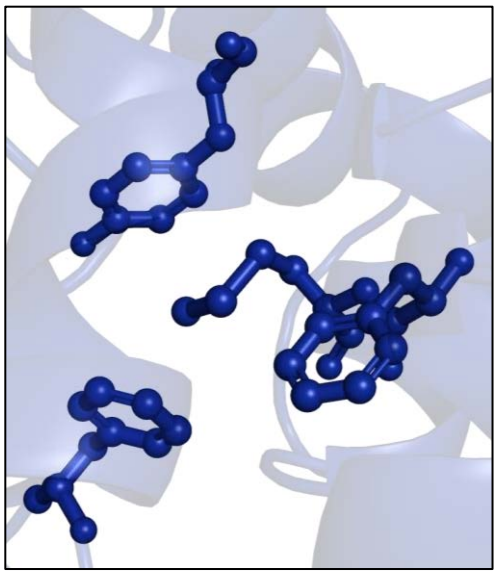

Figure 76. Flexibility colour spectrum for haloalkane dehalogenase using residue B-factors from the PDB. The spectrum from dark purple through white to dark red represent lower to higher areas of flexibility, respectively. PDB ID: 1B6G.[261]

5.4. Summary

Structures where Met is surrounded by three aromatic groups are found in all types of proteins. In contrast to our previous surveys that focused solely on S-π groups,[29,90] this chapter presents a more comprehensive perspective, where dipolar interactions of the entire Met thioether interact with nearby aromatic groups. Inspection of selected examples show that Met-aro 3-bridge clusters could play roles in catalysis and in redox reactions. Analysis using computational methods suggest that clusters can be viewed, in some ways, as weaker analogs of cation-π interactions. The 3-bridges are characterized by a combination of interactions between the Met(S), Met-CH_2 and Met-CH_3 groups, and the π-systems of nearby aromatics. This weaker dipole-dipole interaction may strike an energetic balance between purely hydrophobic interactions and stronger cation-π moieties, allowing a level of protein flexibility while maintaining the protein's native structure. Importantly, the entire Met-thioether is involved in 3-bridge clusters. The interaction is likely comprised of a combination of CH-π interactions, S-π interactions, and S-lone pair-π interactions. Overall, this represents a network of dispersive, electrostatic, and orbital interactions. To some extent, this contrasts with cation-π interactions, where the cationic group (e.g., Lys-NH_3^+) is the key component. Further studies of these Met-aro

3-bridge clusters, and other Met-aro interactions, will yield more insights on their properties and roles in protein structure and function.

5.5. Experimental

5.5.1. Identification of 3-Bridge Clusters in Protein Structures

First, we found closely spaced Met-aro groups meeting the criteria specified by a previously described[29,90] "Met-aro" algorithm (available at https://github.com/dsw7) in a list of 33,819 protein X-ray structures with resolution better than 3 Å and sequence identity of less than 90%. Additional code and a list of structures and coordinates can be downloaded at: https://github.com/dsw7/n-Bridges. A list of PDB IDs, residues, and protein identities used for analysis can be found online.[§§] The dataset was collected from the PDB[264] in September 2019. The cut-off distance between Met and an aromatic residue was set to 6.0 Å and no cut-off angle was specified (approximated as 360°). The long cut-off distance was chosen to allow for weaker interactions to be detected. In previous work,[90] closely spaced Met-aro residues were treated as nodes in an imaginary network and then the NetworkX library (https://networkx.github.io) was used to find 2-bridge interactions. Herein, a similar approach was used to find 3-bridge clusters, which are defined as Met residues with the faces of three aromatic groups (Phe, Tyr, or Trp) oriented in any geometry about the CH_2-S-CH_3 of Met.

5.5.2. Assessing the Position of Aromatic Residues Around Methionine

To better understand how aromatic residues are positioned around Met, the position of various aromatic residues within the spherical region of space surrounding the Met SD was examined. Herein, we were interested in determining whether the aromatic residues assumed a preferential position relative to the Met CG-SD-CE scaffold. All 3-bridge clusters were assumed to consist of six 3-tuples: the CG-SD-CE (i.e., Met CH2-S-CH3) coordinates and three satellite points: C1, C2, and C3. The three satellite points were the centroids of the aromatic groups. All six 3-tuples were first mapped to the origin

[§§] URL for the PDB code and interacting amino acids list is: https://www.mdpi.com/2218-273X/12/1/6.

of a frame where SD assumed the origin (0, 0, 0 position). The system was temporarily isolated to CG-SD-CE and the direction cosine α between SD-CE and the x-axis was found. A Householder rotation of CG-SD-CE about the cross product of SD-CE and the x-axis by −α rendered the SD-CE bond axis colinear with the x-axis. The rotation was performed by a quaternion, Q1, subsequently rendering the CG coordinate free to rotate about the x-axis. Finally, the remaining CG coordinate was rendered coplanar with CE, SD, and the x,y-plane through rotation by angle −β about the x-axis and using a second quaternion, Q2. The aromatic centroids, C1, C2, and C3 were rotated into their final position using a composition of quaternions Q1 and Q2. All homogeneous transformations in this study were done with the assistance of the pyquaternion library (http://kieranwynn.github.io/pyquaternion/ (accessed on 18 March 2020)).

5.5.3. Density Functional Calculations

Calculations were carried out with the ORCA 4.2.1 *ab initio* quantum chemistry program.[243,244] The geometries of the hydrogens were optimized with the BP86 functional and def2-SVP/def2/J basis set[265,266] on all atoms. Single-point energy calculations used the BP86 functional and the def2-TZVP/def2/J basis set.[265,266] All calculations used the RIJCOSX algorithm and the Becke-Johnson damping scheme.[267,268] NBO[245] calculations were carried out using Gaussian16 (Gaussian 16, Revision C.01, Frisch, M. J.; Trucks, G. W.; Schlegel, H. B.; Scuseria, G. E.; Robb, M. A.; Cheeseman, J. R.; Scalmani, G.; Barone, V.; Petersson, G. A.; Nakatsuji, H.; Li, X.; Caricato, M.; Marenich, A. V.; Bloino, J.; Janesko, B. G.; Gomperts, R.; Mennucci, B.; Hratchian, H. P.; Ortiz, J. V.; Izmaylov, A. F.; Sonnenberg, J. L.; Williams-Young, D.; Ding, F.; Lipparini, F.; Egidi, F.; Goings, J.; Peng, B.; Petrone, A.; Henderson, T.; Ranasinghe, D.; Zakrzewski, V. G.; Gao, J.; Rega, N.; Zheng, G.; Liang, W.; Hada, M.; Ehara, M.; Toyota, K.; Fukuda, R.; Hasegawa, J.; Ishida, M.; Nakajima, T.; Honda, Y.; Kitao, O.; Nakai, H.; Vreven, T.; Throssell, K.; Montgomery, J. A., Jr.; Peralta, J. E.; Ogliaro, F.; Bearpark, M. J.; Heyd, J. J.; Brothers, E. N.; Kudin, K. N.; Staroverov, V. N.; Keith, T. A.; Kobayashi, R.; Normand, J.; Raghavachari, K.; Rendell, A. P.; Burant, J. C.; Iyengar, S. S.; Tomasi, J.; Cossi, M.; Millam, J. M.; Klene, M.; Adamo, C.; Cammi, R.; Ochterski, J. W.; Martin, R. L.; Morokuma, K.; Farkas, O.; Foresman, J. B.; Fox, D. J. Gaussian, Inc., Wallingford CT, 2016.) using the BP86 functional and def2-TZVP basis set. Local Energy Dispersion calculations were carried out using DLNPO-CCSD(T) and the cc-pvtz and cc-pvdz basis sets.[246] Electron

density plots were generated using UCSF-Chimera, developed by the Resource for Biocomputing, Visualization, and Informatics at the University of California, San Francisco, with support from NIH P41-GM103311.[81] NBO plots were constructed using Avogadro.[269]

Chapter 6. Conclusions and Future Directions

6.1. Overall Conclusions

6.1.1. Conclusions from Chapter 2

This chapter focused on the effects of the microenvironment surrounding Trp109 (Trp = tryptophan) in two azurin mutants. These mutants were His107Trp109Ala56 (His = histidine, Ala = alanine) and His107Trp109Met56 (Met = methionine) to probe the effects of a Met residue in this protein pocket. The techniques used were UV-Visible (UV-Vis) spectrophotometry, fluorescence spectroscopy, and transient absorption (TA) spectroscopy. The UV-Vis experiments did not show any changes to the absorption properties of the Trp109 residue. This suggests that the Met56 and Ala56 residues are too distant from Trp109 to induce any major electronic changes. Fluorescence of Trp is highly sensitive to changes in its microenvironment and a slight blue-shift is observed when Met is removed. This suggests that there is a small change to the electronic structure of Trp109 imparted by the microenvironment. TA spectroscopy also reveals a dependency on the microenvironment such that Met56 decreases the rate of electron transfer (ET) for Ru(III) reduction.

6.1.2. Conclusions from Chapter 3

This chapter focused on the effects that a Met residue has on a Trp radical in azurin. Using fluorescence, steady-state UV-Vis, and electron paramagnetic resonance (EPR), the properties of Trp108 were evaluated. No major change was observed in the Trp108 fluorescence in either the Met102 or Leu102 mutants suggesting that the microenvironment is largely unchanged between both. However, steady-state UV-Vis suggest that Met102 impacts the photochemical yield of the Trp108 radical, and thus, the microenvironment. This can be attributed to less oxidation of Trp108 by either changing the structural pocket surrounding Trp108, or changing the energy required for Trp108 to undergo oxidation. Trp reduction potentials would help to determine this as they are directly correlated to the driving force described by the Marcus equation. EPR results showed a small increase to the g_x-value and a small change in HFCCs. This suggests that

the potential for hydrogen bonding to occur with the indole nitrogen on Trp108 has been reduced or removed.

6.1.3. Conclusions from Chapter 4

This chapter built upon the previous work that investigated only Met interactions with an aromatic residue and focused on multiple residues that could induce different effects. These included Met, arginine (Arg), glutamine (Gln), and lysine (Lys). Overall, the microenvironment surrounding tyrosine (Tyr) 109 in azurin is impacted by changes to a nearby residue at position 122 with respect to ET kinetics, fluorescence, and reduction potentials. The kinetic studies revealed that Gln122 and Arg122 were similar in their effect on ET and Met122 increases the ET rate. Lys122 was a residue that had previously been investigated in the literature and was used as a comparison to the mutants studied in this chapter. It was also observed that ET rates increased with pH which was expected as this had been seen before in the literature and coincides with Tyr deprotonation which can occur more readily at higher pH values. This is also evident in the reduction potentials for Tyr109 across the same pH range. Fluorescence studies supported these findings to a certain extent when studying tyrosinate ($TyrO^-$) formation. The fluorescence spectra of the Met122 mutant suggested that no $TyrO^-$ formation was occurring. This would mean that no ET could be possible and that the reduction potentials would remain more positive, which is not the case. Furthermore, a different mechanism is preventing $TyrO^-$ fluorescence from occurring but it could not be elucidated with the described experiments.

6.1.4. Conclusions from Chapter 5

A computational method was developed to evaluate Met-aromatic (Met-aro) bridging interactions seen in PDB structures that contained three aromatic groups surrounding a Met residue. These interactions involve the dipolar interactions of the entire Met thioether with the nearby aromatic group and can be grouped into enzyme classes to suggest the Met-aro 3-bridge clusters play roles in catalysis and redox reactions. It is likely that the specific interactions seen here are a combination CH-π interactions, S-π interactions, and S-lone pair-π interactions. More studies focusing on Met-aro interactions will yield more insights into the roles that they may play across many types of enzymes.

6.2. Structural Elucidations for Current Protein Models

6.2.1. Protein Crystallization Studies

As reiterated in Chapter 2, Chapter 3, and Chapter 4 in this thesis, acquiring crystal structures for all of the designed protein models discussed is of great importance. This would provide a more defined pocket where the aromatic amino acids are found (Trp109, Trp108, and Tyr109). Crystallization of the His107Trp109(Met/Ala)56 proteins was attempted but was omitted from its respective chapter due to the lack of results found. Fortunately, this provides a set of conditions at which crystallization does not occur and would provide a starting point for future work. The crystallization of all the proteins in this thesis is a time-consuming project to be undertaken, however, it would be beneficial to the results presented in this thesis.

6.2.2. Nuclear Magnetic Resonance Characterization

Nuclear magnetic resonance (NMR) is commonly used for studying a protein structure. It is a highly sensitive method that can detect structural changes and is widely applicable for studying proteins in physiological relevant conditions.[270] Many of the studies presented in this thesis discuss how hydrogen bonding would impact the physical properties of the aromatic amino acid. ^{1}H NMR studies would provide evidence of changes to chemical shifts of the residues that participate in hydrogen bonding, specifically the indole hydrogen on Trp109 or Trp108 and the phenolic hydroxyl on Tyr109. This work could be convoluted by the size of azurin being ~14 kDa as proteins larger than 10 kDa usually require methods in addition to simpler homonuclear ^{1}H NMR experiments that can be performed on smaller sized proteins.[270] It is also important to note that metal substitution to Zn(II) would prevent any effects from a paramagnetic species in the NMR studies. While structural studies of this Zn(II) variant were not conducted in this thesis, a comparison between Zn(II) and Cu(II) azurin can be completed to confirm that no major structural changes occur with this metal substitution. Zn(II)-azurin crystal structures are available in the PDB.[271,272]

Another method for NMR characterization could involve the use of fluorotyrosine (F_nTyr). Differently substituted F_nTyr have been reported in the literature to be successfully incorporated into proteins and can be used for ^{19}F NMR studies.[273,274] This would provide

a less complex NMR approach as introducing a F_nTyr would create a defined number of ^{19}F nuclei present in the sample and chemical shifts would be easier to observe as changes to the F_nTyr microenvironment occur. This could also be more easily applied as this method for studying a protein's microenvironment has been used in the Warren Lab at SFU previously, and the methods to incorporate F_nTyr into proteins has been well established.

6.3. Development of New Protein Models

This thesis focused on interactions with the microenvironment through a Trp or Tyr residue, however, there is still work to be done. Although Chapter 2 and Chapter 3 both focused on microenvironment effects on a Trp residue, the main focus was on the Met-aro interaction and did not discuss effects of other amino acids unlike Chapter 4. It is of great interest to grow the knowledge base of how different microenvironments play a role on changing the physical properties of Trp. This will help to determine why Trp may be incorporated into a protein's structure at certain places. As stated throughout, Trp plays a role in critical biological ET reactions but it is not fully understood why. Probing the kinetics, electrochemical, fluorescent, and absorption properties of Trp proximal to different types of amino acids is desirable and as such, similar mutations to those used in Chapter 4 have been proposed and prepared. In this future project, the mutation set would be His107Trp109(Arg/Met/Glu/Gln)122 with fluorescence, electrochemistry, and flash-quench kinetics being carried out. Much work has been previously completed in investigating the microenvironment surrounding Trp residues, including fluorescence studies.[159,166,167,275] The emission maximum for Trp in a protein can be anywhere from 310 to 360 nm and is known to be influenced by a variety of factors such as solvent exposure and solvent polarity,[167] however, less is known about interactions with other amino acids, although interactions have been reported in the literature.[89,107,167,276]

Trp has been computationally studied also, similarly to Chapter 5 in this thesis, and interesting results have been obtained that show frequencies at which various amino acids appear nearby to Trp or as a long-range contact.[167] It would be interesting to use these results to inform an *in vitro* experimental design and study how ET pathways would be impacted.

References

(1) Umena, Y.; Kawakami, K.; Shen, J.-R.; Kamiya, N. Crystal Structure of Oxygen-Evolving Photosystem II at a Resolution of 1.9 Å. *Nature* **2011**, *473* (7345), 55–60. https://doi.org/10.1038/nature09913.

(2) Zong, S.; Wu, M.; Gu, J.; Liu, T.; Guo, R.; Yang, M. Structure of the Intact 14-Subunit Human Cytochrome *c* Oxidase. *Cell Res.* **2018**, *28* (10), 1026–1034. https://doi.org/10.1038/s41422-018-0071-1.

(3) Hirst, J. Mitochondrial Complex I. *Annu. Rev. Biochem.* **2013**, *82* (1), 551–575. https://doi.org/10.1146/annurev-biochem-070511-103700.

(4) Beratan, D. N. Why Are DNA and Protein Electron Transfer So Different? *Annu. Rev. Phys. Chem.* **2019**, *70* (1), 71–97. https://doi.org/10.1146/annurev-physchem-042018-052353.

(5) Beratan, D. N.; Liu, C.; Migliore, A.; Polizzi, N. F.; Skourtis, S. S.; Zhang, P.; Zhang, Y. Charge Transfer in Dynamical Biosystems, or The Treachery of (Static) Images. *Acc. Chem. Res.* **2015**, *48* (2), 474–481. https://doi.org/10.1021/ar500271d.

(6) Peters, J. W.; Beratan, D. N.; Bothner, B.; Dyer, R. B.; Harwood, C. S.; Heiden, Z. M.; Hille, R.; Jones, A. K.; King, P. W.; Lu, Y.; Lubner, C. E.; Minteer, S. D.; Mulder, D. W.; Raugei, S.; Schut, G. J.; Seefeldt, L. C.; Tokmina-Lukaszewska, M.; Zadvornyy, O. A.; Zhang, P.; Adams, M. W. A New Era for Electron Bifurcation. *Curr. Opin. Chem. Biol.* **2018**, *47*, 32–38. https://doi.org/10.1016/j.cbpa.2018.07.026.

(7) Warren, J. J.; Ener, M. E.; Vlček, A.; Winkler, J. R.; Gray, H. B. Electron Hopping through Proteins. *Coord. Chem. Rev.* **2012**, *256* (21–22), 2478–2487. https://doi.org/10.1016/j.ccr.2012.03.032.

(8) Marcus, R. A.; Sutin, N. Electron Transfers in Chemistry and Biology. *Biochim. Biophys. Acta* **1985**, *811* (3), 265–322. https://doi.org/10.1016/0304-4173(85)90014-X.

(9) Marcus, R. A. Chemical and Electrochemical Electron-Transfer Theory. *Annu. Rev. Phys. Chem.* **1964**, *15* (1), 155–196. https://doi.org/10.1146/annurev.pc.15.100164.001103.

(10) Sutin, N. Theory of Electron Transfer Reactions: Insights and Hindsights. In *Progress in Inorganic Chemistry*; Lippard, S. J., Ed.; John Wiley & Sons, Ltd: Hoboken, NJ, 1983; Vol. 30, pp 441–498. https://doi.org/10.1002/9780470166314.ch9.

(11) Meyer, T. J.; Taube, H. Electron Transfer Reactions. In *Comp. Coord. Chem.*; Wilkinson, G., Ed.; Comp. Coord. Chem.; Pergamon: New York, 1987; pp 331–384.

(12) Espenson, J. H. *Chemical Kinetics and Reaction Mechanisms*, Second.; McGraw-Hill: New York, 1981.

(13) Marcus, R. A. On the Theory of Oxidation-Reduction Reactions Involving Electron Transfer. II. Applications to Data on the Rates of Isotopic Exchange Reactions. *J. Chem. Phys.* **1957**, *26* (4), 867–871. https://doi.org/10.1063/1.1743423.

(14) Marcus, R. A. On the Theory of Oxidation-Reduction Reactions Involving Electron Transfer. III. Applications to Data on the Rates of Organic Redox Reactions. *J. Chem. Phys.* **1957**, *26* (4), 872–877. https://doi.org/10.1063/1.1743424.

(15) Stubbe, J.; Nocera, D. G.; Yee, C. S.; Chang, M. C. Y. Radical Initiation in the Class I Ribonucleotide Reductase: Long-Range Proton-Coupled Electron Transfer? *Chem. Rev.* **2003**, *103* (6), 2167–2202. https://doi.org/10.1021/cr020421u.

(16) Marcus, R. A. On the Theory of Oxidation-Reduction Reactions Involving Electron Transfer. I. *J. Chem. Phys.* **1956**, *24* (5), 966–978. https://doi.org/10.1063/1.1742723.

(17) Chang, I.-J.; Gray, H. B.; Winkler, J. R. High-Driving-Force Electron Transfer in Metalloproteins: Intramolecular Oxidation of Ferrocytochrome c by Ru(2,2'-Bpy)$_2$(Im)(His-33)$^{3+}$. *J. Am. Chem. Soc.* **1991**, *113* (18), 7056–7057. https://doi.org/10.1021/ja00018a064.

(18) Weinberg, D. R.; Gagliardi, C. J.; Hull, J. F.; Murphy, C. F.; Kent, C. A.; Westlake, B. C.; Paul, A.; Ess, D. H.; McCafferty, D. G.; Meyer, T. J. Proton-Coupled Electron Transfer. *Chem. Rev.* **2012**, *112* (7), 4016–4093. https://doi.org/10.1021/cr200177j.

(19) Gray, H. B.; Winkler, J. R. Long-Range Electron Transfer. *Proc. Natl. Acad. Sci. U.S.A.* **2005**, *102* (10), 3534–3539. https://doi.org/10.1073/pnas.0408029102.

(20) Vallee, B. L.; Williams, R. J. P. Metalloenzymes: The Entatic Nature of Their Active Sites. *Proc. Natl. Acad. Sci. U.S.A.* **1968**, *59* (2), 498–505. https://doi.org/10.1073/pnas.59.2.498.

(21) Malmström, B. G. Rack-Induced Bonding in Blue-Copper Proteins. *Eur. J. Biochem.* **1994**, *223* (3), 711–718. https://doi.org/10.1111/j.1432-1033.1994.tb19044.x.

(22) Giese, B.; Wang, M.; Gao, J.; Stoltz, M.; Müller, P.; Graber, M. Electron Relay Race in Peptides. *J. Org. Chem.* **2009**, *74* (10), 3621–3625. https://doi.org/10.1021/jo900375f.

(23) Balabin, I. A.; Hu, X.; Beratan, D. N. Exploring Biological Electron Transfer Pathway Dynamics with the Pathways Plugin for VMD. *J. Comput. Chem.* **2012**, *33* (8), 906–910. https://doi.org/10.1002/jcc.22927.

(24) Polizzi, N. F.; Migliore, A.; Therien, M. J.; Beratan, D. N. Defusing Redox Bombs? *Proc. Natl. Acad. Sci. U.S.A.* **2015**, *112* (35), 10821–10822. https://doi.org/10.1073/pnas.1513520112.

(25) Kang, S. A.; Hoke, K. R.; Crane, B. R. Solvent Isotope Effects on Interfacial Protein Electron Transfer in Crystals and Electrode Films. *J. Am. Chem. Soc.* **2006**, *128* (7), 2346–2355. https://doi.org/10.1021/ja0557482.

(26) Shih, C.; Museth, A. K.; Abrahamsson, M.; Blanco-Rodriguez, A. M.; Di Bilio, A. J.; Sudhamsu, J.; Crane, B. R.; Ronayne, K. L.; Towrie, M.; Vlček, A.; Richards, J. H.; Winkler, J. R.; Gray, H. B. Tryptophan-Accelerated Electron Flow Through Proteins. *Science* **2008**, *320* (5884), 1760–1762. https://doi.org/10.1126/science.1158241.

(27) Page, C. C.; Moser, C. C.; Chen, X.; Dutton, P. L. Natural Engineering Principles of Electron Tunnelling in Biological Oxidation–Reduction. *Nature* **1999**, *402* (6757), 47–52. https://doi.org/10.1038/46972.

(28) Gray, H. B.; Winkler, J. R. Electron Tunneling through Proteins. *Q. Rev. Biophys.* **2003**, *36* (3), 341–372. https://doi.org/10.1017/S0033583503003913.

(29) Weber, D. S.; Warren, J. J. A Survey of Methionine-Aromatic Interaction Geometries in the Oxidoreductase Class of Enzymes: What Could Met-Aromatic Interactions Be Doing Near Metal Sites? *J. Inorg. Biochem.* **2018**, *186*, 34–41. https://doi.org/10.1016/j.jinorgbio.2018.05.008.

(30) Gray, H. B.; Winkler, J. R. Hole Hopping Through Tyrosine/Tryptophan Chains Protects Proteins from Oxidative Damage. *Proc. Natl. Acad. Sci. U.S.A.* **2015**, *112* (35), 10920–10925. https://doi.org/10.1073/pnas.1512704112.

(31) Warren, J. J.; Herrera, N.; Hill, M. G.; Winkler, J. R.; Gray, H. B. Electron Flow through Nitrotyrosinate in Pseudomonas Aeruginosa Azurin. *J. Am. Chem. Soc.* **2013**, *135* (30), 11151–11158. https://doi.org/10.1021/ja403734n.

(32) Teo, R. D.; Wang, R.; Smithwick, E. R.; Migliore, A.; Therien, M. J.; Beratan, D. N. Mapping Hole Hopping Escape Routes in Proteins. *Proc. Natl. Acad. Sci. U.S.A.* **2019**, *116* (32), 15811–15816. https://doi.org/10.1073/pnas.1906394116.

(33) Takematsu, K.; Williamson, H. R.; Nikolovski, P.; Kaiser, J. T.; Sheng, Y.; Pospíšil, P.; Towrie, M.; Heyda, J.; Hollas, D.; Záliš, S.; Gray, H. B.; Vlček, A.; Winkler, J. R. Two Tryptophans Are Better Than One in Accelerating Electron Flow through a Protein. *ACS Cent. Sci.* **2019**, *5* (1), 192–200. https://doi.org/10.1021/acscentsci.8b00882.

(34) Tazhigulov, R. N.; Gayvert, J. R.; Wei, M.; Bravaya, K. B. EMap: A Web Application for Identifying and Visualizing Electron or Hole Hopping Pathways in Proteins. *J. Phys. Chem. B* **2019**, *123* (32), 6946–6951. https://doi.org/10.1021/acs.jpcb.9b04816.

(35) Hagras, M. A.; Stuchebrukhov, A. A. Electron Tunneling in Proteins Program. *J. Comput. Chem.* **2016**, *37* (15), 1388–1395. https://doi.org/10.1002/jcc.24348.

(36) DiMauro, S.; Schon, E. A. Mitochondrial Respiratory-Chain Diseases. *N. Engl. J. Med.* **2003**, *348* (26), 2656–2668. https://doi.org/10.1056/NEJMra022567.

(37) Rich, P. R.; Maréchal, A. The Mitochondrial Respiratory Chain. *Essays Biochem.* **2010**, *47*, 1–23. https://doi.org/10.1042/bse0470001.

(38) *Biological Inorganic Chemistry: Structure and Reactivity*; Bertini, I., Gray, H. B., Stiefel, E. I., Valentine, J. S., Eds.; University Science Books, 2006.

(39) Johnson, M. P. Photosynthesis. *Essays Biochem.* **2016**, *60* (3), 255–273. https://doi.org/10.1042/EBC20160016.

(40) Shen, J.-R. The Structure of Photosystem II and the Mechanism of Water Oxidation in Photosynthesis. *Annu. Rev. Plant Biol.* **2015**, *66* (1), 23–48. https://doi.org/10.1146/annurev-arplant-050312-120129.

(41) Wege, S. Plants Increase Photosynthesis Efficiency by Lowering the Proton Gradient across the Thylakoid Membrane. *Plant Physiol.* **2020**, *182* (4), 1812–1813. https://doi.org/10.1104/pp.20.00273.

(42) Liu, J.; Chakraborty, S.; Hosseinzadeh, P.; Yu, Y.; Tian, S.; Petrik, I.; Bhagi, A.; Lu, Y. Metalloproteins Containing Cytochrome, Iron–Sulfur, or Copper Redox Centers. *Chem. Rev.* **2014**, *114* (8), 4366–4469. https://doi.org/10.1021/cr400479b.

(43) Barry, S. M.; Challis, G. L. Mechanism and Catalytic Diversity of Rieske Non-Heme Iron-Dependent Oxygenases. *ACS Catal.* **2013**, *3* (10), 2362–2370. https://doi.org/10.1021/cs400087p.

(44) Solomon, E. I.; Heppner, D. E.; Johnston, E. M.; Ginsbach, J. W.; Cirera, J.; Qayyum, M.; Kieber-Emmons, M. T.; Kjaergaard, C. H.; Hadt, R. G.; Tian, L. Copper Active Sites in Biology. *Chem. Rev.* **2014**, *114* (7), 3659–3853. https://doi.org/10.1021/cr400327t.

(45) Lancaster, K. M. Biological Outer-Sphere Coordination. *Struct. Bond.* **2012**, *142*, 119–153.

(46) Warren, J. J.; Lancaster, K. M.; Richards, J. H.; Gray, H. B. Inner- and Outer-Sphere Metal Coordination in Blue Copper Proteins. *J. Inorg. Biochem.* **2012**, *115*, 119–126. https://doi.org/10.1016/j.jinorgbio.2012.05.002.

(47) Berry, S. M.; Ralle, M.; Low, D. W.; Blackburn, N. J.; Lu, Y. Probing the Role of Axial Methionine in the Blue Copper Center of Azurin with Unnatural Amino Acids. *J. Am. Chem. Soc.* **2003**, *125* (29), 8760–8768. https://doi.org/10.1021/ja029699u.

(48) Garner, D. K.; Vaughan, M. D.; Hwang, H. J.; Savelieff, M. G.; Berry, S. M.; Honek, J. F.; Lu, Y. Reduction Potential Tuning of the Blue Copper Center in Pseudomonas Aeruginosa Azurin by the Axial Methionine as Probed by Unnatural Amino Acids. *J. Am. Chem. Soc.* **2006**, *128* (49), 15608–15617. https://doi.org/10.1021/ja062732i.

(49) Lancaster, K. M.; Sproules, S.; Palmer, J. H.; Richards, J. H.; Gray, H. B. Outer-Sphere Effects on Reduction Potentials of Copper Sites in Proteins: The Curious Case of High Potential Type 2 C112D/M121E Pseudomonas Aeruginosa Azurin. *J. Am. Chem. Soc.* **2010**, *132* (41), 14590–14595. https://doi.org/10.1021/ja105731x.

(50) Lancaster, K. M.; Zaballa, M.-E.; Sproules, S.; Sundararajan, M.; DeBeer, S.; Richards, J. H.; Vila, A. J.; Neese, F.; Gray, H. B. Outer-Sphere Contributions to the Electronic Structure of Type Zero Copper Proteins. *J. Am. Chem. Soc.* **2012**, *134* (19), 8241–8253. https://doi.org/10.1021/ja302190r.

(51) Lancaster, K. M.; Farver, O.; Wherland, S.; Crane, E. J.; Richards, J. H.; Pecht, I.; Gray, H. B. Electron Transfer Reactivity of Type Zero Pseudomonas Aeruginosa Azurin. *J. Am. Chem. Soc.* **2011**, *133* (13), 4865–4873. https://doi.org/10.1021/ja1093919.

(52) Gibbs, C. A.; Fedoretz-Maxwell, B. P.; Warren, J. J. On the Roles of Methionine and the Importance of Its Microenvironments in Redox Metalloproteins. *Dalton Trans.* **2022**, *51* (13), 4976–4985. https://doi.org/10.1039/D1DT04387K.

(53) Berry, S. M.; Baker, M. H.; Reardon, N. J. Reduction Potential Variations in Azurin Through Secondary Coordination Sphere Phenylalanine Incorporations. *J. Inorg. Biochem.* **2010**, *104*, 1071–1078. https://doi.org/doi: 10.1016/j.jinorgbio.2010.06.004.

(54) Nar, H.; Messerschmidt, A.; Huber, R.; van de Kamp, M.; Canters, G. W. Crystal Structure Analysis of Oxidized Pseudomonas Aeruginosa Azurin at PH 5.5 and PH 9.0. *J. Mol. Biol.* **1991**, *221* (3), 765–772. https://doi.org/10.1016/0022-2836(91)80173-R.

(55) Marshall, N. M.; Garner, D. K.; Wilson, T. D.; Gao, Y.-G.; Robinson, H.; Nilges, M. J.; Lu, Y. Rationally Tuning the Reduction Potential of a Single Cupredoxin Beyond the Natural Range. *Nature* **2009**, *462* (7269), 113–116. https://doi.org/10.1038/nature08551.

(56) Yanagisawa, S.; Banfield, M. J.; Dennison, C. The Role of Hydrogen Bonding at the Active Site of a Cupredoxin: The Phe114Pro Azurin Variant†,‡. *Biochemistry* **2006**, *45* (29), 8812–8822. https://doi.org/10.1021/bi0606851.

(57) Chen, X.; Tao, Y.; Li, J.; Dai, H.; Sun, W.; Huang, X.; Wei, Z. Aromatic Residues Regulating Electron Relay Ability of S-Containing Amino Acids by Formations of S∴π Multicenter Three-Electron Bonds in Proteins. *J. Phys. Chem. C* **2012**, *116* (37), 19682–19688. https://doi.org/10.1021/jp306154x.

(58) Di Bilio, A. J.; Crane, B. R.; Wehbi, W. A.; Kiser, C. N.; Abu-Omar, M. M.; Carlos, R. M.; Richards, J. H.; Winkler, J. R.; Gray, H. B. Properties of Photogenerated Tryptophan and Tyrosyl Radicals in Structurally Characterized Proteins Containing Rhenium(I) Tricarbonyl Diimines. *J. Am. Chem. Soc.* **2001**, *123* (13), 3181–3182. https://doi.org/10.1021/ja0043183.

(59) Stubbe, J.; van der Donk, W. A. Protein Radicals in Enzyme Catalysis. *Chem. Rev.* **1998**, *98* (2), 705–762. https://doi.org/10.1021/cr9400875.

(60) Lukacs, A.; Eker, A. P. M.; Byrdin, M.; Brettel, K.; Vos, M. H. Electron Hopping through the 15 Å Triple Tryptophan Molecular Wire in DNA Photolyase Occurs within 30 Ps. *J. Am. Chem. Soc.* **2008**, *130* (44), 14394–14395. https://doi.org/10.1021/ja805261m.

(61) Park, H.-W.; Kim, S.-T.; Sancar, A.; Deisenhofer, J. Crystal Structure of DNA Photolyase from *Escherichia Coli*. *Science* **1995**, *268* (5219), 1866–1872. https://doi.org/10.1126/science.7604260.

(62) Birrell, J. A.; Rüdiger, O.; Reijerse, E. J.; Lubitz, W. Semisynthetic Hydrogenases Propel Biological Energy Research into a New Era. *Joule* **2017**, *1* (1), 61–76. https://doi.org/10.1016/j.joule.2017.07.009.

(63) Nicolet, Y.; Piras, C.; Legrand, P.; Hatchikian, C. E.; Fontecilla-Camps, J. C. Desulfovibrio Desulfuricans Iron Hydrogenase: The Structure Shows Unusual Coordination to an Active Site Fe Binuclear Center. *Structure* **1999**, *7* (1), 13–23. https://doi.org/10.1016/S0969-2126(99)80005-7.

(64) Winkler, J. R.; Gray, H. B. Electron Flow Through Biological Molecules: Does Hole Hopping Protect Proteins from Oxidative Damage? *Q. Rev. Biophys.* **2015**, *48* (4), 411–420. https://doi.org/10.1017/S0033583515000062.

(65) Stubbe, J.; Nocera, D. G. Radicals in Biology: Your Life Is in Their Hands. *J. Am. Chem. Soc.* **2021**, *143* (34), 13463–13472. https://doi.org/10.1021/jacs.1c05952.

(66) Minnihan, E. C.; Nocera, D. G.; Stubbe, J. Reversible, Long-Range Radical Transfer in *E. Coli* Class Ia Ribonucleotide Reductase. *Acc. Chem. Res.* **2013**, *46* (11), 2524–2535. https://doi.org/10.1021/ar4000407.

(67) Ravichandran, K. R.; Taguchi, A. T.; Wei, Y.; Tommos, C.; Nocera, D. G.; Stubbe, J. A >200 MeV Uphill Thermodynamic Landscape for Radical Transport in *Escherichia Coli* Ribonucleotide Reductase Determined Using Fluorotyrosine-Substituted Enzymes. *J. Am. Chem. Soc.* **2016**, *138* (41), 13706–13716. https://doi.org/10.1021/jacs.6b08200.

(68) Strushkevich, N.; MacKenzie, F.; Cherkesova, T.; Grabovec, I.; Usanov, S.; Park, H.-W. Structural Basis for Pregnenolone Biosynthesis by the Mitochondrial Monooxygenase System. *Proc. Natl. Acad. Sci. U.S.A.* **2011**, *108* (25), 10139–10143. https://doi.org/10.1073/pnas.1019441108.

(69) Harriman, Anthony. Further Comments on the Redox Potentials of Tryptophan and Tyrosine. *J. Phys. Chem.* **1987**, *91* (24), 6102–6104. https://doi.org/10.1021/j100308a011.

(70) Levine, R. L.; Moskovitz, J.; Stadtman, E. R. Oxidation of Methionine in Proteins: Roles in Antioxidant Defense and Cellular Regulation. *IUBMB Life* **2000**, *50*, 301–307. https://doi.org/10.1080/713803735.

(71) Kim, G.; Weiss, S. J.; Levine, R. L. Methionine Oxidation and Reduction in Proteins. *Biochim. Biophys. Acta* **2014**, *1840* (2). https://doi.org/10.1016/j.bbagen.2013.04.038.

(72) Brunelle, P.; Schöneich, C.; Rauk, A. One-Electron Oxidation of Methionine Peptides — Stability of the Three-Electron S—N(Amide) Bond. *Can. J. Chem.* **2006**, *84* (6), 893–904. https://doi.org/10.1139/v06-079.

(73) Wang, M.; Gao, J.; Müller, P.; Giese, B. Electron Transfer in Peptides with Cysteine and Methionine as Relay Amino Acids. *Angew. Chem. Int. Ed.* **2009**, *48* (23), 4232–4234. https://doi.org/10.1002/anie.200900827.

(74) Sun, W.; Ren, H.; Tao, Y.; Xiao, D.; Qin, X.; Deng, L.; Shao, M.; Gao, J.; Chen, X. Two Aromatic Rings Coupled a Sulfur-Containing Group to Favor Protein Electron Transfer by Instantaneous Formations of Π∴S:Π↔π:S∴π or Π∴π:S↔π:Π∴S Five-Electron Bindings. *J. Phys. Chem. C* **2015**, *119* (17), 9149–9158. https://doi.org/10.1021/acs.jpcc.5b01740.

(75) Orabi, E. A.; English, A. M. Modeling Protein S–Aromatic Motifs Reveals Their Structural and Redox Flexibility. *J. Phys. Chem. B* **2018**, *122* (14), 3760–3770. https://doi.org/10.1021/acs.jpcb.8b00089.

(76) Orabi, E. A.; English, A. M. Sulfur-Aromatic Interactions: Modeling Cysteine and Methionine Binding to Tyrosinate and Histidinium Ions to Assess Their Influence on Protein Electron Transfer. *Isr. J. Chem.* **2016**, *56* (9–10), 872–885. https://doi.org/10.1002/ijch.201600047.

(77) Voet, D.; Voet, J. G. *Biochemistry*, 4th Ed.; John Wiley and Sons: New York, 2010.

(78) Bodner, B. L.; Jackman, L. M.; Morgan, R. S. NMR Study of 1:1 Complexes Between Divalent Sulfur and Aromatic Compounds: A Model for Interactions in Globular Proteins. *Biochem. Biophys. Res. Commun.* **1980**, *94* (3), 807–813. https://doi.org/10.1016/0006-291X(80)91306-6.

(79) Chung, W. J.; Ammam, M.; Gruhn, N. E.; Nichol, G. S.; Singh, W. P.; Wilson, G. S.; Glass, R. S. Interactions of Arenes and Thioethers Resulting in Facilitated Oxidation. *Org. Lett.* **2009**, *11* (2), 397–400. https://doi.org/10.1021/ol802683s.

(80) Monney, N. P.-A.; Bally, T.; Bhagavathy, G. S.; Glass, R. S. Spectroscopic Evidence for a New Type of Bonding between a Thioether Radical Cation and a Phenyl Group. *Org. Lett.* **2013**, *15* (19), 4932–4935. https://doi.org/10.1021/ol402126f.

(81) Pettersen, E. F.; Goddard, T. D.; Huang, C. C.; Couch, G. S.; Greenblatt, D. M.; Meng, E. C.; Ferrin, T. E. UCSF Chimera - A Visualization System for Exploratory Research and Analysis. *J. Comput. Chem.* **2004**, *25* (13), 1605–1612. https://doi.org/10.1002/jcc.20084.

(82) Morgan, R. S.; Tatsch, C. E.; Gushard, R. H.; McAdon, J. M.; Warme, P. K. Chains of Alternating Sulfur and π-Bonded Atoms in Eight Small Proteins. *Int. J. Pept. Protein Res.* **1978**, *11* (3), 209–217. https://doi.org/10.1111/j.1399-3011.1978.tb02841.x.

(83) Reid, K. S. C.; Lindley, P. F.; Thornton, J. M. Sulphur-Aromatic Interactions in Proteins. *FEBS Lett.* **1985**, *190* (2), 209–213. https://doi.org/10.1016/0014-5793(85)81285-0.

(84) Warme, P. K.; Morgan, R. S. A Survey of Amino Acid Side-Chain Interactions in 21 Proteins. *J. Mol. Biol.* **1978**, *118* (3), 289–304. https://doi.org/10.1016/0022-2836(78)90229-2.

(85) Valley, C. C.; Cembran, A.; Perlmutter, J. D.; Lewis, A. K.; Labello, N. P.; Gao, J.; Sachs, J. N. The Methionine-Aromatic Motif Plays a Unique Role in Stabilizing Protein Structure. *J. Biol. Chem.* **2012**, *287* (42), 34979–34991. https://doi.org/10.1074/jbc.M112.374504.

(86) Tatko, C. D.; Waters, M. L. Investigation of the Nature of the Methionine-π Interaction in β-Hairpin Peptide Model Systems. *Protein Sci.* **2004**, *13* (9), 2515–2522. https://doi.org/10.1110/ps.04820104.

(87) Gómez-Tamayo, J. C.; Cordomí, A.; Olivella, M.; Mayol, E.; Fourmy, D.; Pardo, L. Analysis of the Interactions of Sulfur-Containing Amino Acids in Membrane Proteins: Interactions Involving Met and Cys in Membrane Proteins. *Protein Sci.* **2016**, *25* (8), 1517–1524. https://doi.org/10.1002/pro.2955.

(88) Ringer, A. L.; Senenko, A.; Sherrill, C. D. Models of S/π Interactions in Protein Structures: Comparison of the H_2S–Benzene Complex with PDB Data. *Protein Sci.* **2007**, *16* (10), 2216–2223. https://doi.org/10.1110/ps.073002307.

(89) Gibbs, C. A.; Weber, D. S.; Warren, J. J. Clustering of Aromatic Amino Acid Residues around Methionine in Proteins. *Biomolecules* **2022**, *12* (1), 1–6. https://doi.org/10.3390/biom12010006.

(90) Weber, D. S.; Warren, J. J. The Interaction Between Methionine and Two Aromatic Amino Acids Is an Abundant and Multifunctional Motif in Proteins. *Arch. Biochem. Biophys.* **2019**, *672*, 108053. https://doi.org/10.1016/j.abb.2019.07.018.

(91) Kathiresan, M.; English, A. M. LC-MS/MS Suggests That Hole Hopping in Cytochrome *c* Peroxidase Protects Its Heme from Oxidative Modification by Excess H_2O_2. *Chem. Sci.* **2017**, *8* (2), 1152–1162. https://doi.org/10.1039/C6SC03125K.

(92) Kathiresan, M.; English, A. M. LC-MS/MS Proteoform Profiling Exposes Cytochrome *c* Peroxidase Self-Oxidation in Mitochondria and Functionally Important Hole Hopping from Its Heme. *J. Am. Chem. Soc.* **2018**, *140* (38), 12033–12039. https://doi.org/10.1021/jacs.8b05966.

(93) Kim, K.; Erman, J. E. Methionine Modification in Cytochrome-c Peroxidase. *Biochim. Biophys. Acta* **1988**, *954*, 95–107. https://doi.org/10.1016/0167-4838(88)90059-3.

(94) Yukl, E. T.; Williamson, H. R.; Higgins, L.; Davidson, V. L.; Wilmot, C. M. Oxidative Damage in MauG: Implications for the Control of High-Valent Iron Species and Radical Propagation Pathways. *Biochemistry* **2013**, *52* (52), 9447–9455. https://doi.org/10.1021/bi401441h.

(95) Finzel, B. C.; Poulos, T. L.; Kraut, J. Crystal Structure of Yeast Cytochrome c Peroxidase Refined at 1.7-A Resolution. *J. Biol. Chem.* **1984**, *259* (21), 13027–13036. https://doi.org/10.1016/S0021-9258(18)90651-4.

(96) Werst, D. W. Radical-Cation Complexes Formed by π-Lone Pair Interactions. *J. Phys. Chem.* **1992**, *96* (9), 3640–3646. https://doi.org/10.1021/j100188a017.

(97) Yokoi, H.; Hatta, A.; Ishiguro, K.; Sawaki, Y. Formation of σ- and π-Type Dimer Radical Cations by the Photochemical One-Electron Oxidation of Aromatic Sulfides. *J. Am. Chem. Soc.* **1998**, *120* (49), 12728–12733. https://doi.org/10.1021/ja982595s.

(98) Glass, R. S.; Hug, G. L.; Schöneich, C.; Wilson, G. S.; Kuznetsova, L.; Lee, T.; Ammam, M.; Lorance, E.; Nauser, T.; Nichol, G. S.; Yamamoto, T. Neighboring Amide Participation in Thioether Oxidation: Relevance to Biological Oxidation. *J. Am. Chem. Soc.* **2009**, *131* (38), 13791–13805. https://doi.org/10.1021/ja904895u.

(99) Wang, D.; Fujii, A. Spectroscopic Observation of Two-Center Three-Electron Bonded (Hemi-Bonded) Structures of $(H_2S)_n^+$ Clusters in the Gas Phase. *Chem. Sci.* **2017**, *8* (4), 2667–2670. https://doi.org/10.1039/C6SC05361K.

(100) Xie, M.; Shen, Z.; Wang, D.; Fujii, A.; Lee, Y.-P. Spectral Characterization of Three-Electron Two-Center (3e–2c) Bonds of Gaseous $CH_3S\therefore S(H)CH_3$ and $(CH_3SH)_2^+$ and Enhancement of the 3e–2c Bond upon Protonation. *J. Phys. Chem. Lett.* **2018**, *9* (13), 3725–3730. https://doi.org/10.1021/acs.jpclett.8b01491.

(101) Hendon, C. H.; Carbery, D. R.; Walsh, A. Three-Electron Two-Centred Bonds and the Stabilisation of Cationic Sulfur Radicals. *Chem. Sci.* **2014**, *5* (4), 1390–1395. https://doi.org/10.1039/C3SC53432D.

(102) Zhao, Q.; Zhang, S.; Zhang, X.; Lei, L.; Ma, W.; Ma, C.; Song, L.; Chen, J.; Pan, B.; Xing, B. Cation–Pi Interaction: A Key Force for Sorption of Fluoroquinolone Antibiotics on Pyrogenic Carbonaceous Materials. *Environ. Sci. Technol.* **2017**, *51* (23), 13659–13667. https://doi.org/10.1021/acs.est.7b02317.

(103) Rupakheti, C. R.; Roux, B.; Dehez, F.; Chipot, C. Modeling Induction Phenomena in Amino Acid Cation–π Interactions. *Theor. Chem. Acc.* **2018**, *137* (12), 174. https://doi.org/10.1007/s00214-018-2376-z.

(104) Mecozzi, S.; West, A. P.; Dougherty, D. A. Cation-Pi Interactions in Aromatics of Biological and Medicinal Interest: Electrostatic Potential Surfaces as a Useful Qualitative Guide. *Proc. Natl. Acad. Sci. U.S.A.* **1996**, *93* (20), 10566–10571. https://doi.org/10.1073/pnas.93.20.10566.

(105) Sarmah, N.; Bhattacharyya, P. Kr. Behaviour of Cation–Pi Interaction in Presence of External Electric Field. *RSC Adv.* **2016**, *6* (102), 100008–100015. https://doi.org/10.1039/C6RA21334K.

(106) Newberry, R. W.; Raines, R. T. Secondary Forces in Protein Folding. *ACS Chem. Biol.* **2019**, *14* (8), 1677–1686. https://doi.org/10.1021/acschembio.9b00339.

(107) Philip, V.; Harris, J.; Adams, R.; Nguyen, D.; Spiers, J.; Baudry, J.; Howell, E. E.; Hinde, R. J. A Survey of Aspartate−Phenylalanine and Glutamate−Phenylalanine Interactions in the Protein Data Bank: Searching for Anion−π Pairs. *Biochemistry* **2011**, *50* (14), 2939–2950. https://doi.org/10.1021/bi200066k.

(108) Chakravarty, S.; Ung, A. R.; Moore, B.; Shore, J.; Alshamrani, M. A Comprehensive Analysis of Anion–Quadrupole Interactions in Protein Structures. *Biochemistry* **2018**, *57* (12), 1852–1867. https://doi.org/10.1021/acs.biochem.7b01006.

(109) Nishio, M.; Umezawa, Y.; Fantini, J.; Weiss, M. S.; Chakrabarti, P. CH–π Hydrogen Bonds in Biological Macromolecules. *Phys. Chem. Chem. Phys.* **2014**, *16* (25), 12648–12683. https://doi.org/10.1039/C4CP00099D.

(110) Wang, J.; Yao, L. Dissecting C−H···π and N−H···π Interactions in Two Proteins Using a Combined Experimental and Computational Approach. *Sci. Rep.* **2019**, *9* (1), 20149. https://doi.org/10.1038/s41598-019-56607-4.

(111) Lakowicz, J. R. *Principles of Fluoresence Spectroscopy*, 2nd Ed.; Kleuwer Academic/Plenum: New York, 1999.

(112) Slater, L. S.; Callis, P. R. Molecular Orbital Theory of the 1La and 1Lb States of Indole. 2. An Ab Initio Study. *J. Phys. Chem.* **1995**, *99* (21), 8572–8581. https://doi.org/10.1021/j100021a020.

(113) Alexander Ross, J. B.; Laws, W. R.; Rousslang, K. W.; Wyssbrod, H. R. Tyrosine Fluorescence and Phosphorescence from Proteins and Polypeptides. In *Topics in Fluorescence Spectroscopy*; Lakowicz, J. R., Ed.; Topics in Fluorescence Spectroscopy; Kluwer Academic Publishers: Boston, 2002; Vol. 3, pp 1–64. https://doi.org/10.1007/0-306-47059-4_1.

(114) Jovanovic, S. V.; Harriman, A.; Simic, M. G. Electron-Transfer Reactions of Tryptophan and Tyrosine Derivatives. *J. Phys. Chem.* **1986**, *90* (9), 1935–1939. https://doi.org/10.1021/j100400a039.

(115) Wardman, P. Reduction Potentials of One-Electron Couples Involving Free Radicals in Aqueous Solution. *J. Phys. Chem. Ref. Data* **1989**, *18* (4), 1637–1755. https://doi.org/10.1063/1.555843.

(116) Steenken, S.; Neta, P. One-Electron Redox Potentials of Phenols. Hydroxy- and Aminophenols and Related Compounds of Biological Interest. *J. Phys. Chem.* **1982**, *86* (18), 3661–3667. https://doi.org/10.1021/j100215a033.

(117) Smith, A. T.; Doyle, W. A.; Dorlet, P.; Ivancich, A. Spectroscopic Evidence for an Engineered, Catalytically Active Trp Radical That Creates the Unique Reactivity of Lignin Peroxidase. *Proc. Natl. Acad. Sci. U.S.A.* **2009**, *106* (38), 16084–16089. https://doi.org/10.1073/pnas.0904535106.

(118) Sollewijn Gelpke, M. D.; Lee, J.; Gold, M. H. Lignin Peroxidase Oxidation of Veratryl Alcohol: Effects of the Mutants H82A, Q222A, W171A, and F267L. *Biochemistry* **2002**, *41* (10), 3498–3506. https://doi.org/10.1021/bi011930d.

(119) Blodig, W.; Smith, A. T.; Doyle, W. A.; Piontek, K. Crystal Structures of Pristine and Oxidatively Processed Lignin Peroxidase Expressed in Escherichia Coli and of the W171F Variant That Eliminates the Redox Active Tryptophan 171. Implications for the Reaction Mechanism. *J. Mol. Biol.* **2001**, *305* (4), 851–861. https://doi.org/10.1006/jmbi.2000.4346.

(120) Lubitz, W.; Chrysina, M.; Cox, N. Water Oxidation in Photosystem II. *Photosynth. Res.* **2019**, *142* (1), 105–125. https://doi.org/10.1007/s11120-019-00648-3.

(121) Nelson, N.; Yocum, C. F. Structure and Function of Photosystems I and II. *Annu. Rev. Plant Biol.* **2006**, *57* (1), 521–565. https://doi.org/10.1146/annurev.arplant.57.032905.105350.

(122) Styring, S.; Sjöholm, J.; Mamedov, F. Two Tyrosines That Changed the World: Interfacing the Oxidizing Power of Photochemistry to Water Splitting in Photosystem II. *Biochim. Biophys. Acta Bioenerg.* **2012**, *1817* (1), 76–87. https://doi.org/10.1016/j.bbabio.2011.03.016.

(123) Costentin, C.; Robert, M.; Savéant, J.-M.; Tard, C. H-Bond Relays in Proton-Coupled Electron Transfers. Oxidation of a Phenol Concerted with Proton Transport to a Distal Base through an OH Relay. *Phys. Chem. Chem. Phys.* **2011**, *13* (12), 5353. https://doi.org/10.1039/c0cp02275f.

(124) Rhile, I. J.; Markle, T. F.; Nagao, H.; DiPasquale, A. G.; Lam, O. P.; Lockwood, M. A.; Rotter, K.; Mayer, J. M. Concerted Proton−Electron Transfer in the Oxidation of Hydrogen-Bonded Phenols. *J. Am. Chem. Soc.* **2006**, *128* (18), 6075–6088. https://doi.org/10.1021/ja054167+.

(125) Mayer, J. M.; Rhile, I. J.; Larsen, F. B.; Mader, E. A.; Markle, T. F.; DiPasquale, A. G. Models for Proton-Coupled Electron Transfer in Photosystem II. *Photosynth. Res.* **2006**, *87* (1), 3–20. https://doi.org/10.1007/s11120-005-8164-3.

(126) Mayer, J. M.; Rhile, I. J.; Larsen, F. B.; Mader, E. A.; Markle, T. F.; DiPasquale, A. G. Models for Proton-Coupled Electron Transfer in Photosystem II. *Photosynth. Res.* **2006**, *87* (1), 21–24. https://doi.org/10.1007/s11120-006-9053-0.

(127) Karlsson, B. G.; Aasa, R.; Malmström, B. G.; Lundberg, L. G. Rack-Induced Bonding in Blue Copper Proteins: Spectroscopic Properties and Reduction Potential of the Azurin Mutant Met-121 → Leu. *FEBS Lett.* **1989**, *253* (1–2), 99–102. https://doi.org/10.1016/0014-5793(89)80938-X.

(128) Karlsson, B. G.; Nordling, M.; Pascher, T.; Tsai, L.-C.; Sjölin, L.; Lundberg, L. G. Cassette Mutagenesis of Met121 in Azurin from *Pseudomonas Aeruginosa*. *Protein Eng.* **1991**, *4* (3), 343–349. https://doi.org/10.1093/protein/4.3.343.

(129) Murphy, L. M.; Strange, R. W.; Karlsson, B. G.; Lundberg, L. G.; Pascher, T.; Reinhammar, B.; Hasnain, S. S. Structural Characterization of Azurin from Pseudomonas Aeruginosa and Some of Its Methionine-121 Mutants. *Biochemistry* **1993**, *32* (8), 1965–1975. https://doi.org/10.1021/bi00059a013.

(130) Owenius, R.; Engström, M.; Lindgren, M.; Huber, M. Influence of Solvent Polarity and Hydrogen Bonding on the EPR Parameters of a Nitroxide Spin Label Studied by 9-GHz and 95-GHz EPR Spectroscopy and DFT Calculations. *J. Phys. Chem. A* **2001**, *105* (49), 10967–10977. https://doi.org/10.1021/jp0116914.

(131) Stoll, S.; Shafaat, H. S.; Krzystek, J.; Ozarowski, A.; Tauber, M. J.; Kim, J. E.; Britt, R. D. Hydrogen Bonding of Tryptophan Radicals Revealed by EPR at 700 GHz. *J. Am. Chem. Soc.* **2011**, *133* (45), 18098–18101. https://doi.org/10.1021/ja208462t.

(132) Shafaat, H. S.; Leigh, B. S.; Tauber, M. J.; Kim, J. E. Spectroscopic Comparison of Photogenerated Tryptophan Radicals in Azurin: Effects of Local Environment and Structure. *J. Am. Chem. Soc.* **2010**, *132* (26), 9030–9039. https://doi.org/10.1021/ja101322g.

(133) Shafaat, H. S.; Leigh, B. S.; Tauber, M. J.; Kim, J. E. Resonance Raman Characterization of a Stable Tryptophan Radical in an Azurin Mutant. *J. Phys. Chem. B* **2009**, *113* (1), 382–388. https://doi.org/10.1021/jp809329a.

(134) Larson, B. C.; Pomponio, J. R.; Shafaat, H. S.; Kim, R. H.; Leigh, B. S.; Tauber, M. J.; Kim, J. E. Photogeneration and Quenching of Tryptophan Radical in Azurin. *J. Phys. Chem. B* **2015**, *119* (29), 9438–9449. https://doi.org/10.1021/jp511523z.

(135) Warren, J. J.; Shafaat, O. S.; Winkler, J. R.; Gray, H. B. Proton-Coupled Electron Hopping in Ru-Modified *P. Aeruginosa* Azurin. *J. Biol. Inorg. Chem.* **2016**, *21* (1), 113–119. https://doi.org/gray.

(136) Bernini, C.; Andruniów, T.; Olivucci, M.; Pogni, R.; Basosi, R.; Sinicropi, A. Effects of the Protein Environment on the Spectral Properties of Tryptophan Radicals in *Pseudomonas Aeruginosa* Azurin. *J. Am. Chem. Soc.* **2013**, *135* (12), 4822–4833. https://doi.org/10.1021/ja400464n.

(137) Bleifuss, G.; Kolberg, M.; Pötsch, S.; Hofbauer, W.; Bittl, R.; Lubitz, W.; Gräslund, A.; Lassmann, G.; Lendzian, F. Tryptophan and Tyrosine Radicals in Ribonucleotide Reductase: A Comparative High-Field EPR Study at 94 GHz. *Biochemistry* **2001**, *40* (50), 15362–15368. https://doi.org/10.1021/bi010707d.

(138) Lendzian, F.; Sahlin, M.; MacMillan, F.; Bittl, R.; Fiege, R.; Pötsch, S.; Sjöberg, B.-M.; Gräslund, A.; Lubitz, W.; Lassmann, G. Electronic Structure of Neutral Tryptophan Radicals in Ribonucleotide Reductase Studied by EPR and ENDOR Spectroscopy. *J. Am. Chem. Soc.* **1996**, *118* (34), 8111–8120. https://doi.org/10.1021/ja960917r.

(139) Pogni, R.; Teutloff, C.; Lendzian, F.; Basosi, R. Tryptophan Radicals as Reaction Intermediates in Versatile Peroxidases: Multifrequency EPR, ENDOR and Density Functional Theory Studies. *Appl. Magn. Reson.* **2007**, *31* (3–4), 509–526. https://doi.org/10.1007/BF03166599.

(140) Miller, J. E.; Grădinaru, C.; Crane, B. R.; Di Bilio, A. J.; Wehbi, W. A.; Un, S.; Winkler, J. R.; Gray, H. B. Spectroscopy and Reactivity of a Photogenerated Tryptophan Radical in a Structurally Defined Protein Environment. *J. Am. Chem. Soc.* **2003**, *125* (47), 14220–14221. https://doi.org/10.1021/ja037203i.

(141) Berry, B. W.; Martínez-Rivera, M. C.; Tommos, C. Reversible Voltammograms and a Pourbaix Diagram for a Protein Tyrosine Radical. *Proc. Natl. Acad. Sci. U.S.A.* **2012**, *109* (25), 9739–9743. https://doi.org/10.1073/pnas.1112057109.

(142) Chang, T. K.; Iverson, S. A.; Rodrigues, C. G.; Kiser, C. N.; Lew, A. Y.; Germanas, J. P.; Richards, J. H. Gene Synthesis, Expression, and Mutagenesis of the Blue Copper Proteins Azurin and Plastocyanin. *Proc. Natl. Acad. Sci. U.S.A.* **1991**, *88* (4), 1325–1329. https://doi.org/10.1073/pnas.88.4.1325.

(143) Su, Y.; Zheng, Y.; Wang, S.; Zhang, S.; Yu, R.; Zhang, C. Facile Production of Tag-Free Recombinant Human Interleukin-11 by Transforming into Soluble Expression in Escherichia Coli. *Protein Expr. Purif.* **2022**, *197*, 106107. https://doi.org/10.1016/j.pep.2022.106107.

(144) Nag, N.; Khan, H.; Tripathi, T. Strategies to Improve the Expression and Solubility of Recombinant Proteins in E. Coli. In *Advances in Protein Molecular and Structural Biology Methods*; Academic Press, 2022; pp 1–12. https://doi.org/10.1016/B978-0-323-90264-9.00001-5.

(145) Pascher, T.; Bergström, J.; Malmström, B. G.; Vänngård, T.; Lundberg, L. G. Modification of the Electron-Transfer Sites of *Pseudomonas Aeruginosa* Azurin by Site-Directed Mutagenesis. *FEBS Lett.* **1989**, *258* (2), 266–268. https://doi.org/10.1016/0014-5793(89)81670-9.

(146) Karlsson, B. G.; Pascher, T.; Nordling, M.; Arvidsson, R. H. A.; Lundberg, L. G. Expression of the Blue Copper Protein Azurin from *Pseudomonas Aeruginosa* in *Escherichia Coli*. *FEBS Lett.* **1989**, *246* (1–2), 211–217. https://doi.org/10.1016/0014-5793(89)80285-6.

(147) Berera, R.; van Grondelle, R.; Kennis, J. T. M. Ultrafast Transient Absorption Spectroscopy: Principles and Application to Photosynthetic Systems. *Photosynth. Res.* **2009**, *101* (2–3), 105–118. https://doi.org/10.1007/s11120-009-9454-y.

(148) Miao, T. J.; Tang, J. Characterization of Charge Carrier Behavior in Photocatalysis Using Transient Absorption Spectroscopy. *J. Chem. Phys.* **2020**, *152* (19), 194201. https://doi.org/10.1063/5.0008537.

(149) Hagen, W. R. EPR Spectroscopy. In *Practical Approaches to Biological Inorganic Chemistry*; Elsevier, 2020; pp 121–154. https://doi.org/10.1016/B978-0-444-64225-7.00004-3.

(150) Elgrishi, N.; Rountree, K. J.; McCarthy, B. D.; Rountree, E. S.; Eisenhart, T. T.; Dempsey, J. L. A Practical Beginner's Guide to Cyclic Voltammetry. *J. Chem. Educ.* **2018**, *95* (2), 197–206. https://doi.org/10.1021/acs.jchemed.7b00361.

(151) Hosseinzadeh, P.; Marshall, N. M.; Chacón, K. N.; Yu, Y.; Nilges, M. J.; New, S. Y.; Tashkov, S. A.; Blackburn, N. J.; Lu, Y. Design of a Single Protein That Spans the Entire 2-V Range of Physiological Redox Potentials. *Proc. Natl. Acad. Sci. U.S.A.* **2016**, *113* (2), 262–267. https://doi.org/10.1073/pnas.1515897112.

(152) Scott, K. Electrochemical Principles and Characterization of Bioelectrochemical Systems. In *Microbial Electrochemical and Fuel Cells*; Elsevier, 2016; pp 29–66. https://doi.org/10.1016/B978-1-78242-375-1.00002-2.

(153) Venton, B. J.; DiScenza, D. J. Voltammetry. In *Electrochemistry for Bioanalysis*; Elsevier, 2020; pp 27–50. https://doi.org/10.1016/B978-0-12-821203-5.00004-X.

(154) McGaughey, G. B.; Gagné, M.; Rappé, A. K. π-Stacking Interactions. Alive and Well in Proteins. *J. Biol. Chem.* **1998**, *273* (25), 15458–15463. https://doi.org/10.1074/jbc.273.25.15458.

(155) Shao, J.; Kuiper, B. P.; Thunnissen, A.-M. W. H.; Cool, R. H.; Zhou, L.; Huang, C.; Dijkstra, B. W.; Broos, J. The Role of Tryptophan in π Interactions in Proteins: An Experimental Approach. *J. Am. Chem. Soc.* **2022**, *144* (30), 13815–13822. https://doi.org/10.1021/jacs.2c04986.

(156) Dougherty, D. A. Cation-π Interactions Involving Aromatic Amino Acids. *J. Nutr.* **2007**, *137* (6), 1504S-1508S. https://doi.org/10.1093/jn/137.6.1504S.

(157) Gober, J. G.; Ghodge, S. V.; Bogart, J. W.; Wever, W. J.; Watkins, R. R.; Brustad, E. M.; Bowers, A. A. P450-Mediated Non-Natural Cyclopropanation of Dehydroalanine-Containing Thiopeptides. *ACS Chem. Biol.* **2017**, *12* (7), 1726–1731. https://doi.org/10.1021/acschembio.7b00358.

(158) Skrzypczak-Jankun, E.; Bross, R. A.; Carroll, R. T.; Dunham, W. R.; Funk, M. O. Three-Dimensional Structure of a Purple Lipoxygenase. *J. Am. Chem. Soc.* **2001**, *123* (44), 10814–10820. https://doi.org/10.1021/ja011759t.

(159) Burstein, E. A.; Vedenkina, N. S.; Ivkova, M. N. Fluorescence and the Location of Tryptophan Residues in Protein Molecules. *Photochem. Photobiol.* **1973**, *18* (4), 263–279. https://doi.org/10.1111/j.1751-1097.1973.tb06422.x.

(160) Fedoretz-Maxwell, B. P.; Shin, C. H.; MacNeil, G. A.; Worrall, L. J.; Park, R.; Strynadka, N. C. J.; Walsby, C. J.; Warren, J. J. The Impact of Second Coordination Sphere Methionine-Aromatic Interactions in Copper Proteins. *Inorg. Chem.* **2022**, *61* (14), 5563–5571. https://doi.org/10.1021/acs.inorgchem.2c00030.

(161) Callis, P. R. [7] ^1L_a and ^1L_b Transitions of Tryptophan: Applications of Theory and Experimental Observations to Fluorescence of Proteins. In *Methods in Enzymology*; Academic Press, 1997; Vol. 278, pp 113–150. https://doi.org/10.1016/S0076-6879(97)78009-1.

(162) Strickland, E. H.; Billups, C.; Kay, E. Effects of Hydrogen Bonding and Solvents upon the Tryptophanyl ^1L_a Absorption Band. Studies Using 2,3-Dimethylindole. *Biochemistry* **1972**, *11* (19), 3657–3662. https://doi.org/10.1021/bi00769a025.

(163) Valeur, B.; Weber, G. Resolution of the Fluorescence Excitation Spectrum of Indole into the ^1L_a and ^1L_b Excitation Bands. *Photochem. Photobiol.* **1977**, *25* (5), 441–444. https://doi.org/10.1111/j.1751-1097.1977.tb09168.x.

(164) Biswal, H. S.; Wategaonkar, S. Nature of the N−H···S Hydrogen Bond. *J. Phys. Chem. A* **2009**, *113* (46), 12763–12773. https://doi.org/10.1021/jp907658w.

(165) Pan, C.-P.; Barkley, M. D. Conformational Effects on Tryptophan Fluorescence in Cyclic Hexapeptides. *Biophys. J.* **2004**, *86* (6), 3828–3835. https://doi.org/10.1529/biophysj.103.038901.

(166) Broos, J.; Tveen-Jensen, K.; de Waal, E.; Hesp, B. H.; Jackson, J. B.; Canters, G. W.; Callis, P. R. The Emitting State of Tryptophan in Proteins with Highly Blue-Shifted Fluorescence. *Angew. Chem. Int. Ed.* **2007**, *46* (27), 5137–5139. https://doi.org/10.1002/anie.200700839.

(167) Khrustalev, V. V.; Poboinev, V. V.; Stojarov, A. N.; Khrustaleva, T. A. Microenvironment of Tryptophan Residues in Proteins of Four Structural Classes: Applications for Fluorescence and Circular Dichroism Spectroscopy. *Eur. Biophys. J.* **2019**, *48* (6), 523–537. https://doi.org/10.1007/s00249-019-01377-0.

(168) Yuan, T.; Weljie, A. M.; Vogel, H. J. Tryptophan Fluorescence Quenching by Methionine and Selenomethionine Residues of Calmodulin: Orientation of Peptide and Protein Binding. *Biochemistry* **1998**, *37* (9), 3187–3195. https://doi.org/10.1021/bi9716579.

(169) Francuski, B. M.; Novaković, S. B.; Bogdanović, G. A. Electronic Features and Hydrogen Bonding Capacity of the Sulfur Acceptor in Thioureido-Based Compounds. Experimental Charge Density Study of 4-Methyl-3-Thiosemicarbazide. *CrystEngComm* **2011**, *13* (10), 3580. https://doi.org/10.1039/c0ce00760a.

(170) Gregoret, L. M.; Rader, S. D.; Fletterick, R. J.; Cohen, F. E. Hydrogen Bonds Involving Sulfur Atoms in Proteins. *Proteins: Struct. Funct. Genet.* **1991**, *9* (2), 99–107. https://doi.org/10.1002/prot.340090204.

(171) Lobo, I. A.; Robertson, P. A.; Villani, L.; Wilson, D. J. D.; Robertson, E. G. Thiols as Hydrogen Bond Acceptors and Donors: Spectroscopy of 2-Phenylethanethiol Complexes. *J. Phys. Chem. A* **2018**, *122* (36), 7171–7180. https://doi.org/10.1021/acs.jpca.8b06649.

(172) Biswal, H. S.; Wategaonkar, S. Sulfur, Not Too Far Behind O, N, and C: SH···π Hydrogen Bond. *J. Phys. Chem. A* **2009**, *113* (46), 12774–12782. https://doi.org/10.1021/jp907747w.

(173) Biswal, H. S.; Bhattacharyya, S.; Bhattacherjee, A.; Wategaonkar, S. Nature and Strength of Sulfur-Centred Hydrogen Bonds: Laser Spectroscopic Investigations in the Gas Phase and Quantum-Chemical Calculations. *Int. Rev. Phys. Chem.* **2015**, *34* (1), 99–160. https://doi.org/10.1080/0144235X.2015.1022946.

(174) Bricknell, B. C.; Ford, T. A. An Ab Initio Investigation of Some Hydrogen-Bonded Complexes of Methanethiol. *J. Mol. Struct.* **2010**, *976* (1–3), 115–118. https://doi.org/10.1016/j.molstruc.2010.01.025.

(175) Kieninger, M.; Ventura, O. N. Calculations of the Infrared and Raman Spectra of Simple Thiols and Thiol-Water Complexes: Simple Thiols and Thiol-Water Complexes. *Int. J. Quantum Chem.* **2011**, *111* (7–8), 1843–1857. https://doi.org/10.1002/qua.22890.

(176) Cocinero, E. J.; Sánchez, R.; Blanco, S.; Lesarri, A.; López, J. C.; Alonso, J. L. Weak Hydrogen Bonds C–H···S and C–H···F–C in the Thiirane–Trifluoromethane Dimer. *Chem. Phys. Lett.* **2005**, *402* (1–3), 4–10. https://doi.org/10.1016/j.cplett.2004.11.073.

(177) Biswal, H. S.; Wategaonkar, S. O−H···O versus O−H···S Hydrogen Bonding. 3. IR−UV Double Resonance Study of Hydrogen Bonded Complexes of *p*-Cresol with Diethyl Ether and Its Sulfur Analog. *J. Phys. Chem. A* **2010**, *114* (19), 5947–5957. https://doi.org/10.1021/jp100439w.

(178) Domagała, M.; Grabowski, S. J. Hydrocarbons as Proton Donors in C–H···N and C–H···S Hydrogen Bonds. *Chem. Phys.* **2010**, *367* (1), 1–6. https://doi.org/10.1016/j.chemphys.2009.10.018.

(179) Ishigaki, Y.; Shimajiri, T.; Takeda, T.; Katoono, R.; Suzuki, T. Longest C–C Single Bond among Neutral Hydrocarbons with a Bond Length beyond 1.8 Å. *Chem* **2018**, *4* (4), 795–806. https://doi.org/10.1016/j.chempr.2018.01.011.

(180) Zheng, L.; Baumann, U.; Reymond, J.-L. An Efficient One-Step Site-Directed and Site-Saturation Mutagenesis Protocol. *Nucleic Acids Res.* **2004**, *32* (14), e115–e115. https://doi.org/10.1093/nar/gnh110.

(181) Johnson, E. C.; Sullivan, B. P.; Salmon, D. J.; Adeyemi, S. A.; Meyer, T. J. Synthesis and Properties of the Chloro-Bridged Dimer $[(Bpy)_2RuCl]_2^{2+}$ and Its Transient 3+ Mixed-Valence Ion. *Inorg. Chem.* **1978**, *17* (8), 2211–2215. https://doi.org/10.1021/ic50186a038.

(182) Faham, S.; Day, M. W.; Connick, W. B.; Crane, B. R.; Di Bilio, A. J.; Schaefer, W. P.; Rees, D. C.; Gray, H. B. Structures of Ruthenium-Modified *Pseudomonas Aeruginosa* Azurin and $[Ru(2,2'\text{-Ipyridine})_2(Imidazole)_2]SO_4 \cdot 10H_2O$. *Acta Crystallogr. D* **1999**, *55* (2), 379–385. https://doi.org/10.1107/S0907444998010464.

(183) Connick, W. B.; Di Bilio, A. J.; Hill, M. G.; Winkler, J. R.; Gray, H. B. Tricarbonyl(1,10-Phenanthroline) (Imidazole) Rhenium(I): A Powerful Photooxidant for Investigations of Electron Tunneling in Proteins. *Inorganica Chim. Acta* **1995**, *240* (1–2), 169–173. https://doi.org/10.1016/0020-1693(95)04532-5.

(184) Stoll, S.; Schweiger, A. EasySpin, a Comprehensive Software Package for Spectral Simulation and Analysis in EPR. *J. Magn. Reson.* **2006**, *178* (1), 42–55. https://doi.org/10.1016/j.jmr.2005.08.013.

(185) Dokmanić, I.; Šikić, M.; Tomić, S. Metals in Proteins: Correlation Between the Metal-Ion Type, Coordination Number and the Amino-Acid Residues Involved in the Coordination. *Acta Crystallogr. D* **2008**, *64* (3), 257–263. https://doi.org/10.1107/S090744490706595X.

(186) Harding, M. M. The Architecture of Metal Coordination Groups in Proteins. *Acta Crystallogr. D* **2004**, *60* (5), 849–859. https://doi.org/10.1107/S0907444904004081.

(187) Werner, A. Über Die Raumisomeren Kobaltverbindungen. *Justus Liebegs Ann. Chem.* **1912**, *386* (1–2), 1–272. https://doi.org/10.1002/jlac.19123860102.

(188) Högbom, M.; Stenmark, P.; Voevodskaya, N.; McClarty, G.; Gräslund, A.; Nordlund, P. The Radical Site in Chlamydial Ribonucleotide Reductase Defines a New R2 Subclass. *Science* **2004**, *305* (5681), 245–248. https://doi.org/10.1126/science.1098419.

(189) Dill, K. A. Dominant Forces in Protein Folding. *Biochemistry* **1990**, *29* (31), 7133–7155. https://doi.org/10.1021/bi00483a001.

(190) Lyubimov, A. Y.; Lario, P. I.; Moustafa, I.; Vrielink, A. Atomic Resolution Crystallography Reveals How Changes in PH Shape the Protein Microenvironment. *Nat. Chem. Biol.* **2006**, *2* (5), 259–264. https://doi.org/10.1038/nchembio784.

(191) Kessel, A.; Ben-Tal, N. *Introduction to Proteins: Structure, Function, and Motion*, 2nd ed.; Chapman and Hall/CRC, 2018. https://doi.org/10.1201/9781315113876.

(192) Branden, C. I.; Tooze, J. *Introduction to Protein Structure*, 0 ed.; Garland Science, 2012. https://doi.org/10.1201/9781136969898.

(193) Bagley, S. C.; Altman, R. B. Characterizing the Microenvironment Surrounding Protein Sites. *Protein Sci.* **1995**, *4* (4), 622–635.

(194) Bhatnagar, A.; Apostol, M. I.; Bandyopadhyay, D. Amino Acid Function Relates to Its Embedded Protein Microenvironment: A Study on Disulfide-Bridged Cystine: Cystine Function and Protein Microenvironment. *Proteins* **2016**, *84* (11), 1576–1589. https://doi.org/10.1002/prot.25101.

(195) Zimmermann, J.; Thielges, M. C.; Seo, Y. J.; Dawson, P. E.; Romesberg, F. E. Cyano Groups as Probes of Protein Microenvironments and Dynamics. *Angew. Chem. Int. Ed.* **2011**, *50* (36), 8333–8337. https://doi.org/10.1002/anie.201101016.

(196) Schultz, K. C.; Supekova, L.; Ryu, Y.; Xie, J.; Perera, R.; Schultz, P. G. A Genetically Encoded Infrared Probe. *J. Am. Chem. Soc.* **2006**, *128* (43), 13984–13985. https://doi.org/10.1021/ja0636690.

(197) Sigala, P. A.; Fafarman, A. T.; Bogard, P. E.; Boxer, S. G.; Herschlag, D. Do Ligand Binding and Solvent Exclusion Alter the Electrostatic Character within the Oxyanion Hole of an Enzymatic Active Site? *J. Am. Chem. Soc.* **2007**, *129* (40), 12104–12105. https://doi.org/10.1021/ja075605a.

(198) Santos, J.; Pujols, J.; Pallarès, I.; Iglesias, V.; Ventura, S. Computational Prediction of Protein Aggregation: Advances in Proteomics, Conformation-Specific Algorithms and Biotechnological Applications. *Comput. Struct. Biotechnol. J.* **2020**, *18*, 1403–1413. https://doi.org/10.1016/j.csbj.2020.05.026.

(199) Raanan, H.; Pike, D. H.; Moore, E. K.; Falkowski, P. G.; Nanda, V. Modular Origins of Biological Electron Transfer Chains. *Proc. Natl. Acad. Sci. U.S.A.* **2018**, *115* (6), 1280–1285. https://doi.org/10.1073/pnas.1714225115.

(200) Jafari, F.; Samadi, S.; Nowroozi, A.; Sadrjavadi, K.; Moradi, S.; Ashrafi-Kooshk, M. R.; Shahlaei, M. Experimental and Computational Studies on the Binding of Diazinon to Human Serum Albumin. *J. Biomol. Struct.* **2018**, *36* (6), 1490–1510. https://doi.org/10.1080/07391102.2017.1329096.

(201) Millan, S.; Swain, B. C.; Tripathy, U.; Mishra, P. P.; Sahoo, H. Effect of Micro-Environment on Protein Conformation Studied by Fluorescence-Based Techniques. *J. Mol. Liq.* **2020**, *320*, 114489. https://doi.org/10.1016/j.molliq.2020.114489.

(202) Mariam, J.; Hoskere Ashoka, A.; Gaded, V.; Ali, F.; Malvi, H.; Das, A.; Anand, R. Deciphering Protein Microenvironment by Using a Cysteine Specific Switch-ON Fluorescent Probe. *Org. Biomol. Chem.* **2021**, *19* (23), 5161–5168. https://doi.org/10.1039/D1OB00698C.

(203) Pizano, A. A.; Lutterman, D. A.; Holder, P. G.; Teets, T. S.; Stubbe, J.; Nocera, D. G. Photo-Ribonucleotide Reductase B2 by Selective Cysteine L'abeling with a Radical Phototrigger. *Proc. Natl. Acad. Sci. U.S.A.* **2012**, *109* (1), 39–43. https://doi.org/10.1073/pnas.1115778108.

(204) Minnihan, E. C.; Seyedsayamdost, M. R.; Uhlin, U.; Stubbe, J. Kinetics of Radical Intermediate Formation and Deoxynucleotide Production in 3-Aminotyrosine-Substituted *Escherichia Coli* Ribonucleotide Reductases. *J. Am. Chem. Soc.* **2011**, *133* (24), 9430–9440. https://doi.org/10.1021/ja201640n.

(205) Dai, Q.-H.; Tommos, C.; Fuentes, E. J.; Blomberg, M. R. A.; Dutton, P. L.; Wand, A. J. Structure of a de Novo Designed Protein Model of Radical Enzymes. *J. Am. Chem. Soc.* **2002**, *124* (37), 10952–10953. https://doi.org/10.1021/ja0264201.

(206) Martínez-Rivera, M. C.; Berry, B. W.; Valentine, K. G.; Westerlund, K.; Hay, S.; Tommos, C. Electrochemical and Structural Properties of a Protein System Designed To Generate Tyrosine Pourbaix Diagrams. *J. Am. Chem. Soc.* **2011**, *133* (44), 17786–17795. https://doi.org/10.1021/ja206876h.

(207) Okada, K.; Flores, L.; Wong, M.; Petkovic, D. Microenvironment-Based Protein Function Analysis by Random Forest. In *2014 22nd International Conference on Pattern Recognition*; IEEE: Stockholm, Sweden, 2014; pp 3138–3143. https://doi.org/10.1109/ICPR.2014.541.

(208) Bandyopadhyay, D.; Mehler, E. L. Quantitative Expression of Protein Heterogeneity: Response of Amino Acid Side Chains to Their Local Environment. *Proteins* **2008**, *72* (2), 646–659. https://doi.org/10.1002/prot.21958.

(209) Sethuraman, S.; Rajendran, K. Multicharacteristic Behavior of Tyrosine Present in the Microdomains of the Macromolecule Gum Arabic at Various PH Conditions. *ACS Omega* **2018**, *3* (12), 17602–17609. https://doi.org/10.1021/acsomega.8b02928.

(210) Noronha, M.; Lima, J. C.; Lamosa, P.; Santos, H.; Maycock, C.; Ventura, R.; Maçanita, A. L. Intramolecular Fluorescence Quenching of Tyrosine by the Peptide α-Carbonyl Group Revisited. *J. Phys. Chem. A* **2004**, *108* (12), 2155–2166. https://doi.org/10.1021/jp037125l.

(211) Prendergast, F. G.; Hampton, P. D.; Jones, B. Characteristics of Tyrosinate Fluorescence Emission in α- and β-Purothionins. *Biochemistry* **1984**, *23* (26), 6690–6697. https://doi.org/10.1021/bi00321a063.

(212) Wiczk, W.; Rzeska, A.; Łukomska, J.; Stachowiak, K.; Karolczak, J.; Malicka, J.; Łankiewicz, L. Mechanism of Fluorescence Quenching of Tyrosine Derivatives by Amide Group. *Chem. Phys. Lett.* **2001**, *341* (1–2), 99–106. https://doi.org/10.1016/S0009-2614(01)00470-5.

(213) Fitch, C. A.; Platzer, G.; Okon, M.; Garcia-Moreno E., B.; McIntosh, L. P. Arginine: Its pK_a Value Revisited: P<i>K</i$_a$ Value of Arginine. *Protein Sci.* **2015**, *24* (5), 752–761. https://doi.org/10.1002/pro.2647.

(214) Grimsley, G. R.; Scholtz, J. M.; Pace, C. N. A Summary of the Measured p*K* Values of the Ionizable Groups in Folded Proteins. *Protein Sci.* **2009**, *18* (1), 247–251. https://doi.org/10.1002/pro.19.

(215) Churg, A. K.; Warshel, A. Control of the Redox Potential of Cytochrome and Microscopic Dielectric Effects in Proteins. *Biochemistry* **1986**, *25* (7), 1675–1681. https://doi.org/10.1021/bi00355a035.

(216) Capozzi, F.; Ciurli, S.; Luchinat, C. Coordination Sphere versus Protein Environment as Determinants of Electronic and Functional Properties of Iron-Sulfur Proteins. In *Metal Sites in Proteins and Models Redox Centres*; Hill, H. A. O., Sadler, P. J., Thomson, A. J., Eds.; Clarke, M. J., Goodenough, J. B., Jørgensen, C. K., Mingos, D. M. P., Palmer, G. A., Sadler, P. J., Weiss, R., Williams, R. J. P., Series Eds.; Structure and Bonding; Springer Berlin Heidelberg: Berlin, Heidelberg, 1998; Vol. 90, pp 127–160. https://doi.org/10.1007/3-540-62888-6_5.

(217) Ledesma, G. N.; Murgida, D. H.; Ly, H. K.; Wackerbarth, H.; Ulstrup, J.; Costa-Filho, A. J.; Vila, A. J. The Met Axial Ligand Determines the Redox Potential in Cu_A Sites. *J. Am. Chem. Soc.* **2007**, *129* (39), 11884–11885. https://doi.org/10.1021/ja0731221.

(218) Fasman, G. D. *Handbook of Biochemistry: Section D Physical Chemical Data, Volume I*, 3rd ed.; CRC Press, 1976. https://doi.org/10.1201/9781351072427.

(219) Zhdanova, N. G.; Shirshin, E. A.; Maksimov, E. G.; Panchishin, I. M.; Saletsky, A. M.; Fadeev, V. V. Tyrosine Fluorescence Probing of the Surfactant-Induced Conformational Changes of Albumin. *Photochem. Photobiol. Sci.* **2015**, *14* (5), 897–908. https://doi.org/10.1039/C4PP00432A.

(220) VanScyoc, W. S.; Shea, M. A. Phenylalanine Fluorescence Studies of Calcium Binding to N-Domain Fragments of *Paramecium* Calmodulin Mutants Show Increased Calcium Affinity Correlates with Increased Disorder. *Protein Sci.* **2001**, *10* (9), 1758–1768. https://doi.org/10.1110/ps.11601.

(221) Stenstrom, W.; Reinhard, M. The Influence of the PH upon the Ultraviolet Adsorption Spectra of Certain Cyclic Compounds. *J. Phys. Chem.* **1925**, *29* (11), 1477–1481. https://doi.org/10.1021/j150257a015.

(222) Maeno, A.; Matsuo, H.; Akasaka, K. Tyrosine/Tyrosinate Fluorescence at 700 MPa: A Pressure Unfolding Study of Chicken Ovomucoid at PH 12. *Biophys. Chem.* **2013**, *183*, 57–63. https://doi.org/10.1016/j.bpc.2013.07.008.

(223) Perrin, D. D.; Dempsey, B.; Serjeant, E. P. Molecular Factors That Modify PK_a Values. In *pK_a Prediction for Organic Acids and Bases*; Springer Netherlands: Dordrecht, 1981; pp 12–20. https://doi.org/10.1007/978-94-009-5883-8_2.

(224) Shokri, A.; Abedin, A.; Fattahi, A.; Kass, S. R. Effect of Hydrogen Bonds on pK_a Values: Importance of Networking. *J. Am. Chem. Soc.* **2012**, *134* (25), 10646–10650. https://doi.org/10.1021/ja3037349.

(225) Hunter, E. P. L.; Desrosiers, M. F.; Simic, M. G. The Effect of Oxygen, Antioxidants, and Superoxide Radical on Tyrosine Phenoxyl Radical Dimerization. *Free Radic. Biol. Med.* **1989**, *6* (6), 581–585. https://doi.org/10.1016/0891-5849(89)90064-6.

(226) Suprun, E. V.; Shumyantseva, V. V.; Archakov, A. I. Protein Electrochemistry: Application in Medicine. A Review. *Electrochim. Acta* **2014**, *140*, 72–82. https://doi.org/10.1016/j.electacta.2014.03.089.

(227) Costentin, C.; Louault, C.; Robert, M.; Savéant, J.-M. The Electrochemical Approach to Concerted Proton--Electron Transfers in the Oxidation of Phenols in Water. *Proc. Natl. Acad. Sci. USA* **2009**, *106* (43), 18143–18148. https://doi.org/10.1073/pnas.0910065106.

(228) Bonin, J.; Costentin, C.; Louault, C.; Robert, M.; Routier, M.; Savéant, J.-M. Intrinsic Reactivity and Driving Force Dependence in Concerted Proton–Electron Transfers to Water Illustrated by Phenol Oxidation. *Proc. Natl. Acad. Sci. U.S.A.* **2010**, *107* (8), 3367–3372. https://doi.org/10.1073/pnas.0914693107.

(229) Ishikita, H.; Knapp, E.-W. Function of Redox-Active Tyrosine in Photosystem II. *Biophys. J.* **2006**, *90* (11), 3886–3896. https://doi.org/10.1529/biophysj.105.076984.

(230) Gallivan, J. P.; Dougherty, D. A. Cation-π Interactions in Structural Biology. *Proc. Natl. Acad. Sci. U.S.A.* **1999**, *96* (17), 9459–9464. https://doi.org/10.1073/pnas.96.17.9459.

(231) Ma, J. C.; Dougherty, D. A. The Cation−π Interaction. *Chem. Rev.* **1997**, *97* (5), 1303–1324. https://doi.org/10.1021/cr9603744.

(232) Keskin, O.; Gursoy, A.; Ma, B.; Nussinov, R. Principles of Protein−Protein Interactions: What Are the Preferred Ways For Proteins To Interact? *Chem. Rev.* **2008**, *108* (4), 1225–1244. https://doi.org/10.1021/cr040409x.

(233) Babine, R. E.; Bender, S. L. Molecular Recognition of Protein−Ligand Complexes: Applications to Drug Design. *Chem. Rev.* **1997**, *97* (5), 1359–1472. https://doi.org/10.1021/cr960370z.

(234) Martinez, C. R.; Iverson, B. L. Rethinking the Term “Pi-Stacking.” *Chem. Sci.* **2012**, *3* (7), 2191. https://doi.org/10.1039/c2sc20045g.

(235) Dougherty, D. A. The Cation−π Interaction. *Acc. Chem. Res.* **2013**, *46* (4), 885–893. https://doi.org/10.1021/ar300265y.

(236) Schottel, B. L.; Chifotides, H. T.; Dunbar, K. R. Anion-π Interactions. *Chem. Soc. Rev.* **2008**, *37* (1), 68–83. https://doi.org/10.1039/B614208G.

(237) Zauhar, R. J.; Colbert, C. L.; Morgan, R. S.; Welsh, W. J. Evidence for a Strong Sulfur-Aromatic Interaction Derived from Crystallographic Data. *Biopolymers* **2000**, *53* (3), 233–248. https://doi.org/10.1002/(SICI)1097-0282(200003)53:3<233::AID-BIP3>3.0.CO;2-4.

(238) Fishel, L. A.; Farnum, M. F.; Mauro, J. M.; Miller, M. A.; Kraut, J.; Liu, Y.; Tan, X. L.; Scholes, C. P. Compound I Radical in Site-Directed Mutants of Cytochrome c Peroxidase as Probed by Electron Paramagnetic Resonance and Electron-Nuclear Double Resonance. *Biochemistry* **1991**, *30* (7), 1986–1996. https://doi.org/10.1021/bi00221a036.

(239) Barrows, T. P.; Bhaskar, B.; Poulos, T. L. Electrostatic Control of the Tryptophan Radical in Cytochrome *c* Peroxidase. *Biochemistry* **2004**, *43* (27), 8826–8834. https://doi.org/10.1021/bi049531g.

(240) *ProtScale Tool: Amino Acid Composition (%) in the UniProtKB/Swiss-Prot Data Bank.* https://web.expasy.org/protscale/pscale/A.A.Swiss-Prot.html (accessed 2021-02-18).

(241) Brandl, M.; Weiss, M. S.; Jabs, A.; Sühnel, J.; Hilgenfeld, R. C-H···π-Interactions in Proteins. *J. Mol. Biol.* **2001**, *307* (1), 357–377. https://doi.org/10.1006/jmbi.2000.4473.

(242) *The PyMOL Molecular Graphics System, Version 2.0 Schrödinger, LLC*. https://pymol.org/sites/default/files/pymol.bib (accessed 2019-01-11).

(243) Neese, F. The ORCA Program System. *WIREs Comput. Mol. Sci.* **2012**, *2* (1), 73–78. https://doi.org/10.1002/wcms.81.

(244) Neese, F. Software Update: The ORCA Program System, Version 4.0. *WIREs Comput. Mol. Sci.* **2018**, *8* (1), e1327. https://doi.org/10.1002/wcms.1327.

(245) Glendening, E. D.; Landis, C. R.; Weinhold, F. *NBO 7.0*: New Vistas in Localized and Delocalized Chemical Bonding Theory. *J. Comput. Chem.* **2019**, *40* (25), 2234–2241. https://doi.org/10.1002/jcc.25873.

(246) Schneider, W. B.; Bistoni, G.; Sparta, M.; Saitow, M.; Riplinger, C.; Auer, A. A.; Neese, F. Decomposition of Intermolecular Interaction Energies within the Local Pair Natural Orbital Coupled Cluster Framework. *J. Chem. Theory Comput.* **2016**, *12* (10), 4778–4792. https://doi.org/10.1021/acs.jctc.6b00523.

(247) Galgonek, J.; Vymětal, J.; Jakubec, D.; Vondrášek, J. Amino Acid Interaction (INTAA) Web Server. *Nucleic Acids Res.* **2017**, *45* (W1), W388–W392. https://doi.org/10.1093/nar/gkx352.

(248) Scrutton, N. S.; Raine, A. R. C. Cation-π Bonding and Amino-Aromatic Interactions in the Biomolecular Recognition of Substituted Ammonium Ligands. *Biochem. J.* **1996**, *319* (1), 1–8. https://doi.org/10.1042/bj3190001.

(249) Zhong, W.; Gallivan, J. P.; Zhang, Y.; Li, L.; Lester, H. A.; Dougherty, D. A. From *Ab Initio* Quantum Mechanics to Molecular Neurobiology: A Cation–π Binding Site in the Nicotinic Receptor. *Proc. Natl. Acad. Sci. U.S.A.* **1998**, *95* (21), 12088–12093. https://doi.org/10.1073/pnas.95.21.12088.

(250) Burley, S. K.; Petsko, G. A. Amino-Aromatic Interactions in Proteins. *FEBS Lett.* **1986**, *203* (2), 139–143. https://doi.org/10.1016/0014-5793(86)80730-X.

(251) Tsuzuki, S. CH/π Interactions. *Annu. Rep. Prog. Chem., Sect. C: Phys. Chem.* **2012**, *108*, 69–95. https://doi.org/10.1039/c2pc90003c.

(252) Jiménez-Moreno, E.; Jiménez-Osés, G.; Gómez, A. M.; Santana, A. G.; Corzana, F.; Bastida, A.; Jiménez-Barbero, J.; Asensio, J. L. A Thorough Experimental Study of CH/π Interactions in Water: Quantitative Structure–Stability Relationships for Carbohydrate/Aromatic Complexes. *Chem. Sci.* **2015**, *6* (11), 6076–6085. https://doi.org/10.1039/C5SC02108A.

(253) Nishio, M.; Umezawa, Y.; Honda, K.; Tsuboyama, S.; Suezawa, H. CH/π Hydrogen Bonds in Organic and Organometallic Chemistry. *CrystEngComm* **2009**, *11* (9), 1757–1788. https://doi.org/10.1039/b902318f.

(254) Beratan, D. N.; Skourtis, S. S.; Balabin, I. A.; Balaeff, A.; Keinan, S.; Venkatramani, R.; Xiao, D. Steering Electrons on Moving Pathways. *Acc. Chem. Res.* **2009**, *42* (10), 1669–1678. https://doi.org/10.1021/ar900123t.

(255) Skourtis, S. S.; Waldeck, D. H.; Beratan, D. N. Fluctuations in Biological and Bioinspired Electron-Transfer Reactions. *Annu. Rev. Phys. Chem.* **2010**, *61* (1), 461–485. https://doi.org/10.1146/annurev.physchem.012809.103436.

(256) Maté, M. J.; Zamocky, M.; Nykyri, L. M.; Herzog, C.; Alzari, P. M.; Betzel, C.; Koller, F.; Fita, I. Structure of Catalase-A from *Saccharomyces Cerevisiae*. *J. Mol. Biol.* **1999**, *286* (1), 135–149. https://doi.org/10.1006/jmbi.1998.2453.

(257) Gupta, K.; Selinsky, B. S.; Kaub, C. J.; Katz, A. K.; Loll, P. J. The 2.0Å Resolution Crystal Structure of Prostaglandin H2 Synthase-1: Structural Insights into an Unusual Peroxidase. *J. Mol. Biol.* **2004**, *335* (2), 503–518. https://doi.org/10.1016/j.jmb.2003.10.073.

(258) Schanstra, J. P.; Janssen, D. B. Kinetics of Halide Release of Haloalkane Dehalogenase: Evidence for a Slow Conformational Change. *Biochemistry* **1996**, *35* (18), 5624–5632. https://doi.org/10.1021/bi952904g.

(259) Krooshof, G. H.; Ridder, I. S.; Tepper, A. W. J. W.; Vos, G. J.; Rozeboom, H. J.; Kalk, K. H.; Dijkstra, B. W.; Janssen, D. B. Kinetic Analysis and X-Ray Structure of Haloalkane Dehalogenase with a Modified Halide-Binding Site. *Biochemistry* **1998**, *37* (43), 15013–15023. https://doi.org/10.1021/bi9815187.

(260) Otyepka, M.; Damborský, J. Functionally Relevant Motions of Haloalkane Dehalogenases Occur in the Specificity-Modulating Cap Domains. *Protein Sci.* **2002**, *11* (5), 1206–1217. https://doi.org/10.1110/ps3830102.

(261) Ridder, I. S.; Rozeboom, H. J.; Dijkstra, B. W. Haloalkane Dehalogenase from *Xanthobacter Autotrophicus* GJ10 Refined at 1.15 Å Resolution. *Acta Crystallogr. D* **1999**, *55* (7), 1273–1290. https://doi.org/10.1107/S090744499900534X.

(262) Touw, W. G.; Vriend, G. BDB: Databank of PDB Files with Consistent B-Factors. *Protein Eng. Des. Sel.* **2014**, *27* (11), 457–462. https://doi.org/10.1093/protein/gzu044.

(263) Sun, Z.; Liu, Q.; Qu, G.; Feng, Y.; Reetz, M. T. Utility of B-Factors in Protein Science: Interpreting Rigidity, Flexibility, and Internal Motion and Engineering Thermostability. *Chem. Rev.* **2019**, *119* (3), 1626–1665. https://doi.org/10.1021/acs.chemrev.8b00290.

(264) Berman, H. M.; Westbrook, J.; Feng, Z.; Gilliland, G.; Bhat, T. N.; Weissig, H.; Shindyalov, I. N.; Bourne, P. E. The Protein Data Bank. *Nucleic Acids Res.* **2000**, *28* (1), 235–242. https://doi.org/10.1093/nar/28.1.235.

(265) Weigend, F.; Ahlrichs, R. Balanced Basis Sets of Split Valence, Triple Zeta Valence and Quadruple Zeta Valence Quality for H to Rn: Design and Assessment of Accuracy. *Phys. Chem. Chem. Phys.* **2005**, *7* (18), 3297. https://doi.org/10.1039/b508541a.

(266) Weigend, F. Accurate Coulomb-Fitting Basis Sets for H to Rn. *Phys. Chem. Chem. Phys.* **2006**, *8* (9), 1057. https://doi.org/10.1039/b515623h.

(267) Grimme, S.; Antony, J.; Ehrlich, S.; Krieg, H. A Consistent and Accurate *Ab Initio* Parametrization of Density Functional Dispersion Correction (DFT-D) for the 94 Elements H-Pu. *J. Chem. Phys.* **2010**, *132* (15), 154104. https://doi.org/10.1063/1.3382344.

(268) Grimme, S.; Ehrlich, S.; Goerigk, L. Effect of the Damping Function in Dispersion Corrected Density Functional Theory. *J. Comput. Chem.* **2011**, *32* (7), 1456–1465. https://doi.org/10.1002/jcc.21759.

(269) Hanwell, M. D.; Curtis, D. E.; Lonie, D. C.; Vandermeersch, T.; Zurek, E.; Hutchison, G. R. Avogadro: An Advanced Semantic Chemical Editor, Visualization, and Analysis Platform. *J. Cheminformatics* **2012**, *4* (1), 17. https://doi.org/10.1186/1758-2946-4-17.

(270) Hu, Y.; Cheng, K.; He, L.; Zhang, X.; Jiang, B.; Jiang, L.; Li, C.; Wang, G.; Yang, Y.; Liu, M. NMR-Based Methods for Protein Analysis. *Anal. Chem.* **2021**, *93* (4), 1866–1879. https://doi.org/10.1021/acs.analchem.0c03830.

(271) Nar, H.; Huber, R.; Messerschmidt, A.; Filippou, A. C.; Barth, M.; Jaquinod, M.; Kamp, M.; Canters, G. W. Characterization and Crystal Structure of Zinc Azurin, a By-Product of Heterologous Expression in Escherichia Coli of Pseudomonas Aeruginosa Copper Azurin. *Eur. J. Biochem.* **1992**, *205* (3), 1123–1129. https://doi.org/10.1111/j.1432-1033.1992.tb16881.x.

(272) Sjölin, L.; Tsai, L. C.; Langer, V.; Pascher, T.; Karlsson, G.; Nordling, M.; Nar, H. Structure of Pseudomonas Aeruginosa Zinc Azurin Mutant Asn47Asp at 2.4 Å Resolution. *Acta Crystallogr. D Biol. Crystallogr.* **1993**, *49* (5), 449–457. https://doi.org/10.1107/S0907444993005207.

(273) Boeszoermenyi, A.; Ogórek, B.; Jain, A.; Arthanari, H.; Wagner, G. The Precious Fluorine on the Ring: Fluorine NMR for Biological Systems. *J. Biomol. NMR* **2020**, *74* (8–9), 365–379. https://doi.org/10.1007/s10858-020-00331-z.

(274) Mishra, N. K.; Urick, A. K.; Ember, S. W. J.; Schönbrunn, E.; Pomerantz, W. C. Fluorinated Aromatic Amino Acids Are Sensitive ^{19}F NMR Probes for Bromodomain-Ligand Interactions. *ACS Chem. Biol.* **2014**, *9* (12), 2755–2760. https://doi.org/10.1021/cb5007344.

(275) Vivian, J. T.; Callis, P. R. Mechanisms of Tryptophan Fluorescence Shifts in Proteins. *Biophys. J.* **2001**, *80* (5), 2093–2109. https://doi.org/10.1016/S0006-3495(01)76183-8.

(276) Pinheiro, S.; Soteras, I.; Gelpí, J. L.; Dehez, F.; Chipot, C.; Luque, F. J.; Curutchet, C. Structural and Energetic Study of Cation–π–Cation Interactions in Proteins. *Phys. Chem. Chem. Phys.* **2017**, *19* (15), 9849–9861. https://doi.org/10.1039/C6CP08448F.

Appendix A

Supplementary Information from Chapter 2

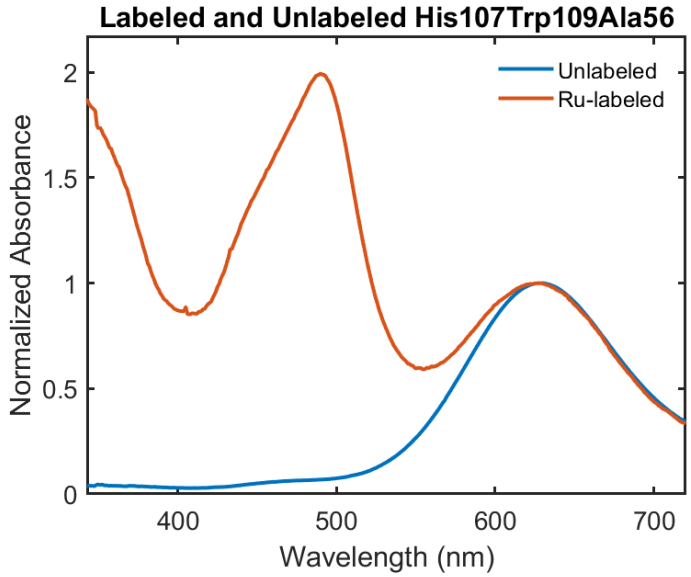

Figure A1. **Confirmation of $[Ru(bpy)_2CO_3]^{2+}$ labeling in His107Trp109Ala56 azurin. Absorbance was normalized to the 628 nm for Cu(II). The chage transfer band at 628 nm can be seen here in both the labeled and unlabeled spectra.**

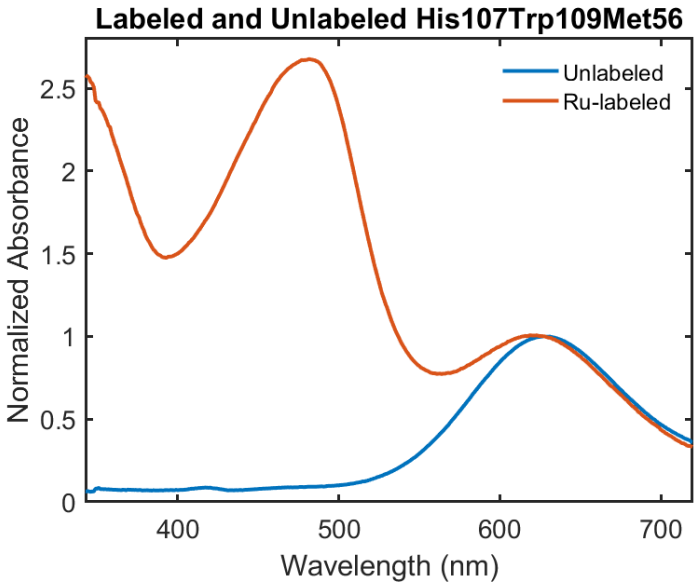

Figure A2. **Confirmation of $[Ru(bpy)_2CO_3]^{2+}$ labeling in His107Trp109Met56 azurin. Absorbance was normalized to the 628 nm for Cu(II). The chage transfer band at 628 nm can be seen here in both the labeled and unlabeled spectra.**

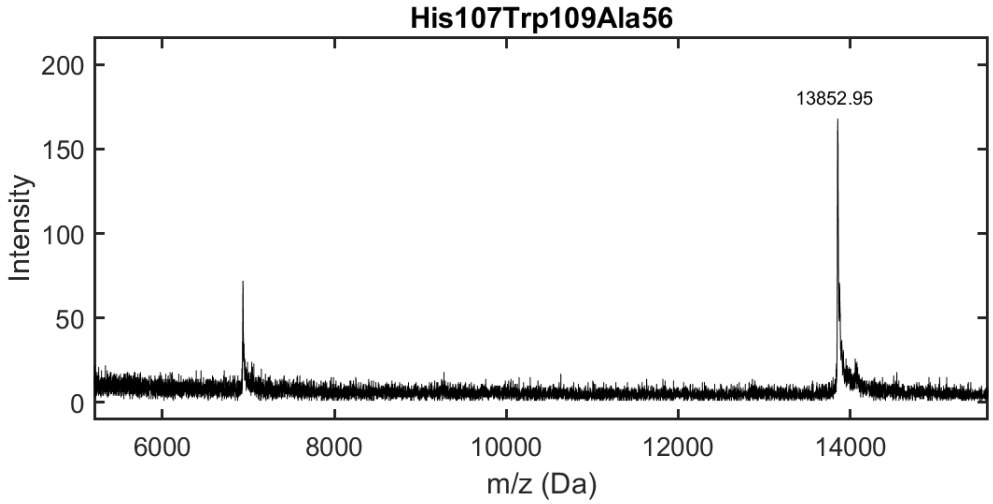

Figure A3. MALDI-TOF mass spectrometry of His107Trp109Ala56. Calculated mass: 13828.65 Da. Observed mass: 13852.95 Da.

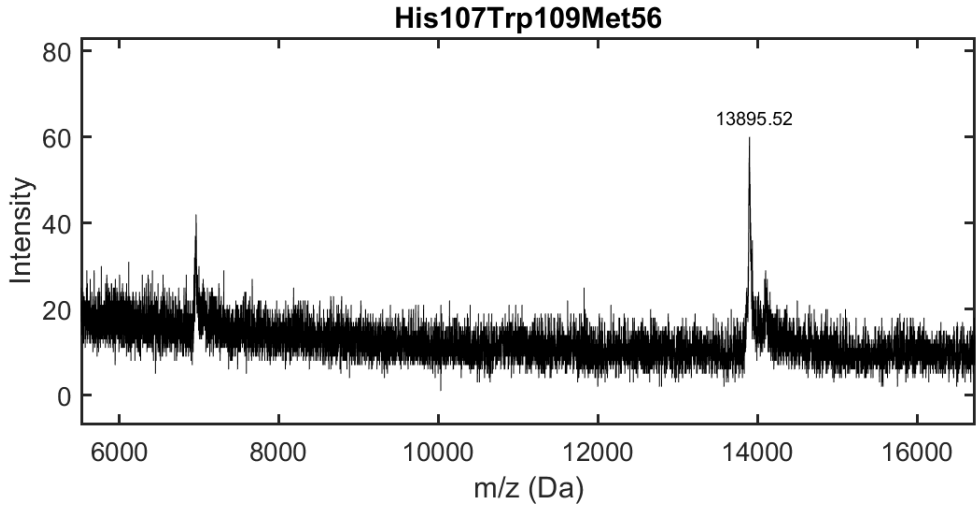

Figure A4. MALDI-TOF mass spectrometry of His107Trp109Met56. Calculated mass: 13888.76 Da. Observed mass: 13895.92 Da.

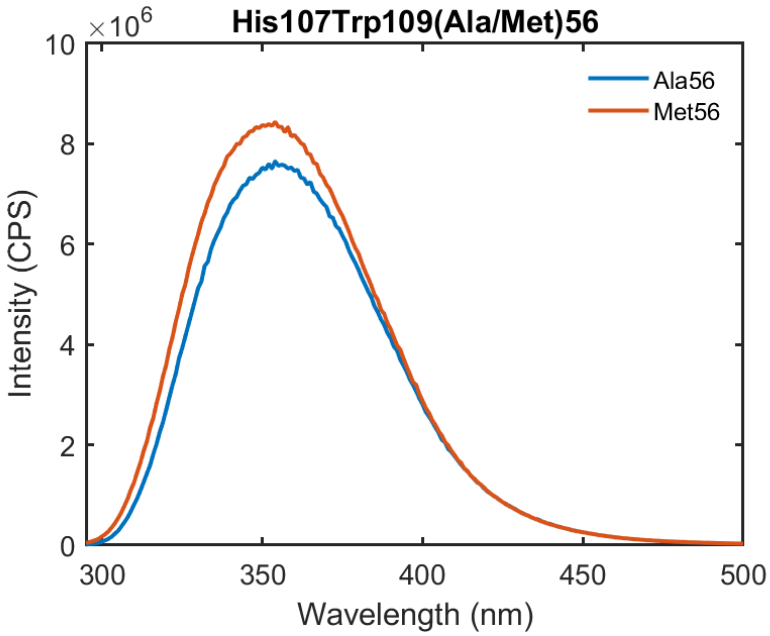

Figure A5. **Raw data for the emission spectra of His107Trp109Ala56 (blue) and His107Trp109Met56 (orange) to investigate whether any fluorescence quenching by Met can be observed.**

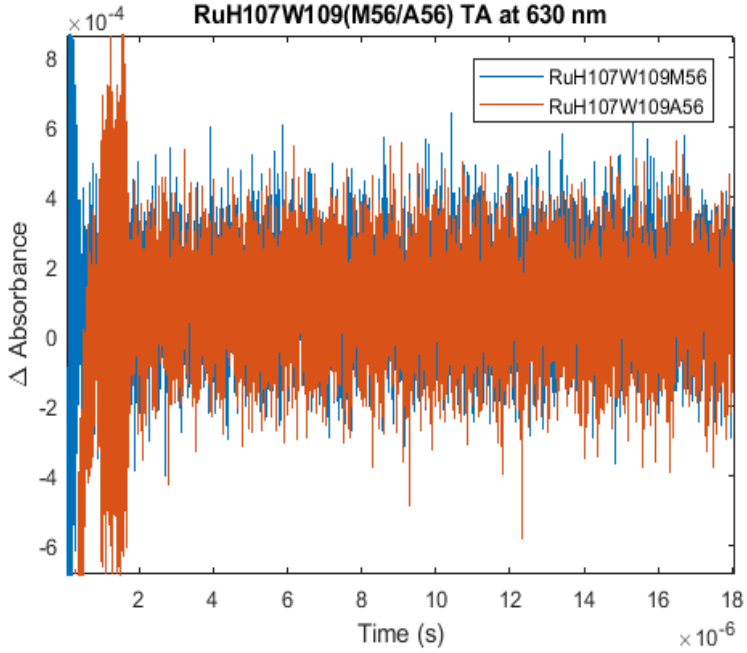

Figure A6. **Attempted Cu(I) oxidation to Cu(II) TA spectra for ruthenium labeled His107Trp109Met56 (blue) and ruthenium labeled His107Trp109Ala56 (orange). In both cases, no change in absorbance can be observed.**

Appendix B

Supplementary Information from Chapter 3

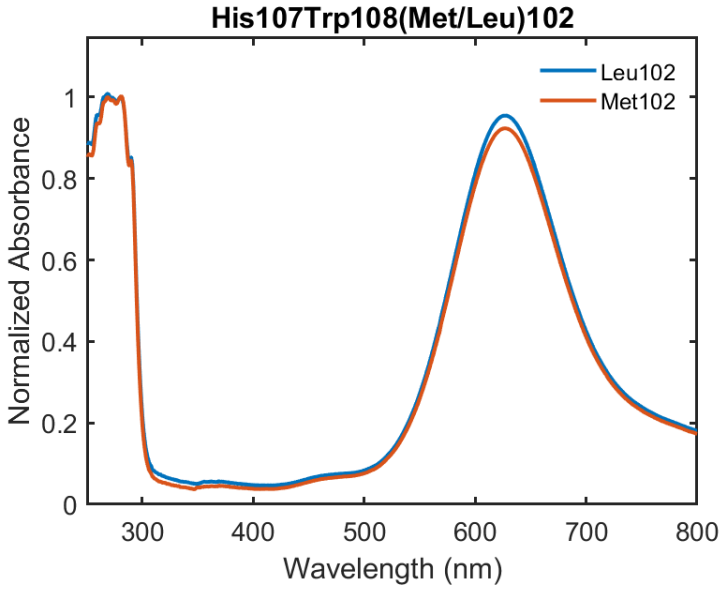

Figure B1. **UV-Vis spectra of His107Trp108Leu102 (blue) and His107Trp108Met102 (orange). The small amount of noise in the 300-400 nm range is due to the source changeover by the instrument. Spectra were normalized to the 280 nm peak for clarity.**

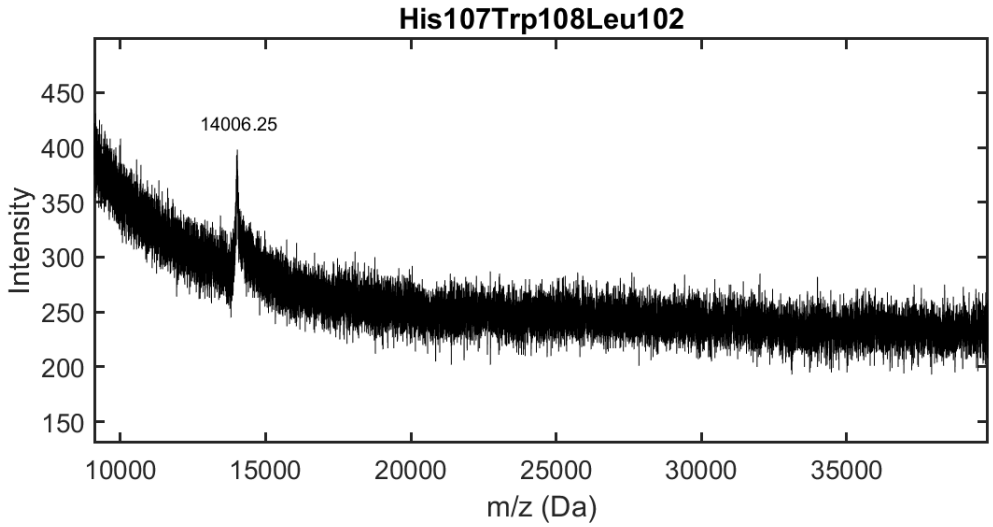

Figure B2. **MALDI-TOF mass spectrometry of His107Trp108Leu102. Calculated mass: 14003.97 Da. Observed mass: 14006.25 Da. The increase in intensity at m/z < 10000 Da is due to contamination within the MALDI-TOF instrument.**

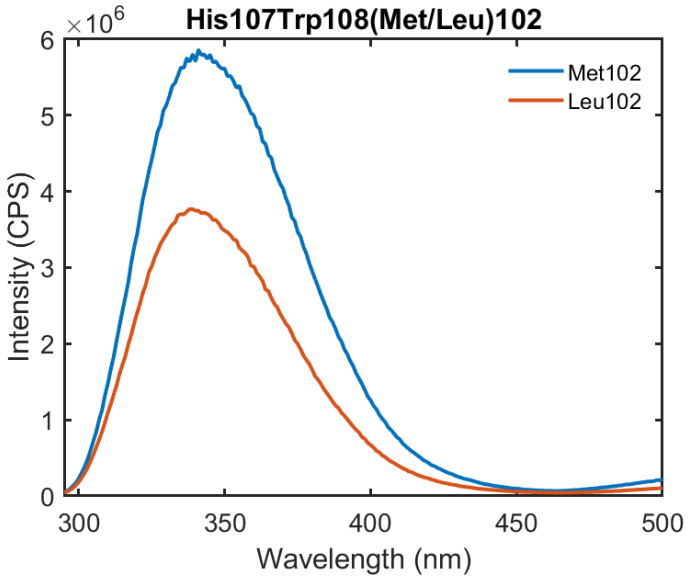

Figure B3. **Raw data for the emission spectra of His107Trp108Met102 (blue) and His107Trp108Leu102 (orange) to investigate whether any fluorescence quenching by Met can be observed.**

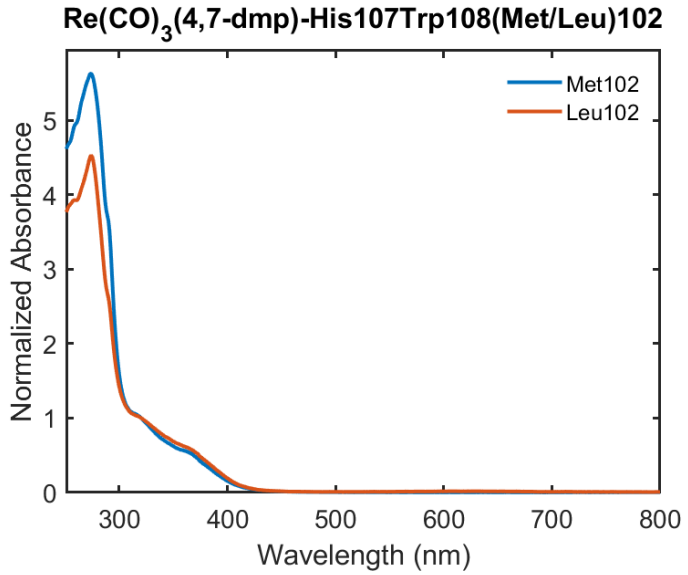

Figure B4. **UV-Vis spectra of $Re(CO)_3$(4,7-dmp)-labeled His107Trp108Leu102 (orange) and His107Trp108Met102 (blue). Spectra were normalized to the 320 nm peak for clarity. Both proteins in this spectra were Zn(II) derivatives.**

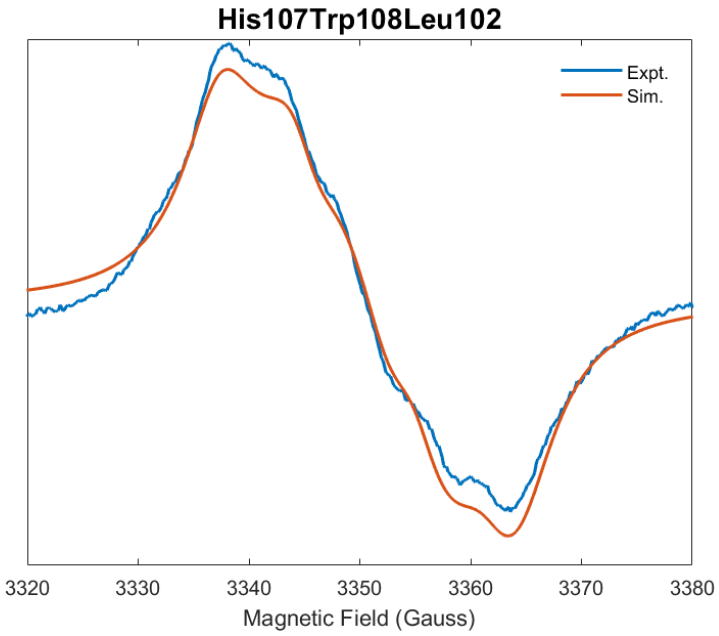

Figure B5. **X-band (9.4 GHz) EPR spectra overlayed for the Trp radical in His107Trp108Leu102 in 50 mM NaP_i at pH 7.5 taken at 100 K. The experimental data are shown in blue and the simulation is in orange.**

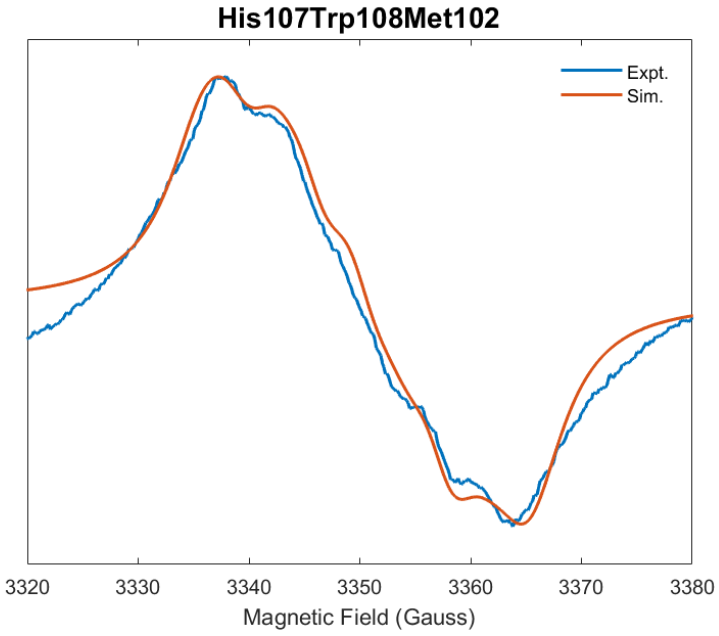

Figure B6. **X-band (9.4 GHz) EPR spectra overlayed for the Trp radical in His107Trp108Met102 in 50 mM NaP_i at pH 7.5 taken at 100 K. The experimental data are shown in blue and the simulation is in orange.**

Appendix C

Supplementary Information from Chapter 4

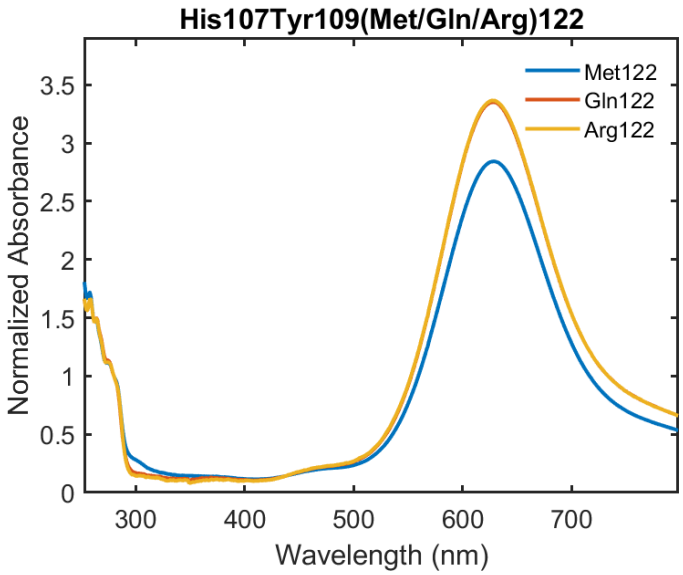

Figure C1. **UV-vis spectra of His107Tyr109Met122 (blue), His107Tyr109Gln122 (orange), and His107Tyr109Arg122 (yellow). Absorbance was normalized to the 280 nm peak.**

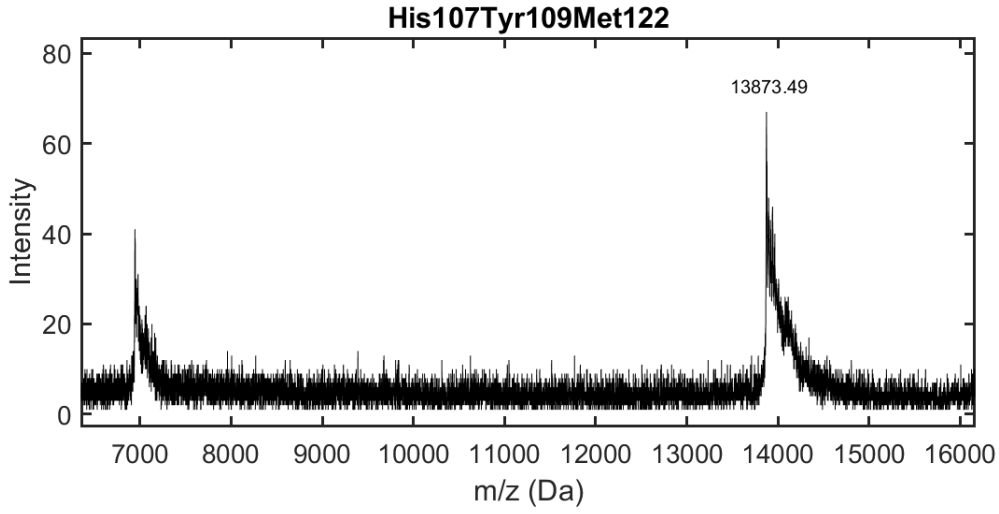

Figure C2. **MALDI-TOF mass spectrometry of His107Tyr109Met122. Calculated mass: 13868.74 Da. Observed mass: 13873.49 Da.**

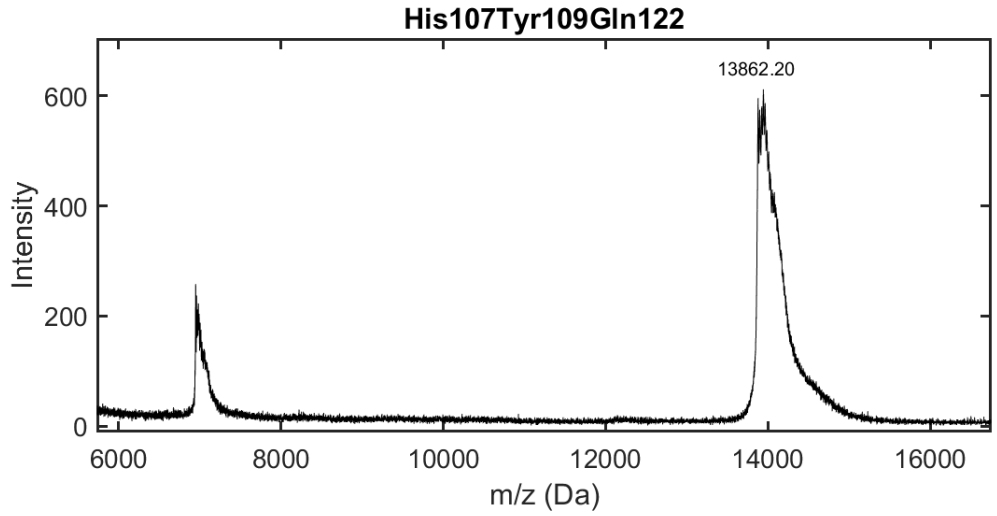

Figure C3. MALDI-TOF mass spectrometry of His107Tyr109Gln122. Calculated mass: 13865.68 Da. Observed mass: 13862.20 Da.

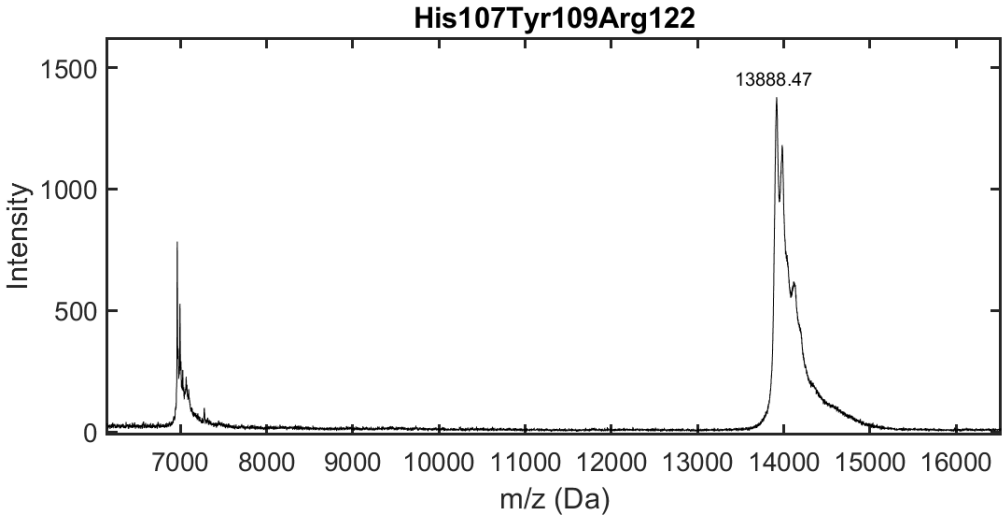

Figure C4. MALDI-TOF mass spectrometry of His107Ty109Arg122. Calculated mass: 13893.74 Da. Observed mass: 13899.47 Da.

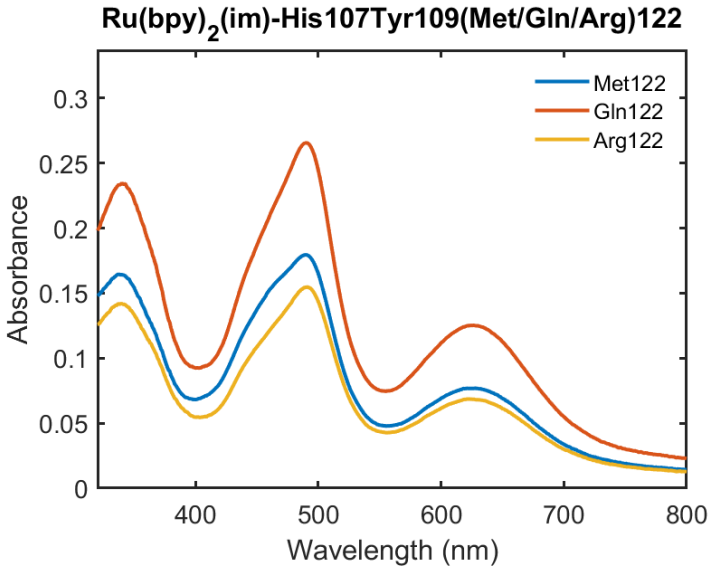

Figure C5. **UV-vis spectra of Ru(bpy)$_2$(im)-labeled His107Tyr109Met122 (blue), His107Tyr109Gln122 (orange), and His107Tyr109Arg122 (yellow). Absorbance was not normalized and concentrations are different for each protein sample.**

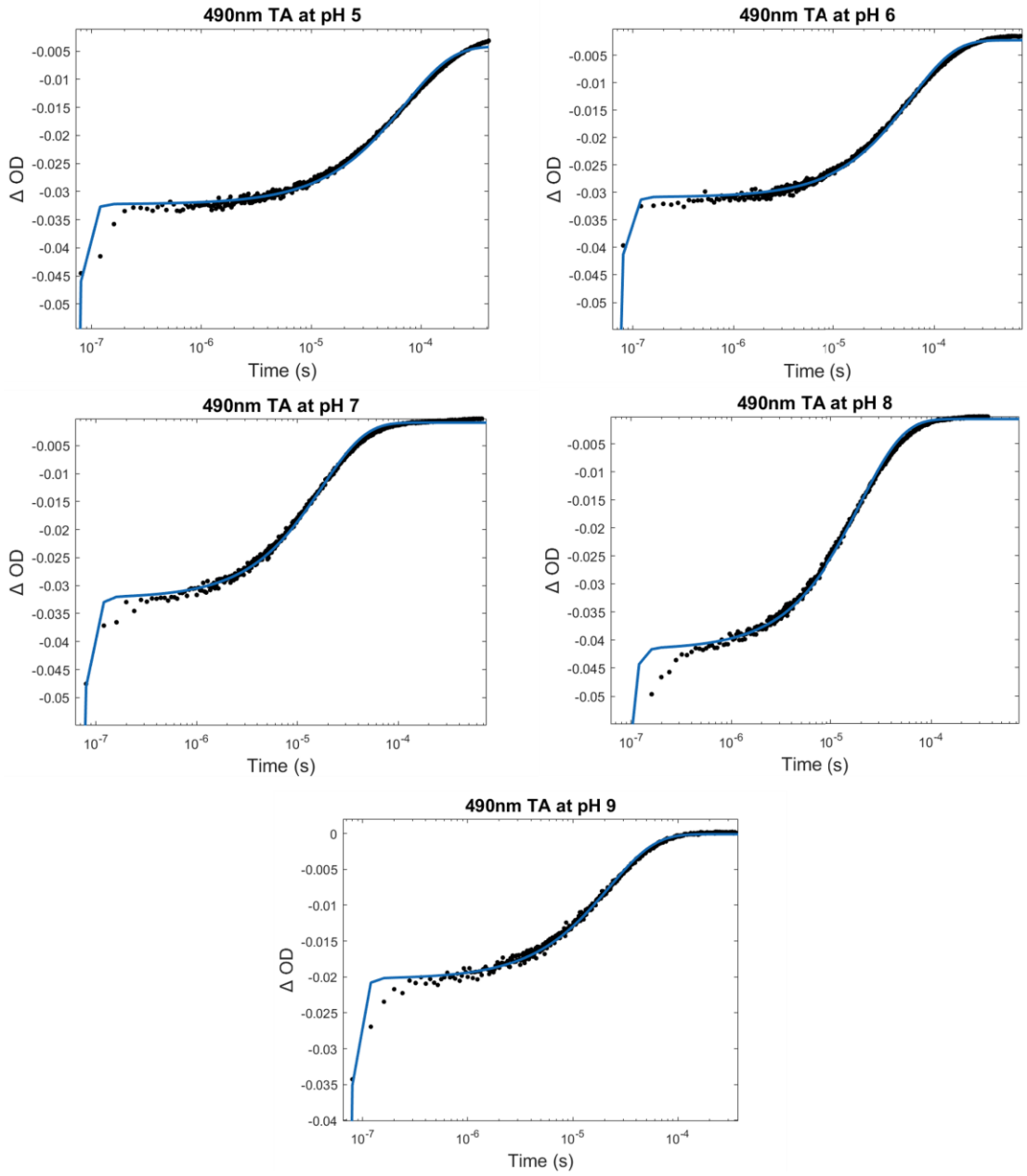

Figure C6. **TA kinetic traces for the reduction of Ru(III) to Ru(II) in 35 μM His107Tyr109Met122 azurin across the pH range of 5-9. Experiments were carried out in 100 mM NaCl, 250 mM imidazole, at their respective pH values. $[Ru(NH_3)_6]^{3+}$ was added to a final concentration of 10 mM. A more detailed description of experimental setup and be found in section 4.4.7.**

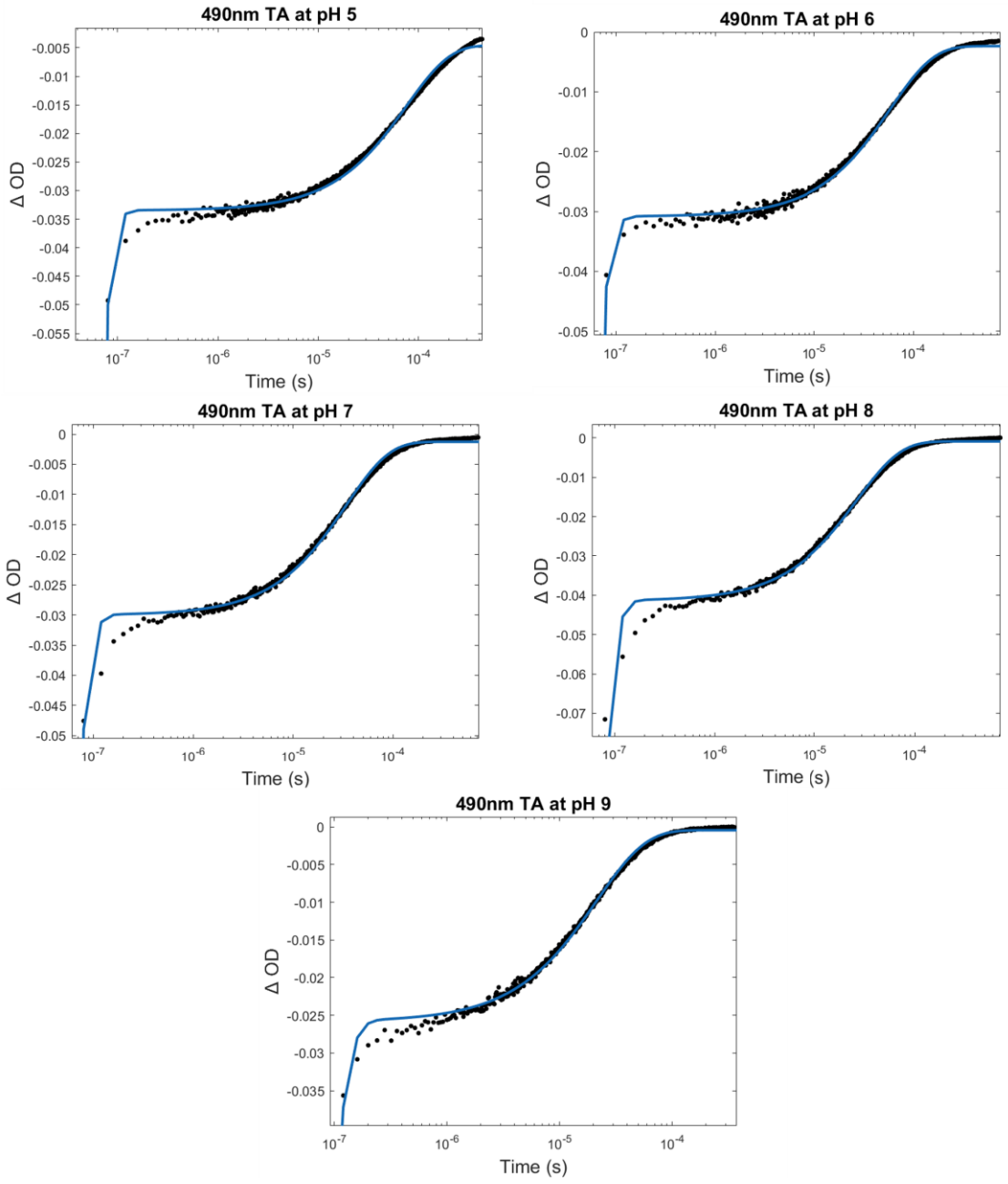

Figure C7. **TA kinetic traces for the reduction of Ru(III) to Ru(II) in 35 μM His107Tyr109Gln122 azurin across the pH range of 5-9. Experiments were carried out in 100 mM NaCl, 250 mM imidazole, at their respective pH values. $[Ru(NH_3)_6]^{3+}$ was added to a final concentration of 10 mM. A more detailed description of experimental setup and be found in section 4.4.7.**

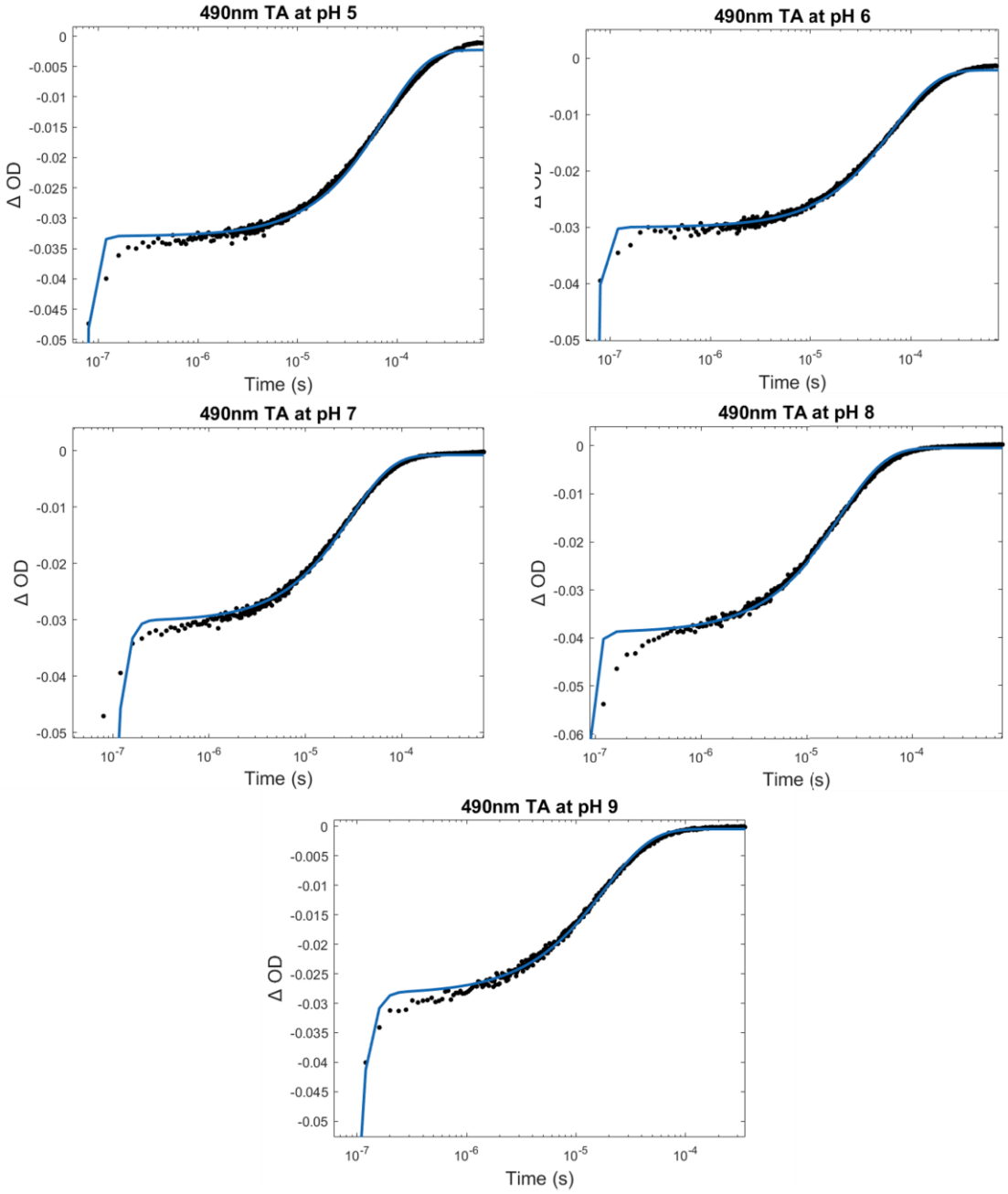

Figure C8. **TA kinetic traces for the reduction of Ru(III) to Ru(II) in 35 μM His107Tyr109Arg122 azurin across the pH range of 5-9. Experiments were carried out in 100 mM NaCl, 250 mM imidazole, at their respective pH values. $[Ru(NH_3)_6]^{3+}$ was added to a final concentration of 10 mM. A more detailed description of experimental setup and be found in section 4.4.7.**

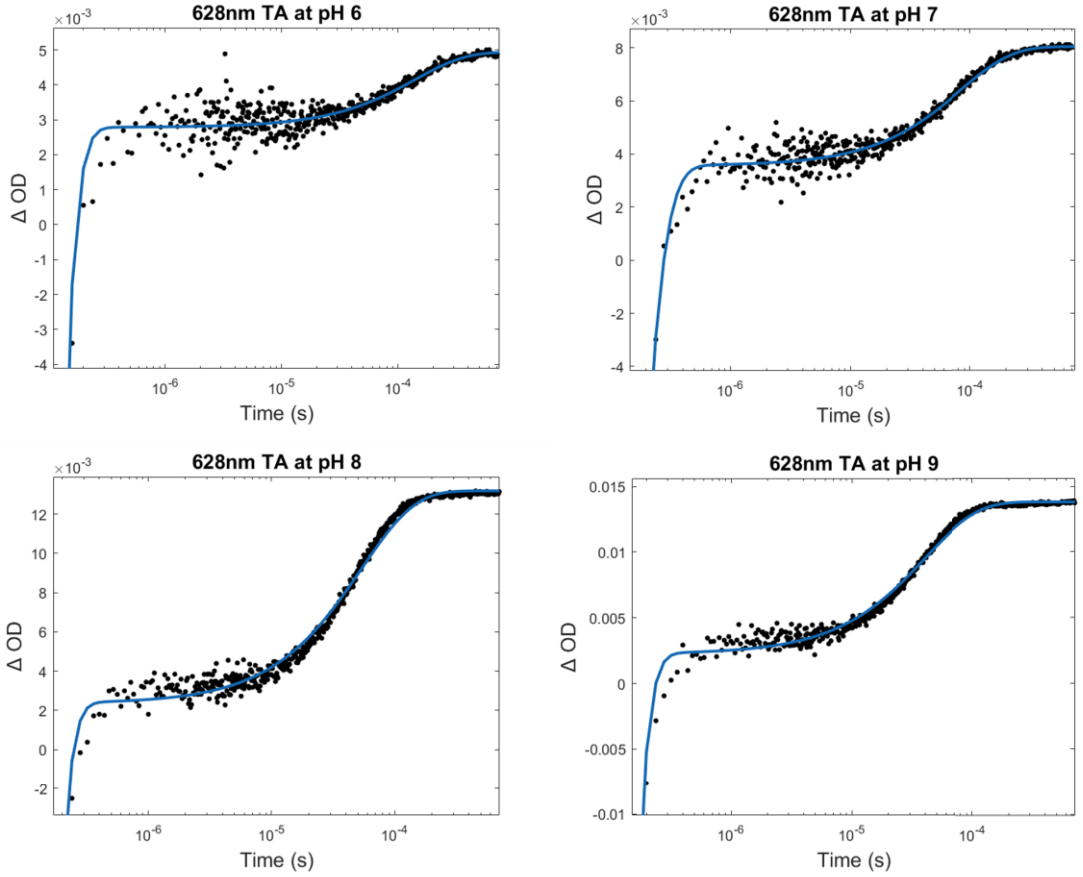

Figure C9. **TA kinetic traces for the oxidation of Cu(I) to Cu(II) in 35 μM His107Tyr109Met122 azurin across the pH range of 5-9. Experiments were carried out in 100 mM NaCl, 250 mM imidazole, at their respective pH values. $[Ru(NH_3)_6]^{3+}$ was added to a final concentration of 10 mM. A more detailed description of experimental setup and be found in section 4.4.7.**

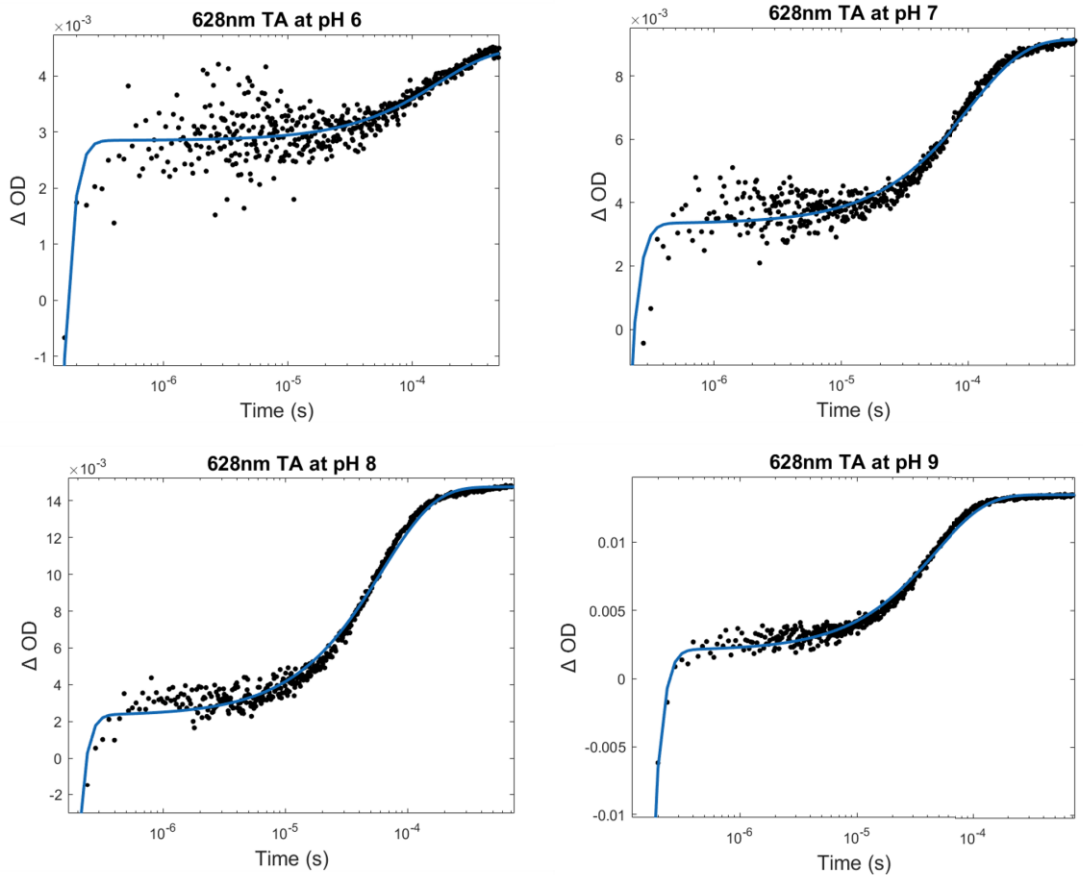

Figure C10. TA kinetic traces for the oxidation of Cu(I) to Cu(II) in 35 μM His107Tyr109Gln122 azurin across the pH range of 5-9. Experiments were carried out in 100 mM NaCl, 250 mM imidazole, at their respective pH values. $[Ru(NH_3)_6]^{3+}$ was added to a final concentration of 10 mM. A more detailed description of experimental setup and be found in section 4.4.7.

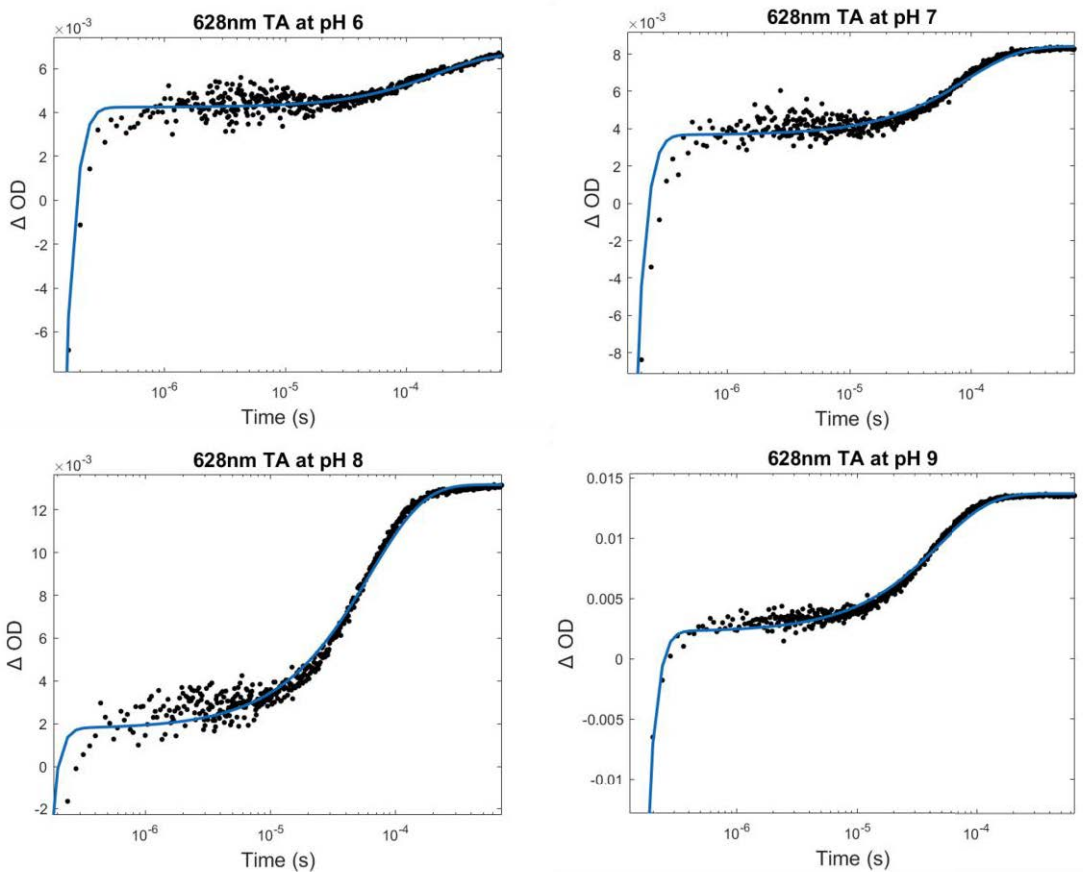

Figure C11. **TA kinetic traces for the oxidation of Cu(I) to Cu(II) in 35 μM His107Tyr109Arg122 azurin across the pH range of 5-9. Experiments were carried out in 100 mM NaCl, 250 mM imidazole, at their respective pH values. $[Ru(NH_3)_6]^{3+}$ was added to a final concentration of 10 mM. A more detailed description of experimental setup and be found in section 4.4.7.**

Appendix D

Supplementary Information from Chapter 5

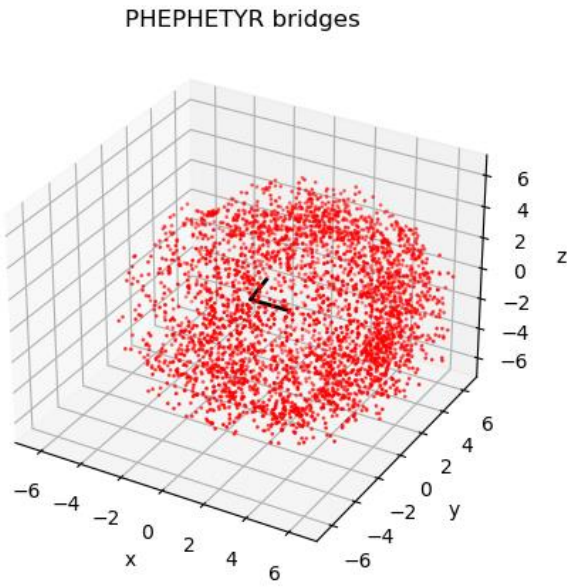

Figure D1. **Plots of clustering of Phe and Tyr around Met in {Phe, Phe, Tyr} bridges. The x, y, and z axes are in Ångstroms. The black V-shape at the origin depicts the CH_3-S-CH_2 thioether of Met. The arm pointing away from the reader (along +y) is the CH_2 group. Each point corresponds to an aromatic centroid for each respective amino acid residue.**

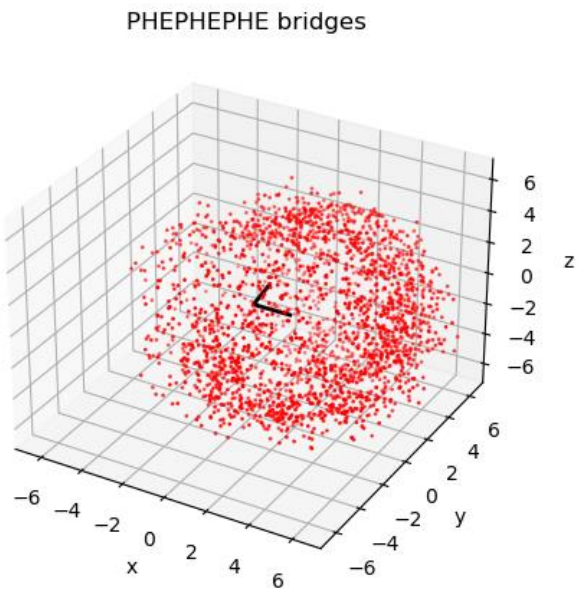

Figure D2. **Plots of clustering of Phe around Met in {Phe, Phe, Phe} bridges. The x, y, and z axes are in Ångstroms. The black V-shape at the origin depicts the CH_3-S-CH_2 thioether of Met. The arm pointing away from the reader (along +y) is the CH_2 group. Each point corresponds to an aromatic centroid for each respective amino acid residue.**

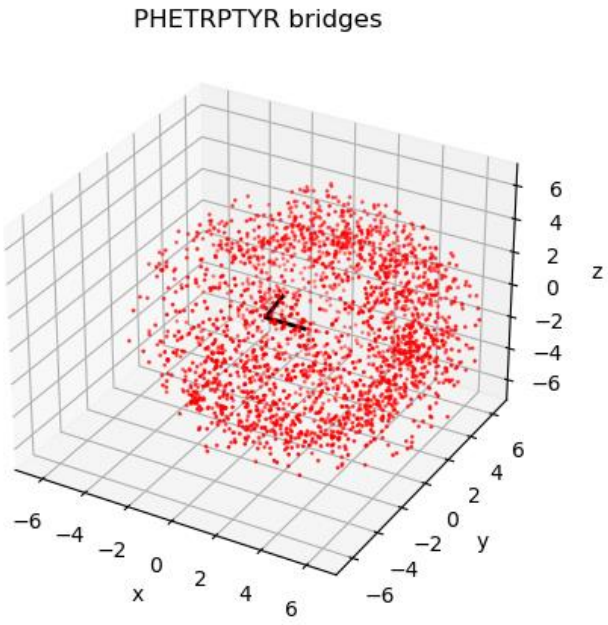

Figure D3. **Plots of clustering of Phe, Trp, and Tyr around Met in {Phe, Trp, Tyr} bridges. The x, y, and z axes are in Ångstroms. The black V-shape at the origin depicts the CH_3-S-CH_2 thioether of Met. The arm pointing away from the reader (along +y) is the CH_2 group. Each point corresponds to an aromatic centroid for each respective amino acid residue.**

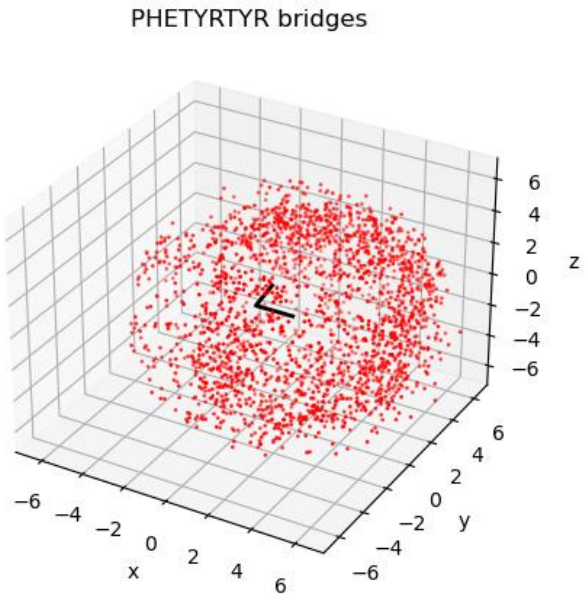

Figure D4. **Plots of clustering of Phe, Tyr, and Tyr around Met in {Phe, Tyr, Tyr} bridges. The x, y, and z axes are in Ångstroms. The black V-shape at the origin depicts the CH_3-S-CH_2 thioether of Met. The arm pointing away from the reader (along +y) is the CH_2 group. Each point corresponds to an aromatic centroid for each respective amino acid residue.**

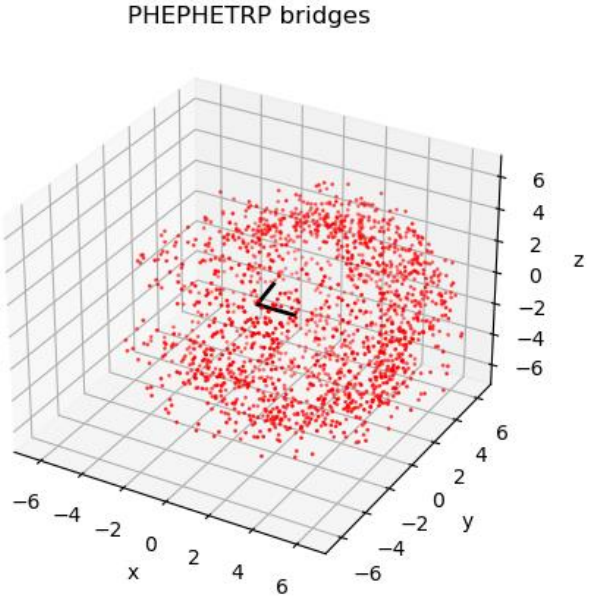

Figure D5. **Plots of clustering of Phe, Phe, and Trp around Met in {Phe, Phe, Trp} bridges. The x, y, and z axes are in Ångstroms. The black V-shape at the origin depicts the CH_3-S-CH_2 thioether of Met. The arm pointing away from the reader (along +y) is the CH_2 group. Each point corresponds to an aromatic centroid for each respective amino acid residue.**

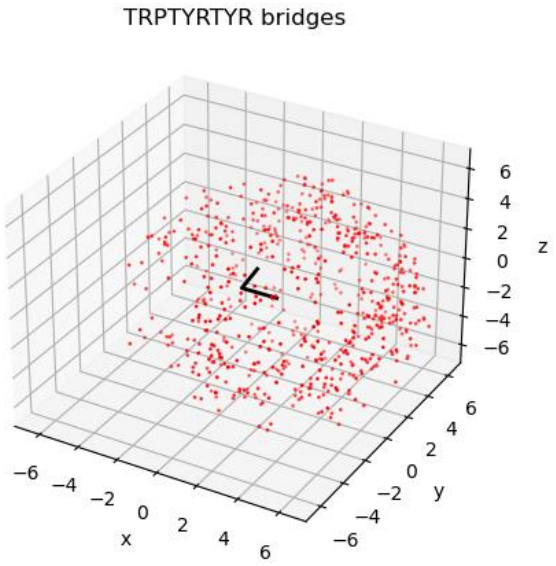

Figure D6. **Plots of clustering of Trp, Tyr, and Tyr around Met in {Trp, Tyr, Tyr} bridges. The x, y, and z axes are in Ångstroms. The black V-shape at the origin depicts the CH_3-S-CH_2 thioether of Met. The arm pointing away from the reader (along +y) is the CH_2 group. Each point corresponds to an aromatic centroid for each respective amino acid residue.**

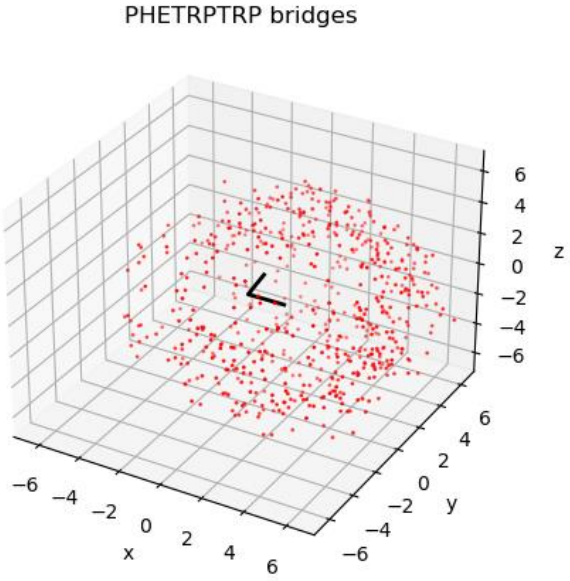

Figure D7. **Plots of clustering of Phe, Trp, and Trp around Met in {Phe, Trp, Trp} bridges. The x, y, and z axes are in Ångstroms. The black V-shape at the origin depicts the CH_3-S-CH_2 thioether of Met. The arm pointing away from the reader (along +y) is the CH_2 group. Each point corresponds to an aromatic centroid for each respective amino acid residue.**

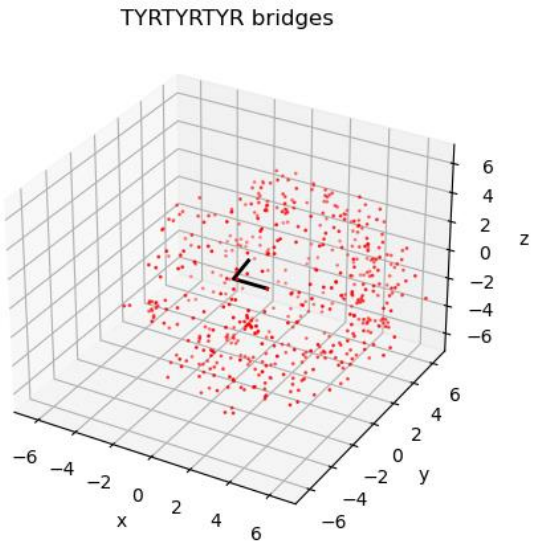

Figure D8. **Plots of clustering of Tyr, Tyr, and Tyr around Met in {Tyr, Tyr, Tyr} bridges. The x, y, and z axes are in Ångstroms. The black V-shape at the origin depicts the CH_3-S-CH_2 thioether of Met. The arm pointing away from the reader (along +y) is the CH_2 group. Each point corresponds to an aromatic centroid for each respective amino acid residue.**

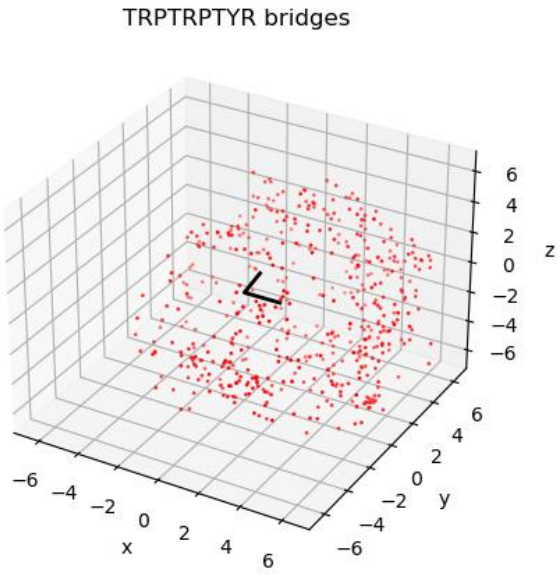

Figure D9. **Plots of clustering of Trp, Trp, and Tyr around Met in {Trp, Trp, Tyr} bridges. The x, y, and z axes are in Ångstroms. The black V-shape at the origin depicts the CH_3-S-CH_2 thioether of Met. The arm pointing away from the reader (along +y) is the CH_2 group. Each point corresponds to an aromatic centroid for each respective amino acid residue.**

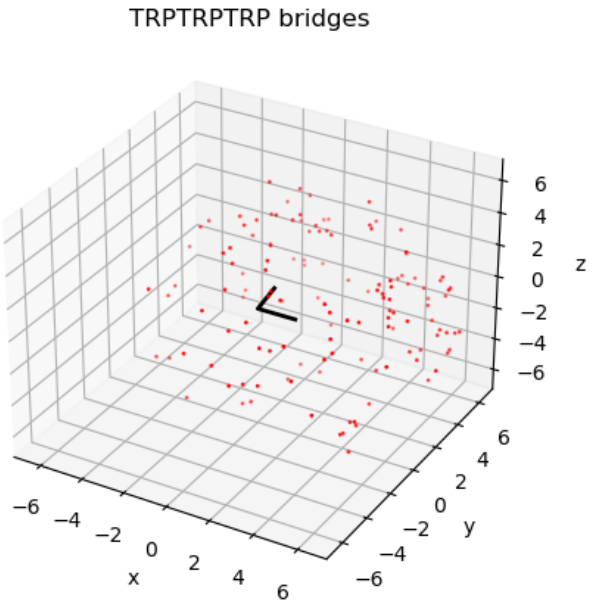

Figure D10. **Plots of clustering of Trp, Trp, and Trp around Met in {Trp, Trp, Trp} bridges. The x, y, and z axes are in Ångstroms. The black V-shape at the origin depicts the CH_3-S-CH_2 thioether of Met. The arm pointing away from the reader (along +y) is the CH_2 group. Each point corresponds to an aromatic centroid for each respective amino acid residue**